Studies on Multi-Harmonic Collinear Accelerating Structures for High Gradient Applications

Lee Robert Carver

School of Physics and Astronomy

A thesis submitted to the University of Manchester for the degree of Doctor of Philosophy in the Faculty of Engineering and Physical Sciences

2015

Studies on Multi-Harmonic Collinear Accelerating Structures for High Gradient Applications

Lee Robert Carver
Supervisor: Prof. Roger Jones

School of Physics and Astronomy,
University of Manchester,
Brunswick Street, Manchester,
M13 9PL, UK

This work was funded by the Science and Technology Facilities Council.

Contents

Abstract

Studies on Multi-Harmonic Collinear Accelerating Structures for High Gradient Applications

Lee Carver
The University of Manchester
For the degree of Doctor of Philosophy

High gradient acceleration is a core challenge of accelerator physics. Achieving high gradients is made challenging by issues relating to rf breakdown and pulsed surface heating, which are caused by intense surface fields in the accelerating cavities. The excitation of multiple harmonically related modes within a cavity could reduce the onset of these effects. The temperature rise from pulsed surface heating can be reduced by lowering the average magnetic surface field squared and rf breakdown could be avoided by creating an asymmetry between the anode and cathode surface electric fields. This thesis will present several different cavity designs that show a reduction in the temperature rise on the surface of over 10% for second and third harmonic cavity structures or an asymmetry in the surface electric anode and cathode fields of a factor of 2. The harmonic mode could have undesirable consequences for beam stability. A study of the longitudinal beam dynamics is included that will derive the equations governing the longitudinal motion and show that the harmonic mode will have a minor and predictable effect on the rf bucket.

The Compact LInear Collider (CLIC) is a major contender for the next generation of lepton linear colliders and is made challenging by high power requirements and distribution throughout the linac. A high current drive beam is decelerated parallel to the main linac in order to create the required rf power, which can overcome some of these issues. This thesis will describe a novel design for a CLIC-like accelerating structure, using collinear acceleration through fundamental mode detuned cavities. The design will accommodate interleaved drive and test bunches, such that the drive bunches are decelerated and the test bunches are accelerated within the confines of the same cavity which can result in high transformer ratios. The analytical theory based on the circuit model will be verified by time domain simulations.

A multi-harmonic detuned accelerating structure is introduced that exhibits the properties of pulsed surface heating reduction and can be used for collinear acceleration. Time domain simulations will verify the transformer ratio to within 3% of theoretical predictions and the average magnetic field squared reduction will be within 20% of the value calculated from eigenmode simulations.

Declaration

No portion of the work referred to in this thesis has been submitted in support of an application for another degree or qualification of this or any other university or other institution of learning.

Lee Robert Carver

Copyright

[1] http://documents.manchester.ac.uk/DocuInfo.aspx?DocID=487
[2] http://www.manchester.ac.uk/library/aboutus/regulations

Acknowledgements

I would like to thank my supervisor Prof. Roger Jones for his countless hours of help and supervision. This thesis would not have been possible without his continuous support and expertise.

I would also like to thank Yong Jiang and Jay Hirshfield for allowing me the opportunity to work and study with them in their laboratory at Yale University for a year. My skills as a physicist improved greatly during my time there and it is all because of their guidance and patience.

I am incredibly grateful for the support of all my friends and family over the past 4 years.

A special mention goes to Aaron Farricker who has kindly agreed to print and bind the thesis on my behalf, and to Ewen Maclean for allowing me to use his thesis template.

Finally, I would like to extend a special thank you to my wife, Carly, who has been a constant source of love and support throughout the entire process.

Lee Robert Carver

Introduction

The size and shape of particle accelerators can vary, from the small cathode ray tubes that formed the early television sets, to the 27 km Large Hadron Collider (LHC) [1] which can accelerate and collide protons up to a centre of mass energy of 13 TeV and recreate the conditions immediately after the big bang. Originally constructed to probe the structure of the atomic nucleus through scattering experiments [2], they have found a wide variety of uses in academia, medicine, defence and security [3–5]. The output energy of particles in particle accelerators have been increasing since the first voltage multipliers were used to accelerate protons in the 1930's [6]. For lepton acceleration at the modern energy frontier, linear accelerators are viable candidates. There is general agreement within the particle physics community that the accelerator to succeed the LHC will be an electron-positron (e^+e^-) linear collider. The Compact LInear Collider (CLIC) is a proposed 48 km room temperature e^+e^- collider with a collision energy of 3 TeV and an average acceleration gradient of 100 MV/m [7]. One of the main challenges associated with CLIC is powering the main accelerating cavities. In order to achieve this, CLIC will decelerate a high current drive beam parallel to the main linac to create the rf power for the test beam, essentially operating the accelerator as a very large klystron. While this is an effective solution that significantly reduces the number of klystrons required, it is an expensive endeavour.

This thesis will demonstrate that an accelerating structure can be built which allows wakefield acceleration with both drive and test bunches travelling collinearly through the cavity. The high current drive beams will experience a decelerating field, expelling rf power into the cavity, and the low current test beam will experience high accelerating fields as a result. This wakefield accelerator could reduce the cost of the machine, as there is no longer any need for the decelerating cavities of the linac or the power transfer structures and

will allow transformer ratios that greatly exceed the current maximum transformer ratio for collinear accelerators while maintaining high beam-to-beam efficiencies. The accelerating structure will be modelled numerically and through simulations in both time and frequency domain and the results will be shown to agree with circuit model theory [8]. This is the first time a structure such as this has been modelled with time domain simulations.

When moving to the high gradients, as proposed for CLIC, many challenges arise that can limit the performance of the accelerator. Intense surface electric and magnetic fields present in the rf cavities can cause the cavities to undergo electrical breakdown [9] and pulsed surface heating [10]. Both of which can severely damage the surface of the cavities and have a negative effect on the luminosity of the accelerator. Multi-harmonic cavities can reduce these effects and this thesis will verify the potential benefits described by introducing and simulating several novel multi-harmonic cavity structures. This can reduce the temperature rise on the cavity surface and potentially prevent the onset of rf breakdown. The additional harmonic can have a negative impact on the longitudinal stability of the cavities, potentially reducing the size of the size of the rf bucket. This thesis will also derive and apply a Hamiltonian that is capable of describing the longitudinal motion of a particle as it moves through a linac that is comprised of a chain of multi-harmonic cavities. This is an original contribution to the field, and could be expanded to apply to a wide variety of multi-harmonic accelerating accelerating linacs with different operational parameters.

This will be followed by theory and simulations that describe a detuned multi-harmonic cavity. A cavity structure that excites multiple harmonics and allows collinear acceleration could form the basis of a highly efficient lepton linear collider that reliably operates at accelerating gradients in excess of 100 MV/m. The simulations will demonstrate for the first time that pulsed surface heating reduction is realistically attainable for multi-harmonic collinear cavities.

Chapters 1-3 introduces some general physics associated with particle accelerators and rf cavities, with emphasis placed on the current status of high-gradient accelerator physics. Chapter 4 provides an overview of wakefield acceleration, including examples of current and future wakefield accelerators. Chapter 5 will provide simulations and numerical models for a fundamental mode detuned accelerating cavity that only excites a single mode. This

will be followed by Chapter 6 which will show the potential benefits of multi-harmonic cavities. This chapter will include a study of the longitudinal stability of multi-harmonic cavities in high-gradient linear accelerators. These two advances in rf technology will then be combined into a full accelerating structure, with frequency and time domain simulations being presented in Chapter 7.

Chapter 1

Particle Accelerators

Particle accelerators can be separated into two main categories: circular and linear. The particle dynamics in each case can effect the suitability of the accelerator for operation with different particle species and different physics goals. A brief introduction into these effects will be given. There are two proposed linear accelerators to succeed the Large Hadron Collider, the International Linear Collider (ILC) and the Compact Linear Collider (CLIC), each of these accelerators will be discussed. When moving to the high gradient regime, many problems arise due to the heating of the cavity surface and electrical breakdown. These high gradient challenges will be introduced.

1.1 The Energy Frontier

The highest energy accelerator currently in operation is the Large Hadron Collider (LHC) at CERN in Geneva, Switzerland. The LHC has a circumference of 27 km, with 4 different interaction points (IP) and at present can accelerate beams of protons up to 6.5 TeV per beam [1]. At each of the different IP's are particle detectors that track and record the trajectories of the particles that are created in the collisions. This energy is extremely challenging to achieve, and requires hundreds of thousands of individual components working in harmony and operating at the forefront of accelerator technology. Each detector is designed and calibrated to observe different particle decays from the exotic particles that are created in the high energy collisions. A large complex is needed in order to accelerate protons up to the injection energy of 450 GeV required for the LHC. The main CERN accelerator complex can be found in figure 1.1. The accelerator complex has many experiments branching off at different proton energies, for example ISOLDE [11] uses the protons from the PS for fixed target experiments to generate exotic heavy nuclei for nuclear physics experiments, and also the AWAKE project [12], which is a planned plasma wakefield experiment that will use the 450 GeV beam from the SPS.

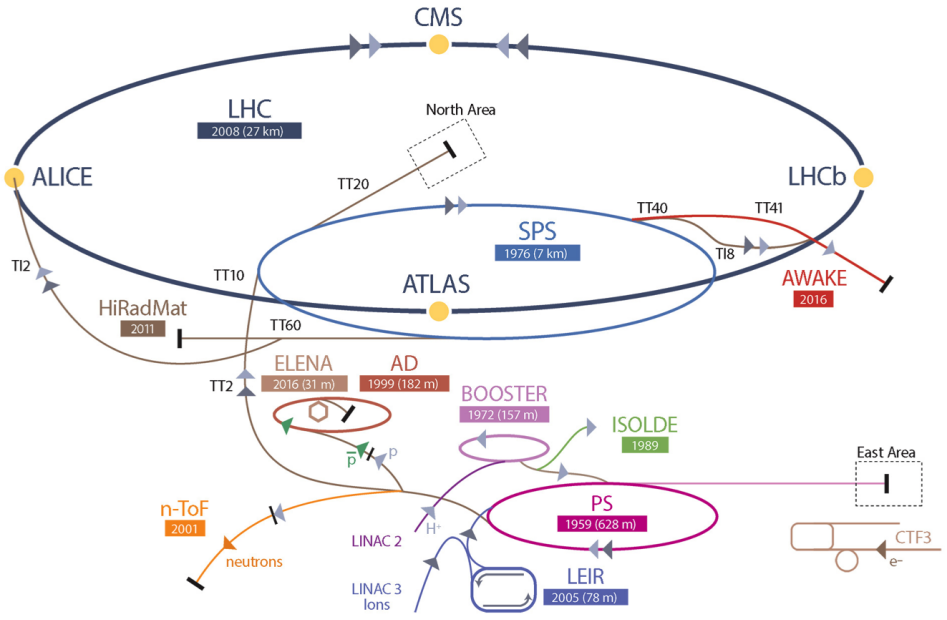

Figure 1.1: The layout of the CERN accelerator complex. The LHC pre-accelerators are LINAC2 (or LINAC3 for ions), the Proton Synchrotron Booster (PSB), the Proton Synchrotron (PS) and the Super Proton Synchrotron (SPS). Many other experiments branch off from these pre accelerators using the proton bunches at different energies.

While the rf cavities of the LHC are normal conducting, much of the accelerator is supercooled to approximately 3 K in order to utilise the superfluidity of ^{3}He [13]. Due to the effectively zero viscosity, the ^{3}He can overcome the forces of gravity and the effects of surface tension, and creep along surfaces allowing it to efficiently cover a wide area. This allows the dipole magnets to be cooled to low temperatures, causing them to become superconducting. Superconducting magnets make it possible to obtain much higher magnetic field strengths (due to the higher currents that the coils can sustain) and improve the stability of the magnetic field (as there is effectively zero power loss in the magnetic coils). This allows the dipole magnets to be powered more efficiently, as well as creating magnetic field strengths greatly in excess of what can be achieved with normal conducting magnets. The LHC superconducting magnets can reach approximately 8 T [1].

Some fundamental parameters that describe the performance and operation of a particle accelerator will now de described.

1.2 Centre of Mass Energy and Luminosity

When discussing beam dynamics, a cartesian co-ordinate system will be used that has a particle moving along the z-axis. A particle of mass m can be expressed by its momentum p^* and energy U which form a four-vector $p = (U, p^*)$ [14]. This gives

$$p^2 = U^2 - (p^*)^2 = m^2. \tag{1.1}$$

In the case of a collision between two particles of masses m_1 and m_2, the total centre of mass energy U_{cm} can be expressed as

$$(p_1 + p_2)^2 = U_{cm}^2 = (U_1 + U_2)^2 - (p_1^* + p_2^*)^2. \tag{1.2}$$

If the collision point is at rest in the laboratory frame ($p_1^* = -p_2^*$), then U_{cm} becomes

$$U_{cm}^2 = (U_1 + U_2)^2, \tag{1.3}$$

whereas when one particle is at rest (fixed target collisions), $p_2 = 0$ then

$$U_{cm}^2 = (m_1^2 + m_2^2 + 2m_2U_1). \tag{1.4}$$

Eqn. 1.4 shows a substantial reduction in the energy available for particle generation and is the reason why colliders are preferred over fixed target collisions for particle physics experiments.

An important parameter that can be used to analyse the performance of an accelerator is the luminosity. The luminosity is defined as ratio of the event rate to the interaction cross section of the colliding particles. In the case of an accelerator colliding bunches head-on, it is given as [14]

$$\mathcal{L} = \frac{N_1 N_2}{4\pi\sigma_x\sigma_y} f_{collision}, \tag{1.5}$$

where N_1 and N_2 are the number of particles per individually circulating bunch, $4\pi\sigma_x\sigma_z$ is the cross sectional area of the bunch at the IP with $\sigma_{x,y}$ referring to the Gaussian width of the transverse beam profile (assuming the bunches are moving in the z-direction), with

$f_{collision} = n_b f_0$ is the beam encountering rate, where n_b is the number of bunches and f_0 is the revolution frequency.

In order to increase the luminosity, much emphasis is placed on reducing the beam size as much as possible. This is achieved by careful design of the magnetic lattice, in particular the magnets comprising the beam delivery system (BDS) just prior to each IP. The BDS must be designed such that there are large areas of field free regions (due to the size of the detectors) either side of the IP. In order to achieve this, the bunches traverse a mini-beta insertion [15]. This involves increasing the beta-functions, and therefore the beam size, and using strong focusing magnets to place the particles within the bunch on a trajectory that will cause them focus and their paths will cross at the IP with very small cross sectional areas. The paths they are following will then diverge until they reach the focusing magnet on the other side of the IP.

In practice, the beams are not colliding head-on but approach and cross at a small angle. This is because each beam has its own separate beam pipe, and for geometric considerations, in order for them to collide they can not do so head-on. A method to increase the luminosity of the LHC for a proposed upgrade (High Luminosity - LHC) and currently being tested for the Compact Linear Collider (CLIC - see Section 1.3.2) is to use crab cavities [16]. These are cavities that apply a rotational kick to the bunch, allowing them to rotate as they reach the IP. As the bunches cross, more of the particles from each bunch are available for collision which increases the luminosity. A comparison of the luminosity for several different machines is given in table 1.1.

	U_{cm} [GeV]	$\mathcal{L}$ $[10^{30}\text{cm}^{-2}\text{s}^{-1}]$
SPS ($p\bar{p}$)	315×315	6
Tevatron ($p\bar{p}$)	1000×1000	50
HERA (e^+p)	30×90	40
LHC (pp)	7000×7000	10000
LEP (e^+e^-)	105×105	100
PEP (e^+e^-)	9×3	3000
KEKB (e^+e^-)	8×3.5	10000

Table 1.1: Luminosities for different machines [17].

The integrated luminosity is a measure of the total luminosity over a period of operation of an accelerator given by

$$\mathcal{L}_{int} = \int_0^t \mathcal{L} dt. \tag{1.6}$$

Both the luminosity and the integrated luminosity are good indicators of the performance of an accelerator. If the luminosity is increased, then more data will be available for physics analysis.

Circular accelerators are typically used to produce beams suitable for high energy particle physics. However, depending on the type of particle and the desired centre of mass energy, linear accelerators may be a more ideal type of accelerator to manufacture. The following section will outline the main motivations for using a linear accelerator over a circular one, and will do so using some fundamental equations for accelerator physics.

1.3 Motivation for a Linear Accelerator

Electrons and positrons are fundamental particles who are part of the lepton family [14]. In a collision between an electron and a positron [18], all of the particles momentum contributes to the creation of new particles. This allows the centre of mass energy of the collisions to be tuned so that a particle with a particular mass can be preferentially produced. Hadrons are not fundamental particles, so their initial state is not known. The total momentum contributing to particle production in this case is no longer constant [19], which causes a wide distribution of particles and their decay products. Hadronic collisions are particularly useful for searches for new particles, due to the wide range of particle masses the collisions could create, whereas lepton collisions are useful for the creation of specific particles with a much cleaner background.

However, it is not possible to simply increase the energy of the protons in the LHC. An important relation that determines the size of a circular accelerator is the beam rigidity [20],

$$|Br_{loc}| = \frac{p_z}{0.3}[\frac{\text{GeV}}{\text{c}}], \tag{1.7}$$

where B is the average magnetic field strength of the dipole magnets in the LHC (which can

also be expressed in terms of the magnetic field intensity H), r_{loc} is the local bending radius and p_z is the particle momentum. This relation shows that for a constant dipole field, there is a linear relation between the momentum of the particle and the radius of the arc of a particle trajectory through the magnet. Additionally, in order to keep a particle on the same bending radius, the magnetic field strength must be scaled in accordance with the particle momentum. Currently, circular accelerators are limited by the strength of the dipole magnetic fields, meaning it is not currently possible to increase the energy of the proton beams in the LHC without completely replacing the dipole magnets. The LHC main superconducting magnets have a field strength of 8.7 T [21], with hope that the field strength of dipole magnets can be increased to strengths of approximately 18 T.

Synchrotron radiation is also a limiting factor for circular accelerators [15]. When a particle is moving through a dipole magnet, it experiences a transverse force due to the Lorentz force law [22]. This force causes a re-orientation of the field vectors emanating from the particle which creates radiation that continues along the original path of the particle. The power of this emitted radiation is given by [23]

$$P_{syn} = \frac{\beta^4 c C_\gamma}{2\pi} \frac{U^4}{r^2}, \tag{1.8}$$

where $\beta = \frac{v}{c}$ is the normalised velocity, U is the energy of the particle, c is the velocity of light and $C_\gamma = \frac{4\pi r_0}{3U_0^3}$, with r_0 the classical radius of the particle and $U_0 = m_0 c^2$ is the rest energy of the particle. The radiative energy loss per revolution then becomes

$$\Delta U = P_{syn}/f_0 = \beta^3 \frac{4\pi r_0}{3(m_0 c^2)^3} \frac{U^4}{r}, \tag{1.9}$$

hence synchrotron radiation scales as mass^{-3}. As the rest mass of an electron is 1836 times less than that of a proton, the synchrotron losses will be far greater for electrons ($\approxeq 1836^3$) [19]. A limit is reached when the particle emits a large amount of energy in a single turn of the machine. This is obtained when the power loss from synchrotron radiation matches the energy gain from the rf cavities. In order to increase this peak energy, hadrons are typically used for circular acceleration. This requires stronger magnets to keep a constant bending radius, but allows higher energies due to lower synchrotron losses.

An illustration of this is LEP (Large Electron Positron Collider) [24], at 100 GeV per beam the energy loss per turn for the electrons and positrons was 2.86 GeV. While for the LHC (during the initial running at 3.5 TeV), the protons lose only 6.66keV per turn [1] (the LHC and LEP are of similar size, with the LHC being housed in many of the same tunnels that were used for LEP, with additional straight sections.)

In order to keep the particles moving on a circular path through the tunnel, between 60% and 80% of a circular machine is comprised of dipole magnets, with quadrupole and sextupole magnets for focusing and damping of non-linear effects [25]. The arcs are typically separated by straight sections where the rf cavities are situated.

A key benefit of circular accelerators is that they do not require high acceleration gradients as they can accelerate slowly over many turns. An accelerator of this type is known as a synchrotron and it operates by allowing the power source of the magnetic lattice to ramp slowly, keeping in time with the increase of the particles momentum. This alleviates many issues associated with wakefields (fields excited by leading bunches that have negative effects on trailing bunches) and rf breakdown currently being experienced in high gradient linear colliders as it minimises the effects of Higher Order Modes (HOM's) (discussed in detail in Chapter 2 and 3).

RF parameters for the LHC can be found in table 1.2. The LHC cavities will operate in continuous wave (CW) mode, which means the cavity will contain accelerating fields on time scales that are much longer than the individual bunch trains, even during periods where there are no bunches present. This results in a much larger bunch spacing so the normally strict requirements on the HOM's can be relaxed.

Parameter	Value	Units
Revolution frequency	11.245	kHz
RF frequency	400.8	MHz
Harmonic Number	35460	-
Total RF Voltage	16	MV
Synchrotron frequency	21.4	Hz

Table 1.2: RF parameters for the LHC at collision energy.

In a linear accelerator the bunches can only collide in a single pass at one IP. The accelerator itself is comprised of almost entirely accelerating cavities to try and maximise the energy gain of the bunches. In order to keep the efficiency of the accelerator as high as possible, the accelerating gradients and beam currents must be high and the bunch spacings must be low to minimise the amount of time the klystrons are running. This causes a much greater effect from the wakefields and it is in this high gradient regime that problems arise due to pulsed surface heating and rf breakdown, which is discussed further in section 1.4. Typically, normal conducting cavities operate with pulsed operation, as they require a large input power that becomes inefficient to continue providing when beam is not present. Whereas superconducting cavities operate with CW which is more efficient due to the much longer filling time.

There are two primary designs for a linear e^+e^- collider that could succeed the LHC, the ILC and CLIC. Both designs have unique features that will be discussed in detail below.

1.3.1 ILC

The ILC is a proposed 31km superconducting e^+e^- linear collider with a centre of mass collision energy of 500 GeV, which could potentially upgrade to 1 TeV (by increasing the length of the accelerator) after reliable operation for a period of time [26]. This machine will be complimentary to the LHC, in that it will be used to provide precise measurements of findings at the LHC, as well as further searching for physics beyond the Standard Model. The ILC will be approximately 31 km long, and will have an acceleration gradient of 31.5 MV/m. The layout of the ILC can be found in figure 1.2 and a list of the main parameters can be found in table 1.3.

The cavities are based on the superconducting 1.3 GHz TESLA cavity [27], shown in figure 1.3. The TESLA cavity is a relatively mature piece of hardware that has been extensively tested at DESY for the X-Ray Free Electron Laser (XFEL) project [28] and forms the basis for many superconducting cavities, both in terms of design but also with regard to surface treatment and conditioning. The niobium cavity is a chain of 9 coupled elliptical cavities. The elliptical nature allows one to optimise the Q of the cavity and to minimise the surface fields, which allows higher gradients to be achieved without quenching the superconducting

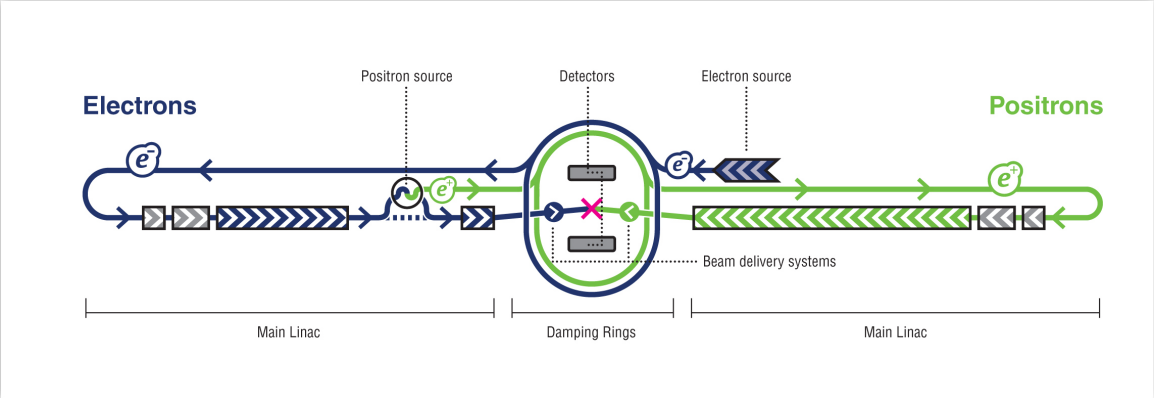

Figure 1.2: A schematic diagram of the ILC accelerator complex.

Parameter	Symbol	Value	Unit
Centre of mass energy	U_{cm}	500	GeV
Main Linac rf Frequency	f_{rf}	1.3	GHz
Luminosity	$\mathcal{L}$	2	$10^{34}\text{cm}^{-2}\text{s}^{-1}$
Linac repetition rate	f_{rep}	5	Hz
No. of particles / bunch	N	2	10^9
No. of bunches / pulse	n_b	2625	
Bunch separation	Δt_b	369.2 (480 periods)	ns
Bunch train length	t_{train}	969000	ns
Beam power / beam	P_b	21	MW
Unloaded / loaded gradient	$E_{unl/l}$	35/31.5	MV/m
Overall two linac length	L_{linac}	22	km
Total beam delivery length	L_{BD}	2 x 2.25	km
Proposed site length	L_{tot}	31	km
Total site AC power	P_{tot}	230	MW
Wall plug to main beam power efficiency	η_{tot}	9.1	%

Table 1.3: Overall parameters for ILC [26].

niobium. On one end is a power coupler which couples rf power into the structure, the power travels through the structure where it will be reflected and set up a standing wave. There is also a higher order mode (HOM) coupler at the opposite end of the structure that removes high frequency, unwanted higher order modes that are excited by the beam.

There are many engineering difficulties involved when building a 31km superconduct-

Figure 1.3: 9-cell superconducting TESLA cavity that is proposed as the main accelerating cavities for the ILC.

ing linac and many lessons are currently being learned by the XFEL project [29]. The low losses in the cavity walls mean they are extremely sensitive to shifts resulting from geometry modifications [30] and small errors. Each cavity must go through a lengthy process of surface conditioning and treatment in order to achieve a smooth inner surface [31, 32] and to minimise frequency errors.

Two detectors are proposed at the IP, the International Large Detector (ILD) and the Silicon Detector (SiD) [33]. A system will be in place that will allow each detector to be slid in and out of of the beam line to allow both detectors to share the single IP.

The ILC is a complex project, with many engineering challenges associated with its size and scale but it is mostly based upon proven technology.

In order to reach higher collision energies, the accelerating gradient needs to be higher. This is not possible with superconducting cavities, which are currently limited at approximately 50 MV/m. At gradients exceeding this, the intense magnetic fields can induce heating that causes the material to heat beyond its critical temperature and become normal conducting. This can lead to a quench. For high gradient machines, superconducting cavities are not suitable.

1.3.2 CLIC

CLIC is a proposed normal conducting multi beam e^+e^- linear collider with a centre of mass energy of 3 TeV and a length of approximately 48 km. Powering the linac with klystrons is costly and inefficient. To overcome this, a high current drive beam (100.5 A) is transported alongside the main linac. This drive beam is decelerated, with the emitted rf power coupled

out of the drive beam linac by the Power Extraction Transfer System (PETS) and coupled into the main linac to be used for acceleration of the colliding bunches. This is the basis on which klystrons operate, albeit on a much larger scale [34]. The key parameters for CLIC can be found in table 1.4 and the layout for the CLIC complex can be found in figure 1.4.

The emittance of a bunch of particles is determined by the average spread of the particles in phase space [15]. For all conserved systems the emittance of a bunch is constant, however synchrotron radiation losses do not satisfy this condition (radiation leaves the system through the walls of the vacuum chamber). This allows the transverse emittance of a bunches to be reduced by allowing them to circulate for many turns in a damping ring (DR) [35]. Each turn in the DR the bunches emit synchrotron radiation in the transverse plane, which reduces the amplitude of its transverse oscillation. Energy is then restored to the bunch by the rf cavities which gives it energy in the longitudinal plane. By allowing the bunches to circulate for many thousands of turns, the transverse emittances of the bunch can be reduced.

The test bunches initially spend time in the DR before they are fed into the booster linac which accelerates the bunches to 9 GeV. The bunches are then separated and transported to the beginning of the main linac. With an average accelerating gradient of 100 MV/m, the bunches are accelerated from 9 GeV to 1.5 TeV over 21.1 km, before entering the BDS prior to the IP.

The drive beam originates in the drive beam accelerator, which accelerates electrons up to 2.38 GeV and transfers them to the combiner rings. The combiner rings take evenly spaced electron bunches, and compress them into high current pulses with much smaller bunch spacings. These combiner rings are used to create the high average current (100.5 A) required to create 100 MW input for the main linacs. These high current bunches are then transported to the drive beam decelerator, where they are decelerated by their own wakefield and the emitted power is fed into the main accelerating cavities.

The power requirements for the ILC are markedly lower than for CLIC, 230 MW as opposed to 392 MW. CLIC requires 4 separate beams to be accelerated (2 drive beams, one electron beam and one positron beam) and reaches a final energy 6 times higher than the ILC so it is unsurprising that this is the case. The ILC cavities operate in CW to minimise the time spent storing the microwave power as field energy in the cavities (this takes a while

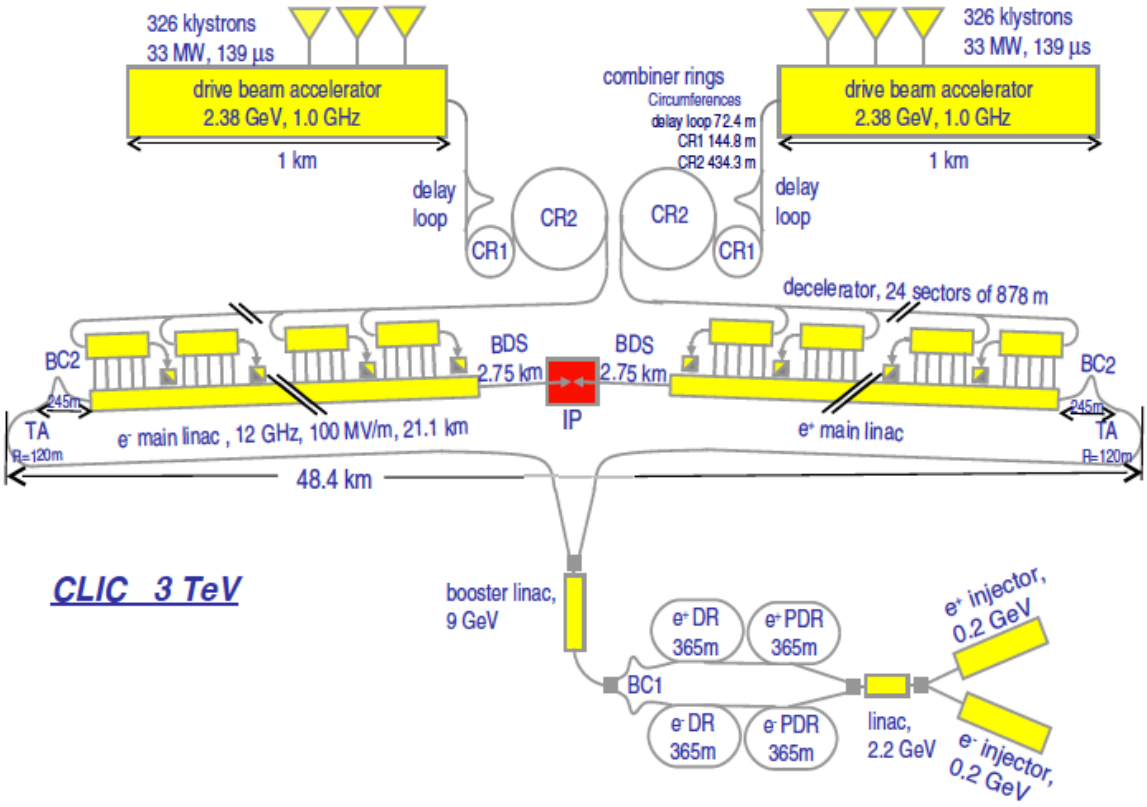

Figure 1.4: Proposed layout for CLIC. Four separate accelerator systems are required in order to achieve high energy electrons and positrons as a separate setup is require for acceleration of the high current drive bunch.

because of the lossless walls). This means the ILC has much longer bunch trains than CLIC (0.969ms vs 156ns) and each train contains many more bunches (2625 for ILC vs 312 for CLIC). Due to the CW nature of the ILC operation, much effort is placed in ensuring HOM's are not resonant with the bunch repetition frequency (which results in strong excitation), as the HOM coupler will provide adequate damping for weakly excited modes, but resonant modes can still remain, even with high bunch spacing (480 rf periods). Conversely, CLIC has pulsed operation, which means the fields must build up to steady state at the beginning of each pulse. In order to keep the efficiency of the accelerator reasonable and to avoid the effect of the transverse wakefield, the bunch spacing had to be made as small as possible ($\Delta t_b = 6$ rf periods). This results in the CLIC cavities being focused on strong and quick

Parameter	Symbol	Value	Unit
Center of mass energy	U_{cm}	3000	GeV
Main Linac RF Frequency	f_{rf}	11.99424	GHz
Luminosity	$\mathcal{L}$	5.9	$10^{34}\text{cm}^{-2}\text{s}^{-1}$
Linac repetition rate	f_{rep}	50	Hz
No. of particles / bunch	N	3.72	10^9
No. of bunches / pulse	n_b	312	
Bunch separation	Δt_b	0.5 (6 periods)	ns
Bunch train length	t_{train}	156	ns
Beam power / beam	P_b	14	MW
Unloaded / loaded gradient	$E_{unl/l}$	120/100	MV/m
Overall two linac length	L_{linac}	42.16	km
Total beam delivery length	L_{BD}	2 x 2.75	km
Proposed site length	L_{tot}	48.4	km
Total site AC power	P_{tot}	392	MW
Wall plug to main beam power efficiency	η_{tot}	7.1	%

Table 1.4: Key parameters for CLIC [7].

damping of all modes so that there is no negative effect on the trailing bunches. The ILC has a higher wall plug to beam efficiency than CLIC, 9.1 % in comparison to 7.1 %, which is due to the fact that not all of the energy is removed from CLIC's drive beam, some is dissipated in the walls of the decelerating structures, or in the power transfer system. The luminosity of CLIC is over double that of the ILC, which is due to CLIC delivering a higher number of particles per second available for collision.

The main accelerating cavities were originally designed to operate with a fundamental mode frequency of 30 GHz, with an average accelerating gradient of 150 MV/m. However, problems with rf breakdown and pulsed surface heating (see section 1.4) for the long pulses required to meet the luminosity needs meant that the several machine parameters needed to be changed, including the cavity frequency [36]. This arose as the result of a large optimisation study that included a wide range of variables that primarily included cost, luminosity and minimisation of surface fields. It was decided to reduce the cavity frequency from 30 GHz to 11.9942 GHz. Additionally, several constraints were placed on the surface electric and magnetic fields in order to avoid these problems in future. These semi-emperical rf constraints are as follows:

1. Surface electric field [37]: $E_{surf}^{max} < 260$MV/m.

2. Pulsed surface heating [38]: $\Delta T^{max} < 56$K.

3. Power [39]: $P_{in}/Ct_p^{1/3} < 18$MW/mm ns$^{1/3}$,

where P_{in}, C and t_p refer to the input power, iris circumference and pulse length respectively. As $\Delta T^{max} \propto \sqrt{t_p}$ and $P_{in}/Ct_p^{1/3}$ depend on the length of the pulse, constraints 2 and 3 can be satisfied by reducing the number of bunches in the train, hence reducing t_p. This has a negative effect on the RF-to-beam efficiency as well as on the luminosity, therefore the train is made as long as possible without providing unreasonable limits on the surface heating and the power.

The transverse wakefield must also be considered in order to ensure that the emittance growth is within the design parameters [7], the long range wakefield needs to have decayed enough prior to the arrival of the next leading bunch. Otherwise the quality of the bunches will degrade along the bunch train, which could lead to a beam break up instability [40]. This allowable limit is given by [7, 41]

$$W_{\perp,max} < \frac{6.67 \times 4 \times 10^9 E_{acc}}{N} \text{[V/(pc mm m)]}, \tag{1.10}$$

where W is the field excited by a leading bunch that acts on a trailing bunch, which is known as a wakefield and is described in Chapter 2, and $E_{acc} = \langle E_0 \rangle$ is the gradient experience by the traversing particle. For $N = 4.2 \times 10^9$, the maximum wakefield at the position of the next trailing bunch must be $W_\perp < 6.3$ V/(pC mm m). Many structures were designed in an attempt to satisfy these constraints [41], with some cavities designed to damp the wakefield strongly, while others attempted to damp moderately but reduce the integrated effect of the wakefield [42]. These types of structures operate by ensuring each cavity cell has a spread in the dipole mode frequencies. The wakefield will quickly decohere while each mode is out of phase, allowing a longer time for adequate damping, before the modes recohere. The CLIC cavitiy is called CLIC G, which was selected after a period of design and optimisation for many different potential structures. The individual cell geometry can be found in figure 1.5 with the full structure shown in figure 1.6.

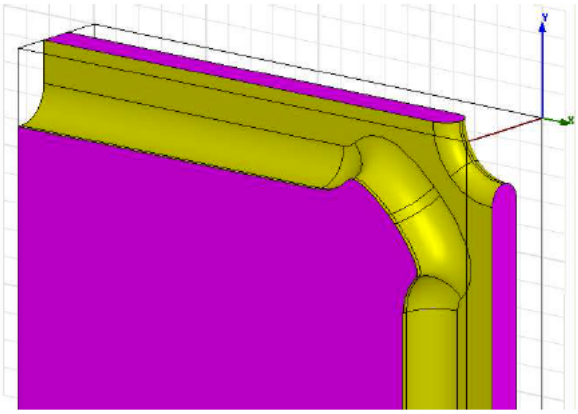

Figure 1.5: One quarter of a CLIC G cell. 28 of these cells will be placed alongside each other, creating a chain of coupled pillbox cavities with heavy waveguide damping (see figure 1.6).

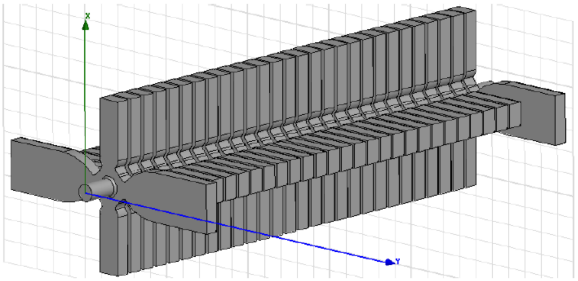

Figure 1.6: A CAD model of a single CLIC G structure [43]. The HOM's are damped with the attached waveguides [44] which prevents them having a degrading effect on trailing bunches.

The cavity cells are manufactured to individual specifications and slotted together and diffusion bonded. Each individual cell has a tuning mechanism that can allow the frequency to be shifted by approximately 5 MHz (corresponding to a geometrical shift of approximately 1 μm [41]). This mechanism also allows a flat field to be achieved between each cell, and the phase advance of the field to be correctly matched. The HOM's are coupled out of the cavity and damped by entering a region of Silicon Carbide (SiC). The material has a very low conductivity, and results in the HOM's power reducing before it returns to the cavity.

Having introduced the CLIC accelerator and its associated challenges, the following section will describe in detail each of the major limiting effects for high gradient acceleration.

1.4 High Gradient Challenges

By entering the high gradient regime, the length of a linear collider can be greatly reduced. However, increasing the input power to the cavities gives rise to some severe effects that can limit the achievable gradient. The high power creates intense electric and magnetic fields on the surface of the cavities, which can cause the surface of the cavity to both heat up and breakdown. Each of these effects results in severe surface degradation. While pulsed surface heating is caused by the magnetic field, it is quite well understood, however the role of the magnetic field within rf breakdown (which is caused by high electric fields) is an active field of study. Each of these effects will be discussed individually.

1.4.1 RF Breakdown

An rf breakdown is a sudden and catastrophic exchange of charge between two electrodes that are separated by vacuum and is caused by a high potential difference [45]. When high power fields (approximately 100 MW at X-band) are present inside a cavity, the surface of the cavity is subject to intense electric and magnetic fields. If the electric field on the surface reaches a certain threshold, the walls of the cavity can breakdown [46].

When a breakdown occurs, the transmission and reflection of the rf power directed towards the structure changes abruptly and significantly [47]. In general, breakdown is accompanied by a burst of x-rays and a bright flash of visible light. A transverse kick of the order of 1kV accompanies the breakdown, which is enough to severely limit the luminosity for that particular bunch train [45]. The behaviour in a breakdown differs slightly between travelling wave (TW) and standing wave (SW) structures. In a TW structure, the transmitted power drops to very low levels with a time constant of 20-200 ns, and up to 80 % of the incident rf power is absorbed by the arc [9]. This value varies depending on the fundamental mode group velocity of the cell where the breakdown occurs [48], with more breakdowns being found at the higher group velocity end of a TW structure. For high group velocity structures, the cavity surface is much more severely damaged, which can further promote breakdowns, while low group velocity structures tend to experience less damage in the result of a breakdown. However for SW structures during a high percentage of the breakdowns, most of the

rf power is reflected from the structure.

The accelerating cavities designed for the Next Linear Collider (NLC) were originally composed of 206 cells, with the group velocity tapering throughout the structure in order to reduce the effects of the transverse wakefield (via cell detuning of the dipole mode) [48]. However, a post mortem of the cavity found that the low group velocity end of the structure was relatively undamaged, with the high group velocity end suffering significant degradation. This study led to a reduction of the group velocity and the power input in an attempt to limit the effect of rf breakdown [49].

The qualitative behaviour of a breakdown event and how it effects the surface and operation of a cavity is relatively well understood, however the event that triggers a breakdown is still an active area of study. An area on the cathode will emit more electrons through field emission than the surrounding material. These areas could be caused by field enhancement due to sharp localised regions within the material. Neutral atoms present in the vacuum can now become ionised by the field-emitted current, which in turn causes them to bombard the surface of the cathode. Both of these factors, ion bombardment and ohmic heating from surface currents, cause the cathode to heat quickly. The temperature increase creates a higher field emission current, increasing the level of ion bombardment. When the cathode location becomes hot enough, it undergoes a phase transition from solid to plasma, creating a plasma sheath that surrounds cathode surface and dramatically increases the electric field. The plasma disperses and the current reduces, and a crater is found at the location of the ion bombardment [9, 45–47]. A measurement of a breakdown crater made using a Scanning Electron Microscope (SEM) can be found in figure 1.7.

In the late 1950's, W.D. Kilpatrick performed a series of experiments to attempt to quantify the behaviour of rf breakdown under various different circumstances [50]. This allowed a numerical relation to be obtained that describes the frequency of the rf field as a function of the maximum achievable electric field, E, inside the cavity, given by [51]

$$\frac{f}{[\text{MHz}]} = 1.64E[\text{MV/m}]^2 e^{-8.5/E[\text{MV/m}]}. \tag{1.11}$$

Eqn. 1.11 is plotted in figure 1.8, which shows a parabolic increase in the allowable rf

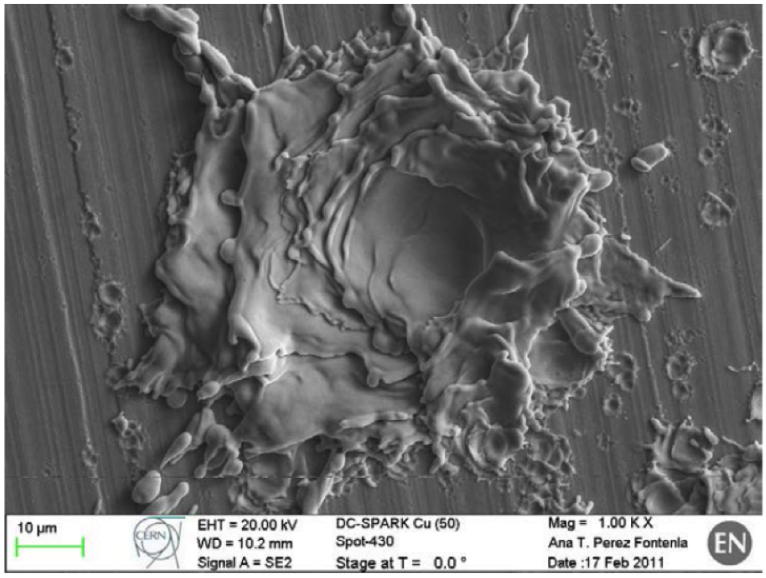

Figure 1.7: SEM measurement of a breakdown crater in copper. Image reproduced courtesy of N. Shipman [45].

frequency with increasing accelerating gradient.

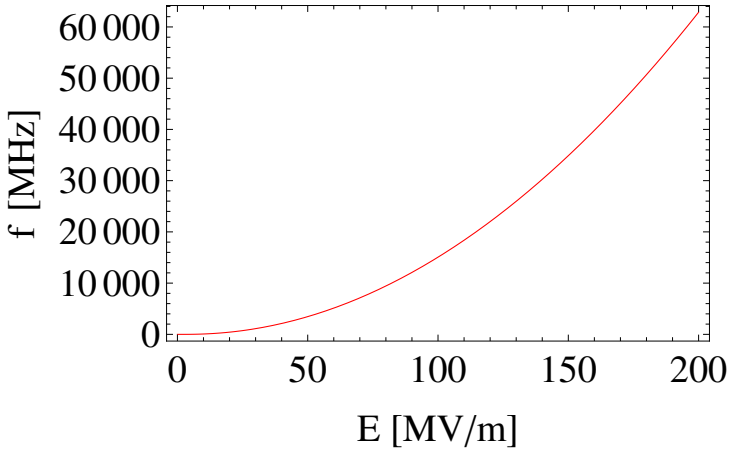

Figure 1.8: The maximum rf frequency allowable for a given accelerating gradient, according to the Kilpatrick limit.

Currently, it is possible to exceed the Kilpatrick limit quite significantly [52]. It has been

found that surface fields in excess of 200 MV/m can be used routinely without significant breakdown issues [53]. This is due to advances in understanding of materials as well as improved surface treatment techniques. At SLAC, an experimental test setup for rf breakdown has been created that allows many different structures to be tested. This has allowed many different cavity parameters to be varied in order to determine its effect on the breakdown rate. For example, the material itself can be varied to allow copper alloys or soft/hard copper, the geometry of the structure (more/less rounding of the iris), the amount of surface conditioning used or the presence of a magnetic field of varying intensity. This has produced a huge amount of experimental data which is enabling a much clearer picture of rf breakdown to be produced.

Through experiments performed at CERN, it has been discovered that the lattice formation plays a role in the susceptibility of a material to breakdown [54]. The lattice formation has a large effect on how lattice dislocations move through the material. This has led to a theory that relates the freedom of dislocations in a material to the development of field enhancement factors on the surface, which could begin the breakdown process [55].

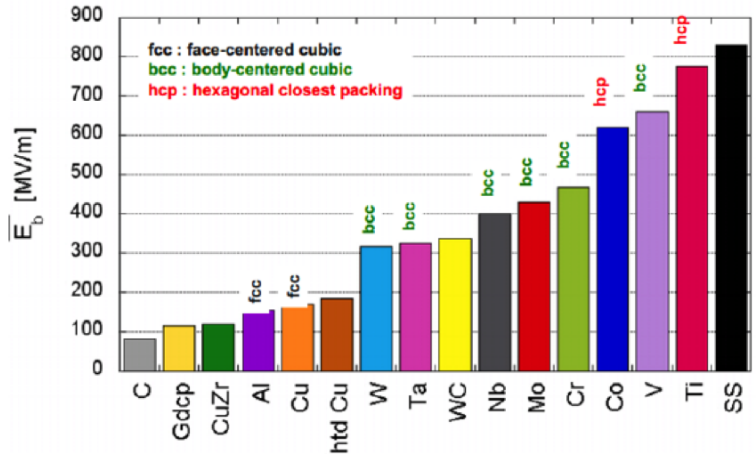

Figure 1.9: Different lattice formations have given rise to a new theory about the material parameters in breakdown [55].

It has been found empirically that the breakdown rate (BDR) scales with approximately E^{30} [45] (to within 5 or 6 orders of magnitude) and a t_p^5 dependence on pulse length. These dependencies have been found across many different experiments using many different ma-

terials. How these guidelines influence the design of a cavity geometry will be explained in further detail in Section 2.8.

1.4.2 Pulsed Surface Heating

The excited fields in a cavity can oscillate for some time, especially for long pulses or multiple short pulses. The intense magnetic fields on the surface of the cavity can flex and shift the metal, causing it to heat up [56]. What may begin as a small micro-fracture (which can create field enhancement and contribute to breakdown) can eventually lead to cracking of the surface. In the dislocation model for rf breakdown, surface heating could potentially play a role in the prevention of breakdown.

The current CLIC baseline design requires a temperature rise of less than 56K on the surface of the cavity [7], which can be calculated according to [57]

$$\Delta T(t) = \frac{1}{\rho C_\epsilon \sqrt{\pi D}} \int_0^{t_p} \frac{dt'}{\sqrt{t-t'}} [\frac{1}{2} R |H_{||}(t')|^2], \tag{1.12}$$

where ρ is the density and C_ϵ is the specific heat of the material, $D = \kappa/\rho C_\epsilon$ with κ as the thermal conductivity, R is the skin resistance, t_p is the pulse length and $H_{||}$ is the tangential magnetic field on the wall. It can be seen from eqn. 1.12 that minimising the magnetic field on the surface is key to keeping the pulsed surface heating within the design constraint. The surface heating is determined by the average value of the $H_{||}^2$-field on the cavity surface. For a single mode cavity, this value is half of the peak $H_{||}^2$ on the surface. The origin of this relation, and further discussion of its implications on cavity design will be found in section 2.8.

An experiment performed at SLAC showed that for a temperature rise of 120K, cracks began to form on the wall of several copper cavities [58]. A temperature rise of 56 K, the constraint placed on the CLIC cavities, will limit to these effects.

1.5 Two-Beam, Two-Mode Accelerating Structure

In order to attempt to overcome the challenges presented by pulsed surface heating and rf breakdown, two novel concepts will be studied in this thesis.

Firstly, by superimposing harmonically related eigenmodes, the average value of $H_{\parallel}^2$ is reduced, which could potentially reduce the surface heating on the cavity wall. Multiple harmonics could also be used to create an asymmetric field profile on the cavity surface that results in the fields pointing into the wall being smaller than fields pointing away. The effect is referred to as the anode-cathode effect [59]. The anode field has the effect of increasing the work function for an electron on the surface, while the cathode field (acting in the opposite direction) reduces the required energy for an electron to be emitted. In some theories of rf breakdown, it is thought that electron emission is a precursor to a breakdown event. This thesis will explore cavity designs that could exhibit each of these effects.

The second concept is that by using a chain of cavities where the fundamental mode is detuned away from the drive bunch frequency (where $f_{cav} \neq f_{rep}$), a high current drive beam and a low current test beam could be interleaved and a transformer ratio (ratio of acceleration field to deceleration field) much greater than two can be achieved [8]. This would remove the need for costly PETS as the energy transfer occurs within the cavity itself, and it would also allow for higher gradients to be achieved without the requirement for fundamental power couplers on the main cavities (which enhance the surface fields). The gradient can easily be varied by adjusting the current of the drive beam, and gradients of up to 100 MV/m could be achieved. Studies verifying the theory with time domain simulations, an original contribution to the field, will be shown here.

This thesis will explore each of these concepts both individually and together within one accelerator structure. This will be the first time that time domain simulations of a collinear multi-harmonic cavity have been presented.

The following Chapters will first give an introduction into the physics of rf cavities and will also describe analytical techniques used to model large chains of coupled cavities. A brief introduction to wakefield acceleration will be presented, before each of the main areas of study will be described.

Chapter 2

Cavities, Wakefields & Impedance

The electromagnetic theory that govern the physics of rf cavities is well documented and thoroughly understood. This chapter aims to give an introduction and overview to the relevant parameters associated with cavity design for the cavities which are the subject of this thesis.

Wakefields and impedances relate the interaction of a particle moving through an accelerator with the surrounding vacuum chamber. A particle traversing an rf cavity can excite fields that have a damaging effect on trailing particles. Fields acting longitudinally can increase the energy spread of a trailing bunch, while transverse fields can cause emittance dilution or form instabilities which could potentially lead to a beam breakup instability (BBU). An introduction to wakefields and impedances will be given, with particular emphasis on the interaction between a particle and an rf cavity. A description of how surface heating and rf breakdown effect cavity design will be described.

The first section will explore the physics that govern the electromagnetic resonances present in a cavity with cylindrical symmetry, before going on to describe how to calculate some key figures of merit for cavities.

2.1 Cavity Modes

Many rf cavities have complex geometries, designed to optimise many different parameters such as the surface electric and magnetic fields, and the efficiency of the cavity in setting up an accelerating field. A large proportion of cavities are based upon a cylindrical resonator cavity because of their inherent symmetry and ease of fabrication, and much can be learnt about the general behaviour of some of these parameters by looking at the analytical solution of the fields inside a cavity of this type. The following work is summarised from [60–62].

Using a cylindrical co-ordinate system, and taking a cylinder of radius a with longitudinal

coordinate z. Parallel conducting plates can be placed at $z = 0$ and $z = g$ to give the geometry for a simple pillbox cavity. In practice, holes are needed on the end plates to allow a beam to pass through, but for simplicity these holes are ignored. By solving the wave equation in cylindrical coordinates [22] and separating the individual parameters, a solution can be found that describes a general field for a pillbox cavity. The most interesting fields are the E_z, E_r and H_θ fields, as it is only these fields that affect the beam and therefore dominate cavity design. These fields are given by [30, 62]

$$E_z^{m,n,p} = \frac{j_n}{a} J_m(j_n \frac{r}{a}) \cos(\frac{\pi p z}{g}) \cos(m\theta) \exp(i\omega_{np} t), \tag{2.1}$$

$$E_r^{m,n,p} = \frac{\pi p}{g} J_m(j_n \frac{r}{a}) \sin(\frac{\pi p z}{g}) \cos(m\theta) \exp(i\omega_{np} t), \tag{2.2}$$

and

$$H_\theta^{n,p} = i\omega_{n,p}\epsilon_0 J_m(j_n \frac{r}{a}) \cos(\frac{\pi p z}{g}) \cos(m\theta) \exp(i\omega_{np} t), \tag{2.3}$$

where J_n and j_n are Bessel functions and zeroes of Bessel functions of the n^{th} kind, m, n and p are the modes numbers for each relevant coordinate and

$$\frac{\omega_{np}^2}{c^2} = (\frac{j_n}{a})^2 + (\frac{\pi p}{g})^2 = \nu_{np}^2 \tag{2.4}$$

determines the eigenvalues of the system (in this case they are the resonant frequencies). These are the ideal field profiles, and can be used to calculate the dependency of cavity figures of merit on cavity parameters [62].

These fields can be used to accurately model any mode excited in a simple pillbox cavity, and can be used to calculate analytical expressions for the cavity figures of merit that can be found in the next section.

2.2 RF Parameters

The quality factor of a resonator is well documented and gives a measure of the level of damping. In the case of an rf cavity, the Q is calculated by [60]

$$Q_n = \frac{\omega_n U_n}{P_c}, \tag{2.5}$$

where P_c is the total power loss of the cavity, ω_n the angular frequency of the mode and U_n is the stored energy of the mode which is defined below. The subscript n refers to the given value for a particular cavity order. A high Q-value corresponds to a lightly damped oscillator and, as such, the mode will remain oscillating for longer than a mode with a low Q-value. The Q also relates to the filling time of a cavity, given by

$$\tau_n = \frac{2Q_n}{\omega_n}. \tag{2.6}$$

The accelerating voltage, or the voltage seen by a single test particle as it traverses the cavity, is given by [27]

$$V_{acc}(r) = \int_0^L E_z(r,z)\exp\left(i\omega_n z/c\right)dz \tag{2.7}$$

where E_z is the z-component of the electric field (so long as the z-component is the direction the beam is travelling), z is the longitudinal position of the beam, r is the radial offset of the beam and L is the length of the cavity. An approximation that r does not change can be made, which is typically true due to the low angle of entry into the cavity. Then the calculation of V_{acc} becomes a straightforward integral. The exponent term in the integral allows the calculation of the voltage to include the oscillation of the field in time.

The total energy stored in the respective mode is given by the volume integral of the field i.e.[27]

$$U_n = \frac{\epsilon_0}{2}\int_{dV} d^3r\left|\mathbf{E_n}\right|^2, \tag{2.8}$$

where ϵ_0 is the permittivity of free space, dV is the volume of the cavity and $\mathbf{E_n}$ is the electric field vector of the mode. At resonance, the stored energy in the electric field is equal to the

stored energy in the magnetic field. Therefore, by replacing ϵ_0 with the magnetic permeability μ_0 and $\mathbf{E_n}$ with the magnetic field intensity, $\mathbf{H_n}$, the stored energy in the magnetic field can be calculated.

An important quantity to consider when studying cavities is the shunt impedance, R_s. This is a measure of how efficiently the cavity can produce a longitudinal voltage. It is defined as [60]

$$R_{s,n} = \frac{|V_{acc}^2|}{P_c}, \tag{2.9}$$

which is often normalised to the cavity length, i.e. $R_{s,n}/L = R'_s$. Therefore superconducting cavities have higher shunt impedances than normal conducting cavities by many orders of magnitude for the same power input, due to the effectively zero power loss on the cavity walls.

From eqn. 2.7 and eqn. 2.8 a loss parameter can be defined for a single mode in the cavity as [27]

$$k_{\parallel,n}(r) = \frac{\left|V_{acc}^{(n)}(r)\right|^2}{4U_n}. \tag{2.10}$$

The loss parameter $k_\parallel$ is a measure of how much energy is deposited into the mode along the axis of acceleration, having been traversed by a particle with charge q [63]. The transverse loss parameter is calculated from the longitudinal loss parameter using the Panofksy-Wenzel theorem (discussed in section 2.3.3) as

$$k_{\perp,n} = \frac{k_{\parallel,n}c}{\omega_n}. \tag{2.11}$$

Using eqn. 2.10, a geometric parameter can be defined as [27]

$$\frac{R_{s,n}}{Q_n} = \frac{1}{r^{2m}}\frac{2k_n(r)}{\omega_n}, \tag{2.12}$$

where m is the azimuthal order of the mode and r is the radial offset of the particle trajectory, i.e for monopole modes $m = 0$, for dipole modes $m = 1$, for quadrupole modes $m = 2$ etc and $k_n = k_{\parallel,n}$ for $m = 0$ or $k_n = k_{\perp,n}$ for higher orders. Eqn. 2.12 is a measure of how effectively the energy in the cavity is being coupled to beam with one key difference: it is

independent of the cavity material; it is a figure of merit that reflects how well the geometry is suited to acceleration. This is useful, as it allows direct comparison between two very different types of cavity (for example between NC and SC cavities).

Finally, the transverse kick factor can be defined which allows the loss parameter to be expressed in such a way that it is independent on the radial offset. It is related to the change in transverse momentum of the beam and it allows the comparison of kicks for different frequency bands and cavity types and is defined as [64]

$$K_n = \frac{c}{2L}\frac{R_{s,n}}{Q_n} = \frac{k_{\parallel,n}c}{\omega_n r^{2m} L}. \tag{2.13}$$

Parameter	Unit	Value
$< E_{acc} >$	MV/m	100
RF frequency: f	GHz	11.994
Phase advance per cell: $\Delta\phi$	Deg	120
Cell length: L	mm	8.333
First and last iris radius: a_1, a_2	mm	3.15,2.35
First and last iris thickness: d_1, d_2	mm	1.67, 1.0
First and last cell Q-factor: Q_1, Q_2	-	6100, 6265
First and last cell shunt impedance: $R_{s,1}, R_{s,2}$	MΩ/m	89, 112
First and last cell group velocity: $v_g/c_1, v_g/c_2$	%	1.66, 0.83
Average a to wavelength ratio: $< a > /\lambda$	-	0.11
Number of particles per bunch: N	-	3.72×10^9
Luminosity per bunch crossing: $\mathcal{L}_b$	m^{-2}	1.22×10^{34}
N_{cell}	-	24
Structure length: L_{cav}	mm	229
Bunch separation: N_s	RF cycles	6
Number of bunches in the train: N_b	-	312
Pulse length: t_p	ns	240.8
Input power: P_{in}	MW	63.8
RF-to-beam efficiency: η	%	27.7

Table 2.1: RF Parameters for the CLIC G accelerating structure [7].

The parameters for the CLIC G cavity can be found in table 2.1. These parameters will be used for comparison throughout the thesis, and are useful for giving an indication of typical values for some of the derived parameters.

Having defined some basic figures of merit associated with cavity design, an introduction to wake potentials and impedances will now be given.

2.3 Wakefields and Wake Potentials

A highly relativistic particle of charge q, moving in the z direction has its electric and magnetic fields transverse to the direction of motion [61]. The angle of the opening of the electric field is proportional to $1/\gamma$, where $\gamma = \frac{1}{\sqrt{1-\beta^2}}$ is the relativistic gamma factor. Additionally, for a particle where $\beta \approx 1$, there are no fields behind or ahead of the particle (due to causality). A test charge moving along the same path as the drive charge but some z offset later would therefore not see any field in the wake of this particle. The effect would remain the same if the drive charge was travelling on axis through a perfectly conducting tube because the image charges found on the surface of the tube will be able to move with the same velocity as the charge itself.

However, if this drive charge is now moving through a pipe that has a finite conductivity, the image charges are not able to keep up with the particle, and the field will begin to lag behind the drive charge [65]. A test charge slightly behind the drive charge experiences a kick from the wakefield of the drive charge. This is also the case if the fields from the drive charge come into contact with any discontinuities in the vacuum chamber (collimators or cavities for instance). The electromagnetic fields would scatter off the discontinuities, causing a wakefield that can cause a kick longitudinally and transversely to any trailing charge travelling behind it.

A wakefield is defined as the fields that are created by moving particles that act on any trailing particles. Wakefields can be separated into two distinct groups, long range wakefields [66], which are caused by a drive bunch and act on any trailing bunches, and short range wakefields, which are caused by the head of the bunch and act on the the tail of the same bunch [67]. In order to compare this short range wakefield, the mesh density of the simulation must be carefully chosen, in order to allow a high enough resolution for the high frequency components to be deduced. The following derivations are summarised from [5, 20, 66, 68, 69].

2.3.1 The Catch Up Problem

This section will describe the catch up problem, which is illustrated by Figure 2.1. The field from a relativistic drive particle travelling along the z-axis, scatters off a metallic boundary placed at a transverse offset b relative to the particle. A test charge travelling at a distance s behind the drive charge doesn't experience the scattered field until it reaches a position z_c, given by

$$z_c \approx \frac{b^2 - s^2}{2s}. \tag{2.14}$$

This catch-up distance can be large for small values of s. Considering the finite γ, the distance for the scattered radiation to catch up to the drive charge itself is $z_c \approx \gamma b$. The opening angle of the relativistic fields in the laboratory frame is given by $1/\gamma$, and the discontinuity is found at $z = 0$. This means to compute the effect of the wakefield just behind the drive particle, the drive particle would need to progress until z_c.

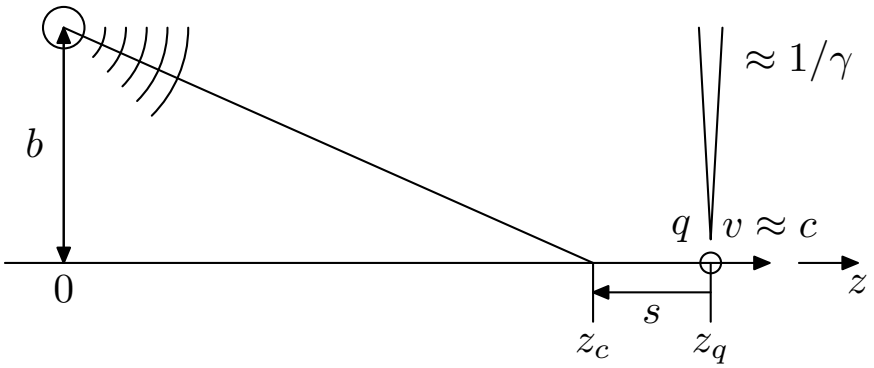

Figure 2.1: The field from a relativistic drive particle scatters off a metallic boundary located at $z = 0$. A particle trailing a distance s behind the particle doesn't experience this scattered field until z_c.

The following sections will describe some general properties of wake potentials and cavity impedances.

2.3.2 Wake Potentials

It is useful to know the integrated effect of the wakefield on a trailing bunch over the length of the structure. The longitudinal and transverse wake potentials for a test bunch travelling

on the same or on a parallel path at a distance s behind the driving charge is given by

$$W_z(\vec{r},\vec{r'},s) = -\frac{1}{q}\int_{z_1}^{z_2} dz[E_z(\vec{r},z,t)]_{t=(z+s)/c}, \tag{2.15}$$

$$W_\perp(\vec{r},\vec{r'},s) = \frac{1}{q}\int_{z_1}^{z_2} dz[\vec{E}_\perp + c(\hat{z}\times\vec{B})]_{t=(z+s)/c}, \tag{2.16}$$

where $\hat{z}$ is the z unit vector in the direction of motion, and $\vec{r'}$ and $\vec{r}$ are the transverse offsets of the driving and test charges from the z axis. Conventionally, the driving charge is assumed to enter the cavity structure at $z, t = 0$ and then exits the cavity at $z = g$. The longitudinal momentum kick imparted to a test particle is therefore

$$\vec{p_z} = -\frac{eq}{c}W_z(s). \tag{2.17}$$

Were e and q both to have the same sign, the longitudinal wake potential is retarding. Similarly, the transverse momentum kick is given by

$$\vec{p_\perp} = \frac{eq}{c}\vec{W}_\perp(s). \tag{2.18}$$

These formulae are only relevant for particles travelling at $v \approx c$, if this is not the case then the path that each particle takes through the structure is altered and the system breaks down.

Eqn. 2.15 gives the wake potentials for a point drive particle. In order to calculate the wake potential behind a driving bunch with an arbitrary charge distribution, the wake potentials above can be represented by a Green function. Assuming a line density of $\lambda(s)$ per unit length, the longitudinal and transverse potentials are convolutions of the relevant wakefield with this offset line density. given as

$$V_z(s) = \int_0^\infty ds'\lambda(s-s')W_z(s') = \int_{-\infty}^s ds'\lambda(s')W_z(s-s'), \tag{2.19}$$

$$\vec{V}_\perp(s) = \int_0^\infty ds'\lambda(s-s')\vec{W}_\perp(s') = \int_{-\infty}^s ds'\lambda(s')\vec{W}_\perp(s-s'). \tag{2.20}$$

The total energy loss to the wakefields can be calculated according to

$$\Delta U = \int_{-\infty}^{\infty} ds\lambda(s)V_z(s) = \int_{-\infty}^{\infty} d\tau I(\tau)V_z(\tau) \tag{2.21}$$

where $\tau = \frac{s}{c} = t - \frac{z}{c}$ and $I(\tau) = c\lambda(s)$. The loss factor can now be defined as

$$k_z = \frac{\Delta U}{q^2}. \tag{2.22}$$

Equivalently, the loss factor for the transverse dimension over the bunch profile is defined by

$$\vec{k}_\perp \equiv \frac{1}{q^2}\int_{-\infty}^{\infty} ds\lambda(s)\vec{V}_\perp(s). \tag{2.23}$$

An important theorem concerning the longitudinal wakefield excited in a cavity can now be derived for a point charge. Assume that the bunch distribution $\lambda(s)$ is short enough for the delta function wake potential to be treated as a constant on the scale of the bunch length, i.e. $W_z(s) = W_z(0^+)$, where 0^+ is a small positive distance. By substitution using eqns. 2.19 and 2.21 this yields

$$\Delta U = \frac{1}{2}q^2 W_z(0^+). \tag{2.24}$$

The energy loss for a point particle is related to the effective wake potential acting on a bunch, by

$$\Delta U = qV(0) = q^2 W_z(0) = q^2 k_\delta, \tag{2.25}$$

where k_δ is the loss factor for a point bunch. This means that the wake potential immediately behind a point charge is twice the effective wake seen by the charge itself i.e.

$$W_z(0^+) = 2W_\delta(0). \tag{2.26}$$

Eqn. 2.26 is known as the fundamental theorem of beam loading. Another way of phrasing it is that in the longitudinal dimension, an exciting particle will see half of the potential in the cavity it excites. This is not the case for the transverse potential.

It will now be shown that the loss parameter found in eqn. 2.10 accounts for this beam loading theorem. Consider a point charge traversing a cavity and exciting only a single mode with resonant frequency ω_n, hence the potential inside the cavity will be

$$V_{z,n}(s) = -\hat{V}_n \cos(\frac{\omega_n s}{c}). \tag{2.27}$$

From eqn. 2.27 the peak value of the induced potential must be

$$\hat{V}_n = qW_z(0^+) = 2qk_{\delta n}, \tag{2.28}$$

which makes the longitudinal wake potential

$$W_{z,n}(s) = -\frac{V_{z,n}(s)}{q} = 2k_{\delta n}\cos(\frac{\omega_n s}{c}), \quad s > 0. \tag{2.29}$$

By combining eqns. 2.28 and 2.25, we obtain

$$k_{\delta n} = \frac{\hat{V}_n^2}{4U_n}, \tag{2.30}$$

which is consistent with the loss parameter obtained in eqn. 2.10.

In order to obtain the longitudinal wakefield for a point charge, the following expression, which is based on the Condon method [70], can be used [66]

$$W_z(s) = \sum_{n=1}^{N} 2k_n\cos(\frac{\omega_n s}{c}), \tag{2.31}$$

whereas for the transverse wakefield it must be

$$W_\perp(s) = 2\Gamma(s)\sum_{n=1}^{N} K_n\sin(\frac{\omega_n s}{c}) \tag{2.32}$$

where $\Gamma(s)$ is the step , N is the total number of modes to be included and K_n is the transverse kick factor.

These equations follow naturally from the previous derivations (eqn. 2.27), where N is the total number of modes. The parameters k_n and ω_n can be obtained by simulation, using various numerical codes. For the longitudinal wakefield, only the TM_{0n0} modes are considered, whereas for the transverse wakefield, both TE_{1n0} and TM_{1n0} must be taken into account.

For both the longitudinal and transverse wakefields, the loss parameters can be replaced

by the respective normalised loss parameters (given in eqn. 2.13). In the case of the transverse wakefield this can be particularly useful, as it removes the need to state any radial offsets. This will not change the units for the longitudinal case, however in the case of the transverse wakefield the units will change from $[\mathrm{V}][\mathrm{C}]^{-1}$ to $[\mathrm{V}][\mathrm{C}]^{-1}[\mathrm{m}]^{-2}$. This is often expressed as $[\mathrm{V}][\mathrm{pC}]^{-1}[\mathrm{mm}]^{-1}[\mathrm{m}]^{-1}$ to reflect the typical orders of magnitude of each parameter.

2.3.3 Panofsky-Wenzel Theorem

If $\mathbf{A}_\perp$ is a vector potential and E_z is the field in a closed cavity of arbitrary geometry with length L, then the total transverse momentum kick experienced by a test particle following a drive particle is given by [68, 71]

$$\vec{p}_\perp = e\int_0^L \left[\nabla_\perp A_z(z,t)\right]_{t=z/c} dz = \frac{ie}{\omega}\int_0^L \left[\nabla_\perp E_z(z,t)\right]_{t=z/c} dz. \tag{2.33}$$

Here it is assumed that there is no field at $z = 0, g$ and that both end plates are parallel to the direction of motion. If the driving charge passes through the cavity i.e. $s > L$ then the longitudinal wake potential can be expressed in terms of the transverse wake potential at $s = ct - z$ as

$$\begin{aligned}\frac{\partial \vec{W}_\perp}{\partial s} &= \frac{c}{eq}\frac{\partial \vec{p}_\perp}{\partial s} \\ &= -\frac{1}{q}\int_0^L \left[\nabla_\perp E_z(z,t)\right]_{t=s+z/c} dz \\ &= \nabla_\perp W_z.\end{aligned} \tag{2.34}$$

This theorem relates the transverse wakefield with the transverse kick experienced from the longitudinal wakefield.

2.4 Impedance & Frequency Domain

The resistance of an AC circuit is given by a complex impedance [61, 72]

$$Z = R + iX, \tag{2.35}$$

where the real part R is the resistance and the imaginary part X is the reactance [22]. As a particle moves through the vacuum chamber it excites currents and voltages from various discontinuities and other components. The total induced voltage along a particles' path relates to the beam current through a coupling impedance. For a beam moving with constant velocity v at an offset r from the z-axis, the longitudinal impedance is given by [72]

$$Z_{\parallel}(r,\omega) = -\frac{1}{\tilde{I}}\int_{-\infty}^{\infty} dz \tilde{E}_z(r,z)\exp(i\omega t), \tag{2.36}$$

here the tilde refers to a time varying quantity. By comparing this with eqn. 2.15, it can be shown that for $v \approx c$, the longitudinal coupling impedance is the Fourier transform of the wake potential, i.e.

$$Z_{\parallel}(\omega) = \int_{-\infty}^{\infty} dt W_z(t)\exp(-i\omega t). \tag{2.37}$$

Alternatively for a cavity, the impedance function is the spectrum of the δ-function wake potential in the frequency domain. By taking the Fourier transform of a wake potential, information about the cavity (ω, Q and k) can be extracted by fitting a Lorentzian [64] to each mode. The Lorentzian is given by

$$L(\omega) = \frac{2Q_n}{\pi\omega_n}\frac{k_n}{1+4Q_n^2(\omega/\omega_n - 1)^2}, \tag{2.38}$$

where the loss factor $k_n = \int_{-\infty}^{\infty} L(\omega)d\omega$.

A typical impedance spectrum for an rf cavity can be found in figure 2.2. The beam pipes at each end of the cavity is a circular waveguide with a characteristic cut-off frequency. Below this frequency, the impedance spectrum shows sharp peaks corresponding to the lower frequency cavity modes [60]. Above this cutoff frequency, the modes can propagate through the beam pipe, lowering their Q and creating an overlapping spectrum and a continuous

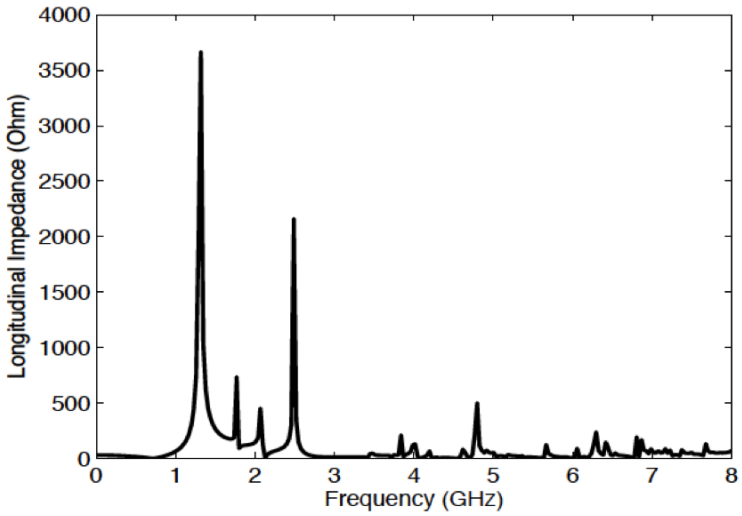

Figure 2.2: The impedance spectrum of a typical cavity. This particular spectrum is the PETRA III longitudinal feedback cavity [73]. Distinct peaks are seen at low frequencies that represent the resonant modes. These modes become more convoluted and overlapping at high frequencies as they are now able to travel through the beam pipe.

broadband distribution. Many different parameters and figures of merit for cavities have been introduced. Now the behaviour of cavities in a variety of different circumstances will be described.

2.5 Normal Conducting vs Superconducting Cavities

Normal conducting (NC) cavities operate at room temperature and are typically made of copper or stainless steel. The Q of a cavity is dependant on the frequency, but for copper at X-band, the Q for monopole modes is typically in the range of 7000-8000. Water cooling is often used to prevent the cavities from heating during pulses. Superconducting (SC) cavities are cooled until they are below the critical temperature T_c for the metal in question, such that the material conducts with low losses. The cavities are normally fabricated using niobium which has a critical temperature of 9.2K, which causes the cavity Q and R_s to become extremely high ($Q \approx 10^{10}$). These cavities typically operate in the region of 2K.

For CW operation, the power requirements for NC are much higher than for SC due to the increased losses. However when accelerating high currents and operating at a low duty

cycle (approximately 1%) [74] the power requirements for SC cavities become much higher and NC becomes preferable.

SC cavities are concerned with intense surface fields, but the cavity design is typically focused on H-field reduction on the surface, with different restraints being set that depend on the critical H-fields (H_c for type-I superconductors or H_{c1} for type-II superconductors). These restraints arise due to the need to prevent the SC cavities from quenching, which could cause serious damage to the cryostat and surrounding systems.

In Appendix A, the frequency scaling for many of the cavity parameters introduced so far is derived. Table 2.2 shows how the parameters scale different based on whether they are NC or SC. By looking at the surface resistance, power dissipation and shunt impedance, one can see that wall losses are much greater at higher frequencies for SC cavities than for NC. This is much more of an issue for SC cavities as they need to avoid temperature rise. The longitudinal and transverse kick factors vary as ω^2 and ω^3 respectively, leading to an increase in wakefield effects for higher frequencies. This motivates utilising larger cavities with reduced frequencies and higher R/Q values. This largely influences SC cavity design, as most SC cavities operate at either 704MHz, 1.3GHz or 3.9GHz, whereas NC cavities can go as high as 30 GHz. The cavity radius, geometric factor and R/Q, are independent of wall material, meaning these parameters are influenced by geometry alone.

Parameter	Superconducting	Normal conducting
Cavity radius (b)	ω^{-1}	ω^{-1}
Surface Resistance (R_s)	ω^{2}	$\omega^{1/2}$
Power dissipation (P_c)	ω^{1}	$\omega^{-1/2}$
Stored energy (U)	ω^{-2}	ω^{-2}
Quality factor (Q_0)	ω^{-2}	$\omega^{-1/2}$
Shunt impedance (R')	ω^{-1}	$\omega^{1/2}$
Geometric factor (G)	ω^{0}	ω^{0}
R over Q (R'/Q)	ω^{1}	ω^{1}
Longitudinal loss factor ($k_{\parallel}$)	ω^{2}	ω^{2}
Transverse kick factor ($k_{\perp}$)	ω^{3}	ω^{3}

Table 2.2: Frequency scaling with cavity parameters for normal and superconducting cases.

This remaining sections of this chapter will describe some simulation techniques used to

model different types of modes in cavities. A brief section on optimisation of surface fields will be included, as well as some basic properties of power couplers. These are important to later Chapters 5 and 6 where novel cavity designs will be introduced.

2.6 Monopole Mode Simulations

Simulating a complete cavity is time consuming and require a lot of computing power. An effective method of solving this problem is to take advantage of any symmetry planes that the cavity may possess. This normally manifests itself as azimuthal-symmetry. Simulation codes are designed to be able to take advantage of this property. Rather than simulating a full 360° cell, a slice of the cell with appropriate boundary conditions can be simulated in a fraction of the time.

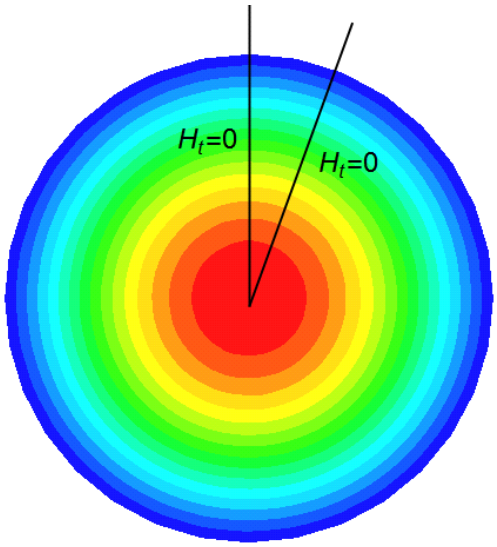

Figure 2.3: The electric field of a TM_{010} monopole mode in a cavity. Boundary conditions that allow magnetic symmetry can reduce the simulation time of a cavity. The boundary $H_t = 0$ refers to the tangential magnetic field at the respective plane.

When simulating the monopole mode, these boundary conditions are two magnetic symmetry boundaries. This can be understood by observing the field patterns of the monopole mode and noting its symmetry [75]. Graphics illustrating this can be found in figure 2.3 and

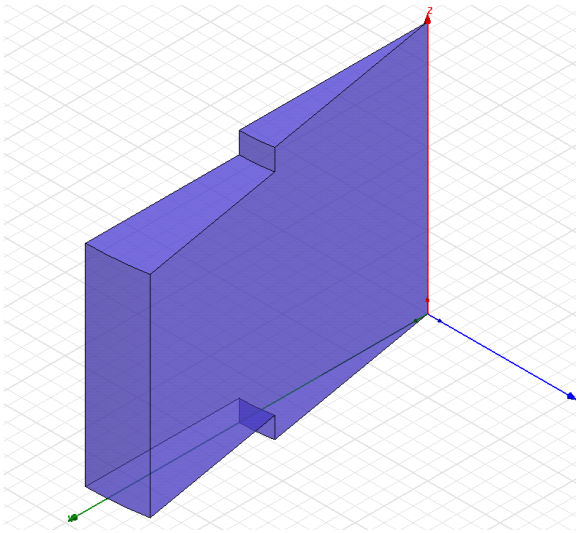

Figure 2.4: By modelling 10 degrees of the cavity and applying appropriate symmetry conditions, simulation times can be greatly reduced.

figure 2.4.

In order to calculate cavity figures of merit, the fields can be extracted and solved numerically. However it isn't always apparent which monopole mode has been simulated, especially when simulating higher order modes. One method of mode determination is to plot the electric and magnetic fields and to compare them alongside mode patterns for either a cylindrical or rectangular waveguide [75]. The cavity geometry can often deform the field pattern making it difficult to accurately determine the mode number, in this case it is possible to determine the m^{th} order by looking at behaviour of the loss parameter for increasing radial offset. For monopole modes, the loss parameter should not vary with offset as there is no radial dependence.

2.6.1 Floquet's Theorem

Cavities are not individual cells, they are chains of smaller cells coupled together by a small opening at the beam pipe. This creates several solutions to the boundary conditions on the phase of the mode imposed at each end of the cavity, and can create a large number of the same mode with different phase advances. This will be covered in detail in Chapter 3.

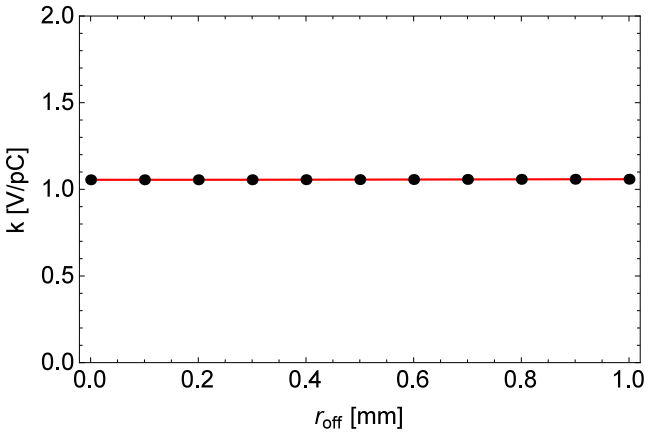

Figure 2.5: The loss parameter $k_{\|}$ as a function of radial offset for a TM_{010} monopole mode, similar to the one shown in figure 2.4.

In a cavity that consists of a chain of coupled cells, it follows that the fields at two different longitudinal cross sections that are separated by one period differ only by a constant factor, which in general is a complex number [60]. In other words, the field at the same point between two adjacent cells varies only by a phase shift. This is known as Floquet's theorem and can be written for a TW structure as

$$E(r, z + L) = E(r, z) \exp(i\phi). \tag{2.39}$$

where ϕ is the phase advance of the cell and L is the cavity period.

Subjecting a cavity to infinite boundary conditions allows periodicity to be assumed from cell to cell. Each cavity mode can be deconstructed into an infinite set of modes with varying ϕ, which is known as a passband, with the gaps in between cavity modes (for example between the TM_{010} and TM_{020} band). When the modes are evanescent it is referred to as a stopband.

When simulating multi-cell structures, Floquet's theorem can be used to obtain the phase advance of a particular mode. By applying eqn. 2.40 the phase is obtained from the electric field as

$$\cos(\phi) = \frac{E(r, z + L) + E(r, z - L)}{2E(r, z)}. \tag{2.40}$$

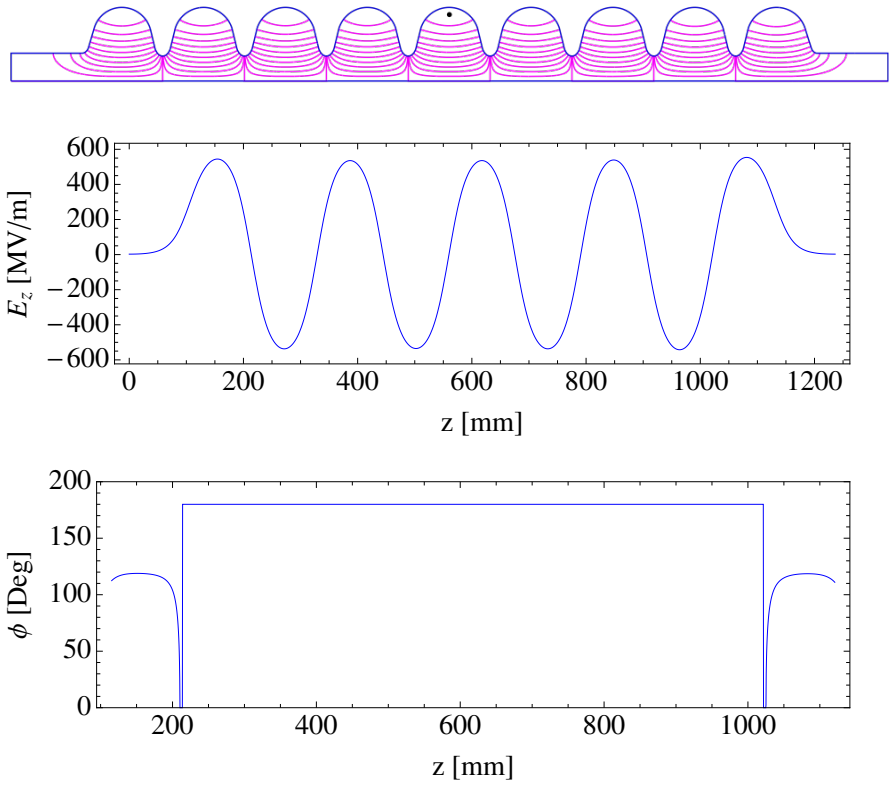

Figure 2.6: Floquets theorem being used to calculate the phase advance of a mode inside the TESLA cavity The electric field is simulated numerically (top), and the z-component of the electric field is extracted (middle). Eqn. 2.40 is then applied to determine the phase advance. In this case, it is clear the cavity is a π-mode.

When simulating numerous coupled cells, this can be used to identify the phase advance of a particular eigenmode when it may not be clear which has been simulated. This is shown in figure 2.6, where the ϕ of a mode found in the TESLA cavity is calculated.

Additionally, it is possible to use Floquet's theorem extract the travelling wave (TW) solution from the standing wave (SW) solution. For example, the *Superfish* code is based on the simulation of SW's. It is possible to extract the TW solution by treating the SW as a sum of two TW's therefore,

$$s(z) = f(z) + f^*(z), \tag{2.41}$$

$$s(z+L) = f(z)\exp(-i\phi) + f^*(z)\exp(i\phi), \tag{2.42}$$

where $s(z)$ refers to the SW solution and $f(z)$ to the TW, the conjugate dictates a TW moving in the opposite direction (i.e. with negative phase advance). This gives

$$s(z+L) - s(z)\exp(i\phi) = f(z)(\exp(-i\phi) + \exp(i\phi)), \tag{2.43}$$

hence

$$f(z) = \frac{s(z+L) - s(z)\exp(i\phi)}{2\cos(\phi)}. \tag{2.44}$$

In order to apply this equation, knowledge of the phase advance per cell is required, which can be obtained by applying eqn. 2.40. The results of such a calculation can be found in figure 2.7.

Floquet's theorem applies equally well to all HOM's, and can be used to determine the characteristics of a simulated mode.

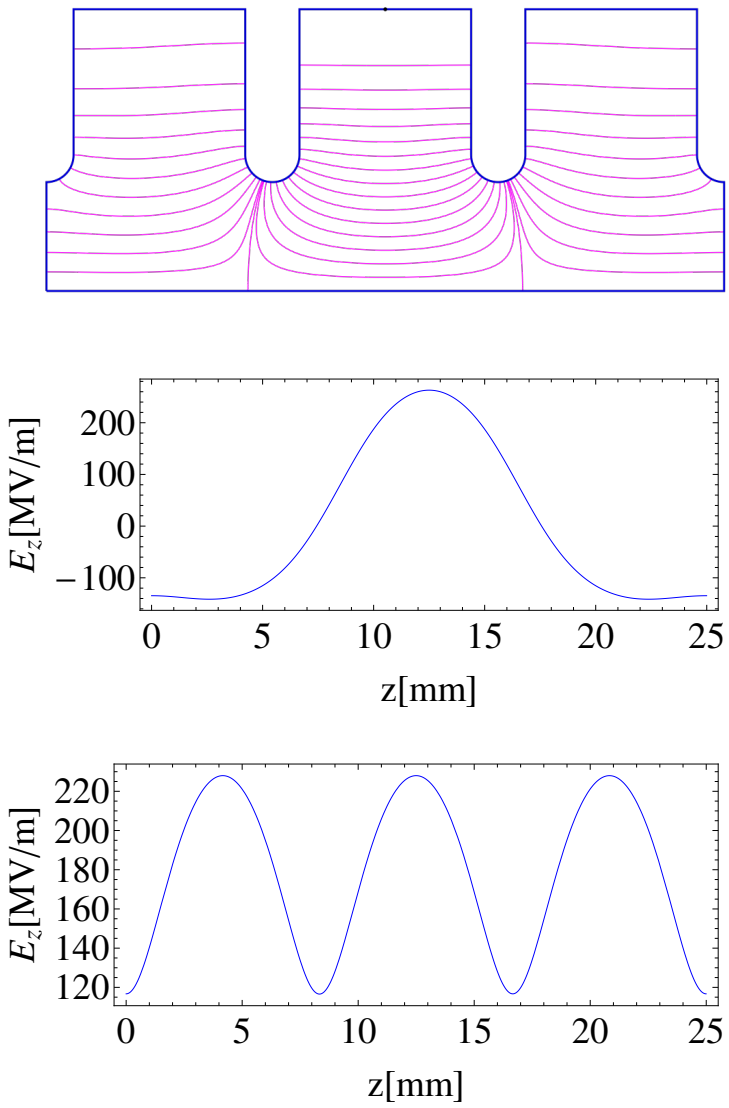

Figure 2.7: The SW electric field is simulated using *Superfish* (top). The z-component of the electric field is extracted on axis (middle), then a combination of eqn. 2.40 and eqn. 2.44 can be applied to determine the TW solution.

2.7 Dipole Mode Simulations

To simulate a dipole mode, a similar method to the monopole mode is applied, however a 90 degree segment is taken, which is shown in figure 2.8. In this case, the appropriate boundary conditions are an electric symmetry boundary and a magnetic symmetry boundary. Again, this is revealed by looking at the field patterns for the dipole mode [75] and selecting the symmetry planes accordingly.

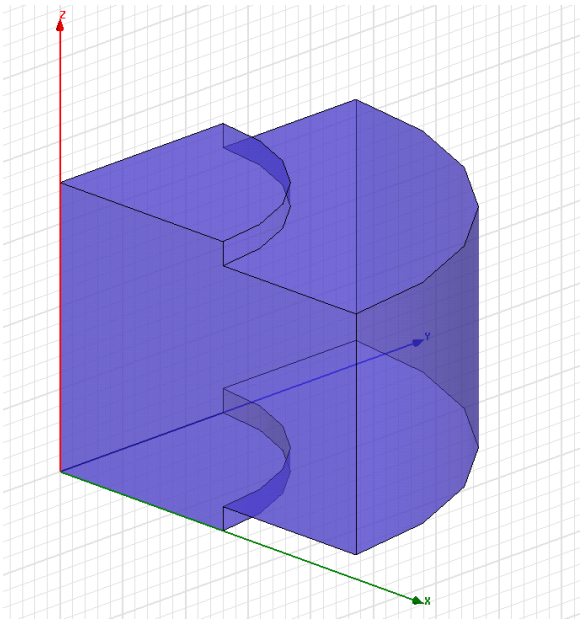

Figure 2.8: By modelling 90 degrees of the cavity and applying appropriate symmetry conditions, simulation times can be greatly reduced when considering dipole modes. Here, a 90 degree section of a cavity is shown.

However, care must be taken because these boundaries also allow for the simulation of sextupoles and other higher order modes. By examining the field patterns and calculating the kicks at various offsets, this problem is eliminated.

For dipole modes, the order of the Bessel function that determines the radial behaviour has changed (see eqn. 2.1), meaning the accelerating voltage should approximately vary linearly with offset close to the origin, with a zero transverse kick at the origin [76]. This is why great effort is made to keep the beam as centred as possible. The quadratic behaviour arises from the V_{acc}^2 term found in eqn. 2.10. When normalising the loss parameter according

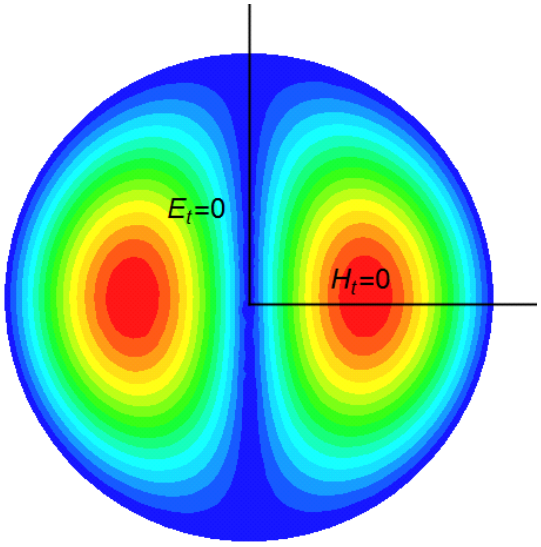

Figure 2.9: Both an electric and magnetic boundary are required. However, this can also allow sextupole modes hence care must be taken when analysing results. The subscript t refers to the transverse field component.

to eqn. 2.13, it can be seen that the variation with offset is removed.

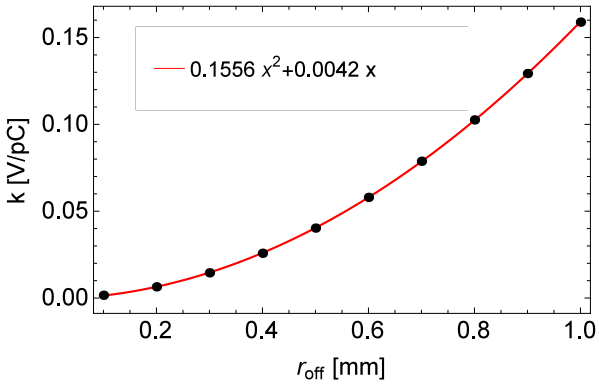

Figure 2.10: The loss parameter $k_\perp$ as a function of radial offset. A quadratic dependence is observed, which follows that $m = 1$.

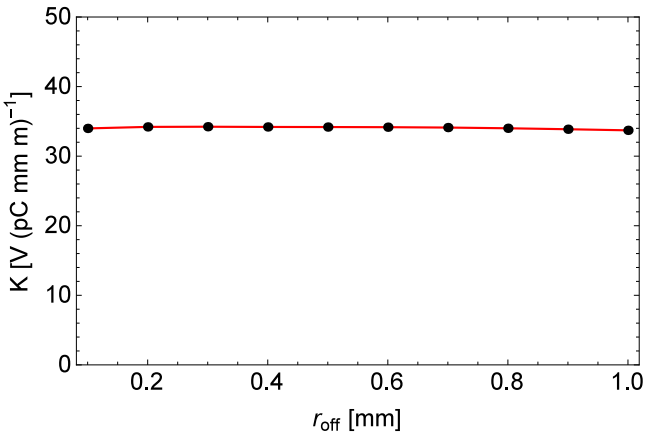

Figure 2.11: The transverse kick factor as a function of the radial offset. The kick factor is normalised such that it is independent on radial offset. This behaviour is seen here.

2.8 Surface Fields

In order to prevent the onset of rf breakdown, the surface electric fields must be minimised. In this section, the effect of geometry modifications on the surface electric and magnetic field will be shown. Figure 2.12 shows a simple unoptimised π-mode pillbox cavity that has been numerically simulated. This is the basic geometry that will be used, before the edges of the geometry will be rounded.

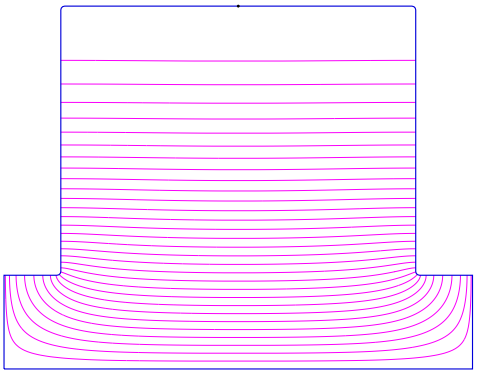

Figure 2.12: Geometry for a simple π-mode pillbox cavity.

Figure 2.13 shows two geometries, one with sharp edges (in red) and one where the iris radius has been rounded (in blue). The surface electric field (normalised to the accelerating field) for the sharp edged geometry has a peak value of 3.3. For high accelerating gradient (in excess of 50 MV/m) or long pulse lengths this leads to unacceptably high electric fields and will result in high breakdown rates. The peak value occurs at the sharp edge close to the iris as the field is focused into this point. A rounded iris spreads the intense fields over a larger area, reducing their peak value. It can be seen that a relatively small amount of rounding on the iris has reduced the peak surface electric field from 3.3 to 2.1, which is within the limits for rf breakdown.

As shown in figure 2.14, a similar effect occurs when rounding the outer edge of the cavity. It is in this vicinity that the magnetic field is the most intense, and therefore when this section is rounded the intense fields are spread over a wider area. As the power loss P_c depends only on the magnetic field, this has the effect of increasing the Q by a factor of 1.13,

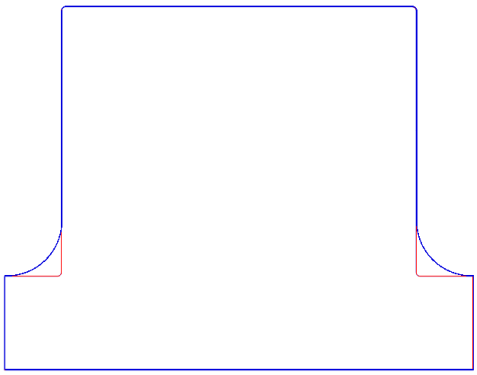

(a) Blue shows a curved geometry with the original sharp geometry in red.

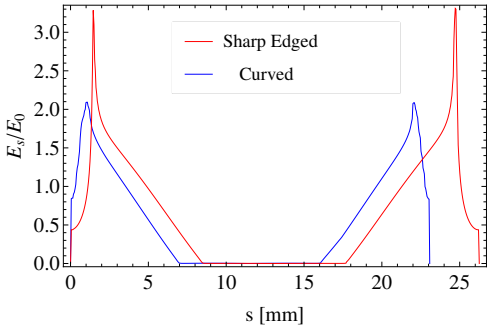

(b) Surface electric field for the each case.

Figure 2.13: Surface electric fields for sharp and curved geometries. The curvature reduces the path length around the cavity.

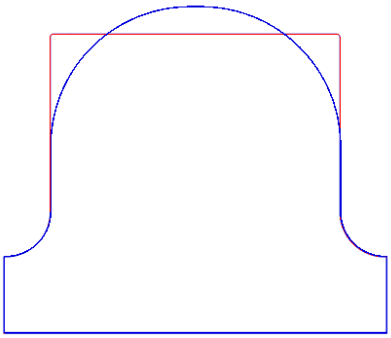

(a) Blue shows a curved geometry with the original sharp geometry in red.

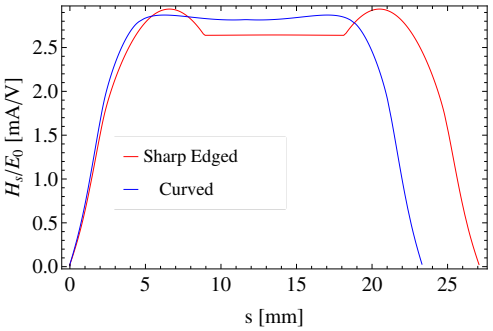

(b) Surface magnetic field for the each case.

Figure 2.14: Surface electric fields for sharp and curved geometries. The curvature reduces the path length around the cavity.

as well as the shunt impedance R_s by a factor of 1.11, this is while reducing the peak surface magnetic field from 3 mA/V to 2.85 mA/V.

Optimal surface fields and figures of merit for a cavity structure are needed in order to achieve the design goals. These can be based on one or two parameter optimisation using a Newton Raphson root seeking method (more information in Section 5) or an N-parameter optimisation based on Monte Carlo algorithms.

2.9 Power Coupling

There are several different methods of coupling rf power into a cavity to set up an accelerating field. Waveguide couplers couple particular modes from a waveguide into the cavity close to the outer radius, typically coupling the magnetic fields of the modes. Coaxial couplers are often used to couple the fields into the beampipes, where they will flow through the cavity and set up a resonance. A comparison between the different coupling methods, and an introduction to the physics of designing power couplers can be found in [77].

The loaded quality factor accounts for all losses that occur within the cavity and is given as

$$Q_L = \frac{\omega U}{P_c + P_{ext}}, \tag{2.45}$$

where P_{ext} is the power flowing through the coupler. The external quality factor can be defined as

$$Q_E = \frac{\omega U}{P_{ext}} \tag{2.46}$$

and the quality factors sum as

$$\frac{1}{Q_L} = \frac{1}{Q_0} + \frac{1}{Q_E}, \tag{2.47}$$

where Q_0 is the intrinsic quality factor of the cavity and Q_E gives the quality factor from any external losses. This allows a coupling coefficient to be defined as

$$\beta = \frac{P_{ext}}{P_c} = \frac{Q_0}{Q_E}, \tag{2.48}$$

which means the loaded quality factor can be re-written as

$$Q_L = \frac{Q_0}{1+\beta}. \tag{2.49}$$

The reflection coefficient is a measure of the amount of power reflected back towards the source when it reaches the coupler, and can be defined as

$$\rho_c = \frac{\beta - 1 - iQ_0\delta}{\beta + 1 + iQ_0\delta}, \tag{2.50}$$

where $\delta = (f - f_{cav})/f_{cav}$ is the level of detuning from the cavity frequency. In design-

ing a power coupler, it is important to minimise the reflection coefficient as it can be very damaging to the power source if power is flowing in the opposite direction (caused by the reflection at the coupler-cavity interface). Waveguide couplers have difficulty varying β once the coupler has been manufactured, but they have a much higher capability for handling high powers. Additionally, waveguides have a lower attenuation meaning more power will be available when the power reaches the cavity.

It is much easier to tune the β using coaxial couplers because the penetration depths of the inner coax can be varied. They are much more compact, but have less capability for handling high powers. Figure 2.15 shows the reflection coefficient for different values of β. The tuners on different cavities will aim to achieve $\beta = 1$, in order to protect the power source and increase the efficient of the power transfer.

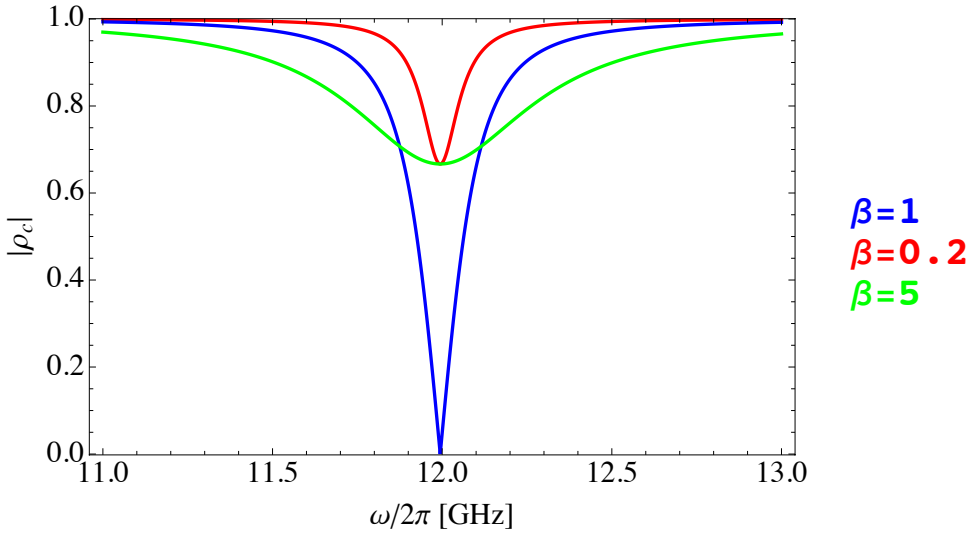

Figure 2.15: Reflection coefficient for different values of β.

The fundamental principles of rf cavities and some of the associated problems with cavity design and optimisation have been introduced and discussed. A useful tool will be introduced in the next chapter, one that allows a rapid determination of cavity mode frequencies for a large number of cells as well as forming a basis for most theoretical analysis of cavity systems. This circuit model will be described in the next chapter.

Chapter 3

Circuit Model

An oscillating cavity field can be represented by an RLC circuit. A chain of several coupled RLC circuits can accurately represent a full cavity structure consisting of many coupled cells. Using this circuit model, detailed calculations of full chains of accelerating cavities can be made without requiring full simulations. The circuit model is a very powerful tool that can accurately model almost any type of cavity excitation.

Some key derivations will be shown that can be used to characterise the monopole modes of a passband excited in a chain of accelerating cavities. This will then be extended to include dipole modes. The circuit model described will enable the modes that comprise the longitudinal and wakefield to be calculated. An important relation that gives the phase shift of an oscillator when it is excited off resonance will also be included.

3.1 RLC Circuit

Simulating a full structure is relatively time consuming and computationally expensive. A method to reduce the simulation time is by approximating the cavity as an RLC circuit [22]. The application of RLC circuits to model a chain of accelerating cavities was first explored by D.E.Nagle *et al* [78] and they can be used to accurately measure the coupling between two adjacent cells in a structure. The inductor, L, represents the oscillating magnetic field, while the capacitor, C, represents the oscillating electric field. The resistor refers to the shunt impedance of the cavity, and is used to account for any material losses in the cavity walls caused by a finite conductivity. It is useful to calculate the impedance of a cavity to determine the effect the cavity will have on the beam. In the case of an RLC resonator connected in parallel as shown in figure 3.1, Kirchoffs law states that the total current in the circuit should be equal to the sum of the currents in each of the components. By calculating the current in

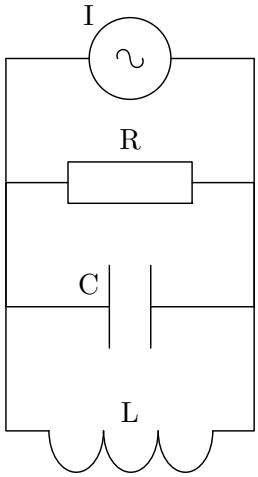

Figure 3.1: A parallel RLC circuit that is analagous to a cavity resonator.

each circuit element, the total current of a parallel RLC circuit is give by

$$I(t) = C\frac{dV}{dt} + \frac{V}{R} + \frac{1}{L}\int V dt. \tag{3.1}$$

If a monochromatic current and voltage is assumed (at a fixed oscillating frequency), then phasor representation is employed as $I(t) = \widetilde{I}\exp(i\omega t)$ and $V(t) = \widetilde{V}\exp(i\omega t)$. Substitution into eqn. 3.1 gives $\widetilde{I} = Y_{par}(\omega)\widetilde{V}$, where the admittance is given by

$$Y_{par}(\omega) = \frac{1}{R} + \frac{1}{i\omega L} + i\omega C. \tag{3.2}$$

The impedance of a parallel circuit is $Z_{par}(\omega) = 1/Y_{par}(\omega)$, then

$$Z_{par}(\omega) = \frac{R}{1 + iR(\omega C - \frac{1}{\omega L})}. \tag{3.3}$$

$Z_{par}(\omega)$ is maximum when the circuit is at resonance. This occurs when

$$\omega C = \frac{1}{\omega L}, \tag{3.4}$$

which means the resonant frequency of the circuit can be given as

$$\omega_0 = \frac{1}{\sqrt{LC}}. \tag{3.5}$$

The circuit has a quality factor determined by

$$Q = \frac{\omega_0}{\Delta\omega}, \tag{3.6}$$

where the bandwidth is given by the ratio of the resistance to the inductance of the circuit,

$$\Delta\omega = \frac{R}{L}. \tag{3.7}$$

This gives the quality factor for the circuit as

$$Q = R\omega_0 C = \frac{R}{\omega_0 L}, \tag{3.8}$$

and allows the impedance of the cavity to be written as

$$Z_{par}(\omega) = \frac{R}{1 + iQ(\frac{\omega}{\omega_0} - \frac{\omega_0}{\omega})}. \tag{3.9}$$

Eqn. 3.9 shows that if the cavity is excited on resonance, the imaginary component becomes zero, and the impedance of the cavity is simply given by the shunt impedance, R. However, cavities are not always excited perfectly on resonance and the behaviour of the cavity in this regime leads to some very interesting results. Exciting the cavity slightly off resonance, i.e. with a small amount of detuning, $\Delta\omega = \omega - \omega_0$ and $\frac{\Delta\omega}{\omega} << 1$, it can be seen that

$$\frac{\omega}{\omega_0} - \frac{\omega_0}{\omega} = \frac{\omega^2 - \omega_0^2}{\omega_0\omega} = \frac{(\omega - \omega_0)(\omega + \omega_0)}{\omega_0\omega} \approx \frac{2\Delta\omega}{\omega}. \tag{3.10}$$

Therefore, the impedance of a cavity can be written as

$$Z_{par}(\omega) \approx \frac{R}{1 + i2Q\delta}, \tag{3.11}$$

where

$$\delta = \frac{\omega - \omega_0}{\omega_0}. \tag{3.12}$$

The impedance, current and voltage are related as

$$V = ZI, \tag{3.13}$$

which means that the voltage in the cavity is given by

$$V = \frac{R}{1 + i2Q\delta} I \tag{3.14}$$

When the cavity is excited off resonance, there is an imaginary component which results in an additional phase shift between the current and voltage. This is shown in fig. 3.2 which is an argand diagram of the real and imaginary components on the impedance. In this case, the impedance has been reduced to

$$V = \frac{A}{1 + iB}. \tag{3.15}$$

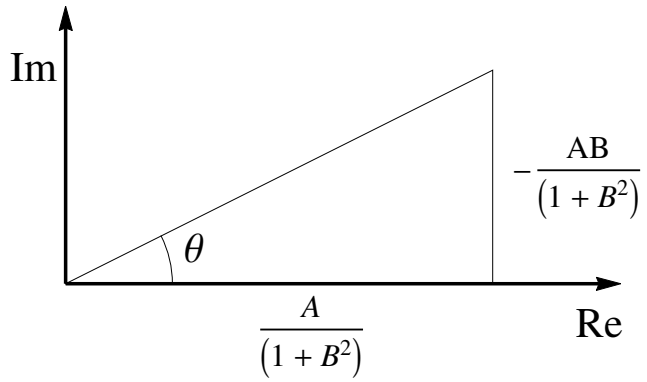

Figure 3.2: A phasor diagram of the impedance with $A = IR$ and $B = 2Q\delta$. The phase shift θ is caused by off resonance excitation.

From the diagram it can be observed that an additional phase shift of θ when not on

resonance. This phase shift can be calculated according to

$$\tan\theta = -2Q\delta \tag{3.16}$$

Eq. 3.16 shows that if a cavity is excited off resonance, then the field will oscillate at the drive frequency but will have a characteristic phase delay that is dependant on the Q-factor and the magnitude of the detuning. This statement is in agreement with the general theory of a driven oscillator [79]. This is an important result that will be of great interest in Chapter 5.

3.2 Single Chain Circuit Model

In practice, a chain of accelerating cavities is used rather than single isolated cavities in order to maximise the energy gain of the particles. The resistance R represents the shunt impedance of each cell, and a chain of N-cells is analagous to a chain of N-resistors connected in series. So the shunt impedances of each cavity can be summed. However, each cavity is now comprised of a series of individual resonant RLC cells. When these cells are placed alongside each other, the fields from each cell couple with neighbouring cells, shifting their resonant frequency. Now, rather than having one TM_{010} mode, there are N TM_{010} modes, where N is the total number of cells. This frequency range of allowed modes is called a passband, while the area in between passbands (for example between the allowable TM_{010} and TM_{020} modes) are called stopbands [60]. The frequency of each mode within the passband is now a function of the phase advance per cell, ϕ.

It is useful to be able to calculate the cell-to-cell coupling between neighbouring cells as this characterises the cavity behaviour. This will also be able to provide information about the stability of an excited mode. If there are other modes that have frequencies that are too close to the operating mode, then it is possible they will be excited instead of the operating mode. This information can be obtained by using a chain of coupled LC circuits, as shown in figure 3.3. Here, the coupling is magnetic in nature (as shown by the coupling occuring through the inductors), however this derivation would also be accurate for capacitive coupling [30], due to the fact that the origin of the coupling is not important as long as it is mathematically consistent. This model represents an infinite chain of coupled cells (with an infinite number

of modes in each passband), however, in this case the cells only couple to their nearest neighbour, as coupling to the next nearest neighbour is negligible unless considering HOM's or very large irises. Hence this model is called nearest neighbour coupling [27, 66].

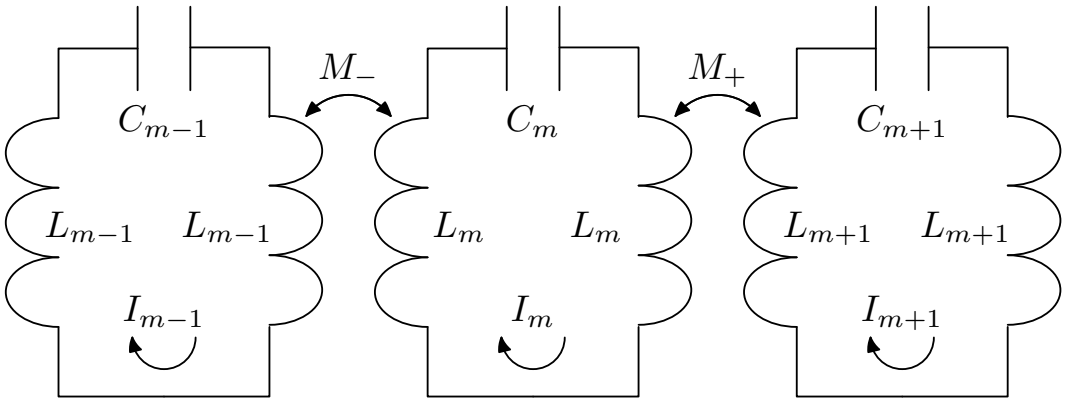

Figure 3.3: A single chain circuit model [41]. The inductors act as couplers between nearest neighbour cells only.

Kirchoffs voltage rule can be applied to cell m to give

$$(2i\omega L_m - \frac{i}{\omega C_m})I_m + iI_{m+1}\omega M_+ + iI_{m-1}\omega M_- = 0, \tag{3.17}$$

where I_m, L_m and C_m are the current, inductance and the capacitance in the m^{th} loop, respectively. M_+ and M_- are the mutual inductances going from loop m into cells $(m+1)$ and $(m-1)$, respectively. By dividing through by $2i\omega L_m$,

$$(1 - \frac{1}{2\omega^2 L_m C_m})I_m + \frac{I_{m+1}M_+}{2L_m} + \frac{I_{m-1}M_-}{2L_m} = 0. \tag{3.18}$$

A resonant frequency can be defined as

$$\omega_m = \frac{1}{\sqrt{2L_m C_m}}, \tag{3.19}$$

which can be substituted back into eq. 3.18 to give

$$(1 - \frac{\omega_m^2}{\omega^2})I_m + \frac{I_{m+1}M_+}{2L_m} + \frac{i_{m-1}M_-}{2L_m} = 0. \tag{3.20}$$

The current can be normalised in terms of an independant variable as

$$I_m = \frac{a_m}{\omega_m \sqrt{L_m}} = \frac{a_m \sqrt{C_m}}{\omega_m}, \tag{3.21}$$

which yields

$$(1 - \frac{\omega_m^2}{\omega^2}) \frac{a_m}{\omega_m \sqrt{L_m}} + \frac{a_{m+1} M_+}{2 L_m \omega_{m+1} \sqrt{L_{m+1}}} + \frac{a_{m-1} M_-}{2 L_m \omega_{m-1} \sqrt{L_{m-1}}} = 0. \tag{3.22}$$

Multipling eq. 3.22 by $\frac{\sqrt{L_m}}{\omega_m}$ to give

$$(\frac{1}{\omega_m^2} - \frac{1}{\omega^2}) a_m + \frac{a_{m+1}}{\omega_m \omega_{m+1} \sqrt{L_m L_{m+1}}} \frac{M_+}{2} + \frac{a_{m-1}}{\omega_m \omega_{m-1} \sqrt{L_m L_{m-1}}} \frac{M_-}{2} = 0. \tag{3.23}$$

The cell to cell coupling can be defined as

$$\eta_{m \pm \frac{1}{2}} = \frac{M_\pm}{\omega_m \omega_{m \pm 1} \sqrt{L_m L_{m \pm \frac{1}{2}}}}. \tag{3.24}$$

Additionally, the coupling coefficient can be expressed as

$$\kappa_{m \pm \frac{1}{2}} = \eta_{m \pm \frac{1}{2}} \omega_m \omega_{m \pm 1}. \tag{3.25}$$

In a structure consisting of cells subjected to an infinite periodic condition, the current will advance by a factor ϕ per cell. This can be introduced as

$$\eta_{m \pm \frac{1}{2}} = \eta, \tag{3.26}$$

$$a_m = a_0 e^{i \phi m}. \tag{3.27}$$

Eqns. 3.26 and 3.27 can be substituted back into eq. 3.25 to give

$$(\frac{1}{\omega_m^2} - \frac{1}{\omega^2}) a_0 e^{i \phi m} + \frac{\eta}{2} a_0 e^{i \phi (m+1)} + \frac{\eta}{2} a_0 e^{i \phi (m-1)} = 0, \tag{3.28}$$

which can be reduced to

$$(\frac{1}{\omega_m^2} - \frac{1}{\omega^2}) + \eta \cos\phi = 0. \tag{3.29}$$

Assuming that the frequencies of each cell are the same, $\omega_m \omega_{m\pm1} = \omega_m^2$, this can be written in terms of the cell to cell coupling to yield

$$(1 - \frac{\omega_m^2}{\omega^2}) + \kappa \cos\phi = 0, \tag{3.30}$$

which can be re-arranged for ω to give

$$\omega = \frac{\omega_m}{\sqrt{1 + \kappa \cos\phi}}. \tag{3.31}$$

This is known as the dispersion relation. It accurately models the coupling and can accurately interpolate the frequency for many intermediate values of ϕ, but for this to happen, accurate values for the frequencies of the 0 and π modes must be provided. In the case of $\phi = \frac{\pi}{2}$, $\omega_{\frac{\pi}{2}} = \omega_m = \omega_r$ is the resonant frequency of the $\pi/2$ mode. By substituting $\phi = 0$ and $\phi = \pi$ into eq. 3.31, it can be shown that ω_r and κ can be expressed in terms of the 0 and π modes.

$$\omega_{\pi/2} = \sqrt{\frac{2\omega_0^2\omega_\pi^2}{\omega_0^2 + \omega_\pi^2}} \tag{3.32}$$

$$\kappa = \frac{\omega_\pi^2 - \omega_0^2}{\omega_0^2 + \omega_\pi^2} \tag{3.33}$$

These are readily obtained by a wide variety of simulation codes.

The dispersion relation is plotted in figure 3.4 for two different pillbox cavities. Each cavity has been tuned so that the $2\pi/3$ mode is 11.9942 GHz, however one has a substantially larger a/λ than the other ($a/\lambda = 0.15$ vs $a/\lambda = 0.12$.) The cell to cell coupling for the cavity with the larger iris is significantly higher, as shown by the increased bandwidth.

As the beam moves through the cavity, it will excite each and every mode within the passband simultaneously. However, it will strongly excite the mode which is synchronous with the speed of light. This is because all of the other modes that are excited will destructively and constructively interfere, as they all have different phase velocities. The mode that

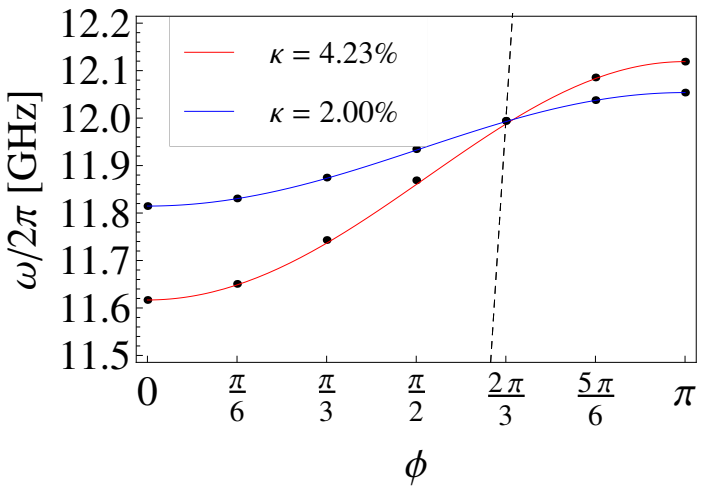

Figure 3.4: Dispersion curves for the TM_{010} mode of two pillbox cavities, blue is for $a/\lambda = 0.12$, while red is for $a/\lambda = 0.15$. The black points are simulation data, while the solid line is the dispersion relation plotted using the 0 and π modes. The dashed line represents the light line.

has the phase velocity of light is considered to be the synchronous phase. This mode is coherently excited and all of the modes superimpose to give a much stronger effect than any of the other modes which average to zero. This can be represented by the light line (LL), as shown in figure 3.4. The LL is a visualisation of the phase velocity of light. Where this line intersects the dispersion curve gives the synchronous mode, the mode that will be strongly excited by the beam (with a normalised velocity, $\beta = 1.$). In this case, the mode excited will have a phase advance of $\frac{2\pi}{3}$. The frequency that corresponds to the LL is given by [27]

$$\omega = \frac{\phi c}{L}, \tag{3.34}$$

where L is the cell period.

As the iris gets larger, the quality of the fit between the simulation and dispersion curve will get worse. This is because eqn. 3.31 has only accounted for nearest neighbour coupling. To accurately model cells with large irises ($a/\lambda > 0.16$) the model must be expanded to include next nearest neighbour coupling [80]. The dispersion relation can then be shown to

become

$$\omega = \frac{\omega_m}{\sqrt{1 + \kappa_1 \cos(\phi) + \kappa_2 \cos(2\phi)}}. \tag{3.35}$$

This must now be applied as a three parameter fit using numerical software in order to calculate the couplings between nearest neighbour and next nearest neighbour.

There are many extensions to the circuit model that allow very accurate determinations of some complex situations. For example, the single RLC resonator can be extended to include a coupler connected to a transmission that removes power from the system [77], which is an analogy to a cavity that has an attached waveguide or coaxial coupler. The circuit model can be used to model beam excitation both in the time domain and the frequency domain [8], and the dispersion curves explored in this Chapter can be used to model cavities with a finite number of cells [80]. The derivations shown here are key to understanding mode behaviour in coupled resonant cavities, and will be used to fully understand the beam excited wakefield.

3.2.1 Group Velocity

As seen in Chapter 2, Section 2.8, the power deposited in a breakdown is strongly dependent on the group velocity of the cell [49]. The group velocity is calculated from [22]

$$v_g = \frac{d\omega}{d\nu}. \tag{3.36}$$

Using $\omega = 2\pi f$, and $\nu = \phi/L$, eqn. 3.36 can be re-written as

$$\frac{v_g}{c} = \frac{2\pi L}{c}\frac{df}{d\phi}. \tag{3.37}$$

The length of the cell, and thus the phase advance, is defined in terms of k and can be re-written according to

$$\begin{aligned} \nu_{acc} &= \frac{\phi_{acc}}{L}, \\ \frac{2\pi f_{acc}}{c} &= \frac{\phi_{acc}}{L}, \\ \frac{\phi_{acc}}{f_{acc}} &= \frac{2\pi L}{c}, \end{aligned} \tag{3.38}$$

which means, by substitution

$$\frac{v_g}{c} = \frac{\phi_{acc}}{f_{acc}} \frac{df}{d\phi}. \tag{3.39}$$

From eqn. 3.31, and taking $\phi_{acc} = \frac{2\pi}{3}$ (CLIC phase advance per cell), the group velocity for a CLIC cell can be determined as

$$\frac{v_g}{c} = \frac{\pi f_r}{3 f_{acc}} \frac{\kappa \sin\phi}{(1 + \kappa \sin\phi)^{3/2}} \tag{3.40}$$

Using typical CLIC values, the group velocity can be plotted as a function of ϕ, which is found below in figure 3.5. As the group velocity is linearly dependent on the derivative of the

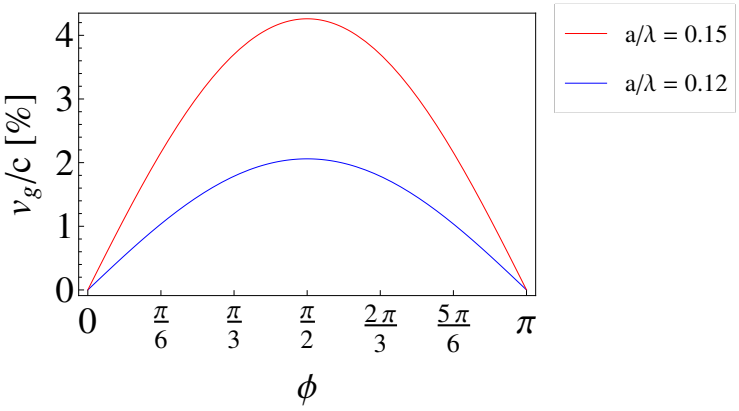

Figure 3.5: Group velocity for the dispersion curves found in figure 3.4.

dispersion curve, the group velocity can be seen to peak at $\phi = \pi/2$, as shown in figure 3.5. The larger the bandwidth of passband, the steeper the gradient will be for similar phases. When designing high gradient accelerating structures, much effort is placed in designing cavities with low group velocities in order to try and minimise the damage from rf breakdown [81].

It has been observed experimentally that cavities suffered more damage from breakdown when the breakdown occured in a cell with a high group velocity [49]. This motivated a model that treats the structure as a transmission line and rf breakdown as a load impedance. The fraction of incident power absorbed during a breakdown, assuming the

breakdown impedance is small compared to the structure impedance, scales as [82]

$$P_{abs} \sim \frac{v_g^2}{(R/Q)^2} \frac{\sin(\phi)}{\phi \sin(\phi) + 2v_g \cos(\phi)} E_{acc}^2, \tag{3.41}$$

where ϕ is the phase advance of the cell, v_g is the group velocity and E_{acc} is the accelerating gradient.

This is a key motivation for keeping the group velocity of a structure low. While it may not affect the breakdown rate, it does affect the ability of a cavity to operate reliably after undergoing several breakdowns.

However power flow through the cavity depends on the group velocity of the structure, therefore the filling time of the cavity depends on the group velocity. An optimum needs to be found for TW structures such that the cavity can fill quickly to maintain a high efficiency, without having a group velocity that will deposit a large amount of power in the event of a breakdown.

3.3 Double Chain Circuit Model

In a single uncoupled pillbox cavity, the dipole modes independent of each other. When an iris is introduced the dipole modes begin to couple with both TE and TM modes in the adjacent cell. The modes are now hybrid and can take the form of both TE and TM modes, and these modes couple to each other with different strengths. The equivalent circuit found in figure 3.6 is capable of accurately modelling dipole mode coupling in a cavity chain. A separate chain of cavities is added, where one chain represents the TE modes, and the other represents the TM modes. These can then couple to all of the other cells in both TE-TE, TE-TM and TM-TM.

A similar treatment can be given to the central cells for both the TE and the TM circuits. In this case, the corresponding parameters for the TM modes are denoted by a hat, and the TE modes are kept clear. Kirchoffs voltage rules can be applied, the current can be normalised with an independent variable as before, and two separate sets of equations can be obtained.

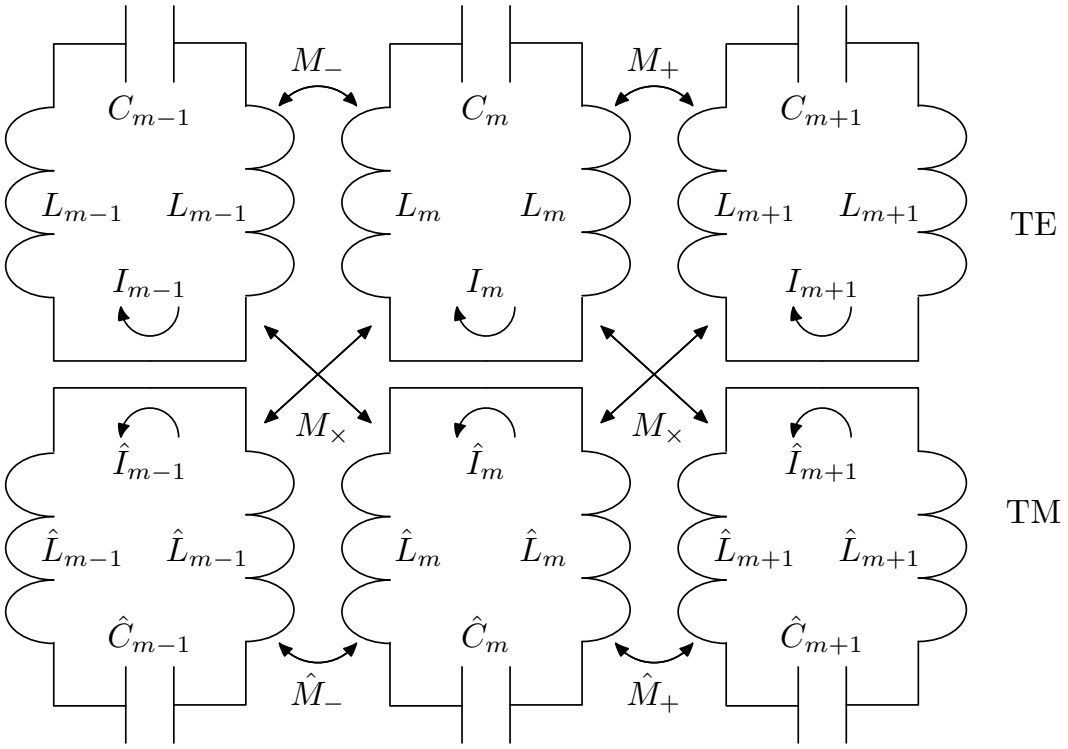

Figure 3.6: A double chain circuit model. A second cavity chain is added so that both the TE and TM modes can be modelled independently, and a term is introduced to allow cross coupling between the modes.

For the TE modes the corresponding equation is given by

$$(\frac{1}{\omega_m^2}-\frac{1}{\omega^2})a_m+\frac{\eta_{m+1/2}}{2}a_{m+1}+\frac{\eta_{m-1/2}}{2}a_{m-1}=\frac{\sqrt{\eta_{m+1/2}\hat{\eta}_{m+1/2}}}{2}\hat{a}_{m+1}-\frac{\sqrt{\eta_{m-1/2}\hat{\eta}_{m-1/2}}}{2}\hat{a}_{m-1}, \tag{3.42}$$

while for TM modes it can be shown that

$$(\frac{1}{\hat{\omega}_m^2}-\frac{1}{\omega^2})\hat{a}_m-\frac{\hat{\eta}_{m+1/2}}{2}\hat{a}_{m+1}-\frac{\hat{\eta}_{m-1/2}}{2}\hat{a}_{m-1}=-\frac{\sqrt{\eta_{m+1/2}\hat{\eta}_{m+1/2}}}{2}a_{m+1}+\frac{\sqrt{\eta_{m-1/2}\hat{\eta}_{m-1/2}}}{2}a_{m-1}, \tag{3.43}$$

where the 'hat' refers to parameters in the TM band, and without the hat refers to parameters in the TE band. The rest of the parameters have the same definitions as found in Section 3.2

As before, the periodic boundary conditions can now be applied by using eqn. 3.27, and the cell to cell coupling can be re-written in terms of κ and $\hat{\kappa}$ using eqn. 3.25 to give for the

TE mode

$$(1-\frac{\omega_m^2}{\omega^2})a + a\kappa\cos\phi = \frac{j\sqrt{\kappa\hat{\kappa}}}{2\hat{\omega}_m}\hat{a}\sin\phi, \tag{3.44}$$

and for the TM mode

$$(1-\frac{\hat{\omega_m}^2}{\omega^2})\hat{a} - \hat{a}\hat{\kappa}\cos\phi = -\frac{j\sqrt{\kappa\hat{\kappa}}}{2\omega_m}a\sin\phi. \tag{3.45}$$

Eqns. 3.44 and 3.45 can be expressed in matrix form as

$$\begin{pmatrix} \frac{1+\kappa\cos\phi}{\omega_m^2} & \frac{j\sqrt{\kappa\hat{\kappa}}\sin\phi}{\omega_m\hat{\omega}_m} \\ -\frac{j\sqrt{\kappa\hat{\kappa}}\sin\phi}{\omega_m\hat{\omega}_m} & \frac{1-\hat{\kappa}\cos\phi}{\hat{\omega}_m^2} \end{pmatrix} \begin{pmatrix} a \\ \hat{a} \end{pmatrix} = \frac{1}{\omega^2}\begin{pmatrix} a \\ \hat{a} \end{pmatrix}. \tag{3.46}$$

Finally, by taking the determinant of eq. 3.46 as $(\mathrm{Det}(H-\frac{1}{\omega^2})=0)$, where H is the 2x2 matrix on the LHS of eqn. 3.46 then the dispersion relation for coupled dipole modes can be calculated as

$$(\frac{1+\kappa\cos\phi}{\omega_m^2}-\frac{1}{\omega^2})(\frac{1-\hat{\kappa}\cos\phi}{\hat{\omega}_m^2}-\frac{1}{\omega^2}) - \frac{\kappa\hat{\kappa}}{\omega_m^2\hat{\omega}_m^2}\sin^2\phi = 0. \tag{3.47}$$

It can be seen that this formula incorporates the individual TE and TM dispersion curves, but also with an added coupling term. It is important that the frequency's for the 0 and π modes are selected correctly, in order to ensure that both coupling coefficients η and $\hat{\eta}$ are positive [80]. This can be done by observing the field patterns, and discerning which mode is a forward travelling wave ($\omega_\pi > \omega_0$) or a backward travelling wave ($\omega_\pi < \omega_0$). As before, the resonant frequency ω_m and $\hat{\omega}_m$ and the coupling coefficients η and $\hat{\eta}$ can be solved in terms of the 0 and π modes, with $\omega_m = \omega_r$ and $\hat{\omega_m} = \hat{\omega_r}$ [80]

$$\omega_r = \sqrt{\frac{2\omega_\pi^2\omega_0^2}{\omega_\pi^2+\omega_0^2}} \quad \text{and} \quad \eta = \frac{\omega_0^2-\omega_\pi^2}{\omega_\pi^2+\omega_0^2} \tag{3.48}$$

$$\hat{\omega_r} = \sqrt{\frac{2\hat{\omega}_\pi^2\hat{\omega}_0^2}{\hat{\omega}_\pi^2+\hat{\omega}_0^2}} \quad \text{and} \quad \hat{\eta} = \frac{\hat{\omega}_\pi^2-\hat{\omega}_0^2}{\hat{\omega}_\pi^2+\hat{\omega}_0^2} \tag{3.49}$$

By combining eqns. 3.47, 3.48 and 3.49, the dispersion curve for the TE_{011} and T_{011} dipole modes can be plotted alongside the light line.

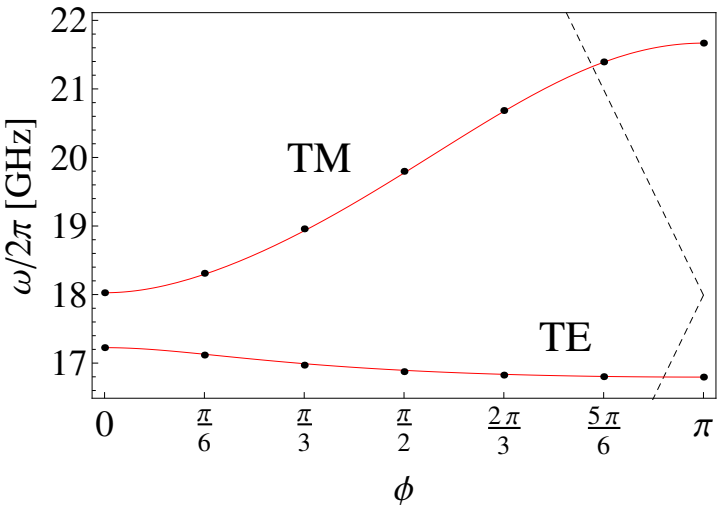

Figure 3.7: Coupled dispersion curves for the TM_{110} and TE_{110} modes of a pillbox cavity. The black points are simulation data, while the red line is the dispersion relation. The dashed line represents the light line. The data required can be obtained by simulation using *HFSS* or *TRANVRS* [83].

Figure 3.7 shows the coupled dispersion curves for the lowest TE and TM modes in a coupled pillbox cavity. The synchronous modes that comprise the transverse wakefield are found at the intersections between the light line and the dispersion curves. The TM mode is the forward travelling wave, while the the TE mode is given by the backward travelling wave. The opening of the iris allows the TE and TM modes in cell n to couple to the TE and TM modes of neighbouring cells. In the absence of coupling, then there would only exist one TE and TM mode, there would constant frequency for any phase advance. When the modes are coupled, it is not possible to excite one mode without exciting the other. This gives rise to the avoided crossing that is often seen in dispersion curves. The closer the modes get to one another, the weaker the coupling between the two modes.

Finally, before a study on collinear acceleration and multi-harmonic cavities can begin, a brief introduction into some fundamental principles of wakefield acceleration will occur. The next chapter will describe some potential candidates for the next generation of high gradient

machines that utilise wakefield acceleration.

Chapter 4

Wakefield Acceleration

This chapter will introduce several different mechanisms for wakefield acceleration. These range from theories developed in the 1980's by G.A.Voss and T.Weiland, to more contemporary methods using plasma physics in order to achieve accelerating gradients on the order of 10 GeV/m or more. Important parameters that determine the efficiency of power transfer, the transformer ratio and the beam to beam efficiency, will first be introduced.

4.1 Overview

There are two important parameters that need to be considered when discussing wake field acceleration schemes. These are the transformer ratio, $\mathcal{T}$, the beam-to-beam efficiency, η.

The general form of the transformer ratio is defined as the ratio of energy gain by a test bunch to the energy lost by a drive bunch, given by

$$\mathcal{T} = \frac{\Delta U_T}{\Delta U_D}, \tag{4.1}$$

however in the case where both the drive and test bunch have Gaussian profiles, and are both travelling with $\beta \approx 1$ through a symmetric cavity, the simpler form

$$\mathcal{T} = \frac{V_T}{V_D} \tag{4.2}$$

can be used, where $V_{T,D}$ is the voltage seen by the center of the test and drive bunch at the center of the cavity. The former case can be applied to any scenario, and is an extremely robust method for calculating the transformer ratio. The latter case is much more specific, and breaks down under many different scenarios (for example, when there is more than one mode present, or when the fields in the cavity do not follow idealised longitudinal profiles).

Several different types of wakefield accelerator will now be described, with some basic theory relevant to each setup provided.

In 1982, G.A. Voss and T. Weiland published an article outlining the concept of a simple wakefield accelerator [84]. A pillbox cavity is used that has three beam tubes attached, one traversing the center of the cavity, and two traversing near the edges of the cavity. A high current low energy drive bunch passes through the outer tubes, moving through an area of low impedance and exciting a field inside the cavity. These fields propagate towards the center of the cavity, where a high energy low current test bunch, moving through an area of high impedance, can be phased to arrive and see the superposition of these two wakefields. The layout is shown in figure 4.1.

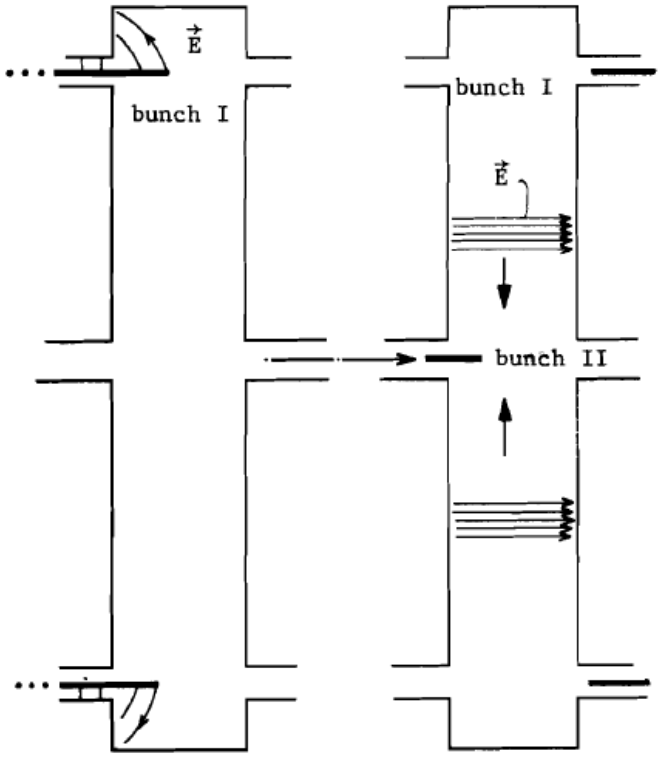

Figure 4.1: Two drive bunches (bunch I) transit a pillbox cavity at the edge, the wakefield moves through the structure to the origin, where a test bunch (bunch II) sees the superposition of the two wakefields.

An experiment of this setup can be used to achieve very high gradients (speculatively

it could reach $E_0 \approx 600$ MV/m with $\eta = 16\%$ for high drive currents). This is because the drive bunches at the outer edge see only a small decelerating field with each particle depositing only a small amount of energy, but because of the high current, the sum of all energy deposited over the entire bunch is very large.

In the case where the drive and the test bunches are moving collinearly (on the same axis) through a cavity on resonance, the potential within the cavity is given by

$$V(t) = -\int_{-\infty}^{t} I(t')W_z(t-t')dt'. \tag{4.3}$$

The contribution of mode n to W_z is $2k_n \cos(\omega_n t)$. With a constant current I, the potential inside a rectangular bunch ($-t_b < t < t_b$) is

$$V^-(t) = -I\int_{-t_b}^{0} W_z(t-t')dt' = -2I\frac{k_n}{\omega_n}\sin\left(\omega_n(t+t_b)\right) \tag{4.4}$$

The potential behind the bunch is

$$V^+ = -I\int_{-\infty}^{t} W_z(t-t')dt' = -4I\frac{k_n}{\omega_n}\cos\left(\omega_n t\right)\sin\left(\omega_n t\right) \tag{4.5}$$

Setting $\omega_n t = \frac{\pi}{2}$ allows the minimum potential inside and the maximum potential outside the bunch to be calculated as

$$V_m^- = -2\frac{k_n I}{\omega_n} \tag{4.6}$$

$$V_m^+ = 4\frac{k_n I}{\omega_n} \tag{4.7}$$

therefore $\mathcal{T} = 2$ [85].

It is possible to increase this maximum limit. One method is to have additional modes at harmonics of the fundamental frequency. Applying a similar method to before it can be shown that in this case $T \leq 2\sqrt{2}$. A different approach is to vary the drive bunch distribution in such a way that each particle within the bunch sees the same decelerating field [86]. This was explored by K.L.F. Bane *et al* and they found that using a ramped drive bunch, each particle within the bunch can deposit the same amount of energy, this allows transformer

ratios up to values of between 6 and 8. However, any deviation from the planned ramped bunch shape gives a sharp drop in T and reduces the efficiency of the transfer.

Annular drive beams have been explored by Lau *et al* [87], that show by using a cylindrical drive beam to excite a TM_{020} in a normal conducting cavity, transformer ratios approaching 14 can be achieved. In this case the test beam traverses the centre of the cavity. These studies show that larger transformer ratios than 2 can be achieved, however these bunch profiles can be difficult to generate and maintain.

There are two methods for wakefield acceleration that have been under extensive study, and will likely become the basis for high gradient acceleration. These will be described in the following two sections.

4.2 Plasma Wakefield Acceleration

Acceleration via rf technology is currently limited by issues with rf breakdown and pulsed surface heating. Despite this, the achievable gradient is also limited by current klystron technology, with issues occurring beyond approximately 150 MW. In order to push the accelerating gradient beyond the current limit of approximately 150 MV/m, new technologies need to arise that will take particle acceleration into a new phase of operation. Plasma wakefield acceleration is one of these new technologies.

The concept of plasma wakefield acceleration entails a drive bunch (electron, proton or laser) being sent through a column of plasma. The space charge fields from the drive bunch repel nearby plasma electrons. These electrons are now attracted back to the ions (which have remained stationary) and set up an oscillating wakefield. A test bunch is phased to arrive at the peak electric field of the oscillating plasma wakefield and experience a high accelerating gradient.

The electron plasma waves can sustain electric fields on the order of [88]

$$E_0 = \frac{cm_e\omega_p}{e}, \tag{4.8}$$

where m_e is the mass of the electron with charge e, and ω_p is the electron plasma frequency,

given by

$$\omega_p = \sqrt{\frac{n_0 e^2}{m_e \epsilon_0}}, \tag{4.9}$$

where n_0 is the ambient electron density and ϵ_0 is the permittivity of free space. Accelerating fields are therefore proportional to the electron density as

$$E_0[\text{V/cm}] \simeq 0.96 n_0^{1/2}[\text{cm}^{-3}]. \tag{4.10}$$

For $n_0 = 10^{18}$ cm^{-3}, $E_0 \simeq 100$ GV/m, which is approximately three orders of magnitude larger than conventional rf technology [88].

In the case where the drive bunch consists of protons, the plasma electrons are now attracted toward the drive bunch. This gives rise to a similar effect, but it occurs in reverse and the phase of the oscillating waves is altered. There are two distinct regimes that govern the theory of the plasma oscillations, the linear regime and the blowout regime. In the linear regime, a much simpler formalism can be used to describe the behaviour of the plasma electrons [88]. When all of the plasma electrons are cleared from the the region behind the bunch leaving only the ions within the ion channel, it is known as the blowout regime. The blowout regime is not formalised within linear theory, however it is included in models using non-linear theory and is confirmed by simulation [89].

In order to analyse the beam to beam efficiency of such a setup, the analysis must be split into two components. The efficiency of transferring drive beam energy to the wake, and the efficiency of transferring energy of the wake into the test beam. The first part can be calculated by determining the wake excitation and the distance over which it acts. This is limited by drive beam depletion [90]. The second can be determined by beam loading calculations.

Beam to wake efficiency in the blowout regime is typically higher than the 50-60 % estimated from linear theory. Simulations with a Gaussian distributed drive bunch with 3x10^{10} electrons and a plasma density of 10^{16}cm^{-3} have shown that the peak decelerating field is at a maximum close to the beam centre and is constant in radius [90]. In this case, 81% of the drive beam energy was transferred to the wake. As mentioned in the previous section, this

value can be increased by tailoring the drive bunch such that all particles deposit the same amount of energy into the wake. This could potentially increase the beam to wake efficiency to approximately 90%.

It is possible to obtain beam loading efficiencies of 100%. This occurs when the wake behind the test bunch is 0, or when the test bunch is very short (at the expense of 100% energy spread). However, when the bunch becomes too short, the test bunch itself begins to excite non-linear wakes, thereby complicating the issue [91]. Tzoufras *et al* [92] have developed a theoretical framework for beam loading in the non linear regime. They conclude that for shaped test bunches, beam loading efficiencies can exceed 90% while maintaining low energy spreads and emittances. However, for unshaped Gaussian bunches, high efficiencies and low energy spread can still be acquired.

The transformer ratio for a plasma wakefield accelerator adheres to the guidelines set in the previous section for collinear acceleration, it is not greater than 2 for symmetric bunches.

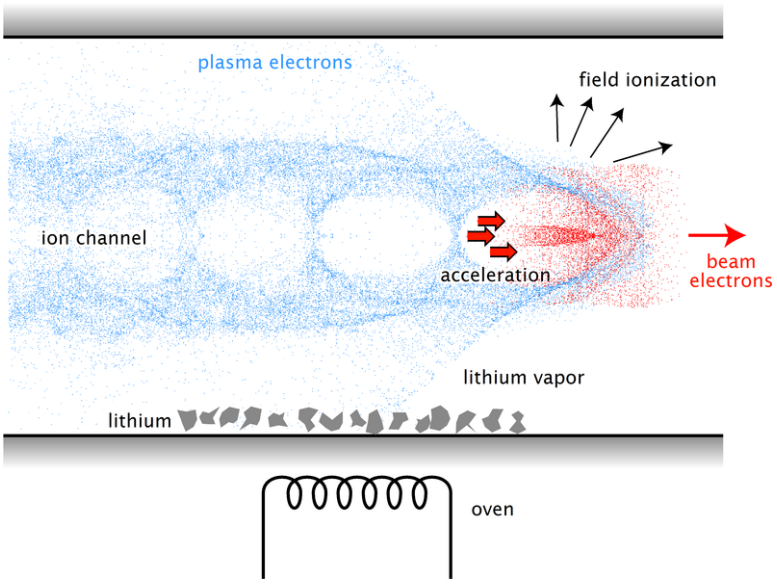

Figure 4.2: Image courtesy of R. Ischebeck. The drive bunch clears away the electrons as it traverses the plasma. The electrons fall back towards each and set up an oscillation, forming regions of dense electrons where high gradients are observed.

The high gradients predicted by theory have been shown experimentally by I. Blumenfeld *et al* at SLAC [93] and a figure of the experimental setup can be found in figure 4.2. A drive

bunch consisting of 42 GeV electrons traversed an 85 cm long column of lithium vapour. Rather than use a separate test bunch, a long drive bunch is used that will allow the tail of the bunch to see the high accelerating fields created by the head. As long as the radial electric field of the bunch exceeds the field ionisation threshold, then ionisation will occur in a very narrow region in front of the beam. This ionisation front produces a plasma that has a radius that is much larger than the beam itself. Keeping the beam density above this plasma density threshold, the plasma electrons will constantly expelled from the volume of the electron pulse, leaving the more massive ions behind. This then initiates the procedure described previously to set up an oscillating plasma wakefield. This longitudinal wakefield varies along the bunch, decelerating the core of the bunch but accelerating the particles along the back. The ions that remain in the plasma also provide a focusing force for the electron drive bunch, allowing the bunch to move beyond many diffraction lengths [93].

After the bunch has traversed the lithium column, a 1 m dipole magnet bends the particles with a radius that is dependant on the particle energy, which then collides with a series of YaG screens in order to determine the energy of the bunch.

Fig. 4.3 shows the results of this experiment. As expected, the majority of the bunch energy remains constant, however there are some particles which have been accelerated up to 85 GeV, over doubling their initial energy. The experiment is well predicted with PIC simulation. This energy gain corresponds to an acceleration gradient of approximately 52 GV/m. This indicates that such gradients can be sustained over lengths on the order of 1m, achieving the same energy gain as in that distance as the SLC achieved over 3km. However, one of the fundamental challenges facing plasma wakefield acceleration is showing that high gradients can be achieved with little energy spread. Even so, these results are promising for future high gradient machines, and show that plasma wakefield acceleration could be a viable method of acceleration in the future. The next key step in this area would be to attempt to accelerate a compact bunch with high gradients while maintaining a small energy spread.

4.3 Dielectric Wakefield Acceleration

Another scheme that could provide high gradient acceleration is the dielectric wakefield accelerator [94]. In this case an intense electron drive bunch traverses the hollow core of a

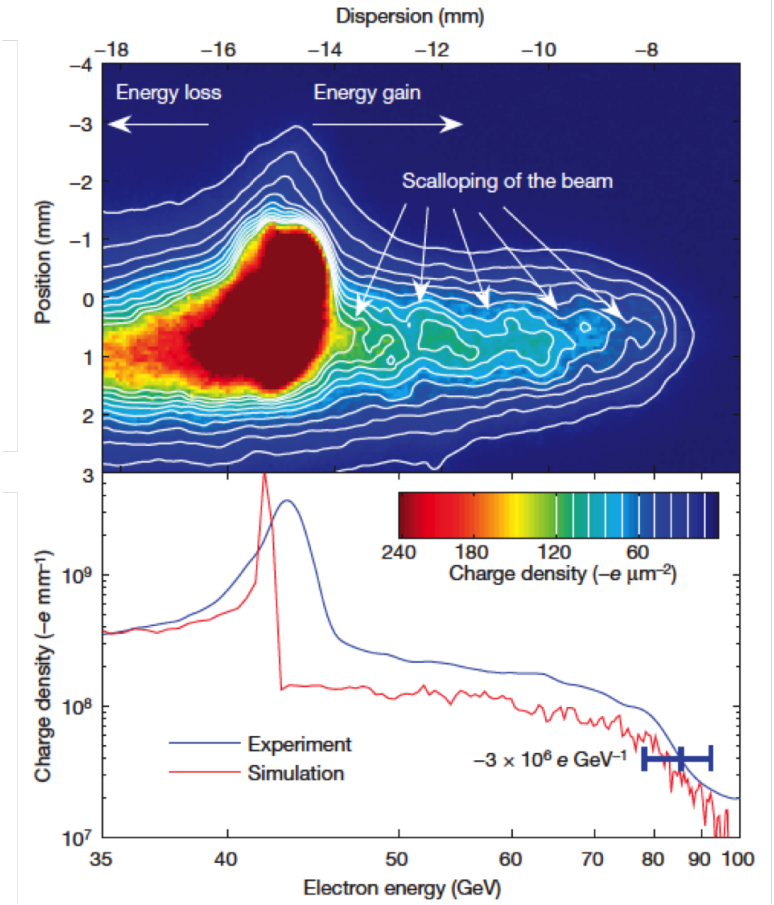

Figure 4.3: Plasma wakefield experiment performed at SLAC. A 42 GeV electron beam has managed to double the energy of a small amount of electrons [93].

cylindrical dielectric pipe (found in fig. 4.4.) This bunch excites e.m. fields in the form of Čerenkov radiation (if the particle is travelling at a velocity faster than the velocity of light in the medium). The emission is due to an asymmetric polarisation of the medium in front and at the rear of the bunch, giving rise to a varying electric dipole momentum. These fields can then be used to accelerate a test bunch of lower intensity.

All of the excited modes have a phase velocity equal to the velocity of the bunch (in this case, $\nu = c$). The amplitudes of these modes depend upon the pulse length and the profile of the drive bunch. For a Gaussian drive bunch of N particles with width σ_z, the excited E_z

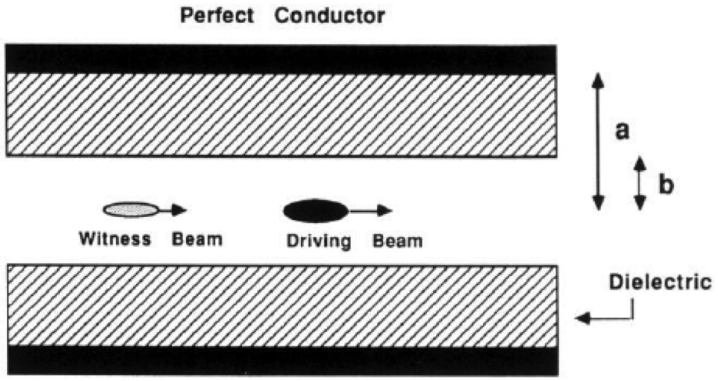

Figure 4.4: A typical setup for a dielectric wakefield accelerator [94].

field at a distance z_0 behind the drive bunch is given by [95]

$$E_z = \frac{2Ne}{\epsilon b}\sum_{\lambda}[\frac{J_0(s_\lambda b)N_0(s_\lambda a) - N_0(s_\lambda b)J_0(s_\lambda a)}{(d/ds)[J_1(sb)N_0(sa) - J_0(sa)N_1(sb)]|_{s=s_\lambda}}]\cos(\frac{\omega_\lambda}{\nu}z_0)\exp(-\frac{(\omega_\lambda\sigma_z)^2}{2c^2}), \tag{4.11}$$

where the wave numbers s_λ are the roots of

$$J_1(s_\lambda b)N_0(s_\lambda a) - J_0(s_\lambda a)N_1(s_\lambda b) = 0, \tag{4.12}$$

with J_n and N_n referring to the nth order Bessel Functions of the first and second kinds, respectively.

The resonant frequencies of the modes excited by the beam are given by

$$\omega_\lambda = \frac{s_\lambda c}{(\epsilon - 1)^{1/2}}. \tag{4.13}$$

As can be seen in eqn. 4.11, there is a inverse relation on b. This means that if b is reduced, the excited E_z field increases. Proof of principle experiments have been performed at Argonne's Advanced Accelerator showing gradients of 10 MV/m at X-band ($b \sim cm$) [96]. Experiments on dielectric breakdown in structures with small b (THz-scale) have been performed at the final focus test beam facility at SLAC, with dimensions $a = 162\mu$m and $b = 50\mu$m [97]. With these parameters, a maximum accelerating gradient of 16 GV/m was

found with a peak decelerating field seen by the beam was $E_z = -11$ GV/m [98]. This gives a peak transformer ratio of 1.45. However, it is unknown whether these gradients can be sustained over meter long distances while maintaining coherent acceleration.

Methods of increasing the transformer ratio have been investigated by A. Kanareykin and A. Altmark [99]. They have found that by introducing a type of coaxial dielectric waveguide structure, shown in figure 4.5, and exciting the structure using an annular drive bunch. Then transformer ratios up to 4.5 can been simulated.

The structure itself consists of a typical dielectric cylindrical waveguide being surrounded by a larger waveguide made of a different dielectric material. Vacuum fills the gap in between the two coaxial cylinders. An annular drive bunch traverses this gap, exciting fields within the inner region of the dielectric waveguide, where a test bunch sees the excited field.

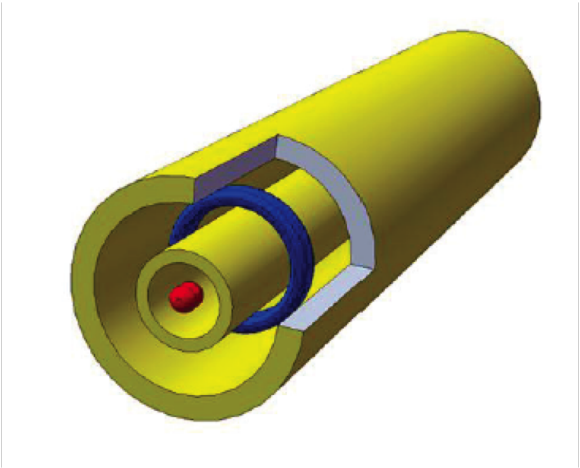

Figure 4.5: A coaxial dielectric structure capable of transformer ratios > 2. Blue is the annular drive bunch, while red is the test bunch.

Another method of high gradient acceleration that could potentially provide gradients in excess of 100 MV/m, while not succumbing to the damaging effects of rf breakdown and pulsed surface heating is the two beam acceleration concept described in preceding chapters. This concept could potentially bridge the gap between current rf technology and future plasma or dielectric technology.

Chapter 5

Single Mode Detuning

A method of beam driven acceleration by intentional cavity detuning will be explored, with derivations of the transformer ratio and the beam to beam efficiency also being included. This chapter will then verify, both by numerical modelling and simulation, the key principles of cavity detuning for a π-mode SW cavity.

5.1 Fundamental Mode Detuning for Collinear Two-Beam Acceleration

A high transformer ratio two beam accelerator using detuned cavities was first proposed by Kazakov *et al* [100] in 2008. Much of this section is based on the work originally proposed by Kazakov *et al* [100, 101] and the theoretical work was performed by Y. Jiang *et al* [8]. The numerical modelling and time domain simulations found in the final section of this chapter are an original contribution to the study.

A cylindrical cavity that has its TM_{010} mode frequency slightly detuned away from the drive bunch frequency can allow high current drive bunches to be decelerated and the low current test bunches to be accelerated. Both drive and test bunches are interleaved such that they propagate collinearly along the cavity origin, however as it will emerge, the bunches can be travelling either in the same direction or in opposite directions. This concept also allows the excitation of several harmonically related modes within the cavity for the raising of breakdown and pulsed heating thresholds, however this section is limited to the discussion of single mode detuned cavities.

When a drive bunch excites a cavity on resonance, the E_z-field builds up over time until it reaches a steady state value that depends on the cavity Q with a field oscillating at the cavity frequency. It is clear in this case that the transformer ratio will not be able to exceed

unity for symmetric drive bunches as the drive bunch is arriving at the peak decelerating field within the cavity. However, if the cavities are detuned, then the system begins to act as an oscillator driven off resonance. This results in two modes being excited, initially a mode at the cavity frequency, but the cavity mode decays and the result is an oscillation at the drive bunch frequency with a phase shift. This means the drive bunch is no longer arriving at the peak decelerating field. This is shown in figure 5.1. The solutions to a lightly damped drive harmonic oscillator [79] are plotted for two different cases. For resonant driving it can be seen the amplitude builds up over time before reaching a steady state value. For driving off resonance it shows a small amount of beating for low t before the oscillator mode decays and steady state is reached where it is now oscillating at the drive frequency.

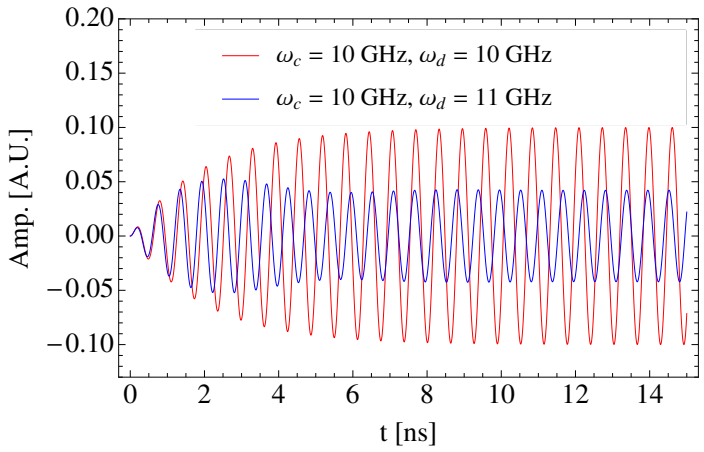

Figure 5.1: The solutions for a lightly damped drive harmonic oscillator, for the cases where the cavity is driven on resonance (red) and off-resonance (blue).

Without loss and driven off-resonance, the current and voltage are $\pi/2$ out of phase, meaning the peak electric field in the cavity occurs $\pi/2$ after the drive current. However, since a test bunch can be phased to arrive at an arbitary time after the drive bunch, drive beam voltage and test beam current can be in phase so that work is done on the test beam particles by the drive beam [102]. Thus, energy is gained by the test beam and an equal energy is lost by the drive beam. The transformer ratio in this case is the ratio of the currents $\mathcal{T} = \frac{I_D}{I_T}$.

With losses included in a detuned cavity, the drive beam voltage will lag or lead the drive

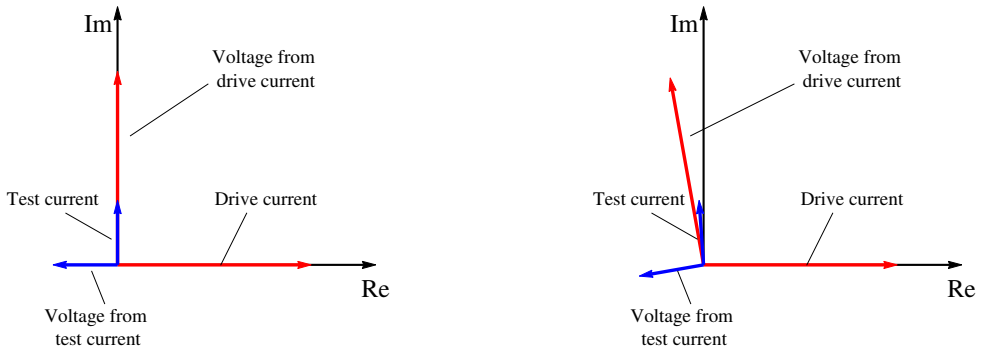

Figure 5.2: A phasor diagram of a cavity driven off resonance without loss (left) and with loss (right).

beam current depending on the sign of the detuning. This differs from the typical situation of cavities driven at resonance, where the induced voltage has a phase to give maximum deceleration which is linked to the arrival phase of bunches in the gap. With a non negligible test beam current, each current comprises a source that induced a voltage across the cavity gap which is a phasor sum of voltages seen by both beams [102]. The phase differences depend upon the degree of detuning, and an optimum difference can be found by simply adjusting the magnitude of the detuning.

This principle of two beam acceleration using detuned cavities does not depend upon the mass of either drive or test bunch. Hence this is also a mechanism that could allow acceleration of protons muons or heavy ions using an electron or proton drive beam.

5.2 Theory

Appendix B contains a full derivation for off-resonance beam driven cavities. The theory is derived by first considering a chain of coupled RLC circuits which are then excited by bunches that have been decomposed into their Fourier components. The definitions for each parameter can all be found in the Appendix and the important results will be discussed here.

For simplicity, the magnitude of detuning assumed to be the same for all cavities, however it may be advantageous to employ different signs of detuning in alternate cavities. These are henceforth referred to as ”fixed” and ”alternate” detuning.

The test beam current $I_T(z,t)$ propagates along the $\hat{z}$ direction, with the drive beam current $I_D(z,t)$ propagating along either the $\hat{z}$ or the $-\hat{z}$ direction. Both beams are travelling on axis and both of these currents can be considered as a superposition of harmonically related modal currents, with frequencies ω_s and wave numbers k_{T_s} and k_{D_s},

$$I_T(z,t) = \sum_s I_{T_s} e^{i(\omega_s t - k_{T_s} z + \phi_{T_s})}, \tag{5.1}$$

and

$$I_D(z,t) = \sum_s I_{D_s} e^{i(\omega_s t - k_{D_s}(z-z_0) + \phi_{D_s})}, \tag{5.2}$$

where ϕ_{T_s} and ϕ_{D_s} are the initial temporal phases of the modes, the wave numbers $k_{T_s} = \frac{\omega_s}{\beta_T c}$ and $k_{D_s} = \frac{\omega_s}{\beta_D c}$ with β_T and β_D the normalised particle velocities, s is the mode index and z_0 is the separation between the drive and the test bunches.

Therefore,

$$I(z)e^{i\omega_s t} = I_{D_s}(z,t) + I_{T_s}(z,t). \tag{5.3}$$

The steady state electric field in the n^{th} cavity can be written as a Fourier series

$$E_z(z,t) = \sum_s E_s(z) e^{i\omega_s t}, \tag{5.4}$$

where $E_s = \frac{V_s}{g}$ and g is the cavity gap. The electric field for each mode is given as

$$E_s(z) = \frac{R_s}{2g^2} \frac{1}{1 + i2Q\delta} \int_{n\Lambda - \frac{g}{2}}^{n\Lambda + \frac{g}{2}} I(z) dz. \tag{5.5}$$

It can be shown that the E_s-field in the cavity is

$$E_s(z) = \frac{R_s}{2g} \frac{e^{-i\theta_n}}{\sqrt{1 + 4Q^2\delta^2}} I_D \Theta_D (\xi e^{-i(\phi_T + k_T n\Lambda)} + e^{-i(\phi_D + k_D(n\Lambda - z_0))}), \tag{5.6}$$

where $\theta_n = \tan^{-1}(2Q\delta_n)$ is the phase angle between the electric field and current. $\delta_n = (-1)^{\xi n}\delta$ for $\xi = 0, 1$ (fixed or alternate detuning), $\Theta_{T,D}$ is the transit time factor, Λ is the cavity period and r_s is the shunt impedance.

The propagator is now calculated [102]. This is the factor that propagates the electric field and the current from one cavity into the next. The first term required is

$$\Pi_E = \frac{E_z(z=\Lambda)}{E_z(z=0)}, \tag{5.7}$$

which can be calculated by substituting $n = 1$ and $n = 0$ into eqn. B.20 and taking the ratio. Therefore, the following expression can be obtained

$$\Pi_E = \frac{\xi e^{-ik_T\Lambda + i\phi_T} + e^{-k_D(\Lambda - z_0) + i\phi_D}}{\xi e^{i\phi_T} + e^{i(k_D z_0 + \phi_D)}} e^{-i2\xi\theta}. \tag{5.8}$$

The second required term is

$$\Pi_T = \frac{I_T(z=\Lambda)}{I_T(z=0)} = e^{-ik_T\Lambda}. \tag{5.9}$$

In order to achieve phase synchronism, it is necessary for the ratio $\frac{\Pi_T}{\Pi_E}$ be equal to a real number i.e. with a zero imaginary component. For this to occur, there are four cases that can be explored. Fixed and alternate detuning with parallel and anti-parallel beams.

Firstly, for fixed detuning $\xi = 0$, the imaginary component vanishes when

$$\beta_T = \frac{\beta_D}{1 + \frac{2m\pi c\beta_D}{\Lambda\omega}}, \tag{5.10}$$

while for alternate detuning $\xi = 1$ so it is necessary to evaluate the relation in the limit where the modified current ratio $\varsigma \to 0$, i.e. that the test beam current is much smaller than the drive beam current. This leads to

$$\beta_T = \frac{\beta_D}{1 - (m + \frac{\theta}{\pi})\frac{2\pi c\beta_D}{\Lambda\omega}}. \tag{5.11}$$

These synchronism conditions give some straightforward guidelines about the architecture of a two beam accelerator for various parameter regimes. It is assumed that $\beta_T > 0$ but that $\beta_D > 0$ for parallel beams or $\beta_D < 0$ for antiparallel beams. With fixed detuning and highly relativistic test particles ($\beta_T \approx 1$) and drive particles ($\beta_D \approx 1$) it can be seen for the case of $m = 0$ from eqn. B.29 that synchronism can be achieved for arbitrary values of

$2\pi c/\omega\Lambda = \lambda/\Lambda$, where λ is the bunch spacing. For $m = 1$, synchronism requires $\Lambda \approx \lambda/2$ but only for antiparallel beams. This places a restriction on the transit time factor, and can also can make the gap g much smaller than the cavity spacing Λ.

The acceleration of moderately relativistic particles ($\beta_T < 1$) with a highly relativistic drive beam ($|\beta_D| \approx 1$), is possible for fixed detuning with parallel beams so long as $m \geq 1$. However, this would require $\Lambda << \lambda$ for low values of β_T, which results in low energy gain for test particles crossing each cavity. This is the same with fixed detuning and antiparallel beams for small values of β_T.

As a result from these restrictions, the ideal configuration for a two beam accelerator of initially low β_T test particles is with alternate detuning. Synchronism can now be obtained with antiparallel beams $\beta_D \approx -1$ for $\theta \approx -\pi/2$ and $\beta_T \leq 1$, for all values of negative m including zero, and for values of Λ/λ that satisfy eqn. B.30. For low values of β_T, synchronism can prevail if $\Lambda\lambda$ is low enough. If this is too low, a scheme with M cavities detuned positively followed by M detuned negatively can be used. These schemes can yield transit time factors close to 1. This is the favoured choice for acceleration of low- β_T particles, i.e. protons into the GeV range, while parallel beams are better suited for acceleration of electrons or positrons into the TeV range.

The transformer ratio can now be calculated by imposing the synchronism conditions on 5.6. An additional factor $\exp(i\omega t)$ needs to be included to account for the time varying field in the cavity. By calculating the real part of the E_s field at the correct time, the transformer ratio can be calculated from $\mathcal{T} = \frac{E_T}{E_D}$. It can be shown that the corresponding fields for the drive and test bunches are given by

$$\begin{aligned} E_T(n\Lambda, t_T) \quad &= \tfrac{R_s}{2g}\tfrac{\Theta_D I_D}{1+4Q^2\delta^2}(\varsigma\cos\phi_T + 2Q\delta\varsigma\sin\phi_T \\ &\quad + \cos[k_D z_0 - (k_D - k_T)n\Lambda + \phi_D] \\ &\quad + 2Q\delta\sin[k_D z_0 - (k_D - k_T)n\Lambda + \phi_D]) \end{aligned} \tag{5.12}$$

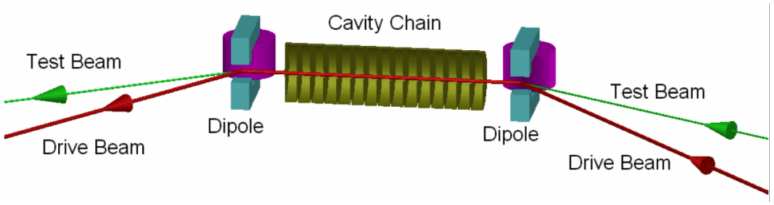

(a)

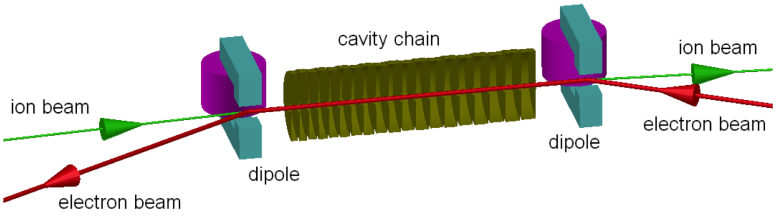

(b)

Figure 5.3: High transformer ratios can be achieved in the case where the drive and test bunches are propagating collinearly in both parallel and anti-parallel situations. (a) can utilise fixed detuning while the setup in (b) can be used for alternate detuning. Image reproduced courtesy of Y. Jiang [103].

and

$$\begin{aligned} E_D(n\Lambda, t_D) \quad &= \tfrac{R_s}{2g}\tfrac{\Theta_D I_D}{1+4Q^2\delta^2}(\cos\phi_D + 2Q\delta\sin\phi_D \\ &+\varsigma\cos[k_D z_0 - (k_D - k_T)n\Lambda - \phi_T] - \\ &2Q\delta\varsigma\sin[k_D z_0 - (k_D - k_T)n\Lambda - \phi_T]). \end{aligned} \tag{5.13}$$

Eqs. 5.12 and 5.13 provide the basis from which a range of parameters for an accelerator setup can be explored. Here, only the electron model will be mentined.

For ultra relativistic electron acceleration, the drive beam and the test beam have $\beta_T \approx \beta_D \approx 1$, the beams propagate in the same direction so $k_T = k_D = k = \frac{\omega}{c}$. The transit time factors are equal $\Theta_D = \Theta_T = \Theta$ which means the modified current ratio is just the current ratio itself $\varsigma = \frac{I_T}{I_D}$. The initial phases are chosen to be $\phi_T = \phi_D = 0$. This gives the field seen by the electron test beam as

$$E_T(n\Lambda, t_T) = \frac{R_s}{2g}\frac{\Theta I_D}{1+4Q^2\delta^2}(\varsigma + \cos kz_0 + 2Q\delta\sin kz_0), \tag{5.14}$$

while for the co-propagating electron drive bunch the electric field is given by

$$E_D(n\Lambda, t_D) = \frac{R_s}{2g}\frac{\Theta I_D}{1+4Q^2\delta^2}(1+\varsigma\cos kz_0 - 2Q\delta\varsigma\sin kz_0). \tag{5.15}$$

By choosing the appropriate phase delay between the test beam and the drive beam, then the equation for the transformer ratio can be determined. Therefore

$$\mathcal{T} = \frac{(\varsigma+\cos kz_0 + 2Q\delta\sin kz_0)}{(1+\varsigma\cos kz_0 - 2Q\delta\varsigma\sin kz_0)}. \tag{5.16}$$

For $z_0 = (2j-\frac{1}{2})\frac{\pi}{k}$ with $j = 0$ or an integer, then

$$\mathcal{T} = \frac{\varsigma - 2Q\delta}{1+2Q\delta\varsigma} \tag{5.17}$$

Eqn. 5.17 is the beam loaded transformer ratio, and it takes into account the field excited by the test bunch as the well the drive bunch. It is clear to see that when $\varsigma = 0$, the equation reduces to the unloaded case, which is simply given by

$$\mathcal{T} = -2Q\delta, \tag{5.18}$$

which is simply the magnitude of the detuning (as seen in eqn. 3.16).

The beam to beam efficiency can be shown to be given by

$$\eta = -\varsigma\mathcal{T} = \frac{2Q\delta\varsigma - \varsigma^2}{2Q\delta\varsigma + 1}. \tag{5.19}$$

Transformer ratios in excess of 1 are easily achievable by designing cavities according to this equation. Beam loading causes a large reduction in the transformer ratio while increasing the beam to beam efficiency, as can be seen in figure 5.4. For small values of ς, the transformer ratio is very sensitive to the test beam current. The transformer ratio depreciates rapidly until the test bunch current is approximately 20 % the drive bunch current. By this time the transformer ratio has reduced to about 25 % the of the unloaded case.

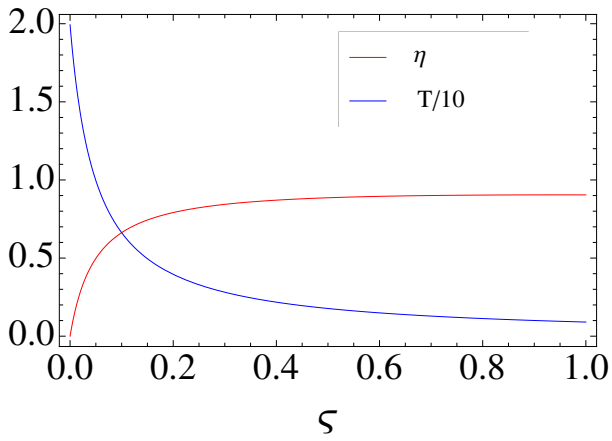

Figure 5.4: Transformer ratio and beam to beam efficiency as a function of the modified current ratio.

These results are important and show that efficient collinear acceleration is possible. These findings will be verified by modelling and time domain simulations in the following section.

5.3 Modelling and Simulations

5.3.1 Standing Wave Pillbox Cavity

A pillbox cavity geometry will be used for a variety of simulations in order to verify the fundamental detuning principles. The cavity geometry can be found in figure 5.5. The λ specified in the parameters is the λ corresponding to the drive frequency of 11.9942 GHz. The height of the end cells and the central cell is optimised in order to achieve a field flatness of less than 0.1% with a fundamental frequency of 12.1156 GHz, which allows $\mathcal{T} = 10$ for $Q = 500$. The conductivity of the material is varied arbitrarily to achieve the required Q value.

The field contours can be found in figure 5.6, the beampipes are of a length that allows the cavity field to attenuate sufficiently prior to the beampipe. The length was made slightly longer than required to avoid any issues with stray charges on the boundaries when perform-

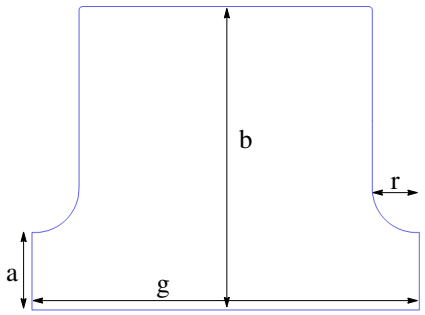

Parameter	Units	Value
b	mm	9.6
r	mm	1.5
a	a/λ	0.1
g	-	$\lambda/2$
b_{end}	mm	9.6

Figure 5.5: Geometry of a single cell with parameters listed on the right.

ing the time domain simulations found later in the chapter.

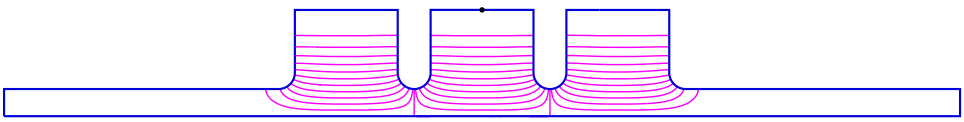

Figure 5.6: Field contours of a three cell SW π-mode cavity.

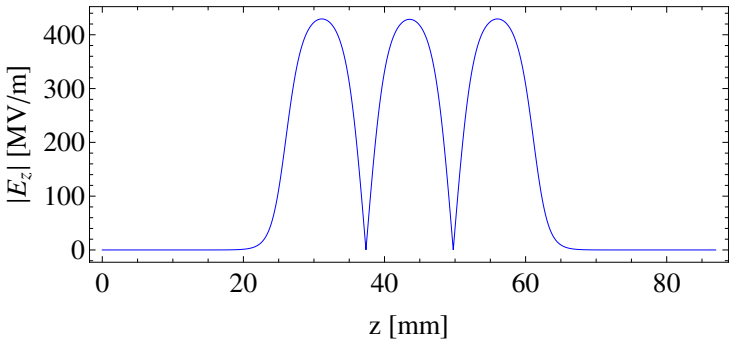

Figure 5.7: Axial E_z-field profile of a three cell SW π-mode cavity. The average accelerating gradient is normalised to 100 MV/m.

RF parameters for this cavity can be found in table 5.1. Here, Θ refers to the transit time factor for a single cell of the cavity. Multi-harmonic cavities will undergo similar simulations in Chapter 7, therefore it is important to be able to verify the surface properties between eigenmode simulations and time domain simulations of detuned accelerating structures. The

Parameter	Units	Value
f_c	GHz	12.1156
$k_{\parallel}$	V/pC	9.12
Q	-	500
Θ	-	0.724
ϕ	-	π
$E_{s,max}/E_0$	-	4.69
$H_{s,max}/E_0$	mA/V	8.7

Table 5.1: RF parameters for a three cell pillbox cavity.

surface fields of the cavity were extracted and plotted and will be used as a benchmark for the time domain simulations shown in Section 5.3.4.

This cavity design can maintain a high degree of field flatness for a large number of cells. The rf parameters of this cavity will be modelled numerically for the case of a single mode detuned accelerating structure, both by theory and particle tracking. The discussion will then move onto time domain simulations verifying the key principles.

5.3.2 Excitation Model

This section will derive a simple model based upon the simple behaviour of fields in a cavity after the passage of a bunch. This model can be applied to a detuned regime and the transformer ratio can be calculated.

The voltage left in a cavity after the passage of a bunch with a Gaussian distribution is given by [30]

$$V_q = 2k_n Q_b \exp(-\frac{\omega_n^2 \sigma_z^2}{2c^2}) = 2k_n Q_b \exp(-\frac{\omega_n^2 \sigma_t^2}{2}), \tag{5.20}$$

where Q_b is the bunch charge and $\sigma_{z,t}$ is the one sigma bunch length in z and t respectively.

A bunch is only effective at exciting modes for $1/\sigma_t \gtrsim \omega_n$. If $1/\sigma_t \gg \omega_n$ then the bunch can be treated as a point charge, whereas if $1/\sigma_t \ll \omega_n$ then the induced voltage is much less than for a point charge. Therefore, any HOM where $1/\sigma_t \ll \omega_n$ need not to considered as it is not strongly excited.

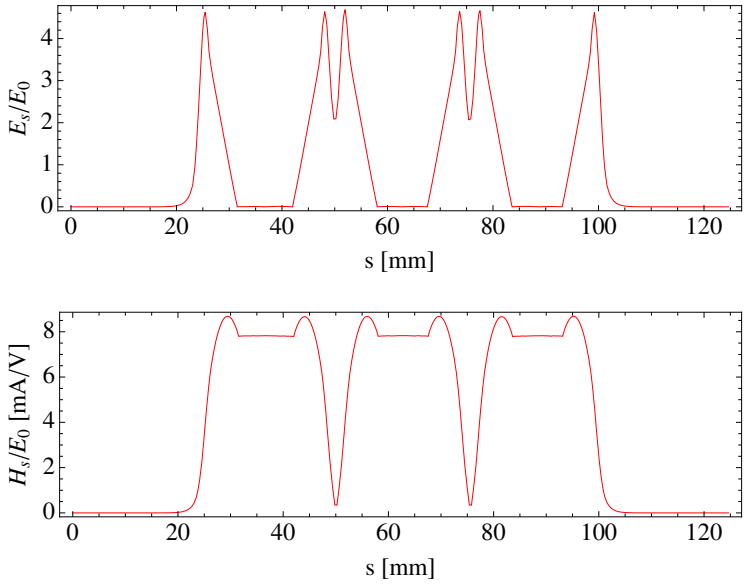

Figure 5.8: Normalised electric (top) and magnetic (bottom) fields along the surface of a three cell pillbox cavity.

The voltage in the cavity oscillates and decays according to

$$V_b = V_q \exp(i\omega_n t) \exp(-\frac{t}{\tau}), \tag{5.21}$$

with τ as the decay constant given as $\tau = \frac{2Q_L}{\omega_n}$. In the case of a train of bunches separated in time by t_b, the cavity voltages evolves as

$$V = \sum_{n_b=0}^{N} V_b(t - n_b t_b), \tag{5.22}$$

where V_b is zero for $t < 0$. This model manifests itself into two distinct regimes, on-resonance and off-resonance excitation. If the cavity is excited on-resonance, then the drive frequency equals the cavity frequency i.e. $f_d = f_c$, whereas off-resonance excitation occurs when $f_d \neq f_c$. In the case of off-resonance excitation, it will be shown that the steady state field profile undergoes a phase shift calculated by $\phi = \arctan(-2Q\delta)$, which causes the drive bunch to no longer experience a peak decelerating field, but instead experiencing a low decelerating field, greatly increasing the transformer ratio.

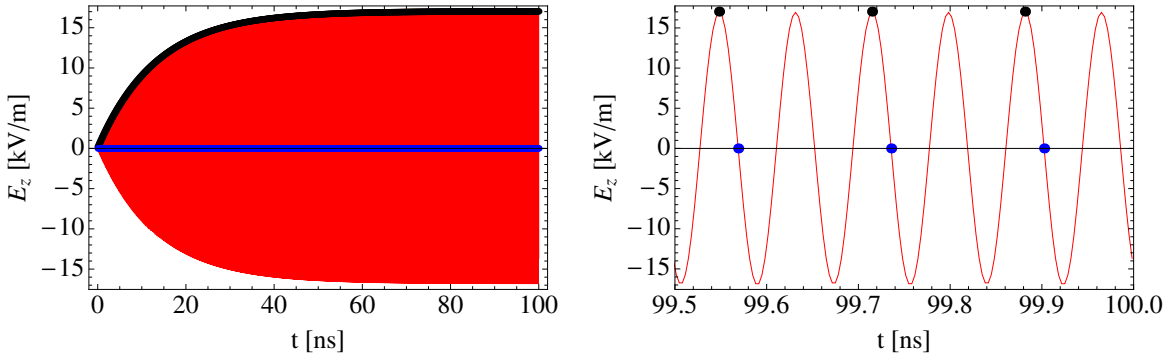

Figure 5.9: The cavity voltage as a function of time for resonant excitation with a zoomed plot to show the arrival time of the bunches on the right.

Resonant Excitation

For the case of resonant excitation, the fields from each bunch are synchronous and the voltage increases until steady state is reached. Figure 5.9 shows a plot of eqn. 5.22 for the case where only a single mode is considered and $f_c = f_d$. This figure was constructed using the cavity parameters from 5.1, $\sigma_z = 3$ mm with $Q_b = 1$ pC and a bunch spacing $t_b = 2t_{rf}$ which gives a current $I = Q_b/t_b$, the steady state field amplitude can be seen to be given by 17.03 kV/m.

In practice, a unit step function was applied to the function in order to keep the voltage zero for $t < 0$. However, this meant that the model did not work for $t_b = t_{rf}$ as there was a discontinuity arising at the arrival time of the bunch. As it was shown in Chapter 4 that the transformer ratio remains the same for integer spacings of t_{rf}, the bunch spacing was doubled and the transformer ratio was calculated on the oscillation without the discontinuity.

The drive bunches (black points) arrive at the crest of each rf cycle, seeing the peak decelerating field of the wakefield from the leading bunches. The transformer ratio can also be calculated from the ratio of the fields $\mathcal{T} = E_T/E_D$. It is clear that for a test bunch trailing behind the drive by $\pi/2$ then $\mathcal{T} = 0$, whereas for a trailing distance of π then $\mathcal{T} = 1$. In the current setup it is not possible for the transformer ratio to exceed unity as the drive bunch sees the peak decelerating field.

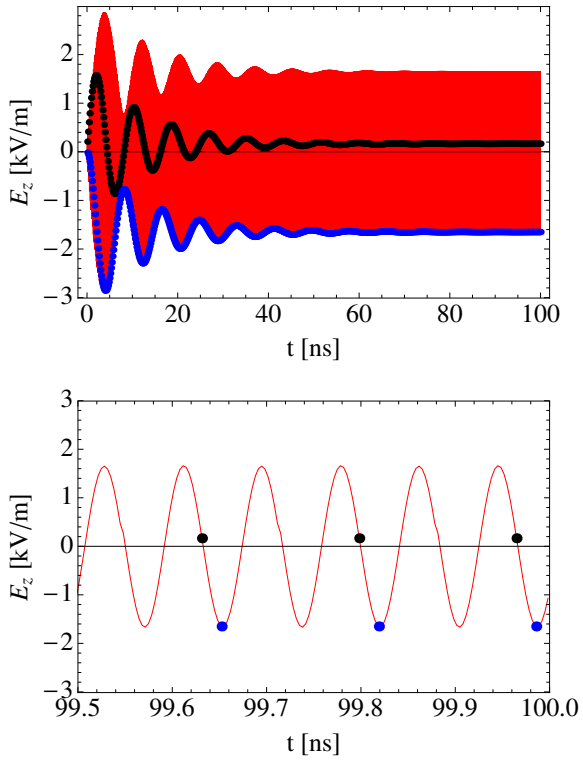

Figure 5.10: The cavity voltage as a function of time for off-resonant excitation with a zoomed plot to show the arrival time of the bunches on the right.

The steady state field profile for resonant excitation can be approximated by

$$E_{ss} = IR_{s,n} \cos(\omega_n t) \tag{5.23}$$

where I is the bunch current and R_n is the shunt impedance of the mode. The model returns a field amplitude that is within 0.5% of the expected value, despite the fact that discontinuities brought in by the unit step function are excluded from the analysis.

Off-Resonance Excitation

Using the CLIC drive frequency $f_d = 11.9942$ GHz and the same bunch and cavity parameters as specified in the previous section, the cavity is now excited off-resonance.

Figure 5.10 shows the field profile in this case, with the cavity frequency being excited

for small t and beating while it decays leaving a steady state field which oscillates at the drive frequency.

The steady state field for off resonant excitation can be approximated by

$$E_{ss} = IR_{s,n} \cos(\phi) \cos(\omega_n t + \phi), \tag{5.24}$$

where $IR_{s,n} \cos(\phi)$ is the amplitude of the oscillation. The steady state amplitude found in the model is within 0.2% of the expected theoretical value of 1.66 kV/m.

Eqn. 5.24 shows that for high transformer ratios (ϕ approaching $\frac{\pi}{2}$) there is a substantial reduction in the steady state field amplitude (17kV/m vs 1.8kV/m). There is also a further reduction in the amplitude when considering the need to maximise the inter bunch spacing in order to mitigate the effect of HOM's. This gives the need for much higher drive bunch currents in order to achieve gradients similar to CLIC.

The following section will verify one of several methods of calculating the transformer ratio, by integrating a bunch profiles with the correct phase offset throughout the entire cavity field.

5.3.3 Energy Tracing

ASTRA (A Space-charge TRacking Algorithm) is a tracking code that allows particle distributions to be iteratively traced through a series of fields that are either user specified or by providing lattice parameters.

By inputting a cavity field profile and stating an initial phase and oscillation frequency, a particle's energy gain/loss can be calculated through the structure. ASTRA was used to track the energy of both the drive beam and the test beam through a field profile extracted from eigenmode simulations. A 9-cell version of the previous SW π-mode cavity was used for this tracking.

The cavity geometry and field profiles can be found in figure 5.11. The field oscillates with the CLIC drive frequency and the particles are travelling with $\beta \approx 1$.

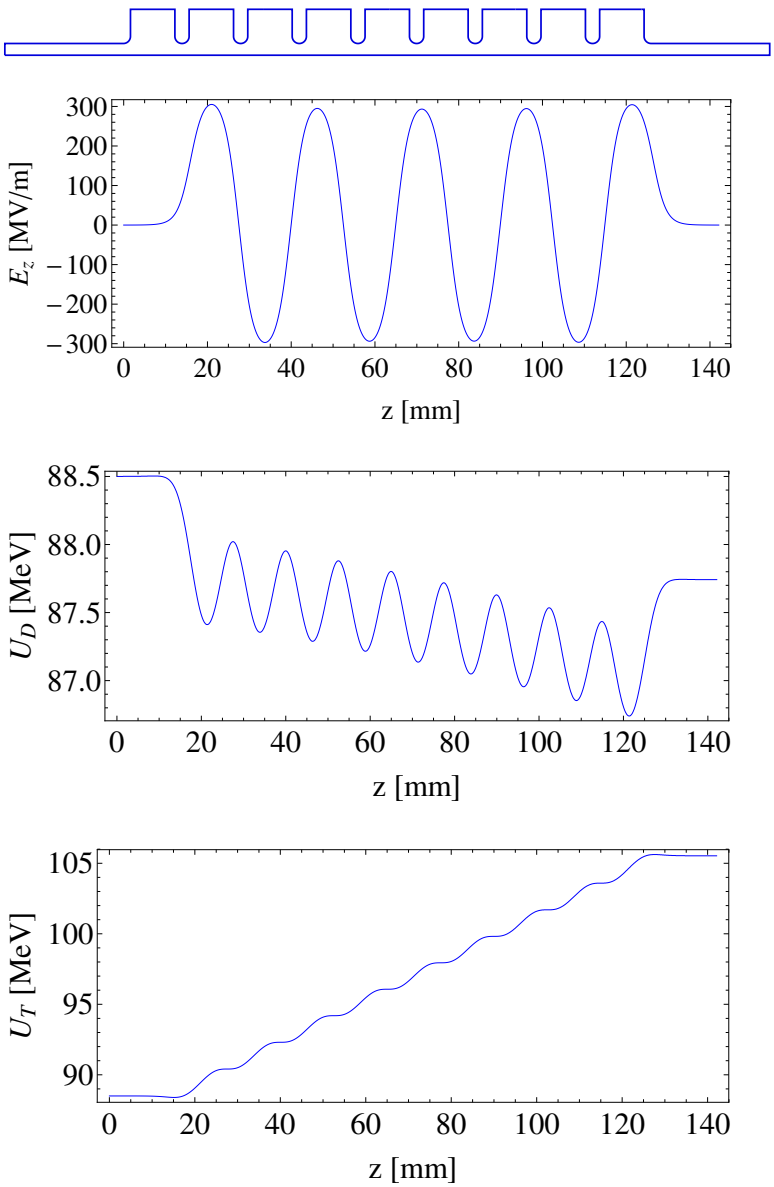

Figure 5.11: Top and second from top give the geometry and field profile, while second from bottom and bottom show the energy loss by drive beam and energy gain by test for $T = 22.5$.

The energy gain and energy loss was calculated for a range of different transformer ratios. For each case, the transformer ratio was found to be accurate to less than 0.2% of the expected value. Shown here is the case for $\mathcal{T} = 22.5$. For this simulation, $\Delta U_D = 0.758$ MeV and $\Delta U_T = 17.03$ MeV. This gives $\mathcal{T} = 22.47$, 0.14% away from the predicted value. Errors arise from the discrete sampling used in the iterative procedure and the fact that these types of simulations typically only use $\approx 10,000$ macro particles to represent the bunch.

This mechanism can be used to calculate the transformer ratio with the fields extracted from time domain simulations, which will be described in the next section.

5.3.4 Time Domain Simulations

ACE3P is a suite of advanced simulation codes developed by SLAC [104]. It includes a time domain code called T3P which allows bunches to traverse structures and accounts for the excitation of fields on the bunch, but also includes effects from the bunches on the field.

This section will describe the techniques used in calculating the transformer ratio and the surface parameters for a cavity. Initially, this will be calculated for $\mathcal{T} = 10$ and $Q_c = 500$ both with and without beam loading. Results will then be stated for similar simulations using different cavity parameters.

The cavity can now be excited by a train of bunches on axis. Each bunch has a charge of 1 pC, a repetition frequency of $11.9942/2$ GHz (CLIC rf frequency with every other bucket filled), a σ_z of 3 mm with a $4\sigma_z$ cutoff. Probes are placed at evenly spaced points on axis throughout the cavity which store the fields for each time step of the simulation. When simulating a cavity in the time domain, many HOM's are also excited along with the fundamental. Therefore, each of the probe signals undergoes a Direct Fourier Transform (DFT) [105] and has all higher frequency components removed by applying a window in the frequency domain. 3-dimensional field monitors are used to record the full cavity field once the cavity has reached steady state. A snapshot of the steady state field can be found in figure 5.12.

A cavity may be designed from eigenmode simulations to have a certain amount of detuning, however time domain simulations use different algorithms to numerically solve the

Figure 5.12: The E_z-field profile of the steady state field as simulated in t3p. The bunch profiles can also be seen.

fields and so the predicted values of f_c and Q_c may not necessarily be the same as what is simulated using eigenmode solvers. Therefore, the expected transformer ratio will correspond to the amount of detuning caused by the f_c and Q_c that has been simulated in the time domain, not the eigenmode. In order to calculate these parameters, the field from a probe placed at the centre of the cavity can be extracted, and the arrival time of each drive bunch can be overlaid The cavity parameters can then be obtained by applying a numerical fit of the drive bunches to the following function

$$f(t) = A\cos((\omega_c - \omega_d)t + \phi)\exp(\frac{-\omega_c t}{2Q_c}) + C, \tag{5.25}$$

where A and C are constants.

The results of such a fit can be found in figure 5.13. Good agreement is found between the fit and the data points. It emerges that $Q_{c,fitting} = 482$ compared to the expected value of $Q_{c,eigen} = 500$ and the $f_{c,fitting} = 12.1113$ GHz compared to $f_{c,eigen} = 12.1215$ GHz. The calculated Q_c is within 5% of the expected value, with possible errors likely arising due to asymmetric fields within the cavity from energy being deposited by the bunch in different cells at different times. The error on f_c is not due to the mesh representation because both simulations are using identical meshes, it arises from the different algorithms used to compute the eigenmode and the time domain fields. The eigenmode solver numerically solves Maxwells equations for the given mesh with appropriate boundaries, whereas the time domain solver casts Maxwells equations into a second order wave equation solver by combining Ampere's and Faraday's law. The changes in parameters mean that the expected transformer ratio from the simulation is $\mathcal{T} = 9.31$.

The transformer ratio will first be calculated without beam loading according to $\mathcal{T} =$

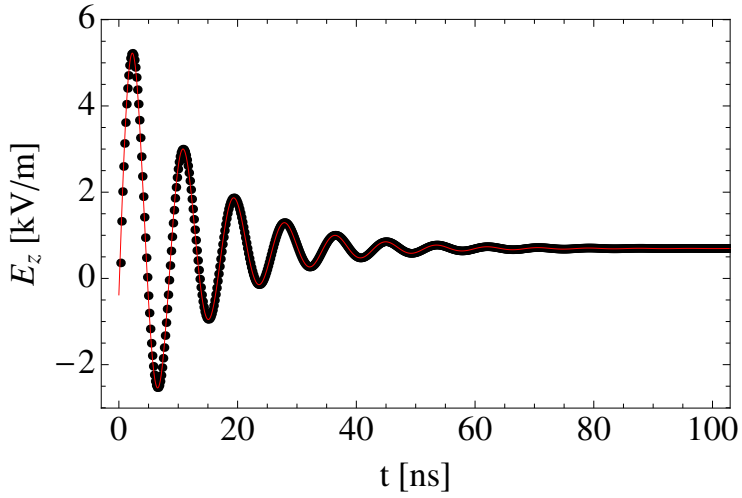

Figure 5.13: The equation proves to give an excellent fit to the decay of the cavity field. Here, the fit is given by the red curve and the black dots are the drive bunch locations.

$\Delta U_t/\Delta U_d$, given that

$$\Delta U_{d,t} = \frac{c}{L}\int_{-t_{rf}}^{2t_{rf}}\int_{0}^{L} g_{d,t}(z,t)E_z(z,t)dzdt, \tag{5.26}$$

where E_z is the steady state electric field and $g_{d,t}$ is the current distribution (in this case Gaussian) representing the drive or test bunch and is given by

$$g(z,t) = \frac{1}{\sqrt{2\pi}\sigma_z}\exp\left(-\frac{(z+(t_0-t)c)^2}{2\sigma_z^2}\right), \tag{5.27}$$

where t_0 is the offset of bunch calculated from the exported data. The limits on the time integral are quite arbitrary, so long as it incorporates the entire passage of the drive through the field. This is because if the bunch is not inside the cavity, the result of the integral for that particular time step will be 0. Figure 5.14 shows a drive and test Gaussian traversing the cavity field.

Applying eqn. 5.26 allows a transformer ratio of $\mathcal{T} = 9.34$ to be calculated. This is within 0.5% of the transformer ratio expected from eigenmode calculations. The σ_z used in the integration method was small ($\approx 0.1mm$) in order to ensure there was no overlap

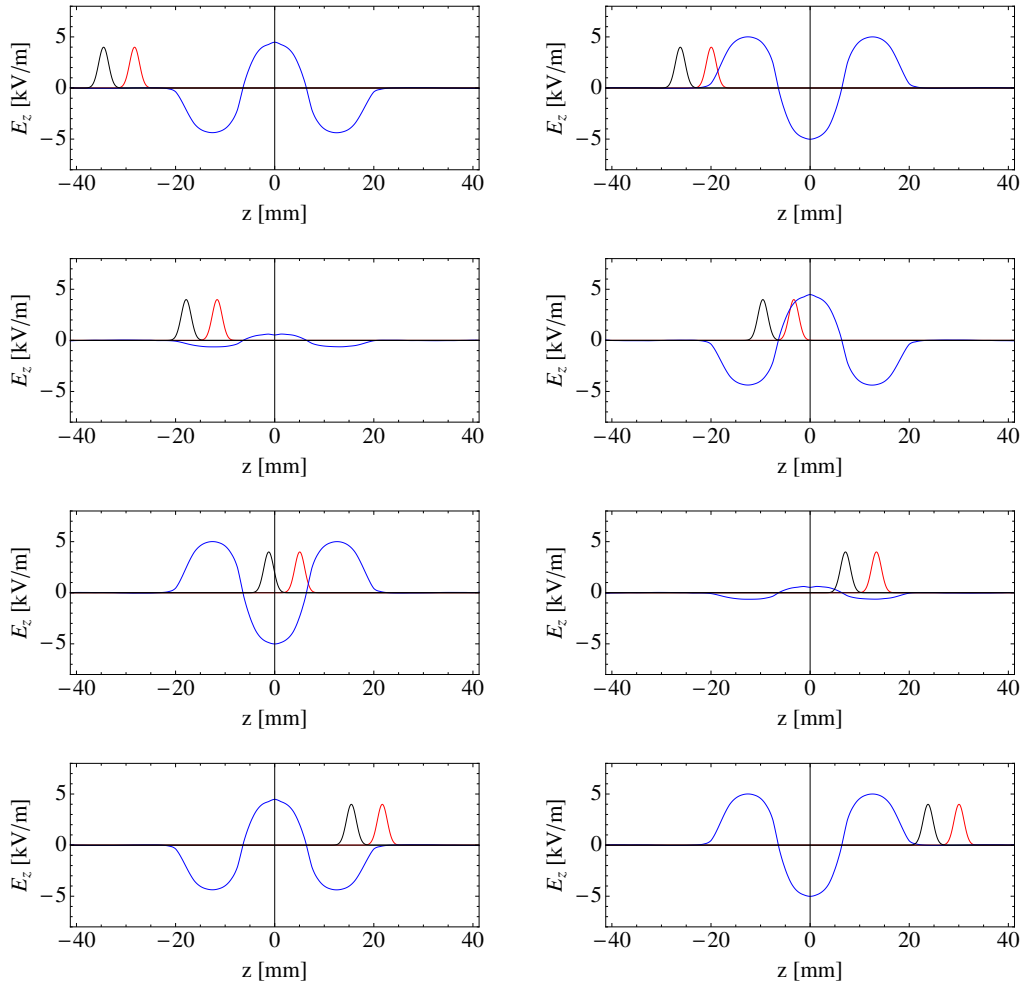

Figure 5.14: Snapshots of Gaussian bunches representing drive and test bunches traversing the cavity field. Time separation is $1/3 f_d$.

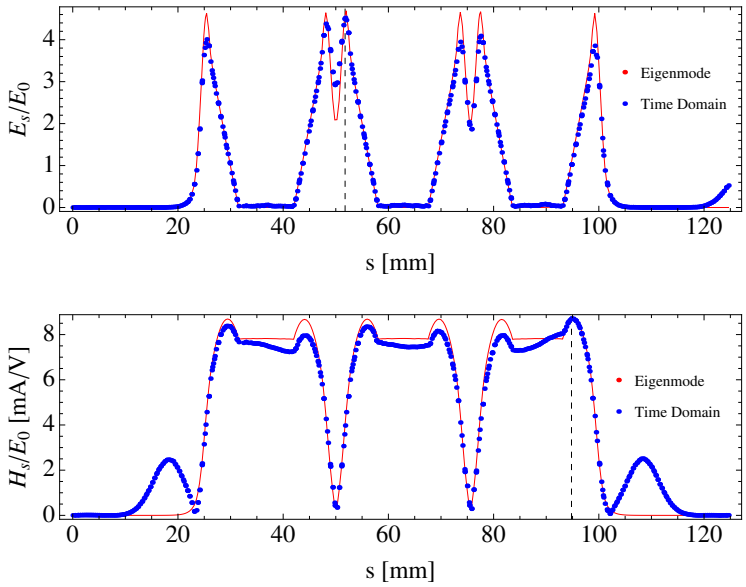

Figure 5.15: A comparison between eigenmode and time domain results for the excited electric and magnetic fields respectively.

between the cells, the time step of the integration was also small ($t_{rf}/500$) to ensure an accurate calculation.

In Chapter 7, simulations will be performed on a multi-harmonic detuned cavity in order to verify the principles of multi-harmonic detuning and surface field reduction. Therefore, it is important to verify that the fields excited in the single mode detuned case agree with eigenmode calculations. A comparison between the eigenmode and time domain surface fields can be found in figure 5.15.

The maximum surface electric and magnetic fields in the time domain are given as $E_s/E_0 = 4.51$ and $H_s/E_0 = 8.67$ mA/V, compared to their eigenmode counterparts $E_s/E_0 = 4.69$ and $H_s/E_0 = 8.69$ mA/V. Discrepancies can arise from bunch fields contributing directly to the surface fields. The inward lean of the magnetic field profile in the time domain is caused by the passage of the bunch and time since the last energy deposition in the cell. The bunch fields are visible in the magnetic field plot and just visible on the far right of the electric field plot.

In order to account for beam loading, a variety of methods can be used. From the eqn.

5.17 a value of $\mathcal{T} = -2Q\delta = 9.34$ can be inserted into the equation with $\varsigma = 0.1$ to give $\mathcal{T}_{bl} = -4.78$. This can be approximated from the unloaded simulation data by using

$$E_{loaded} = E_{unloaded}(z,t) + \varsigma E_{unloaded}(z, t + t_0), \tag{5.28}$$

where $t_0 = \pi/2$ is the offset of the test bunch from the drive bunch. Using this process $\mathcal{T} = -4.78$, a result consistent with theory. In order to further verify the theory, a simulation was performed that had an identical bunch train to the drive bunch, except it was shifted in time by $\pi/2$ and had a bunch charge that was $0.1Q_{b,drive}$, a snapshot of which can be found in figure 5.16. Performing the same procedure and calculating the transformer ratio achieved $\mathcal{T} = -4.78$. The accuracy of these results mean that simulations involving a drive and a test bunch are not required as the analytical equation and the approximation are sufficient.

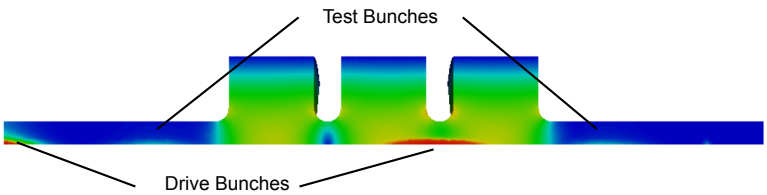

Figure 5.16: A snapshot of the steady state field profile as simulated in t3p. The drive bunches and test bunch locations can be seen.

Parameter	Eigenmode	Time Domain	Notes
f_c [GHz]	12.1215	12.1113	-
Q_c	500	482	-
$\mathcal{T} = -2Q_c\delta$	10.25	9.34	Expected result
$\mathcal{T}$	-	9.31	Simulation result
$\mathcal{T}_{bl}$	-	-4.78	Calculated from eqn. 5.17
$\mathcal{T}_{bl}$	-	-4.78	Single bunch train simulation
$\mathcal{T}_{bl}$	-	-4.78	Multi-bunch train simulation
$E_{s,max}/E_0$	4.51	4.69	-
$H_{s,max}/E_0$ [mA/V]	8.67	8.69	-

Table 5.2: Summary of time domain results for a three cell pillbox cavity with $T = 10$ and $Q_c = 500$.

Using the same mesh, a similar set of simulations was performed that had a higher conductivity, $\sigma_c \to 4\sigma_c$, $Q_c \to 2Q_c$. This allowed the expected transformer ratio to double to $\mathcal{T} = 18.64$. The simulation result was within 0.11% of this expected value.

A cavity of the same geometry, but tuned such that its frequency was lower than the drive frequency was designed and simulated. The results for this cavity can be found in table 5.3.

Parameter	Eigenmode	Time Domain	Notes
f_c [GHz]	11.7292	11.7197	-
Q_c	500	481	-
$\mathcal{T} = -2Q_c\delta$	22.59	22.53	Expected result
$\mathcal{T}$	-	23.22	Simulation result
$\mathcal{T}_{bl}$	-	-20.0866	Calculated from eqn. 5.17
$\mathcal{T}_{bl}$	-	-20.0861	Single bunch train simulation
$\mathcal{T}_{bl}$	-	-17.6533	Multi-bunch train simulation
$E_{s,max}/E_0$	4.63	4.38	-
$H_{s,max}/E_0$ [mA/V]	8.51	8.91	-

Table 5.3: Summary of time domain results for a three cell pillbox cavity with $\mathcal{T} = 22.5$ and $Q_c = 500$.

This chapter has derived the theory relating to a single mode collinear accelerating structure. The theory was tested against numerical modelling, particle tracking and time domain simulations. In each case it was shown that the level of agreement was very good. For the numerical modelling and particle tracking, agreement was within 1% of the value expected from theory. Whereas for time domain simulations it was within 0.5%.

It has been shown that the basic principles of cavity detuning and the effect of beam loading on the transformer are valid, with time domain simulations verifying the surface parameters and the transformer ratio for two different cavity structures. Multi-harmonic cavities will now be introduced in Chapter 6 before a multi-harmonic detuned accelerating structure will be shown in Chapter 7.

Chapter 6

Multi-Harmonic RF Cavities

Cavities that excite multiple harmonic eigenmodes give rise to two beneficial effects: pulsed surface heating reduction and the anode-cathode effect. The pulsed surface heating reduction occurs because the average magnetic field squared on the surface, which is the key contributor to temperature rise, can be reduced. This will be shown in the frequency domain for single cells as well as for multi-cell structures for second and third harmonic cavities. The anode-cathode effect could potentially be used to allow reliable operation of accelerating cavities beyond 100 MV/m without the onset of rf breakdown. Cavity geometries that display each of these effects will be introduced and simulation results will be presented.

In addition to analysing the electromagnetic fields, this chapter also includes a detailed analysis of the longitudinal beam dynamics. Understanding the longitudinal motion of a bunch of particles undergoing acceleration in a multi-harmonic cavity is critical to their development and use. Equations of motion that describe this longitudinal behaviour will be derived and applied to a multi-harmonic cavity that accelerates high energy protons.

6.1 Background

Multi-mode cavities (several modes with independant frequencies) have long been considered for efficient accelerating cavities [84, 106], however only with the advance of engineering practices have they become a practical consideration. Multi-mode cavities have a wide variety of applications, ranging from highly efficient accelerating cavities [107] to beam positioning monitors and rf guns [108]. They have also been used in experiments that try to determine the role of the magnetic field in rf breakdown [109]. The results of one such experiment which was performed at SLAC found that the breakdown rate in soft copper [110] was increased with the presence of a magnetic field from an additional cavity mode [111]. However, whether this is because the magnetic field can cause fractures and create regions of enhanced electric field which then triggers a breakdown event, or if their is something more fundamental occuring with the electric and magnetic field in a breakdown, is not yet clear.

This result and other similar results increases the experimental data to allow a firmer picture of rf breakdown.

A cavity that excites several harmonically related eigenmodes simultaneously could potentially reduce the pulsed surface heating on the material boundary of the cavity by lowering the average magnetic field squared on the surface. A cavity could also be designed that allows for an asymmetric field profile along the wall, which allows the surface electric field to have a stronger field pointing into the wall than away from it. Cavities that utilise the anode-cathode effect could potentially operate at high gradients with the increase in beam lifetime. These claims are investigated in this chapter with a campaign of simulations.

Throughout this chapter, CLIC-like cavity parameters will be used. However, smaller temperature increases are expected for the designs that will be shown here compared to the current CLIC structures. This is because the CLIC structure is TW with input couplers and HOM dampers. The surface field can be strongly enhanced in the vicinity of the couplers [43]. However, the relative reduction in temperature is still an informative parameter to calculate, as fundamentally the temperature reduction could still have an effect on more complex structures.

Initially, a symmetric cavity design originally optimised by Y. Jiang [112] will be introduced that excites two harmonically related eigenmodes, it will be shown that there is a reduction to the pulsed surface heating that is in good agreement with theoretical predictions. Then, an asymmetric cavity geometry will be introduced that could potentially have a decreased probability of rf breakdown due to the anode-cathode effect. This field asymmetry will be shown, and a multi-harmonic coupler design will be introduced that could be used in a future experiment. The coupler and cavity design was originally introduced by Y. Jiang for a potential S-band experiment, but has been re-optimised to X-band for inclusion here to highlight some of the challenges facing these types of cavity.

Finally, the longitudinal beam dynamics of a multi-harmonic cavity will be described [113]. This will begin with the derivation of the single mode equations of motion, and will then be extended to account for additional harmonic modes. This is an original contribution to the field and is currently in preparation for submission to a journal.

The next section will describe the physics of pulsed surface heating and then introduce a cavity based on CLIC-like parameters that is capable of utilising this effect.

6.2 Pulsed Surface Heating Reduction

In order to determine how multiple harmonics can effect the pulsed surface heating. An important relation needs to be derived that describes how an oscillating magnetic field in a cavity translates into a physical temperature rise. The full derivation can be found in Appendix C. The appendix that starts with the diffusion equation and ends with the temperature rise of the wall of an accelerating cavity in the presence of an oscillating magnetic field [10]. This well-known expression is given by

$$\Delta T(t) = \frac{1}{\rho C_\epsilon \sqrt{\pi \alpha_d}} \int_0^{t_p} \frac{dt'}{\sqrt{t-t'}} [\frac{1}{2} R |H_{||}(t')|^2], \tag{6.1}$$

where ρ, C_ϵ and κ are the density, specific heat capacity and thermal conductivity of the material, t_p is the pulse length, $\alpha_d = \kappa/\rho C_\epsilon$, R is the skin resistance and $H_{||}$ is the tangential magnetic field on the surface. It can be seen that the main contributor to the temperature rise is the from the $H_{||}^2$, which when integrated over the pulse length, is approximately the time-average of the $H_{||}^2$ field. This section is devoted to exploring how this temperature rise changes in the presence of different harmonic modes.

A simple model can be used to calculate the expected orders of magnitude of the average $H_{||}^2$ field. The electric and magnetic fields for the fundamental and harmonic modes, $\tilde{E}_1, \tilde{E}_2, \tilde{H}_1, \tilde{H}_2$ can all be normalised such that $\tilde{E}_1 = G\frac{E_1}{A_1}$, $\tilde{E}_2 = G\frac{E_2}{A_2}$, $\tilde{H}_1 = G\frac{E_1}{A_1}$, $\tilde{H}_2 = G\frac{H_2}{A_2}$ where the 'tilde' represents a time varying quantity, $A_{1,2}$ is the initial accelerating gradient of the mode and $G = 100$MV/m for consideration of CLIC-like parameters. Therefore, the total field in a multi-harmonic cavity can be given as

$$\tilde{E} = (1-\alpha)\tilde{E}_1 + \alpha\tilde{E}_2, \tag{6.2}$$

$$\tilde{H} = (1-\alpha)\tilde{H}_1 + \alpha\tilde{H}_2, \tag{6.3}$$

where α is the contribution factor from the additional mode.

As can be seen in eqn. 6.1, the surface heating is proportional to the average of the square of the H-field, $< H^2 >$. Therefore, considering that the average of a linear time varying field (assuming cosine like behaviour) is zero,

$$< \tilde{H}^2 >= (1-\alpha)^2 \tilde{H}_1^2 + \alpha^2 \tilde{H}_2^2 = \tilde{H}_1^2[(1-\alpha)^2 + (\eta\alpha)^2], \tag{6.4}$$

where $\eta = \sqrt{\frac{\tilde{H}_2^2}{\tilde{H}_1^2}} \sim \frac{H_2^{max}}{H_1^{max}}$. Eqn. 6.4 can be plotted as a function of α for various different values of η. This is found below in figure 6.1.

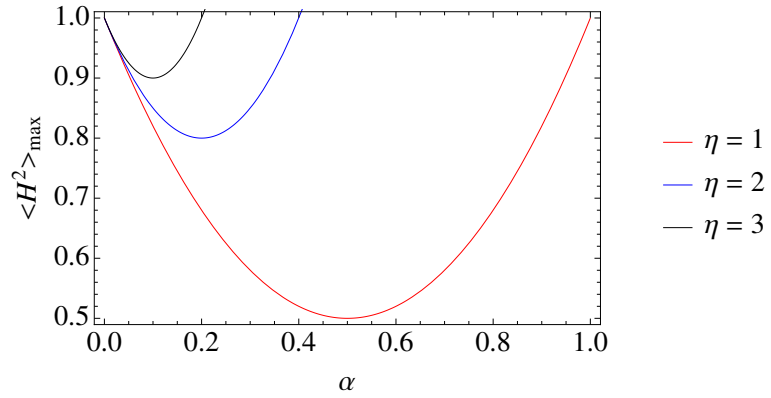

Figure 6.1: Surface heating reduction as a function of α. Red is for $\eta = 1$, blue is for $\eta = 2$ and black is for $\eta = 3$.

By decreasing the value of η, the peak H-field of the second mode is closer to the value of the peak H-field from the fundamental mode. This is maximum for $\eta = 1$ and $\alpha = 0.5$, showing that the two modes are now equivalent and the reduction is 50%. It also can be seen that in order to achieve the peak surface heating reduction for the given η, the surface fields of the second mode must be optimised to have a value of $\alpha = \frac{1}{1+\eta^2}$, corresponding to the minumum point on the curve.

There are several possible mode configurations for this type of structure. Here, only SW cavities will be considered for pulsed surface heating reduction. The first mode combination that will be considered is a fundamental mode with a second harmonic mode i.e. TM_{010}+TM_{011}. Afterwards, a second configuration that compares this with a fundamental mode and a third harmonic mode: TM_{010}+TM_{012} will be shown.

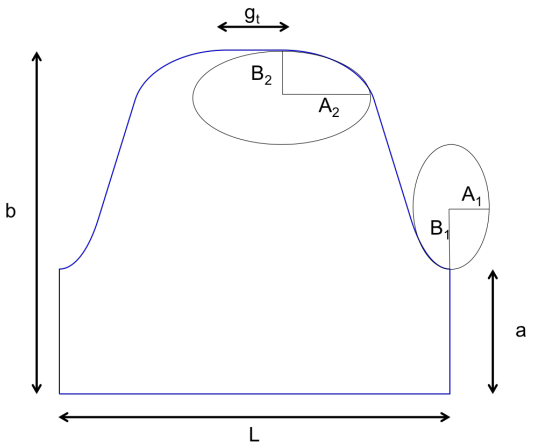

Parameter	Units	Value
a	$1/\lambda$	0.15
g	-	$\lambda/2$
A_1	mm	1.68
B_1	mm	4.872
A_2	mm	1.222
B_2	mm	1.195

Figure 6.2: Geometry of a single elliptical cell with parameters listed on the right.

The higher the harmonic number of the additional mode, the greater η becomes, reducing the benefit gained from this effect. For that reason, no mode configurations are considered above the third harmonic.

The geometry of a single cell multi-harmonic cavity is found in figure 6.2. The cavity has elliptical edges and is rounded near the iris and the cavity radius, with the addition of a flat top, which provides a second variable (in addition to the cavity radius) for frequency tuning. This now allows the cavity to have both the fundamental and additional harmonic optimised by the variation of these two parameters.

An optimisation algorithm based on the Newton-Raphson method [114] was used in order to tune the frequencies of each mode in the single cell cavity. An initial set of coordinates $\{x_0, y_0\}$ (corresponding in this case to cavity radius, b and flat top length, g_t) was provided to a function $f(x, y, n)$ where n is the mode number with ouput z_n where z_n is the absolute difference between the frequency simulated and frequency goal. A matrix was constructed that calculated how each frequency difference varied with a small length deviation dz, with a new set of values being output after each iteration. i.e.

$$\{x_0, y_0\} = \{x_n, y_n\}$$

$$\{f(x_n, y_n, 1), f(x_n, y_n, 2)\} = \{z_1, z_2\}$$

$$J = \begin{pmatrix} \frac{f(x_n+dz,y_n,1)-z_1}{dz} & \frac{f(x_n,y_n+dz,1)-z_1}{dz} \\ \frac{f(x_n+dz,y_n,2)-z_2}{dz} & \frac{f(x_n,y_n+dz,2)-z_2}{dz} \end{pmatrix}.$$

$$\{x_{n+1}, y_{n+1}\} = \{x_n, y_n\} - J^{-1}.\{z_1, z_2\}$$

This process was iterated until the value remained unchanged (within a specified tolerance). The values attributed to the ellipses were obtained from manual optimisation of the curves in order to optimise the Q values.

6.2.1 Second Harmonic Cavity

The field profiles for the TM_{010} and TM_{011} cavity are shown in figure 6.3. For this particular geometry $b = 11.223$ mm and $g_t = 3.22$ mm. The rf parameters of this cavity can be found in table 6.1. The percentage contribution from the additional mode is calculated according to $\alpha = \frac{R_{s,2}}{R_{s,1}+R_{s,2}} = 0.2$, while $\eta = \frac{H_{2,max}}{H_{1,max}} = 2.2$. This corresponds to an anticipated peak field reduction of 15%. Each field profile was normalised such that $E_{acc}\Theta = 100$ MV/m. This is to ensure that the total gradient experienced by a particle remains constant when the effect from the harmonic mode is included.

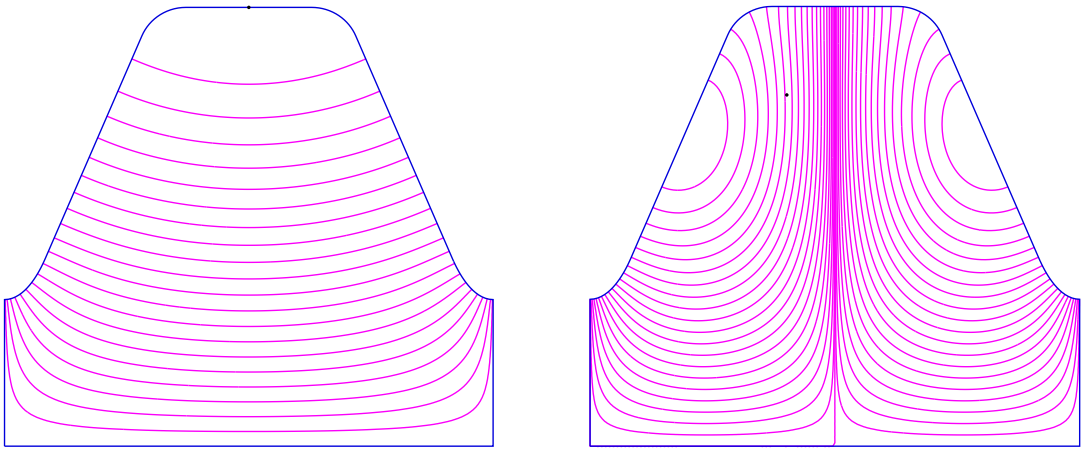

Figure 6.3: Field profiles for the TM_{010} (left) and TM_{011} (right) modes of a single second harmonic elliptical cell.

The surface magnetic fields for the TM_{010} and TM_{020} are plotted as a function of the path length s and can be found in figure 6.4. The square of the surface magnetic field can now be plotted as a function of time in order to determine the field behaviour. This can

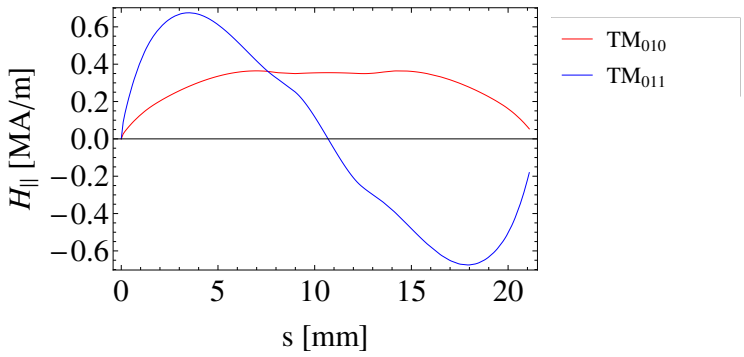

Figure 6.4: Surface magnetic fields following a path length s over the surface of the cavity for TM_{010} and TM_{011} modes.

Parameter	Units	TM_{010}	TM_{011}
f	GHz	11.9942	23.9884
Q	-	8830	10,338
Θ	-	0.77	0.78
$E_{s,max}$	MV/m	222.42	376.1
$H_{s,max}$	MA/m	0.364	0.675
R_s	Ω	107.9	33.5
R'_s/Q	Ω/m	128.54	45.0

Table 6.1: RF parameters for a second harmonic cavity where $E_{acc}\Theta = 100$MV/m.

be found in figure 6.5. The solid line represents the time varying field, with the dashed line representing the average field for that point on the surface over one rf cycle, with red referring to the TM_{010} alone and blue referring to TM_{010}+TM_{011}. It can be seen that there is a decrease of approximately 20%, in the $< H_{\|}^2 >$ field on the surface at the outer radius of the cavity. Along the side walls there is no discernible difference between the two configurations. For the given value of α and η, an approximate prediction for the decrease is $< H_{\|}^2 >= (1-\alpha)^2 + (\eta\alpha)^2 = 15\%$.

In order to calculate how this average reduction corresponds to a decrease in the temperature rise, eqn. 6.1 was used. As each mode has different values for the surface resistance,

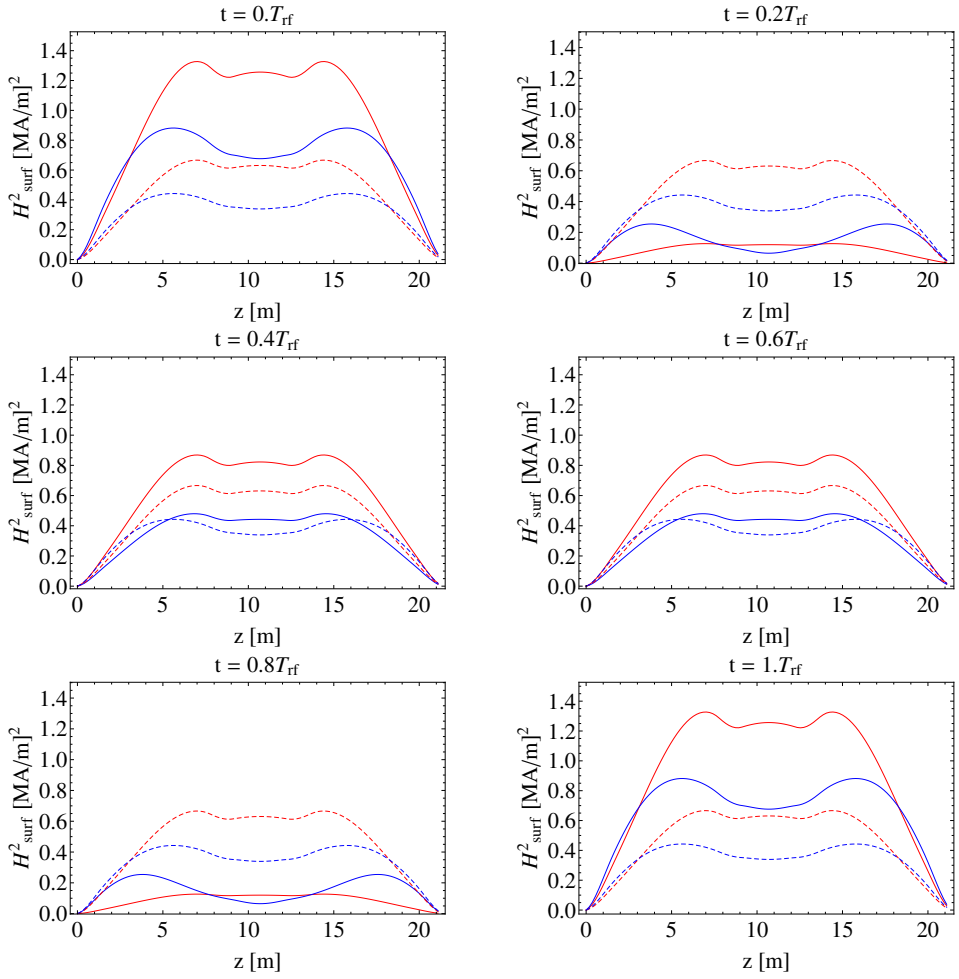

Figure 6.5: Surface magnetic field squared as a function of time for a second harmonic cavity. The solid is the time varying field and the dashed is the average field over one cycle. The red refers to the fundamental mode alone with the blue referring to the case for TM_{010}+TM_{011}.

the expression was split into two seperate integrals.

$$\Delta T_1(t) = \frac{1}{2\rho C_\epsilon \sqrt{\pi \alpha_d}} \int_0^{t_p} \frac{dt'}{\sqrt{t-t'}} [R_1 (1-\alpha)^2 |H_{\parallel,1}(t')|^2], \tag{6.5}$$

and

$$\Delta T_2(t) = \frac{1}{2\rho C_\epsilon \sqrt{\pi \alpha_d}} \int_0^{t_p} \frac{dt'}{\sqrt{t-t'}} [R_2 \alpha^2 |H_{\parallel,2}(t')|^2], \tag{6.6}$$

where the total temperature rise is given by

$$\Delta T = \Delta T_1 + \Delta T_2 \tag{6.7}$$

and the surface resistance is calculated by

$$R_n = \sqrt{\frac{2\pi f_n \mu_0}{2\sigma_c}} \tag{6.8}$$

The location of the maximum reduction in the average $H_{\|}^2$ along the surface was calculated and the temperature rise at this location was plotted and can be found on the left of figure 6.6. The CLIC pulse length is 240.8 ns. The single mode temperature at 250 ns is 15 K, with multi-mode case maximum as 11 K. Additionally, the temperature rise at 250 ns was plotted along the surface of the cavity and can be found on the right of figure 6.6. It can be seen that large temperature reductions are present on the surface in the center of the cavity. Whereas, there is little difference in the temperature rise between single and multi-mode on the side walls of the cavity. This is much lower than the CLIC requirement of 56K because there are no fundamental power couplers included or HOM dampers. These couplers introduce significant levels of field enhancement on the surface of the cavity, and are responsible for much of the temperature rise in the CLIC structures. Here, we are interested in relative decrease with the addition of a harmonic mode.

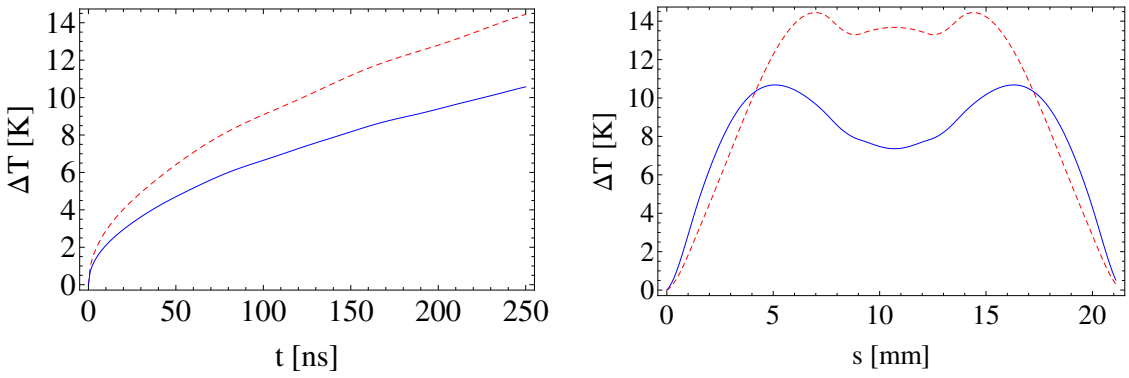

Figure 6.6: Temperature rise at the location of peak magnetic field (left), and temperature rise for $t_p = 250$ns (right) for a second harmonic cavity. In both cases, the red dashed line is the TM_{010}, and the blue solid is the TM_{010}+TM_{011}.

The cavity geometry can now be extended to include end cells, chokes and beam pipes. The purpose of the chokes is to prevent the second harmonic from leaking down the beam pipes, which allows the field to be entirely contained within the simulation domain. The end cell geometries are identical to the mid cells, except with $b_{end} = 11.2093$ mm and $g_{t,end} = 3.10163$mm. The beam pipes have the same radius as the cavity iris, i.e. $a_{end} = a$. Figure 6.7 shows the full geometry and field contours for the TM_{010} mode and TM_{011} respectively.

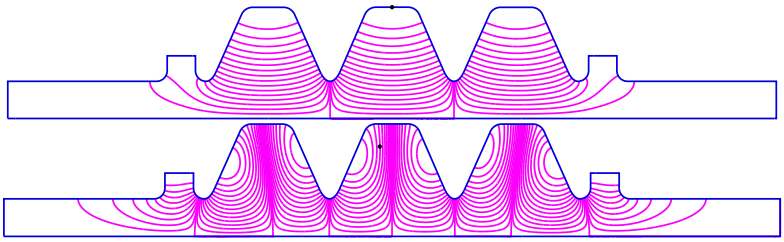

Figure 6.7: Field contours and geometry for the TM_{010} mode (top) and TM_{011} modes (bottom).

The temperature rise on the surface for a full structure is approximately the same as that found in the single mode case. The peak temperature rise is given in figure 6.8 and the temperature rise at $t_p = 250$ns can be found in figure 6.9. Differences between the single mode cavity and the full structure arise from the difficulty in optimising the field flatness as well as the frequencies for both modes. While the fundamental mode has a field flatness to within less than 1%, it was not always possible to obtain the same level of flatness for the harmonic mode. Typically, the end cells were approximately 30-40% larger than the field in the mid cell.

A clear benefit can be obtained by exciting both the fundamental and second harmonic in the same cavities, however one of the many issues that face a cavity such as this is in how the mode is excited. It could potentially be excited by external power couplers, however this would then increase the surface fields in the vicinity of the coupler and is explored in greater detail for the anode-cathode effect in Section 6.3. Another possibility is excitation by a drive beam, which is explored in detail in Chapter 7. In the next section, a similar set of calculations will be repeated for a cavity that excites the fundamental and the third harmonic TM_{012} mode.

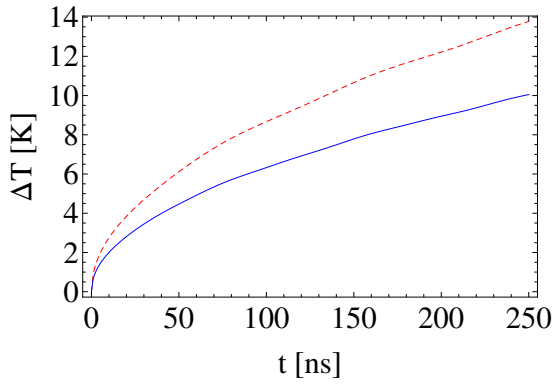

Figure 6.8: Temperature rise as a function of time for the location of the maximum temperature rise. The red dashed is the TM_{010}, and the blue solid is TM_{010}+TM_{011}.

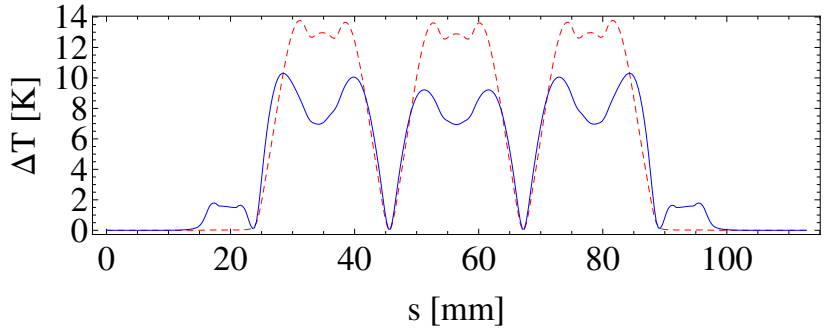

Figure 6.9: Temperature rise at $t = 250$ ns along the surface of the geometry. The red dashed line is the TM_{010}, and the blue solid line is for TM_{010}+TM_{011}.

6.2.2 Third Harmonic Cavity

Despite the large temperature reduction on the surface seen with the second harmonic, a third harmonic may also be employed. Third harmonic modes typically have much smaller shunt impedances than second harmonics, and would have a much smaller and more predictable effect on the cavity, both in terms of the surface field and the longitudinal dynamics (discussed later in Section 6.4). A third harmonic cavity was designed that contained the TM_{010} and TM_{012} modes. The basic geometry is the same as with the second harmonic cavity, with $b = 11.017$ mm and $g_t = 1.771$ mm. For this cavity, $\alpha = 0.1$ and $\eta = 3.3$. This corresponds to an approximate average $H_{\|}^2$ reduction of 10%. The single cell field profiles can be found in figure 6.10 and the rf parameters for each mode can be found in table 6.2. The surface magnetic field of the fundamental and third harmonic can be found in 6.11. As the longitudinal mode number $p = 2$, there are 2 variations longitudinally.

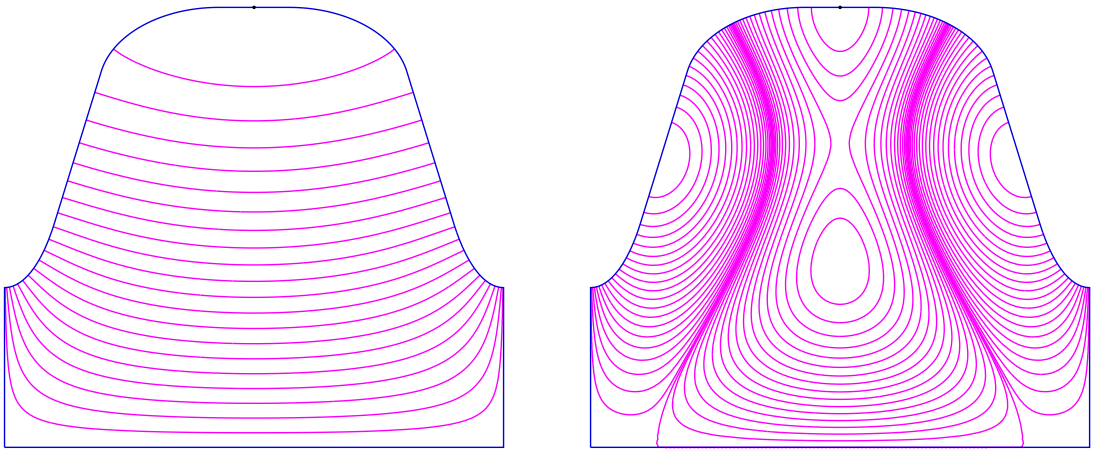

Figure 6.10: Geometry and field contours of a single elliptical cell for TM_{010} (left) and TM_{012} (right).

The time varying fields can be found in figure 6.12. As before, the solid lines refer to the time varying field with the dashed lines showing the average field for that point. The red lines are TM_{010} alone and the blue lines are TM_{010}+TM_{012}. It can be seen that the instantaneous field is much larger for multi-mode than for single mode at $s \approx 11$ mm, however less time is spent at these intense fields which reduces the average value throughout the course of one

Parameter	Units	TM_{010}	TM_{011}
f	GHz	11.9942	35.9826
Q	-	9427	13,348
Θ	-	0.77	0.372
$E_{s,max}$	MV/m	234.8	397.0
$H_{s,max}$	MA/m	0.347	1.190
R_s	Ω	106.4	9.5
R'_s/Q	Ω/m	135.1	73.481

Table 6.2: RF parameters for the fundamental mode and third harmonic mode of a multi-harmonic cavity.

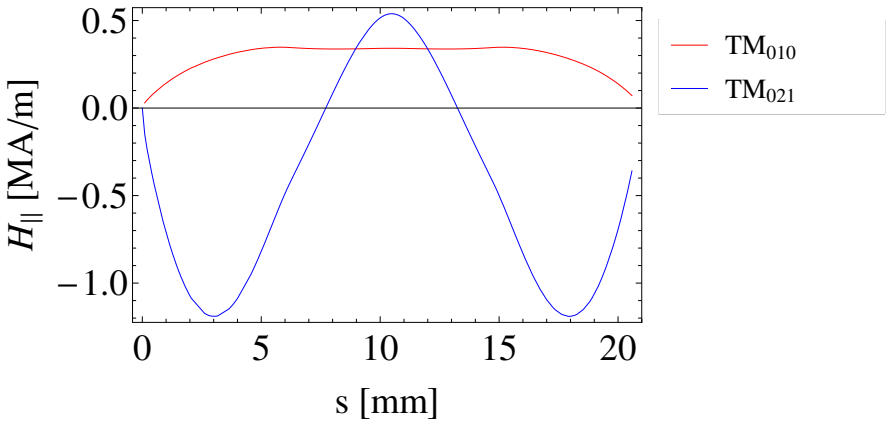

Figure 6.11: Surface magnetic fields for the fundamental and third harmonic modes of a multi-harmonic cavity.

rf cycle. Over the surface there is a reduction in the average $H_{\|}^2$ field on the order of 10%, which is in agreement with what was expected from the approximation.

As before, the temperature rise is split into the temperature increase from each mode individually. The surface resistance for the third harmonic mode is $R_3 = 0.8\ m\Omega$. The maximum temperature rise is plotted as a function of the pulse length and can be seen in figure 6.13 alongside the surface temperature rise. It can be seen that the maximum temperature rise is reduced by approximately 9% for multi-mode compared to single mode alone. When looking at the temperature rise along the surface, a similar behaviour to the second harmonic cavity is found, with slight increases on the side walls, but overall a large reduction in the

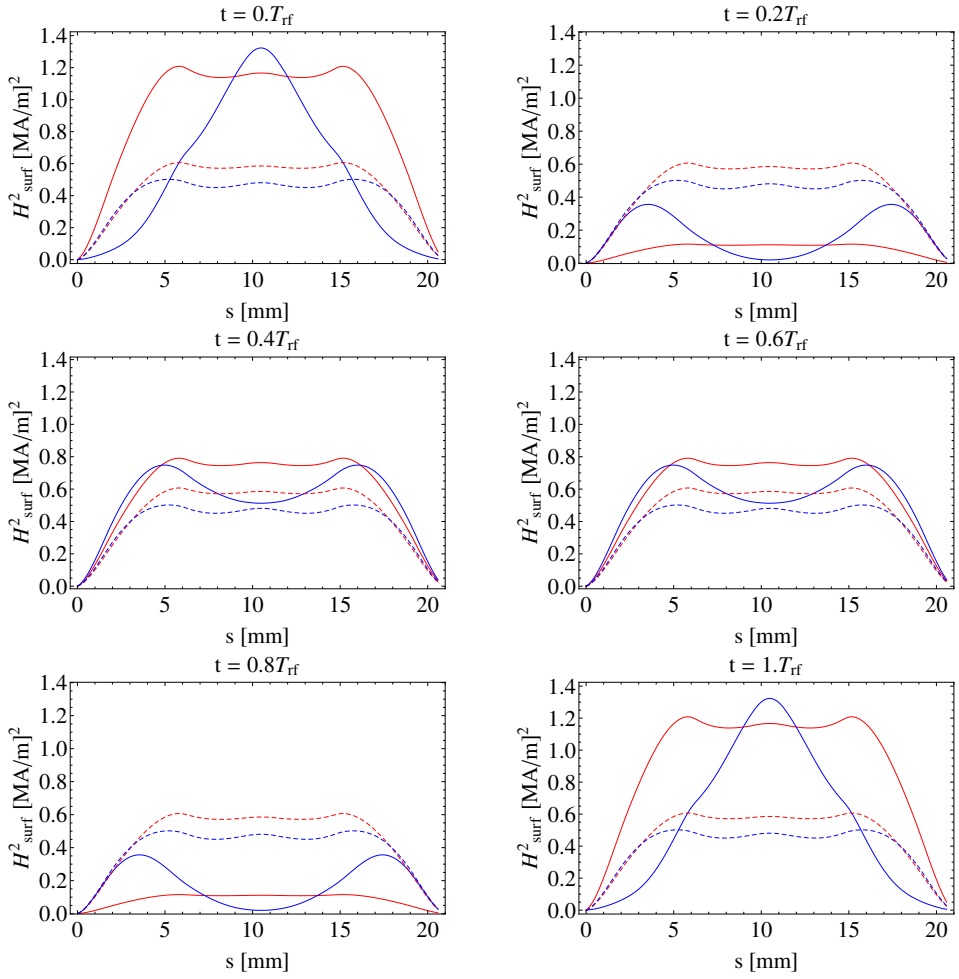

Figure 6.12: Surface magnetic field squared as a function of time for a third harmonic cavity. The solid is the time varying field and the dashed is the average field over one cycle. The red refers to the fundamental mode alone with the blue referring to the case for TM_{010}+TM_{012}.

temperature rise throughout the regions of strong magnetic field.

The full geometry and fields for the third harmonic cavity can be found in figure 6.14. The end cells are identical to the mid cells, except with $b_{end} = 10.861$mm and $g_{t,end} = 1.840$ mm. The chokes serve the same purpose as in the second harmonic cavity. It was found that three small chokes were required to suppress the third harmonic field enough such that the beampipe boundaries did not have an effect on the eigenmode solution. It should be noted, however that these chokes are not intended as a practical design, they are an artifice of the optimisation procedure. Due to the low impedance of the chokes, they have very little effect

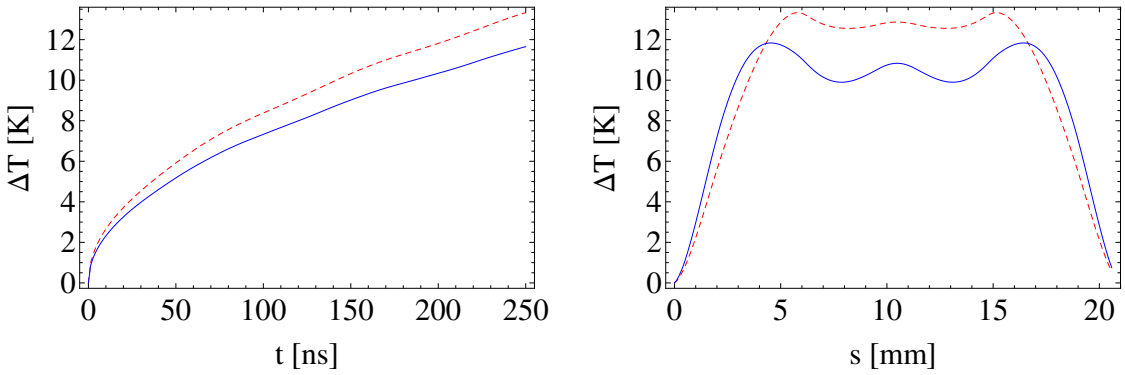

Figure 6.13: Peak temperature rise (left) and temperature rise over the surface for $t_p = 250$ns (right) for a third harmonic cavity. In both cases, the red dashed line is for TM_{010} and blue solid line is TM_{010}+TM_{012}.

on the shunt impedance of the mode itself and thus do not contribute to the overall results of the simulations. It can be seen from the surface temperature rise in figure 6.16 that the chokes heat slightly more than the surrounding beam pipe, however compared to the heating directly on the cavities, this is negligible. During the optimisation procedure, a flat field was not able to be obtained for both the TM_{010} and the TM_{012}. This is why the temperature rise is slightly increased for the center cell over the two end cells.

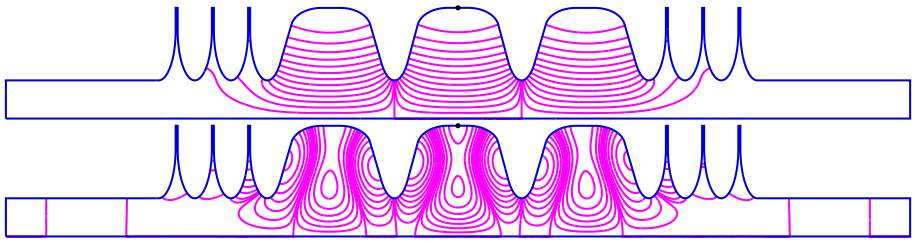

Figure 6.14: Field contours and geometry for the TM_{010} mode (top) and TM_{012} modes (bottom).

It is quite clear that exciting several harmonically related eigenmodes in a single accelerating cavity can lower temperature rise from the intense magnetic fields. Throughout the previous calculations, the total accelerating gradient was kept constant at constant 100 MV/m. The approximation found in 6.4 gives a good indication on the magnitude of the temperature reduction for a variety of different cases, but the temperature reduction strongly depends on the specific cavity geometry rather than individual parameters of α and η.

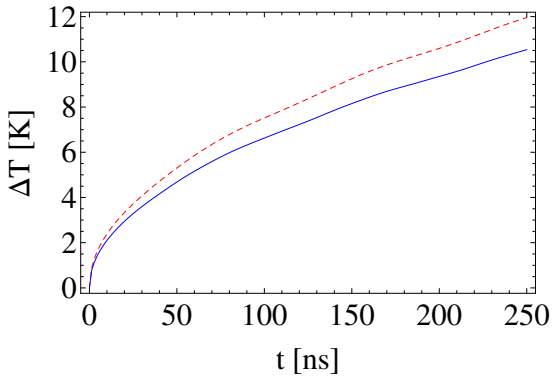

Figure 6.15: Maximum temperature rise as a function of time for single mode (red dashed line) and multi-mode (blue solid line) .

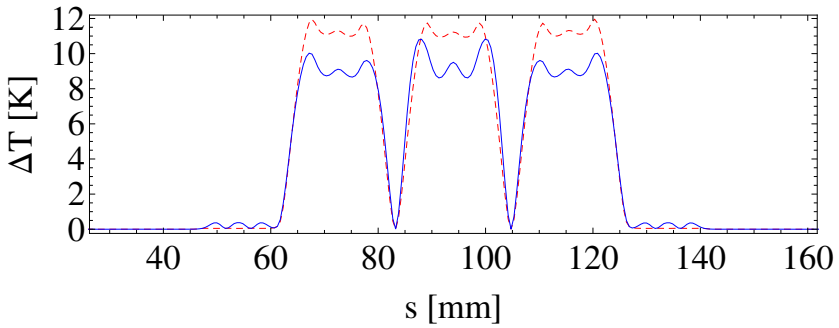

Figure 6.16: Temperature rise for $t = 250$ ns along the surface of the structure. Red is TM_{010} and blue is TM_{012}.

However, the cavity geometries that have been introduced are not yet fully optimised. These designs illustrate the fundamental principles of the reduction in surface field that can be achieved with multi-harmonic cavities. A further optimisation study will be required in order to design a more realistic cavity that suitable for use in an accelerator.

In the next section another concept will be introduced, one that could potentially prevent the onset of rf breakdown at high accelerating gradients. A cavity of this type could form the basis of high gradient accelerating cavity, or it could be used in order to probe the fundamental nature of rf breakdown. This will be explored in the next section.

6.3 Anode-Cathode Effect

By carefully selecting the relative phases between a fundamental mode and an additional harmonic, an asymmetric field profile can be obtained that allows the anode electric field and the cathode electric field to have different magnitudes. A field profile of this type could prevent the onset of rf breakdown, by raising the work function barrier for electrons on the cavity surface, which could prevent field and secondary emmission. Figure 6.17 shows the potential for an electron on the surface. The cathode-like field (pointing into the wall) reduces the work function barrier for surface electrons, making it easier for electrons to be emitted and potentially initiating the process of rf breakdown. The anode-like field (pointing away from the wall) increases the work function for surface electrons, which means stronger electric fields would be required to intiate rf breakdown.

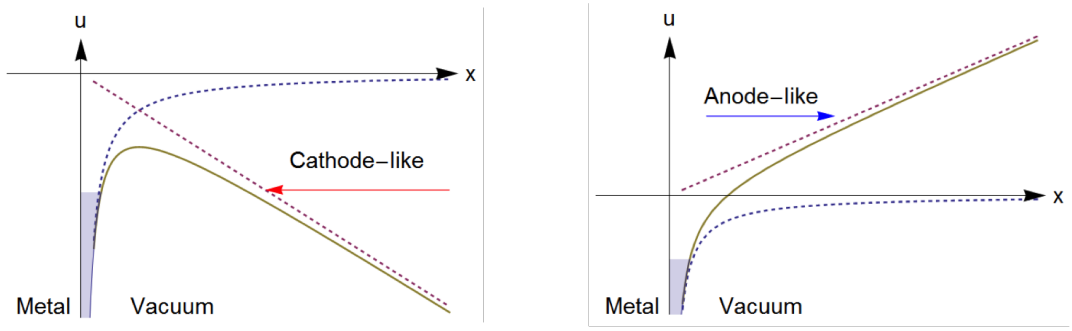

Figure 6.17: Work function potential for surface electrons. The cathode-like field (left) reduces this potential, making it easier for electrons to be emitted which may initiate rf breakdown. Figures reproduced courtesy of Y. Jiang [103].

Figure 6.18 shows how a field profile of this type can be achieved. The phase axis refers to the time oscillation of the field at a specific point. It can be seen that with an appropriate phase relationship between the fundamental and the second harmonic, then asymmetric field profiles can be obtained.

There are ongoing studies that intend to provide experimental verification to the relationship between the anode and cathode fields and rf breakdown [59, 115, 116]. Using a multi-harmonic rf source that is currently being setup at Yale University, the breakdown rates of materials being subjected to strong anode fields will be compared to those subjected to strong cathode fields. This will probe the fundamental nature of rf breakdown by deter-

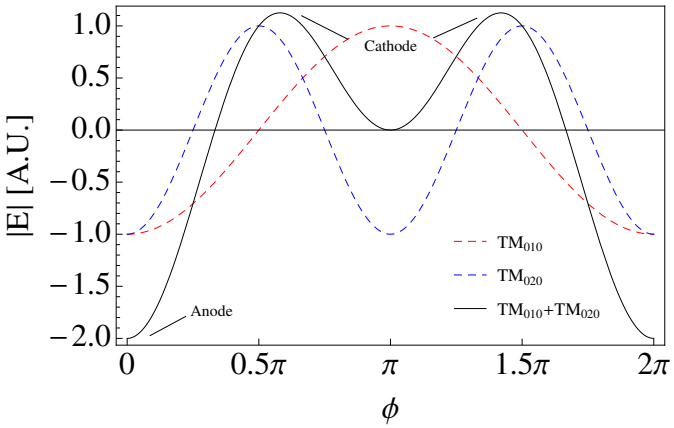

Figure 6.18: The superimposition of two fields with appropriate phase delays can create an asymmetry between the strengths of the anode and cathode fields. Here, red and blue dashed are TM_{010} and TM_{020} modes respectively, and black is the sum of each individual mode.

mining specifically how the electric field acts on the material to initiate a breakdown, as well as determining if cavities of this type can be used in accelerator applications. A cavity design will now be introduced that is capable of exciting such asymmetric fields.

6.3.1 Second Harmonic Asymmetric Cavity

For a cavity to be designed that allows the peak anode and peak cathode fields to have different magnitudes, the cavity must be asymmetric about the z-axis. The asymmetry allows creates weaker fields on one side of the cavity, and stronger fields on the other. When the two harmonic modes are combined, they can sum on the surface to create profiles that create the anode-cathode effect. This will be described below.

The most suitable type of cavity for this application is a TW cavity that is powered by external rf couplers. Beam driven cavities are not possible because the group velocities of the two excited modes need to be comparable in order achieve synchronicity. Even when using a phase advance of $2\pi/3$, the group velocities are the same but have opposite signs (as seen in Chapter 3, and shown in figure 6.19).

Here we describe a cavity design originally optimised by Y. Jiang [112] for S-band applications that is capable of utilising the anode cathode effect. The geometry has been re-

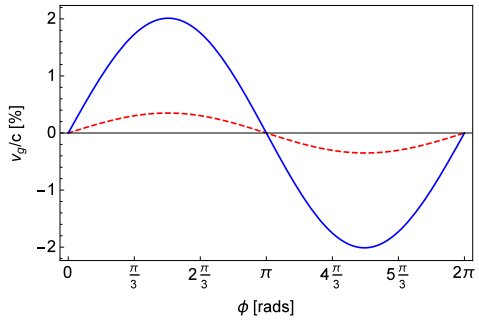

Figure 6.19: Group velocity as a function of phase advance for TM_{010} (red, dashed) and TM_{020} (blue, solid) modes.

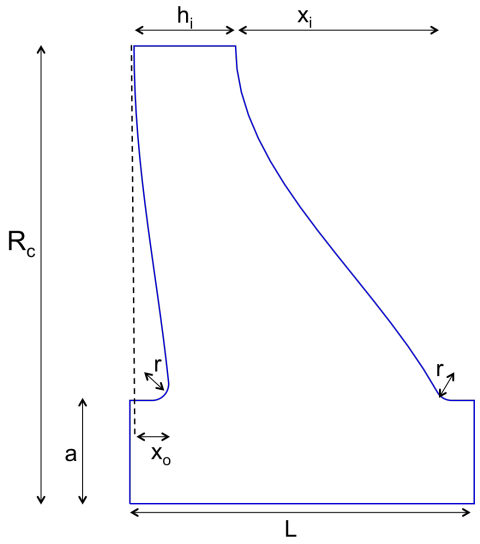

Parameter	Units	Value
R_c	mm	11.10873
a	λ	0.1
L	-	$\lambda/3$
r	mm	0.4
x_0	-	$L - x_i - h_i - 0.1$mm
x_i	mm	5.608
h_i	mm	2.536

Figure 6.20: Geometry and parameters for a single cell asymmetric second harmonic cavity.

optimised here for X-band and can be found in figure 6.20, alongside a table of geometry parameters. A simpler design without the complex curved surface was first introduced in [8], this curved design is an optimised version of that cavity. RF parameters can be found in table 6.3. A plot of the dispersion curves can be found in figure 6.21. It can be seen that both synchronous modes have similar same phase advance, except their group velocities have opposite signs.

Figures 6.22 and 6.23 show the field profile and field vectors for the TM_{010} and TM_{020} modes of the asymmetric cavity. When considering one mode alone, the anode cathode effect

Parameter	Units	TM_{010}	TM_{020}
f	GHz	11.9942	23.9884
Q	-	500	500
k	V/pC	1.335	1.349
R_s/Q	Ω	35.4	17.9
ϕ	rad	$2\pi/3$	$4\pi/3$
$E_{s,max}$	MV/m	399	379.5
$H_{s,max}$	MA/m	0.483	0.537

Table 6.3: RF parameters for a second harmonic asymmetric cavity.

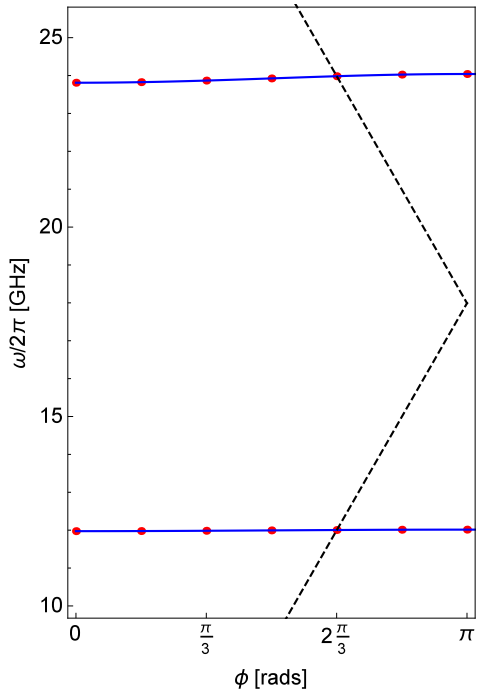

Figure 6.21: Dispersion curves for a second harmonic cavity, blue curves are semi-emperical fits, red points are simulation data and black dashed line is the light line.

is not present. It is the combination of both modes that allows different points of the cycle to have different field strengths. This can be seen in figure 6.24 for the case where $\alpha = 0.222$. This value of α is typical for an optimised second harmonic beam driven cavity [59], and is a useful marker when considering equivalent rf driven cavities. It can be seen in this series of figures that the peak anode field is 405MV/m compared to the peak cathode field which is 203MV/m. This is approximately on the order of a factor of 2 in the differences

between the peaks. This significant reduction in the surface field could potentially allow larger accelerating gradients. However, experimental confirmation of this effect is required to compare with these theoretical predictions.

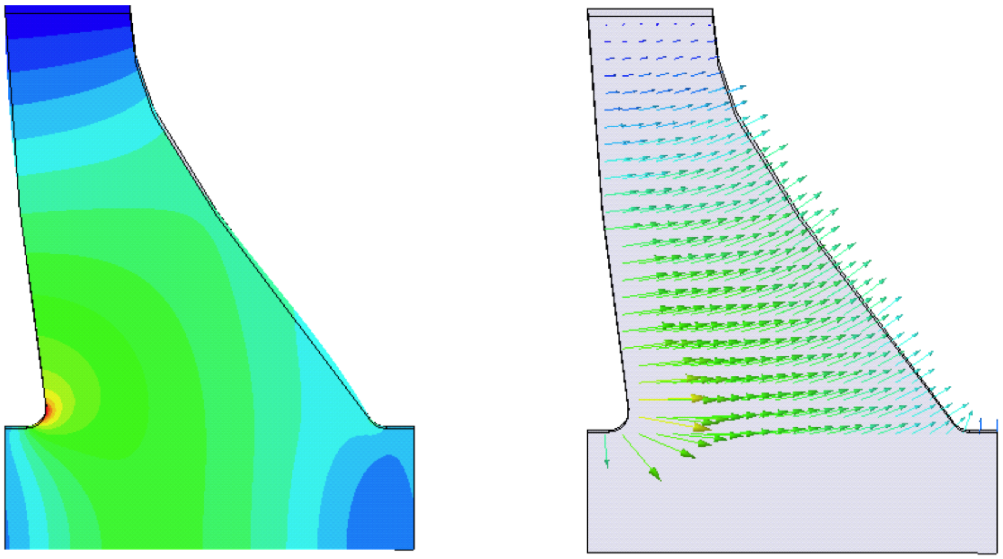

Figure 6.22: Electric field profile and field vectors for a TM_{010} mode. The size and direction of the arrow indicates the relative strength at the arrows origin.

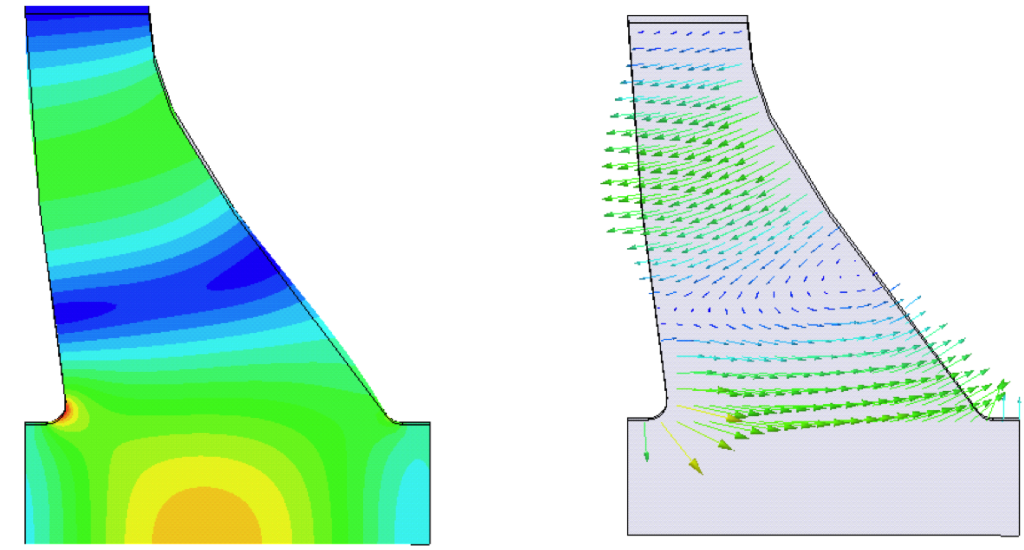

Figure 6.23: Electric field profile and field vectors for a TM_{020} mode. The size and direction of the arrow indicates the relative strength at the arrows origin.

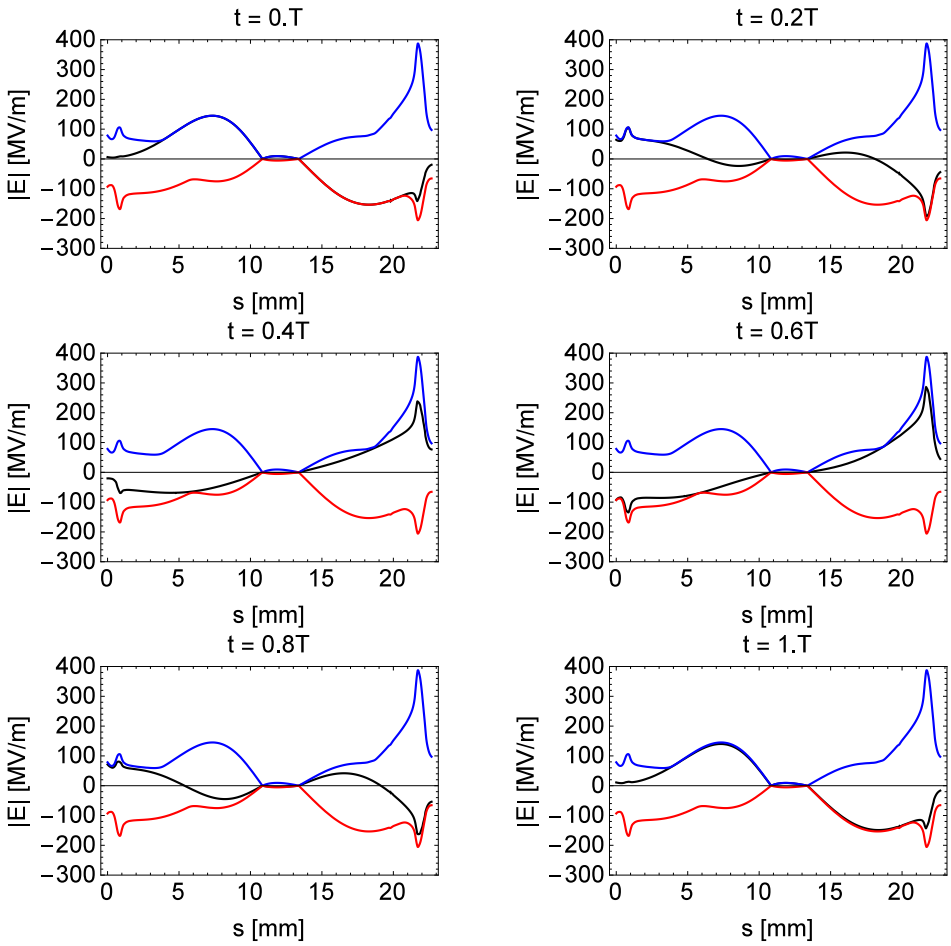

Figure 6.24: Magnitude of the surface electric field for $\alpha = 0.222$. The blue curve shows the peak anode field, the red shows the peak cathode field and the black line gives the time varying field over one rf cycle of the fundamental mode.

It is now required to design power couplers for these structure. This requires two separate couplers that can simultaneously couple TM_{010} and TM_{020} modes into the cavity. This work was performed at S-band by Y. Jiang [112], but re-optimised for X-band for the applications described here. This design can be found in figure 6.25 for the TM_{010} field profile and figure 6.26 for the TM_{020} field profile. Both coupler designs are simple waveguide couplers, however a modification has had to be made to the fundamental power coupler which is on the right hand side of both figures. A choke has had to be added in order to prevent the second harmonic mode from coupling into the cavity and then immediately out into the waveguide. The scattering parameters for the reflection from each mode can be found in figure 6.27.

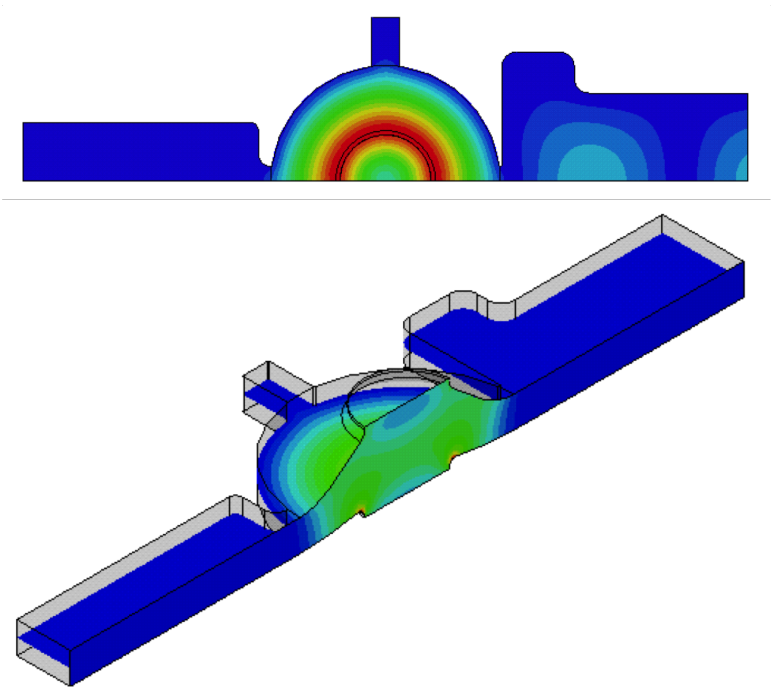

Figure 6.25: Field profile from a driven modal simulation showing the excited TM_{010} mode. The fundamental mode coupler comes in from the right hand side, while the harmonic mode comes in from the left.

This is still an ongoing optimisation process, and there are many stages of design still required before the cavity can be considered for use in an accelerator. For example, tuning mechanisms will be required that can affect both the fundamental and second harmonic mode independently. This is required in order to ensure that the impedances of the cavity can

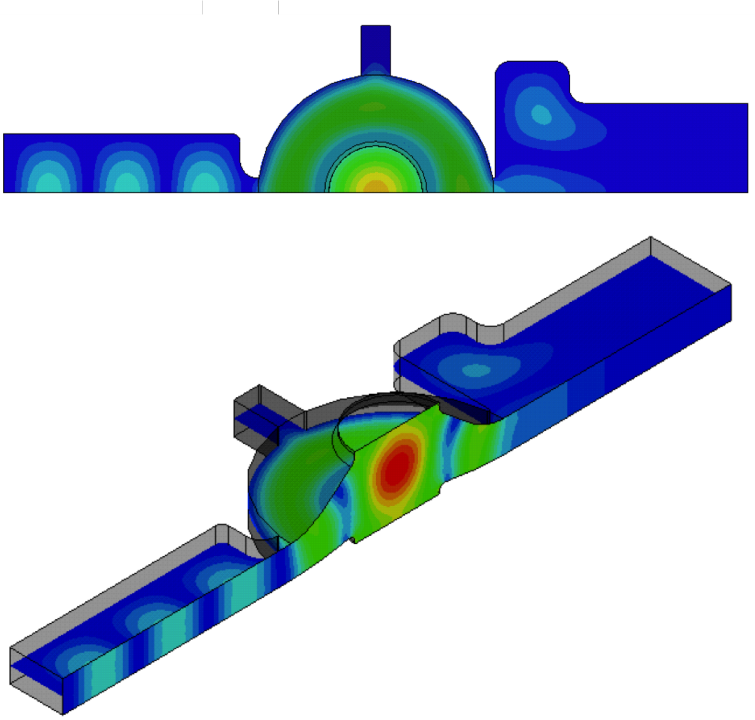

Figure 6.26: Field profile from a driven modal simulation showing the excited TM_{020} mode. The fundamental mode coupler comes in from the right hand side, while the harmonic mode comes in from the left.

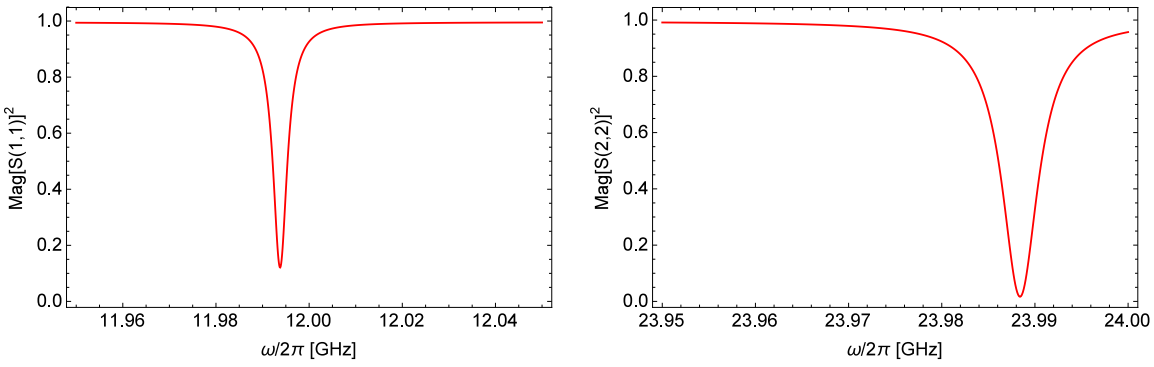

Figure 6.27: Scattering parameters for each coupler, where port 1 refers to the fundamental power coupler and port 2 refers to the harmonic coupler.

be matched to the waveguide. The manufacturing tolerances on a cavity of this type will be much stricter than on similar single mode cavities of the same frequency (due to the requirement of accurate frequencies at 24GHz as well as 12GHz). Additionally, the coupler

design shown here works well for a single cell, however for multiple cells connected in a chain this design may not be the most efficient. It may be a more suitable design if one coupler traverses each cell in one long unbroken chain, similar to the CLIC design. Studies on these and other designs are currently ongoing.

Two different types of multi-harmonic cavity have been shown. The first showed from simulation that the pulsed surface heating can be reduced for second and third harmonic cavities. The second cavity showed that, if the cathode field is responsible for the onset of rf breakdown, then the probability for the initiation of rf breakdown could be reduced by design of an asymmetric cavity. This is still an active area of study, with current designs set to be improved before initial prototypes are fabricated. Experimental verification of these theoretical predictions is essential.

This chapter has analysed multiple harmonic modes and has shown that they can reduce the pulsed heating on the surface (compared to single mode) or, with certain configurations, used as a potential structure for rf breakdown experiments.

The presence of an additional harmonic mode is going to alter the E_z field experienced by a particle traversing the cavity. This will affect the size of the stable accelerating region (rf bucket). To determine the effect of the additional harmonic on the longitudinal stability, a Hamiltonian will be derived in the next section that allows a single particle to be tracked through a chain consisting of multi-harmonic cavities. The remainder of this chapter is dedicated to this study.

6.4 Longitudinal Beam Dynamics in Multi-Harmonic Cavities

As discussed previously, accelerating cavities that excite multiple modes at integer harmonics of the fundamental frequency have the potential to suppress the onset of rf breakdown and can reduce the pulsed surface heating at high accelerating gradients. Understanding the effect of an additional harmonic cavity mode on the longitudinal beam dynamics is an important step to the fabrication and eventual use of multi-harmonic cavities in accelerator applications. A Hamiltonian that describes the longitudinal motion of a particle as it traverses a chain of multi-harmonic cavities will be derived and is applied to second and third

harmonic cavities [113]. The Hamiltonian is based upon formalisms found in literature and it is extended to include different longitudinal field distributions and harmonic frequencies. The following section is an original contribution to this area of study. In this section, high-β protons will be the focus of the study. This is because for longitudinal stability in linacs is used for $\beta < 1$. Different acceleration techniques are used for electrons as they quickly reach $\beta \approx 1$.

Accelerators have long been utilising harmonic rf systems to affect the longitudinal motion of the particles within a bunch [117, 118]. However, these rf systems rely on the fabrication of additional cavities operating with a TM_{010} mode at a frequency of h times the accelerating mode frequency of the main accelerating cavities [119]. The harmonic cavities can be phased such that the entire bunch sees a relatively linear field [120]. This reduces the energy spread and lengthens the bunch, allowing for much higher beam lifetimes. This is particularly important for the European XFEL project [121], for example, where the energy spread reduction can result in a laser with much higher brilliance.

For multi-harmonic cavities to be used in an accelerator, the effect of the additional harmonic on the longitudinal dynamics needs to be explored. This is to ensure that the additional harmonic does not negatively impact the longitudinal stability. To achieve this, a Hamiltonian is derived that describes the behaviour of particles with deviations from a particle with idealised phase and energy (the synchronous particle).

Multi-harmonic accelerating cavities have additional harmonic modes present that follow different longitudinal field profiles on-axis, for example the TM_{010} follows a $\cos(kz)$ whereas the TM_{011} follows a $\sin(2kz)$. Formalisms currently found in literature do not model different longitudinal profiles as they only account for single TM_{010} modes which follow ideal cosine distributions [60, 122].

The general Hamiltonian for a standing wave (SW) multi-harmonic cavity that excites a TM_{010} mode with either an even harmonic or an odd harmonic mode will be derived. The Hamiltonian will be applicable to a variety of modal configurations, and will describe the longitudinal motion of particles as they traverse a linear accelerator comprising a chain of multi-harmonic cavities. Protons with initial energies of several GeV will be used throughout. Small accelerating gradients (on the order of 10kV/m) will be used initially, which

allows the general features of the stable region for acceleration to determined. Then, high accelerating gradients (on the order of 10MV/m) will be studied, which is more useful for applying this work to specific linacs.

The next section provides a model of a single mode cavity using the well known Hamiltonian. This provides the basis for the formalism which will be enhanced with additional modes in the forthcoming sections. This is followed by Section 6.4.2 which gives a derivation of a general Hamiltonian for a particle traversing a cavity that can excite two harmonic modes. This Hamiltonian for multi-harmonic cavities is then be applied to two configurations. In Section 6.4.3, the particle dynamics of a bunch of particles traversing a cavity that consists of a fundamental accelerating TM_{010} mode with a second harmonic TM_{011} mode will be investigated. The relative phase between the first and second harmonics is varied, and the energy gain of the synchronous particle is scaled such that it is kept constant. Section 6.4.4 provides a model of the particle dynamics of a cavity that operates with a fundamental accelerating TM_{010} mode with a third harmonic TM_{012} mode. The relative phase between the two modes is kept constant, but the relative field contribution of each mode is varied. This allows a study of the region in between the primary accelerating buckets to determine when secondary accelerating buckets to emerge. Comparisons to results from tracking simulations are shown throughout, and the effects of acceleration on the rf buckets will also be studied in each case.

6.4.1 Single Mode Hamiltonian

The multi-harmonic Hamiltonian is an extension of the single mode analysis. Therefore it is important to fully describe the single mode case in order to introduce the relevant parameters and to understand how the additional harmonic perturbs the single mode rf bucket. The following section provides a summary of work on the single mode Hamiltonian originally found in refs. [60, 122].

For an infinite chain of SW cavities, the longitudinal profile is $\cos(kz)$ for a TM_{010} mode where z is the longitudinal position within the cavity which is centred on $z = 0$, $k = \frac{2\pi}{\beta_s \lambda}$, β_s is the normalised velocity of the synchronous particle and λ is the wavelength of the fundamental mode. In order to derive a Hamiltonian that governs the longitudinal motion

of a group of particles traversing this chain, equations concerning the evolution of the phase and energy of the particles with respect to the longitudinal coordinate s must be determined.

For a π-mode SW cavity, the phase advance of the rf field from one cavity to the next is given by

$$\phi_n = \phi_{n-1} + \omega \frac{g}{\beta_{n-1} c}, \tag{6.9}$$

where

$$g = \beta_{s,n-1} \lambda / 2 \tag{6.10}$$

is the cavity gap, c is the velocity of light and ω as the angular frequency of the mode. The subscript s refers to the synchronous particle, with β referring to the particle's normalised velocity at cavity n. From this, the phase advance of a particle relative to the synchronous particle from gap $(n-1)$ to gap n is given by

$$\Delta(\phi - \phi_s)_n = \Delta\phi_n - \Delta\phi_{s,n} = \pi \beta_{s,n-1} [\frac{1}{\beta_{n-1}} - \frac{1}{\beta_{s,n-1}}]. \tag{6.11}$$

Applying a Taylor expansion for a small perturbation about β_s gives

$$\frac{1}{\beta} - \frac{1}{\beta_s} = \frac{1}{\beta_s + \delta\beta} - \frac{1}{\beta_s} \approxeq \frac{\delta\beta}{\beta_s^2}, \tag{6.12}$$

where $\delta\beta = \delta W / mc^2 \gamma_s^3 \beta_s$, m is the mass of the particle and γ_s is the relativistic gamma factor. This leads to the difference equation that shows how the particles phase evolves with cavity number. It is useful to quote the energy gain of a particle in terms relative to the synchronous particle, this is achieved by defining the dimensionless variable $w = \delta W / mc^2 = (\Delta W_n - \Delta W_{s,n}) / mc^2$. This normalisation allows the results to be independent of mass. The phase difference equation is

$$\Delta(\phi - \phi_s)_n = -\pi \frac{w}{\gamma_{s,n-1}^3 \beta_{s,n-1}^2}. \tag{6.13}$$

The SW electric field of a TM_{010} mode is a combination of the field profile in the z-direction and the oscillation at a specific frequency, given by

$$E_T = E_0 \cos(kz) \cos(\omega t + \phi). \tag{6.14}$$

where ϕ is the phase of the field when the particle is at $z = 0$ and E_0 is the field amplitude. The energy gain of a particle as it crosses a single cavity is given by

$$W = qE_0 \int_{-g/2}^{g/2} \cos(kz) \cos(\omega t + \phi) dz \tag{6.15}$$

$$= qV_0 T \cos(\phi) \tag{6.16}$$

where V_0 is the axial rf voltage, given by

$$V_0 = E_0 \int_{-g/2}^{g/2} \cos(kz) dz \tag{6.17}$$

and T is the transit time factor, which is determined by

$$T(\beta) = \frac{E_0 \int_{-g/2}^{g/2} \cos(kz) \cos(\frac{\omega z}{\beta c}) dz}{V_0} - \tan(\phi) \frac{E_0 \int_{-g/2}^{g/2} \cos(kz) \sin(\frac{\omega z}{\beta c}) dz}{V_0} \tag{6.18}$$

The difference equation for the energy of the particle is calculated by evaluating the energy gain of a particle with respect to the synchronous particle as

$$\Delta W_n - \Delta W_{s,n} = qgE_1 T(\beta)(\cos(\phi_n) - \cos(\phi_s)) \tag{6.19}$$

where $E_1 = V_0/g$ is accelerating gradient

Eqns. 6.13 and 6.19 can be written as a continuous function, rather than having the discrete action of the particles at the centre of each cavity. Using $n = 2s/\beta_s \lambda$ they can be expressed as

$$\frac{d\phi}{ds} = -2\pi \frac{w}{\gamma_s^3 \beta_s^3 \lambda} = \frac{\partial H}{\partial w} \tag{6.20}$$

and

$$\frac{dw}{ds} = q \frac{E_1 T(\beta)}{mc^2} (\cos(\phi) - \cos(\phi_s)) = -\frac{\partial H}{\partial \phi}. \tag{6.21}$$

As ϕ and w are variables canonically dependant on s, a Hamiltonian can be constructed that describes the particle motion in phase space, which is given as

$$H = -\frac{\pi}{\beta_s^3 \gamma_s^3 \lambda} w^2 - q\frac{E_1 T(\beta)}{mc^2}[\sin(\phi) - \phi\cos(\phi_s)]. \tag{6.22}$$

This is consistent with the usual form of a Hamiltonian $H = K + V$ where K is the kinetic energy and is represented by the w-dependent term (first term in the expression) and V is the potential represented by the ϕ-dependent term (second term in the expression). A particle that has a deviation in phase or energy will orbit the synchronous particle in phase space according to the eqns. 6.20 and 6.21. A particle orbit is found by plotting the ϕ and w points for a set of initial coordinates. For increasingly large deviations, the particles orbit becomes wider, until eventually it becomes unstable. A stable orbit is one that follows a closed curve, whereas an unstable orbit is an open curve that trails off giving rise to high energy and phase differences. It is important to know where the boundary between stable and unstable orbits lie. This boundary is known as the separatrix and it can be determined by two points, the stable fixed point and the minimum phase for stable motion. The stable fixed point lies at $(\phi = -\phi_s, w = 0)$. This is the maximum phase difference a particle can have because at this point the particle will be gaining the same energy as the synchronous particle, therefore no phase space motion is expected. The minimum phase for stable motion lies at zero kinetic energy $(\phi = \phi_2, w = 0)$, which arises when the potential at this point is the same as for the stable fixed point.

To calculate the value of the Hamiltonian on the separatrix, ϕ_2 needs to be determined. This is found by equating the value of the potential at the minimum and maximum phase boundaries. The potential at these points are the same, i.e.

$$V(\phi = \phi_2) = V(\phi = -\phi_s). \tag{6.23}$$

Fig. 6.28 shows typical profiles pertaining to a 2 GeV proton experiencing an accelerating gradient of $E_0 = 10$kV/m. The uppermost plot is the energy gain of a particle across one cavity as a function of its phase offset ϕ. The middle plot is the potential of the cavity on the separatrix, where it can be seen that a potential well exists in the region of stability. The

lower plots shows the phase space region, which has been solved for various initial phase offsets and covers both stable and unstable orbits, as well as the separatrix The acceptance of a cavity is determined by calculating the area of the rf bucket, and loosely refers to the maximum allowed bunch emittance within the bucket. A bunch with a small enough energy and phase spread that is completely enclosed within the bucket will be accelerated in a stable manner. The conventional unit of longitudinal acceptance is eV.s. However here, for convenience, normalised energy is used. Therefore, the acceptance of the seperatrices shown here are in units of radians (which is related to time through the fundamental frequency). Henceforth, for convenience when referring to the normalised acceptance, the term acceptance will be used.

In order to ensure the Hamiltonian is accurate, a particle tracker based on eqn. 6.15 was written in *Mathematica* that numerically tracks a particle through a chain of cavities for a given offset ϕ and initial energy deviation w. This tracker does not rely on any of the assumptions relating to constant energy and velocity that followed in the derivation of the Hamiltonian, and can be used as an indicator of the accuracy of the Hamiltonian under a given set of parameters (for example initial energy and accelerating gradient). A comparison between the Hamiltonian and the tracking code for a 2GeV proton with $E_0 = 10$kV/m can be found in Fig. 6.29. The phase width of the separatrix is agreement with the Hamiltonian and the particle tracker. The maximum discrepancy was 0.5%.

A Hamiltonian inherently makes an important assumption regarding the energy of the particle, that is $\beta_s\gamma_s$ is assigned to a constant, C. While this is not true in the case of linear accelerators where moderate to high gradients are required, the separatrix for the case with little to no acceleration offers insight into the particle dynamics, and reveals some important physics of the longitudinal phase space. Some of the unique features found with no acceleration can then be found in cases when acceleration is included.

The validity of these approximations will now be discussed and calculate the Jacobian determinant to verify the accuracy of the linear map [60].

Small accelerating fields are used and we assume $\beta_s\gamma_s$ is constant throughout the interaction. One case we consider is $E_0 = 10$kV/m, $\Delta\beta_s\gamma_s = \mathcal{O}(10^{-7})$. When tracked over 100,000 cavities, this discrepancy is less than 0.01% (as it is accumulated as the particle is

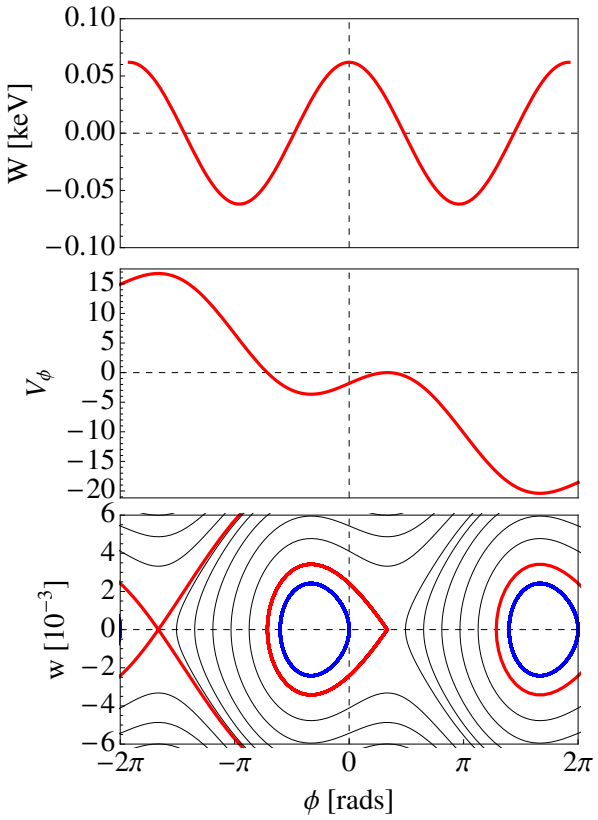

Figure 6.28: Top: Energy gain as a function of phase offset for particle traversing a single cavity. Middle: Potential for separatrix. Bottom: Phase space contours in black, separatrix in red and stable orbits in blue.

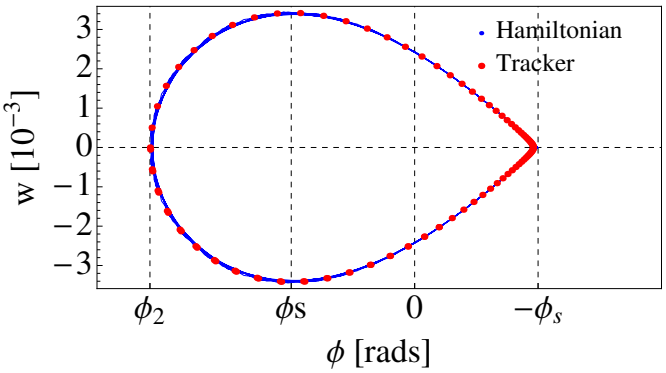

Figure 6.29: Comparison of the Hamiltonian found in eqn. 6.22 with results from a particle tracker based on the fundamental principle of the energy gain of a particle as it traverses a cavity, found in eqn. 6.15. Agreement to within 0.5% is observed.

tracked along the linac). This bares comparison to a field three orders of magnitude larger, for $E_0 = 10$MV/m, $\Delta\beta_s\gamma_s = \mathcal{O}(10^{-4})$, which gives rise to a 10% discrepancy over the same tracking length.

The Jacobian determinant provides the phase space area preserving property (or a magnification factor for the single particle emittance) and is equal to unity for any particle transformation with a constant velocity. However when acceleration is present a deviation from unity occurs. This is because the particle is gaining a significant amount of energy (with respect to its current energy) and therefore velocity deviations occur as it traverses the gap. It is therefore important to calculate the magnitude of this deviation in order to ensure the linear map is accurate. This can be calculated for a transformation either side of a thin lens for a drift-kick-drift model. Here, the phase before and after remains the same, $\phi_f = \phi_i$ while the energy is increased after crossing the gap. This gives the final energy as $W_f = W_i + qgE_1T(\beta)\cos(\phi_i)$. The Jacobian determinant can be shown to be

$$\begin{aligned}\frac{\partial(W_f,\phi_f)}{\partial(W_i,\phi_i)} &= \begin{vmatrix} \frac{\partial W_f}{\partial W_i} & \frac{\partial \phi_f}{\partial W_i} \\ \frac{\partial W_f}{\partial \phi_i} & \frac{\partial \phi_f}{\partial \phi_i} \end{vmatrix} \\ &= 1 - \frac{qgE_1}{2W_i}kT'(k)\cos(\phi_i)\end{aligned} \tag{6.24}$$

where $T'(k) = \frac{dT(k)}{dk}$. The determinant is clearly equal to unity for no acceleration and it can be seen that when acceleration is present the transit time factor changes across the gap, causing the determinant to deviate from unity. There are two ways of reducing this deviation, either the acceleration gradient is reduced, or the initial energy particle is increased. This allows the determinant to be very close to unity, which allows the phase space behaviour of particles to be accurately modelled in the regime where moderate gradients are present. As seen in [60], a phase correction can be applied that can correct for any error that occurs when crossing the boundary, however for the regimes which are being discussed here this is not needed. For example, with an initial energy in the region of 6 times the proton rest mass, the discrepancy is $\mathcal{O}(10^-3)$ for 10kV/m.

When acceleration is present an analytical solution for each trajectory cannot be derived because β_s and γ_s are changing as the particle progresses through the linac. The trajectory

must now be solved numerically. This is achieved by tracking the synchronous particle through the desired length of linac, and calculating β and γ as functions of s. This regime is entered when E_0 increases such that $\beta_s\gamma_s \neq C$ where C is a constant. As the particle accelerates, $\beta \rightarrow 1$ and $\frac{d\beta}{dW} \rightarrow 0$. This causes adiabatic phase damping which results in larger energy spreads. This can be seen by the spiral-like trajectories found in fig. 6.30.

This behaviour is a consequence of the kinetic energy term in the Hamiltonian. As $\beta_s\gamma_s$ increases, the kinetic term of the Hamiltonian is decreasing. Therefore the term separatrix loses its meaning as there is no longer a contour that represents the boundary between stable and unstable orbits [60]. Instead, the input acceptance is calculated numerically, which specifies which initial positions for an ensemble of particles will be stable. The input acceptance is a boundary in phase space for the initial coordinates of a bunch of particles. If a particle's initial coordinates are within the input acceptance, then the particle will undergo a stable orbit and be captured by the bucket. This effect is shown in fig. 6.30, the particle undergoes phase damping, which results in an growth on the energy axis. It is also possible for particles that have very high initial phase and energy values to be captured by the bucket because the tail from the separatrix extends until high values. A particle with an initial position inside this tail will take a long time to reach the bucket, but will eventually be captured with the rest of the bunch. This type of behaviour is unique to linacs and has been seen at many different facilities [123].

A Hamiltonian that describes the motion in phase space of a particle as it traverses through a cavity oscillating in a single mode has been derived. In the next section, this formalism will be extended to allow the modelling of two harmonically related modes with different longitudinal field profiles.

6.4.2 Hamiltonian for Multi-Harmonic Cavities

Here, a Hamiltonian is derived that facilitates an arbitrary variation of the fundamental mode with an additional harmonic. The electric field in a multi-harmonic cavity can be generalised

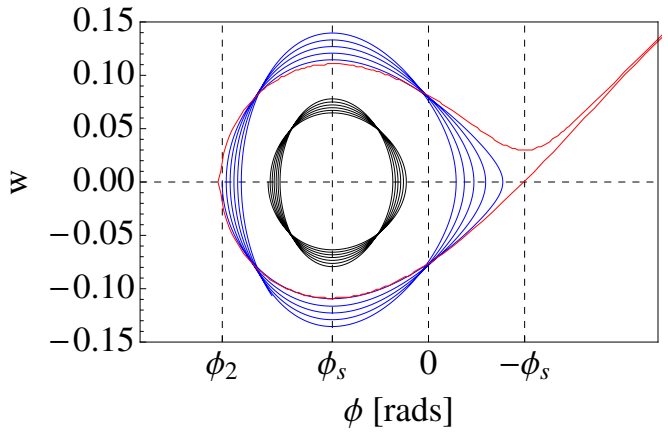

Figure 6.30: A single input acceptance is shown for $E_0 = 10$MV/m. The red curve is the boundary of the input acceptance and the blue and black curves are particle trajectories with different initial positions. The trajectory can move beyond the boundary as the boundary only applies to the initial position of the particles. The spiral nature is caused by the adiabatic phase damping due to the increasing β.

as

$$\begin{aligned} E_T = \quad & (1-\alpha)E_{z1}(z)\cos(\omega t+\phi) \\ & +\alpha E_{zh}(h,z)\cos(h(\omega t+\phi)+\phi_{nh}) \end{aligned} \tag{6.25}$$

where h is the harmonic number of the mode, ϕ_{nh} is the phase shift for the time-dependent component of the harmonic mode, α is the percentage mode contribution from the harmonic mode and $E_{z1}(z)$ and $E_{zh}(h,z)$ are the longitudinal field profiles for the fundamental and harmonic modes respectively. The energy gain of a particle traversing this field is given by

$$\begin{aligned} W = \quad & q[(1-\alpha)\int_{-g/2}^{g/2} E_{z1}(z)(\cos(\omega t)\cos(\phi) \\ & -\sin(\omega t)\sin(\phi))dz \\ & +\alpha\int_{-g/2}^{g/2} E_{zh}(h,z)(\cos(h\phi)\cos(h\omega t+\phi_{nh}) \\ & -\sin(h\phi)\sin(h\omega t+\phi_{nh}))dz], \end{aligned} \tag{6.26}$$

which can be simplified to

$$\begin{aligned} W = \quad & q[(1-\alpha)(V_1 \cos(\phi) - V_2 \sin\phi) \\ & +\alpha(V_{h1}\cos(h\phi) - V_{h2}\sin(h\phi))], \end{aligned} \tag{6.27}$$

where

$$V_1 = \int_{-g/2}^{g/2} E_{z1}(z)\cos(\omega\frac{z}{\beta c})dz, \tag{6.28}$$

$$V_2 = \int_{-g/2}^{g/2} E_{z1}(z)\sin(\omega\frac{z}{\beta c})dz, \tag{6.29}$$

$$V_{h1} = \int_{-g/2}^{g/2} E_{zh}(h,z)\cos(h\omega\frac{z}{\beta c} + \phi_{nh})dz, \tag{6.30}$$

$$V_{h2} = \int_{-g/2}^{g/2} E_{zh}(h,z)\sin(h\omega\frac{z}{\beta c} + \phi_{nh})dz. \tag{6.31}$$

The difference equation for the energy gain can now be given as

$$\begin{aligned} \Delta W_n = \quad & qW_0[(1-\alpha)(V_1[\cos(\phi) - \cos(\phi_s)] \\ & -V_2[\sin(\phi) - \sin(\phi_s)]) \\ & +\alpha[V_{h1}(\cos(h\phi) - \cos(h\phi_s)) \\ & -V_{h2}(\sin(h\phi) - \sin(h\phi_s))]] \end{aligned} \tag{6.32}$$

where W_0 is a scaling factor introduced to ensure the energy gain of the synchronous particle is the same for each variation within each study.

As described in the previous section, one can now move from discrete cavity gaps to continuous longitudinal coordinates, using $dn = ds/g$ and $w = (W - W_s)/mc^2$, this allows

the coupled equations to be obtained as

$$\begin{aligned}\frac{dw}{ds} &= \frac{q}{gmc^2}[(1-\alpha)(V_1[\cos(\phi)-\cos(\phi_s)] \\ &-V_2[\sin(\phi)-\sin(\phi_s)]) \\ &+\alpha[V_{h1}(\cos(h\phi)-\cos(h\phi_s)) \\ &-V_{h2}(\sin(h\phi)-\sin(h\phi_s))]] = -\frac{\partial H}{\partial \phi},\end{aligned} \tag{6.33}$$

and

$$\frac{d\phi}{ds} = -2\pi\frac{w}{\gamma_s^3\beta_s^3\lambda} = \frac{\partial H}{\partial w}. \tag{6.34}$$

The latter is unchanged from the single mode case.

By following the same procedure as described in the previous section, a Hamiltonian is derived from eqns. 6.33 and 6.34 as

$$\begin{aligned}H = \quad & -\frac{\pi}{\beta_s^3\gamma_s^3\lambda}w^2 - \frac{qW_0}{gmc^2}[(1-\alpha)(V_1[\sin(\phi)-\phi\cos(\phi_s)] \\ & +V_2[\cos(\phi)+\phi\sin(\phi_s)]) \\ & +\alpha[V_{h1}(\frac{\sin(h\phi)}{h}-\phi\cos(h\phi_s)) \\ & +V_{h2}(\frac{\cos(h\phi)}{h}+\phi\sin(h\phi_s))]].\end{aligned} \tag{6.35}$$

The kinetic energy term remains unchanged from the single mode case, this is because if a particle moves away from the synchronous particle by $d\phi$ in terms of the fundamental, then the movement for the additional harmonic will be $hd\phi$, which is taken into account in the potential. The Hamiltonian simplifies when a particular longitudinal profile is specified. For $E_{z1}(z) = E_0\cos(kz)$, i.e. an even function, then $V_2 = 0$ and $V_1 = \int_{-g/2}^{g/2} E_0\cos(kz)\cos(\frac{\omega z}{\beta c})dz$, whereas a reverse effect happens for an odd longitudinal function. Similarly, this also occurs for the harmonic mode when $\phi_{nh} = 0$. Depending on whether $E_{zh}(h,z)$ is even or odd, V_{h1} or V_{h2} becomes 0 respectively. However, for cases when $\phi_{nh} \neq 0$, this simplification does not occur.

The synchronous phase in a multi-harmonic cavity becomes more difficult to select as there are now two independent modes in the cavity, and the contribution from each one is

dependent on its specific parameters. In order to remain consistent between the treatment of each set of parameters, a new method is used that allows an appropriate synchronous phase to be determined. The phase corresponding to the peak energy gain across the cavity is found, Φ_s. The synchronous phase that would normally be applied in the single mode case as $-\pi/3$ (for example) is now applied to Φ_s. Therefore, your synchronous phase is given by $\Phi_s + \phi_s$. This allows a consistent treatment to each particle scenario. Typically, we will use $\phi_s = -\pi/3$, which results in a gradient reduction of 50%. This is much larger than is typically be used in a practical accelerator, but it allows an insight into the physics of the longitudinal dynamics for each case as it increases the phase width of the rf bucket.

The linear map for this Hamiltonian is similar to the single mode case, with an extension to include the additional mode. As before, the phases before and after the transformation are the same, i.e. $\phi_f = \phi_i$, the energy transformation is now

$$\begin{aligned} W_f \quad &= W_i + q[(1-\alpha)(V_1(k)\cos(\phi_i) - V_2(k)\sin(\phi_i)) \\ &+\alpha(V_{h1}(k)\cos(h\phi) - V_{h2}(k)\sin(h\phi_i))]. \end{aligned} \tag{6.36}$$

The Jacobian determinant of the Hamiltonian is given by

$$\begin{aligned} \frac{\partial(W_f,\phi_f)}{\partial(W_i,\phi_i)} &= \begin{vmatrix} \frac{\partial W_f}{\partial W_i} & \frac{\partial \phi_f}{\partial W_i} \\ \frac{\partial W_f}{\partial \phi_i} & \frac{\partial \phi_f}{\partial \phi_i} \end{vmatrix} \\ &= 1 - \frac{qk}{2W_i}[(1-\alpha)(V_1'(k)\cos(\phi_i) - V_2'(k)\sin(\phi_i)) \\ &+\alpha(V_{h1}'(k)\cos(h\phi_i) - V_{h2}'(k)\sin(h\phi_i))] \end{aligned} \tag{6.37}$$

where $V'(k) = dV/dk$. The derivative of the harmonic voltages give rise to an h factor from the longitudinal profile. This results makes the harmonic mode more sensitive to errors in the linear map. However, for similar gradients and initial energies, the error is not anticipated to be beyond 0.03 % in the worst case.

Eqn. 6.35 is now applied to glean some insight into the beam dynamics in second harmonic and third harmonic cavities.

6.4.3 Second Harmonic Cavity

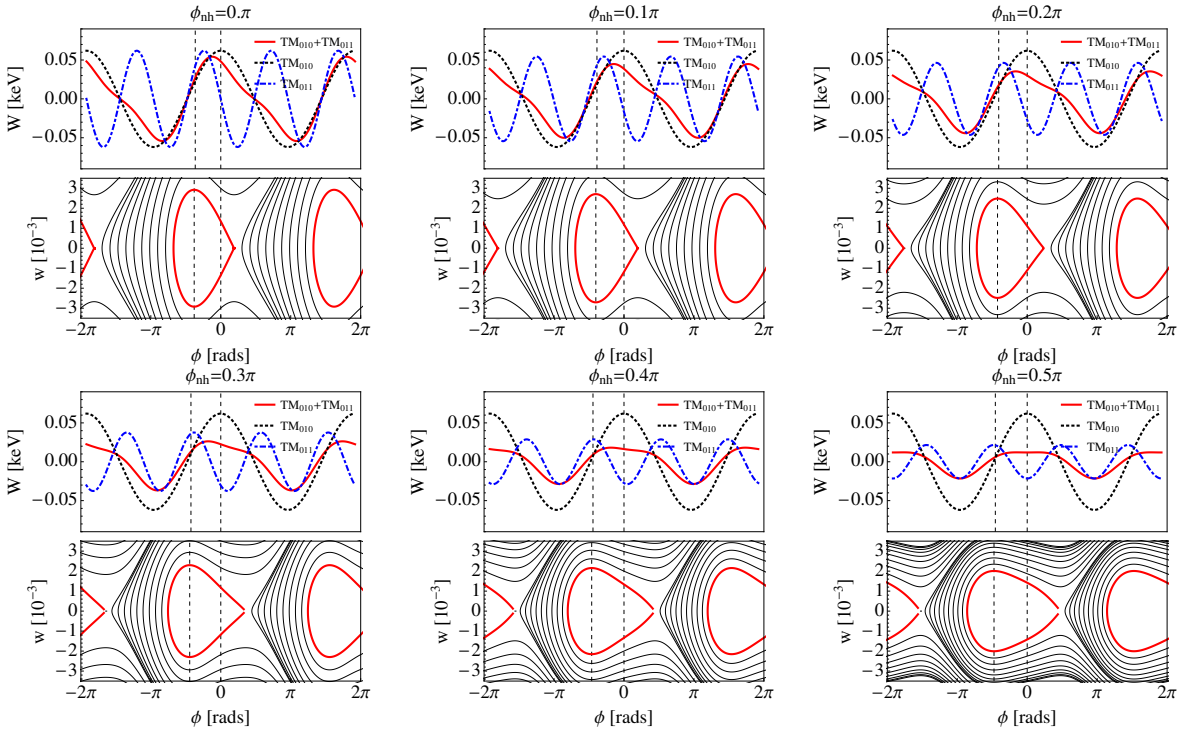

Figure 6.31: Phase space plots for a cavity exciting both the TM_{010} and TM_{011} modes. A phase shift is gradually applied to the TM_{011} mode and the gradient is kept constant for each step. For all steps, $E_0 = 10$ kV/m. The upper plot in each step is the energy gain over the cavity as a function of ϕ and the bottom is the phase space plots, where the red line marks the separatrix.

When considering a second harmonic cavity that excites TM_{010} and TM_{011} modes simultaneously, the harmonic number is $h = 2$ and $E_{zh}(h, z) = E_0 \sin(hkz)$. As discussed, a gradient reduction corresponding to a synchronous phase of $\phi_s = -\pi/3$ is used, with the synchronous phase being recalculated for each step as described in Section 6.4.2.

Here, ϕ_{nh} is varied from 0 to $\frac{\pi}{2}$ and the acceptance of the rf bucket is determined for each step. Throughout the variation of ϕ_{nh}, a constant value of $\alpha = 0.222$ is used. This value arises from an optimisation of a second harmonic cavity suitable for beam driven applications [59]. The particle trajectories are solved for different initial conditions for a proton with an initial energy of 7 times its rest mass. These plots are shown for different values of ϕ_{nh} in fig. 6.31.

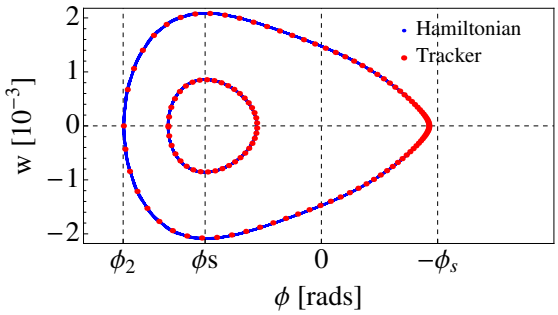

Figure 6.32: Comparison between particle tracking based on fundamental principles with Hamiltonian from eqn. 6.35 for $\phi_{nh} = 0.5\pi$. The larger contour is for the separatrix, with the smaller trace showing a small phase deviation.

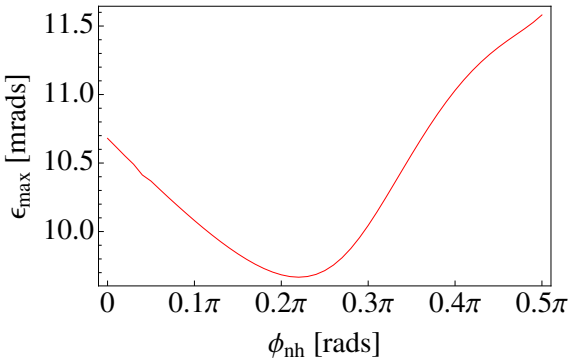

Figure 6.33: The normalised acceptance of the rf bucket vs the phase shift of the TM_{011} mode.

For $\phi_{nh} = 0$, a slight distortion in the energy gain as a function of ϕ is observed around $\phi = \pi/2$. In the region of the synchronous phase however, the energy gain is approximately sinusoidal. This is why the shape of the separatrix does deviate significantly from the single mode case. When ϕ_{nh} increases, the energy gain of a particle in the region of $\phi > 0$ begins to increase and draw level with the energy gain at $\phi < 0$. This culminates in a flattening of the bucket at $\phi_{nh} = 0.5\pi$ around $\phi = 0$. The bucket is now much wider, and is flatter at the highest energy excursion. This flattening is similar to some of the results obtained at the PSB [118] and ELETTRA [119] where this type of behaviour can increase the lifetime of the beam.

In order to verify the plots found in fig. 6.31, single particle tracking based on fundamental principles was performed and compared with the Hamiltonian for $\phi_{nh} = \frac{\pi}{2}$. The reason

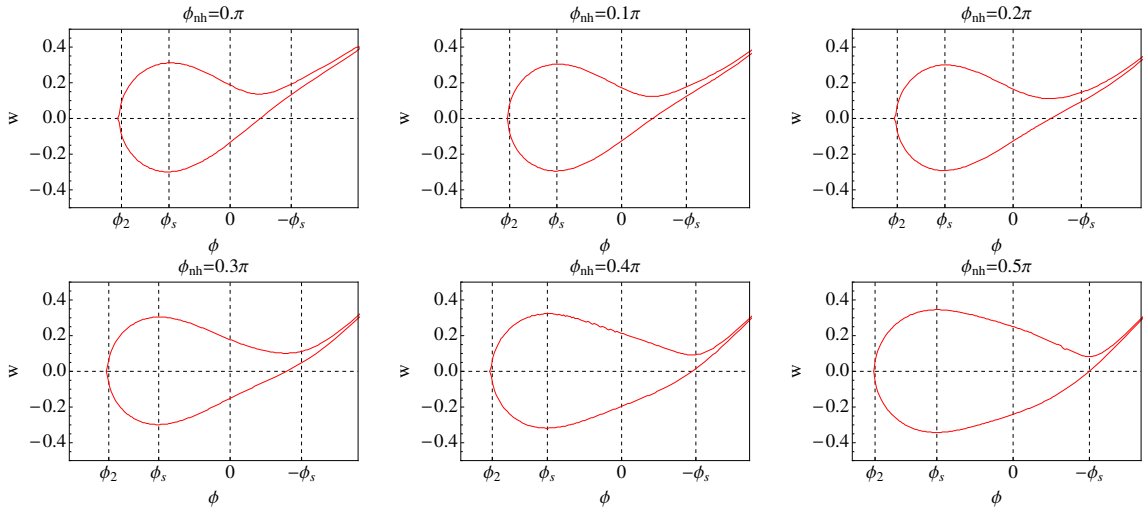

Figure 6.34: Input acceptance for a TM_{011} second harmonic cavity for $E_0 = 10$ MV/m and $W_i = 7m$. In each case, ϕ_2 corresponds to respective ϕ_2 found from the case where no acceleration is present.

for choosing this particular step is because it is the most distinctive plot and differs the most from a single mode separatrix. The results from the tracking can be found in fig. 6.32. The tracking was found to be in agreement, with the phase behaviour perfectly matching the Hamiltonian and an amplitude difference of less than 0.5%, a similar discrepancy was found in the single mode case.

The acceptance of each rf bucket can be found by numerically calculating the area of the separatrix. This is plotted in Fig. 6.33. It can be seen that initially, the acceptance reduces because the gradient of the energy gain is reducing. However, as the bucket begins to flatten, the phase width increases which causes the acceptance of the bucket to increase.

With the same set of cavity parameters, the case when $E_0 = 10$MV/m is now modelled. The input acceptance is calculated for each step and the main features from each of the graphs shown in fig. 6.34 are still present. Here, the spiral like trajectories are omitted from the figures as they do not provide any new insight into the dynamics. It can be seen that as the energy gain is flattening in the area around $\phi = 0$ for ϕ_{nh} approaching 0.5π, the input acceptance begins to distort and expand around $-\phi_s$. In the plots, the point ϕ_2 refers to the position of the edge of the separatrix from the case without acceleration. This is to show any additional phase width that may be gained by including acceleration. The area of the input

acceptance behaves the same in the case with acceleration as it does without acceleration, while also retaining the same key features observed.

These simulations show that a second harmonic cavity can be used to accelerate bunches of particles and that the rf bucket can be manipulated in a precise and predictable way.

Having modelled the acceptance of the rf bucket in a cavity that can excite a fundamental and second harmonic mode, a similar procedure is now applied to a cavity that excites a fundamental and a third harmonic mode in the following section.

6.4.4 Third Harmonic Cavity

For the third harmonic, a cavity that excites a TM_{010} mode with a third harmonic TM_{012} is considered. It therefore follows that for this regime, $h = 3$, $\phi_{nh} = 0$ and $E_{zh}(h, z) = E_0 \cos(hkz)$.

In this section, α will be varied in order to determine the behaviour of the area in between the main rf buckets. Here, the value of α at which additional buckets begin to emerge between the primary rf buckets is to be determined. To achieve this, energy gain and phase space plots for a proton with an initial energy of 7 times its rest mass are plotted for a third harmonic cavity while maintaining a constant gradient, these results are displayed in fig. 6.35.

As α is increased, it can be seen that the phase space contours begin to distort as the effect of the third harmonic becomes much more prominent. This is shown by the particularly dense region of contours that begin to emerge in between the main rf buckets. However, it is not until $\alpha \approx 0.65$ that a stable region develops. The reason the secondary bucket emerges at this point, is because the additional peak in the energy gain plot has an amplitude that exceeds the energy gain of the synchronous particle. Once this occurs, small stable regions can develop that are localised to the additional peak, but can freely move to positive and negative values of w. It can then be seen that when $\alpha = 1$, the case for just the third harmonic alone is present, as expected.

As found in previous sections, tracking was performed in order to verify the figures

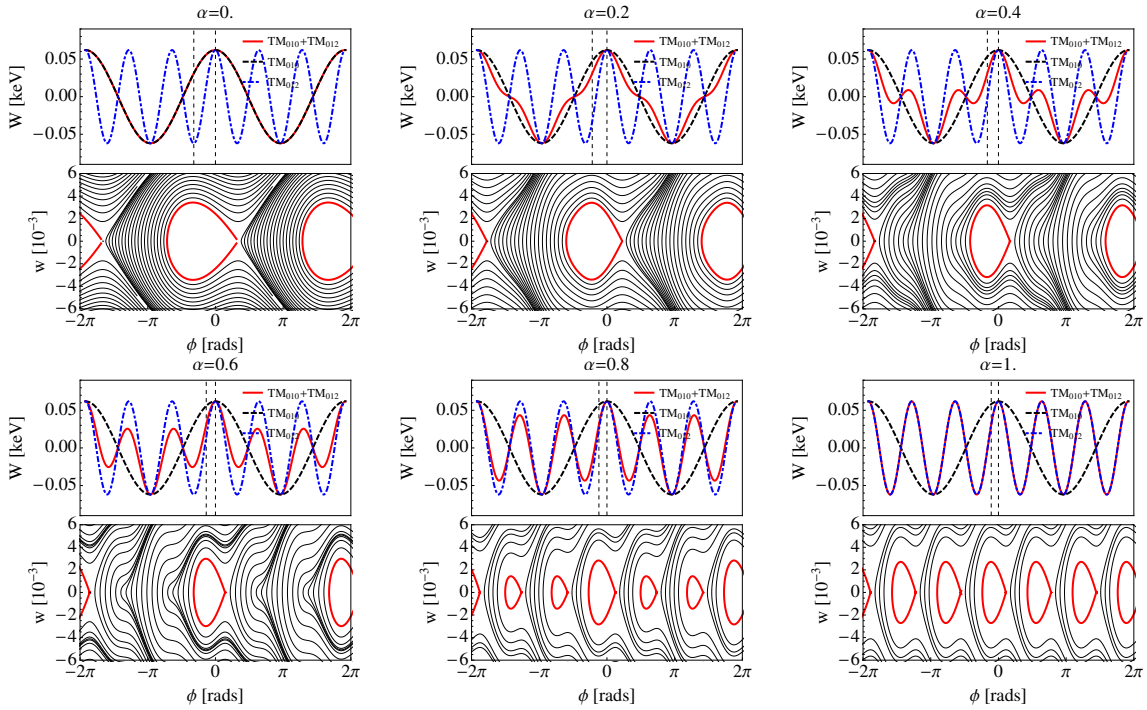

Figure 6.35: Phase space plots for a TM_{012} mode for varying α with $E_0 = 10$ kV/m. The gradient is kept constant for each step. Top is the energy gain as a function of phase offset and bottom is the phase space contours.

shown. For this case $\alpha = 0.8$ was used, because a secondary bucket was present but with reduced amplitude. Two initial positions were selected such that they were both on the seperatrices of their respective buckets. This can be found in Fig. 6.36. Good agreement was found, with the amplitude errors being no more than 0.3%.

Fig. 6.37 shows the acceptance of the rf bucket as a function of α. The acceptance slowly reduces as α increases, starting with the acceptance for a single mode cavity alone and ending with the acceptance of just the third harmonic alone. Due to the increased frequency of the third harmonic, the phase width of the bucket is also reduced by a factor of three. Considering that each step in this study is scaled such that the energy gain of the synchronous particle is constant, the acceptance behaves in a manner that is anticipated.

The input acceptance behaves in a similar manner to the previous cases. This is displayed in fig. 6.38. The shrinking of the input acceptance is clearly visible with a reduction in the phase width of the main buckets.

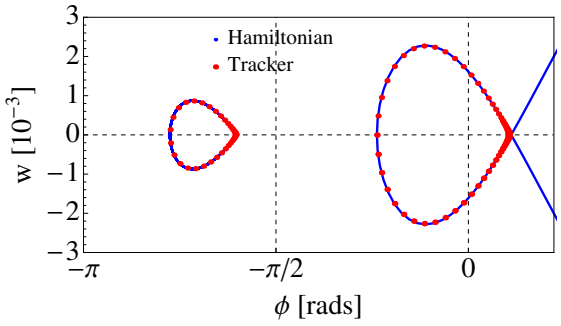

Figure 6.36: Comparison between particle tracking based and Hamiltonian from eqn. 6.35 for $\alpha = 0.8$. The contour on the right is the separatrix of the main rf bucket, while the separatrix for the secondary bucket can be seen on the left.

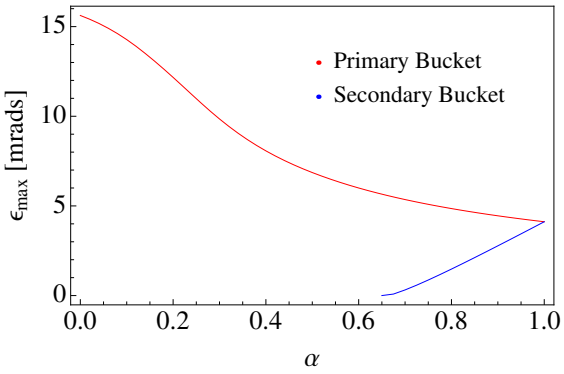

Figure 6.37: The normalised acceptance of the stable region in the rf bucket vs α.

The Hamiltonian for a particle traversing a multi-harmonic cavity has been derived and applied to a second and third harmonic cavities. This work is applicable for medium to high energy proton linacs operating at high gradients, or low energy proton linacs operating at low gradients.

In Chapter 5 the principles of single mode detuning for collinear were introduced and verified with simulation. Here, in Chapter 6 we have shown the potential benefits of exciting multiple harmonic modes within the confines of a single rf cavity. Finally, to complete the discussion, a cavity geometry will be described that allows multiple harmonic modes to be detuned to allow collinear acceleration with high transformer ratios as well as pulsed surface heating reduction. This will be described in detail in Chapter 7.

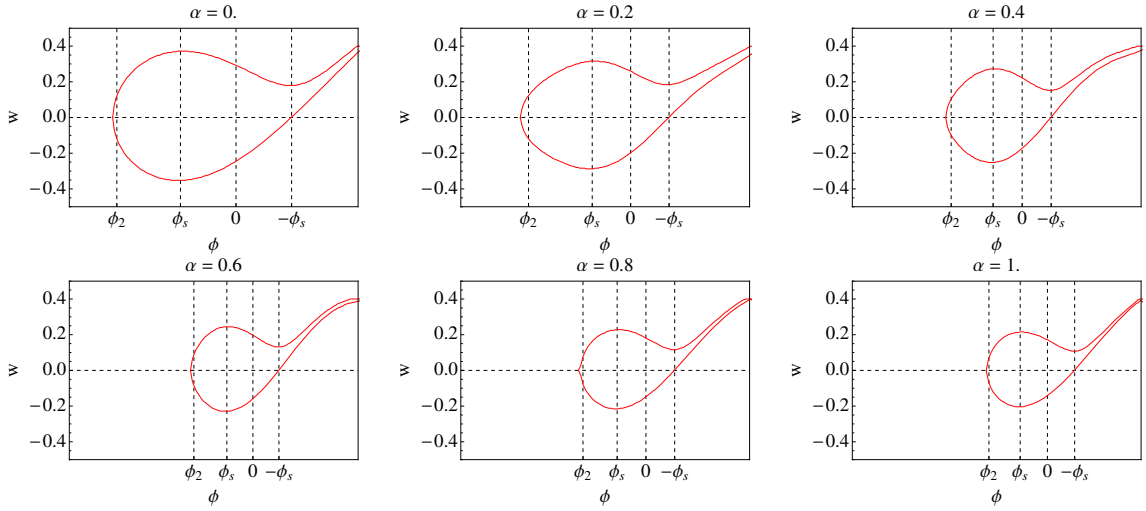

Figure 6.38: Input acceptance for $E_0 = 10$ MV/m. In each case, ϕ_2 corresponds to respective ϕ_2 found from the case where no acceleration is present.

Chapter 7

Multi-Harmonic Detuned Accelerating Structure

The fundamental principles of single mode cavity detuning have been verified, and the benefits of exciting multiple harmonically related modes have been shown. This chapter will combine these two effects, and introduce a cavity geometry that is capable of being used a detuned multi-harmonic accelerator structure. A structure of this type could potentially be used as a basis for future high gradient lepton linear colliders. The transformer ratio and the pulsed surface heating reduction will be verified from numerical modelling and time domain simulations.

The longitudinal and transverse wakefield pose serious threats to the stability of trailing bunches in close proximity to the driving bunches. An analysis of the longitudinal and transverse modes of the cavity will be performed, and the results will be compared to wakefield simulation results from t3p. This will be followed by a discussion on how the transverse wakefield affects the design of such a cavity.

In the previous chapters, several different types of cavity have been introduced. Chapter 5 showed a single mode cavity that is capable of being used in two beam acceleration schemes. While Chapter 6 showed simulations of multi-harmonic cavities that can have reduced surface temperature rise. This chapter will combine these two effects, which will result in a cavity that excites multiple harmonic modes and can be used in two beam acceleration schemes. The transformer ratio and pulsed surface heating reduction will be verified by both eigenmode and time domain simulations. In order to determine the feasibility of such a cavity, this chapter will finish by discussing the transverse wakefield of this multi-harmonic detuned accelerating structure.

Initially, expressions regarding the multi-harmonic transformer ratio need to be introduced to guide the design of the structure. This theory was originally developed by Y. Jiang [112] and is then verified with time domain simulations, the first time a cavity of this kind has been studied in this way.

7.1 Multi-Harmonic Transformer Ratio

The transformer ratio for a cavity that excites one accelerating mode has been shown to be valid in time domain simulations in Chapter 5. However, when multiple accelerating modes are present, the overall transformer ratio is the parameter of interest. Here, the multi-harmonic transformer ratio will be derived from the steady state field profile from each of the modes.

Assuming an ideal π-mode pattern, the longitudinal steady state field profile for the detuned beam-excited fundamental mode is given by

$$E_1(z,t) = I_1 R_{s,1} \cos(\phi_1) \exp i(\omega_1 t + \phi_1) \cos(\frac{\pi}{L} z), \tag{7.1}$$

where L is the cavity length, I_n, $R_{s,n}$ and ϕ_n is the contributing current component, the shunt impedance and the detuning angle respectively for the nth mode. This is the similar to the previous form found in eqn. 5.24. The deceleration gradient of a particle arriving at the center of the cavity at $t, z = 0$ is therefore

$$D_1 = \frac{1}{L}\text{Re}\int_{-L/2}^{L/2} E_1(z, t = z/c)dz = \frac{I_1 R_{s,1}}{2}\cos^2(\phi_1), \tag{7.2}$$

while the accelerating gradient for a particle travelling one quarter of a period of the fundamental frequency later is

$$A_1 = \frac{1}{L}\text{Re}\int_{-L/2}^{L/2} E_1(z, t = z/c + \pi/2\omega_d)dz = -\frac{I_1 R_{s,1}}{4}\sin(2\phi_1). \tag{7.3}$$

For the second harmonic mode, the wave number for is twice that of the fundamental mode, therefore it can be treated as a shorter cavity with length $L/2$ where the virtual cavity center is now offset by $L/4$ to the real cavity center for a TM_{011} mode. The longitudinal field profile is therefore

$$E_2(z,t) = I_2 R_{s,2} \cos(\phi_2) \exp i(\omega_2 t + \phi_2) \cos(\frac{2\pi}{L} z), \tag{7.4}$$

with decelerating gradients given by

$$D_2 = \frac{2}{L}\text{Re}\int_{-L/4}^{L/4} E_2(z, t = z/c)dz = \frac{I_2 R_{s,2}}{2}\cos^2(\phi_2). \tag{7.5}$$

The second harmonic has twice the phase velocity of the fundamental mode, therefore (in terms of phase) the field advances for particle that is offset by a fixed amount by twice as much as the fundamental. Therefore the phase delay in this case is π.

$$A_2 = \frac{2}{L}\text{Re}\int_{-L/4}^{L/4} E_2(z, t = z/c + \pi/2\omega_d)dz = -\frac{I_2 R_{s,2}}{2}\cos^2(\phi_2) \tag{7.6}$$

The transformer ratio is -1 for a second harmonic. This same relation applie for all even harmonics.

For an ideal third harmonic cavity the steady state field is

$$E_3(z, t) = I_3 R_{s,3}\cos(\phi_3)\exp i(\omega_3 t + \phi_3)\cos(\frac{3\pi}{L}z). \tag{7.7}$$

Similary, the decelerating and accelerating gradients can be calculated as

$$D_3 = \frac{1}{L}\text{Re}\int_{-L/6}^{L/6} E_3(z, t = z/c)dz = \frac{I_3 R_{s,3}}{2}\cos^2(\phi_3) \tag{7.8}$$

and

$$A_3 = \frac{3}{L}\text{Re}\int_{-L/6}^{L/6} E_3(z, t = z/c + \pi/2\omega_d)dz = \frac{I_3 R_{s,3}}{4}\sin(2\phi_3) \tag{7.9}$$

As has been shown before, the transformer ratio is calculated as

$$\mathcal{T} = \frac{A}{D}, \tag{7.10}$$

where A and D are the total accelerating and decelerating gradients. For a single mode cavity, this is simply given by

$$\mathcal{T} = \frac{A_1}{D_1} = -\tan(\phi_1) = 2Q\delta. \tag{7.11}$$

In the case of a cavity that excites a fundamental and a second harmonic mode, the accelerating and decelerating gradients are given as

$$A = A_1 + A_2 = -\frac{I_1 R_{s,1}}{4}\sin(2\phi_1) - \frac{I_2 R_{s,2}}{2}\cos^2(\phi_2) \tag{7.12}$$

and

$$D = D_1 + D_2 = \frac{I_1 R_{s,1}}{2}\cos^2(\phi_1) + \frac{I_2 R_{s,2}}{2}\cos^2(\phi_2). \tag{7.13}$$

This gives the transformer ratio as

$$\mathcal{T} = \frac{A_1 + A_2}{D_1 + D_2} = -\frac{\sin(2\phi_1) + 2\chi\cos^2(\phi_2)}{2\cos^2(\phi_1) + 2\chi\cos^2(\phi_2)}. \tag{7.14}$$

When $\phi_1 = \phi_2 = \phi$, this reduces to

$$\mathcal{T} = -\frac{\tan(\phi_1) + \chi}{1 + \chi}, \tag{7.15}$$

where $\chi = I_2 R_{s,2}/I_1 R_{s,1}$. The presence of a second harmonic mode does not contribute to the total transformer ratio experienced by the beam, the stronger the second harmonic mode is excited, the lower the transformer ratio becomes.

Eqn. 7.14 can be plotted to show the behaviour of the transformer ratio for changing the detuning angle and the contribution to the total field of the second harmonic. This can be found in fig. 7.1. The figure shows that for any detuning angle or second harmonic contribution, the transformer ratio is reduced for the second harmonic and any even harmonics.

For a multi-harmonic cavity that excites the fundamental mode with a third harmonic mode, the acceleration gradient is

$$A = A_1 + A_3 = -\frac{I_1 R_{s,1}}{4}\sin(2\phi_1) + \frac{I_3 R_{s,3}}{4}\sin(2\phi_3) \tag{7.16}$$

with a decelerating gradient of

$$D = D_1 + D_3 = \frac{I_1 R_{s,1}}{2}\cos^2(\phi_1) + \frac{I_3 R_{s,3}}{2}\cos^2(\phi_3). \tag{7.17}$$

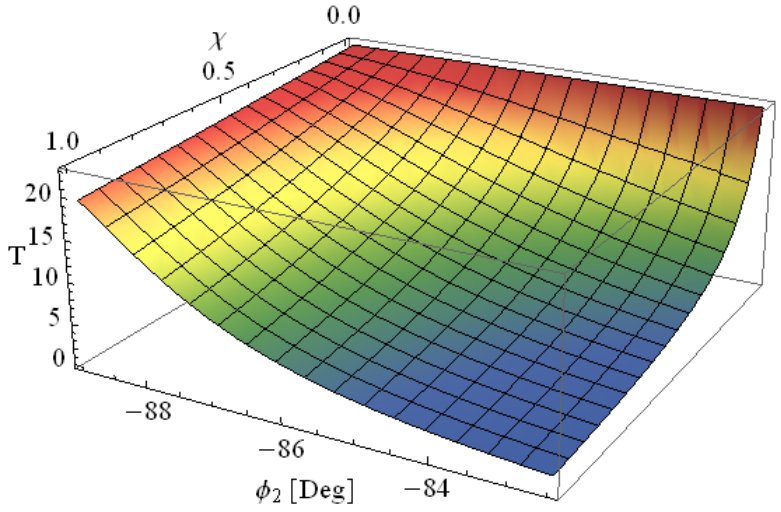

Figure 7.1: Transformer ratio as a function of the second harmonic contribution and detuning angle. For this figure, we choose $\phi_1 = 87.5°$ which gives $\mathcal{T}_1 = 22.5$.

This gives a transformer ratio of

$$\mathcal{T} = \frac{A_1 + A_3}{D_1 + D_3} = -\frac{\sin(2\phi_1) - \chi \sin(2\phi_3)}{2(\cos^2(\phi_1) + \chi \cos^2(\phi_3))} \tag{7.18}$$

where $\chi = I_3 R_{s,3}/I_1 R_{s,1}$. When $\phi_1 = -\phi_3 = \phi$, the transformer ratio simplifies to

$$\mathcal{T} = \tan(\phi) = -2Q\delta \tag{7.19}$$

A 3D plot of the third harmonic transformer ratio can be seen in fig. 7.2. The transformer ratio for the fundamental mode alone is 22.5, and it can be seen that with the correct detuning angle and small values of χ, the transformer ratio can be maintained or even increased. This provides the main motivation for selecting a third harmonic cavity for the studies shown here.

Now the percentage contribution from the third harmonic mode α for a beam driven cavity is calculated in terms of the ratio of the shunt impedances χ. The percentage contribution

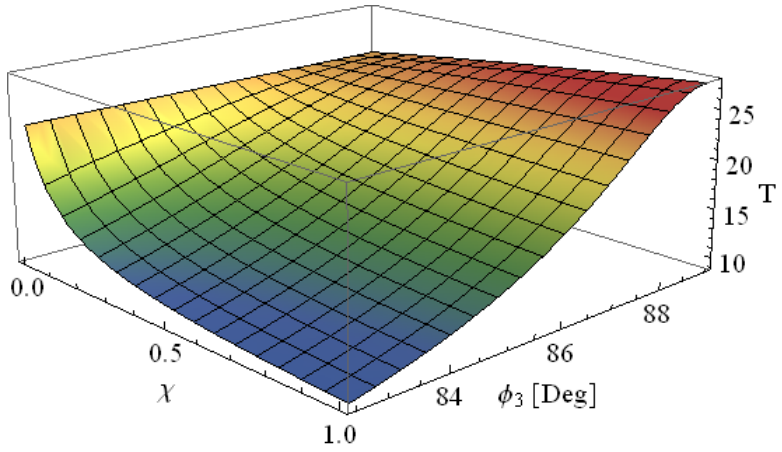

Figure 7.2: Transformer ratio as a function of the third harmonic contribution and detuning angle. For this figure, we choose $\phi_1 = 87.5°$ which gives $\mathcal{T}_1 = 22.5$.

of the field from the additional harmonic to the total field is given by

$$\alpha = |E_3/E_{total}| = |\frac{-\chi \sin(2\phi_1)}{\sin(2\phi_1) - \chi \sin(2\phi_3)}| \tag{7.20}$$

This reduces to $\alpha = \chi/(1+\chi)$ for $\phi_1 = -\phi_3 = \phi$.

If it was required to increase the contribution from the additional harmonic, shorter Gaussian bunch sizes can be used to maximise the magnitude of the excitation of each mode. By taking the ratio of the current components for each mode, a relation for the bunch length σ in terms of the fundamental frequency can be determined. i.e.

$$\frac{I_h}{I_1} = \frac{\exp(\frac{-2\pi^2\sigma^2}{\lambda_h^2})}{\exp(\frac{-2\pi^2\sigma^2}{\lambda_1^2})} = \exp(\frac{(-2h^2+2)\pi^2\sigma^2}{\lambda_1^2}) \sim 1, \tag{7.21}$$

provided

$$\frac{(2h^2-2)\pi^2\sigma^2}{\lambda_1^2} \ll 1, \tag{7.22}$$

which allows a minimum bunch length to be defined as

$$\sigma \ll \frac{\lambda_1}{\pi\sqrt{2h^2-2}}. \tag{7.23}$$

This relation can also be used to limit the contribution from the harmonic mode by lengthening the bunch size. This is particularly useful when performing single mode simulations on a multi-harmonic cavity. The longer bunch length reduces the component from higher order modes and only strongly excites the fundamental mode.

7.2 Cavity Simulations

This section will describe the design process and simulation results of a detuned multi-harmonic cavity. The transformer ratio and average magnetic field squared will be calculated with eigenmode simulations and will be followed up with verification from time domain simulations.

7.2.1 Eigenmode

From the calculations found in Section 7.1, a third harmonic cavity was selected as the most suitable type of cavity for beam driven multi-harmonic cavity two beam accelerator. The same techniques and base geometry found in Chapter 6 can be used with slight changes in order to tune the cavity frequencies. Table 7.1 gives the geometric parameters that arose from an optimisation of the third harmonic cavity found in Chapter 6. The geometry can be found in figure 6.2. As seen in Chapter 6, chokes were included on either end of the cavity. These were purely for simulation purposes, in order to prevent the third harmonic mode from leaking out through the iris which would cause the boundary conditions to effect the simulation results.

The field profiles for the TM_{010} and the third harmonic TM_{012} modes can be found in figure 7.3 and rf parameters for each mode can be found in table 7.2. In the design of this cavity, several aspects had to be considered. Firstly, the quality factor of the fundamental mode needed to be low. This is because the rise time of a mode is calculated by eqn. 2.6, i.e. linearly with Q_e. In order to perform time domain simulations, the cavity needs to be simulated until steady state is reached, which does not occur until approximately 5 times the rise time of the most dominant mode. For this reason, the surface conductivity was artificially lowered until the quality factor for the fundamental mode was 500. This was a compromise

Parameter	Units	Value
a	a/λ	0.15
L	-	$\lambda/2$
A_1	mm	1.68
B_1	mm	4.872
A_2	mm	1.222
B_2	mm	1.195
b	mm	11.097
b_{end}	mm	11.109
g_t	mm	1.535
$g_{t,end}$	mm	1.327

Table 7.1: Geometry parameters for a third harmonic detuned cavity.

between attainable simulation times and quality factors that were high enough for the model to remain accurate.

Additionally, it was intended that the cavity be designed such that $\phi_1 = -\phi_3$, which would give $\mathcal{T} = -2Q\delta$. However, a field flatness for the fundamental mode was critical for accurate simulations. The resulting transformer ratios are therefore $\mathcal{T}_1 = 8.936$ and $\mathcal{T}_3 = -10.633$. Therefore, the expected transformer ratio for these parameters needs to be calculated.

For a drive beam of Gaussian width $\sigma_z = 1$mm, the current contributions can be calculated as $I_1 = 0.969$, $I_3 = 0.756$, which means the third harmonic mode is being excited at 78% of the magnitude of the fundamental, which gives $\chi = 0.0489$. Substituting each of these relevant parameters into eqn. 7.18, gives the anticipated transformer ratio of $\mathcal{T} = -9.0115$ when the cavity is being excited by a drive bunch train with a repetition frequency of $f_d = 11.9942$ GHz and $\sigma_z = 1$mm.

Following a similar process to that found in Chapter 6, the reduction in the surface magnetic field will be calculated for this cavity, first with eigenmode, then with time domain simulations.

The magnetic field on the surface of a detuned cavity for a single mode is given by

$$H_{\|}(s,t) = H(s)\sin(\omega t - \phi_1). \tag{7.24}$$

Parameter	Units	TM_{010}	TM_{012}
f	GHz	11.888	36.2693
Q	-	500	672.46
Θ	-	0.7684	0.421
$E_{s,max}$	-	6.16	8.33
$H_{s,max}$	mA/V	13.42	39.514
R_s	$k\Omega/m$	278.08	17.44
R'_s/Q	Ω/m	556.2	25.9

Table 7.2: RF parameters for a beam driven third harmonic cavity.

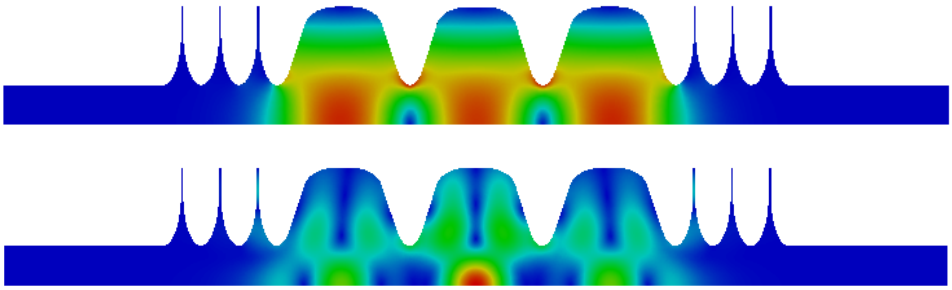

Figure 7.3: Field profiles for the TM_{010} (top) and TM_{012} (bottom) modes of a three cell third harmonic elliptical cavity with chokes.

For two modes, the peak magnetic field is given by

$$H_{\|}(s,t) = H(s)[(1-\alpha)\sin(\omega t - \phi_1) + \eta(s)\alpha\sin(3\omega t - \phi_3)] \tag{7.25}$$

where $\eta(s)$ is a function of the ratios of the magnetic field strength along the surface. The average magnetic field squared along the surface is calculated for this third harmonic cavity and is displayed in fig. 7.4. The reduction in the average of the magnetic field squared for the multi-harmonic cavity has a peak reduction of 19.3% compared to the single mode case. The corresponding temperature rise is calculated and can be found in fig. 7.5.

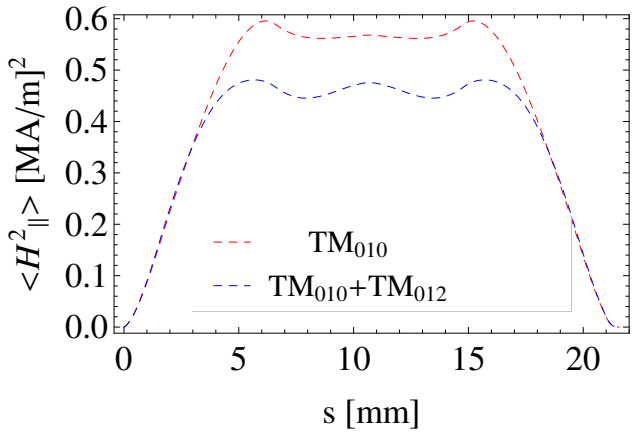

Figure 7.4: Average magnetic field squared on the surface of the cavity, the red line is TM_{010} alone and the blue line is TM_{010}+TM_{012}.

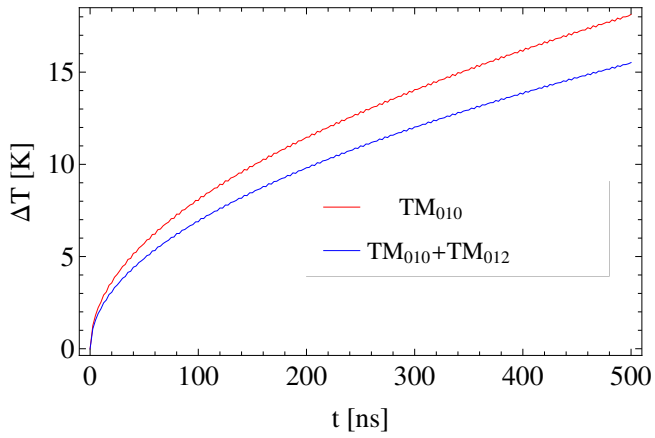

Figure 7.5: Peak surface heating as a function of time. The red line is TM_{010} alone and the blue line is TM_{010}+TM_{012}.

7.2.2 Excitation Model

The excitation model describe in Chapter 5 can be applied to the third harmonic cavity, in order to show that the two methods of calculating the transformer ratio are both applicable to a cavity of this type, and that results can be obtained that are in agreement with theoretical predictions.

Firstly, by taking a point at the center of the cavity, the model can be expanded to include the additional harmonic present in the cavity. This then allows the arrival time of each drive and test bunch to be calculated (the same method found in Chapter 5), and the relative field they experience can be determined. The transformer ratio taken only at the center of each cavity is calculated as $\mathcal{T} = -9.004$, which is excellent agreement with the expected value. The excited fields and bunch locations can be found in fig. 7.6.

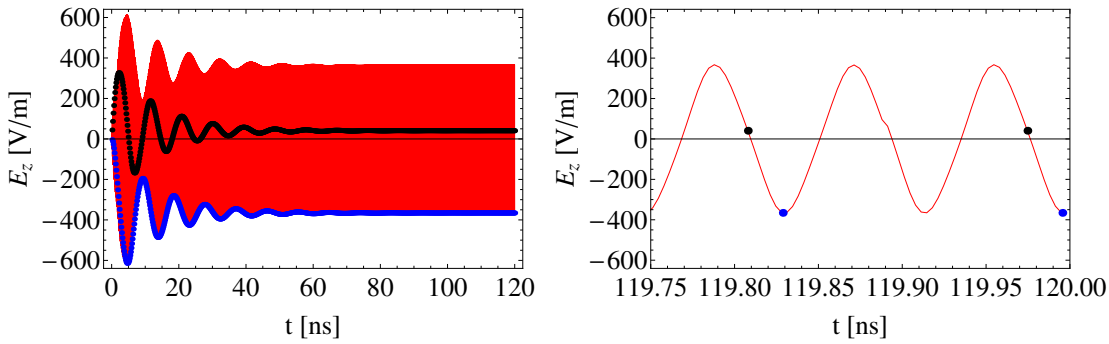

Figure 7.6: Fundamental and third harmonic field oscillations are summed over time to replicate a drive bunch excitation. The left figure shows the full probe signal at the center of the cavity, while the right shows drive bunch points (blue) and test bunch points (black).

Alternatively, the transformer ratio can be calculated by integrating gaussian bunches through a field that is composed of both the fundamental and third harmonic mode and determining the ratio of the energy gain of the test bunches to the drive bunches. This gives a transformer ratio of $\mathcal{T} = -8.9722$.

In the next section, time domain simulations will be shown that verify both the reduction in the average magnetic field squared on the surface and the multi-harmonic transformer ratio.

7.2.3 Time Domain Simulations

Time domain simulations on the collinear multi-harmonic cavity were performed using the code T3P. The cavity was excited by a drive bunch train with reptition frequency $f_d = 11.9942/2$ GHz (corresponding to the CLIC rf frequency with every other bucket filled).

In order to be able to compare the surface fields and transformer ratios for single mode excitation and multi-mode excitation, two simulations needed to be performed.

The first simulation was with a bunch train where each bunch had a gaussian width of $\sigma_z = 4$mm. This allowed a strong excitation of the fundamental mode and a weak excitation of higher order modes. Then, using the same geometry and mesh, the cavity field was excited with a bunch train that has a gaussian width of $\sigma_z = 1$mm. This allowed strong excitation of both the fundamental mode and the third harmonic mode.

The cavity parameters for the fundamental and third harmonic mode can be obtained from the simulation with $\sigma_z = 1$mm. A frequency filter could be applied that removed the fundamental mode such that only the third harmonic (or the fundamental mode) is present. As shown in Chapter 5, the field experienced by the drive bunch at the center of the cavity can be can be plotted, and a numerical fit applied to obtain the cavity frequency and quality factor.

Parameter	TM_{010}	TM_{012}	TM_{010}+TM_{012}
σ_z [mm]	4	1	1
f_c [GHz]	11.888	36.2693	-
Q_c	500.0	672.0	-
$\mathcal{T}_{\text{analytical}}$	8.94	-10.63	9.01
$\mathcal{T}_{\text{simulation}}$	8.85	-10.27	9.04

Table 7.3: Summary of time domain results for a detuned multi harmonic cavity.

Table 7.3 summarises the results relating to the transformer ratio for time domain simulations of a collinear multi-harmonic cavity. There is excellent agreement with analytical prediction and time domain simulations for the transformer ratio, with a discrepency of less than 0.5%.

For each simulation presented, the surface electric and magnetic fields were extracted

for two complete rf cycles at steady state. This allowed the average magnetic field squared on the surface to be calculated for single mode excitation and compared to multi-harmonic excitation.

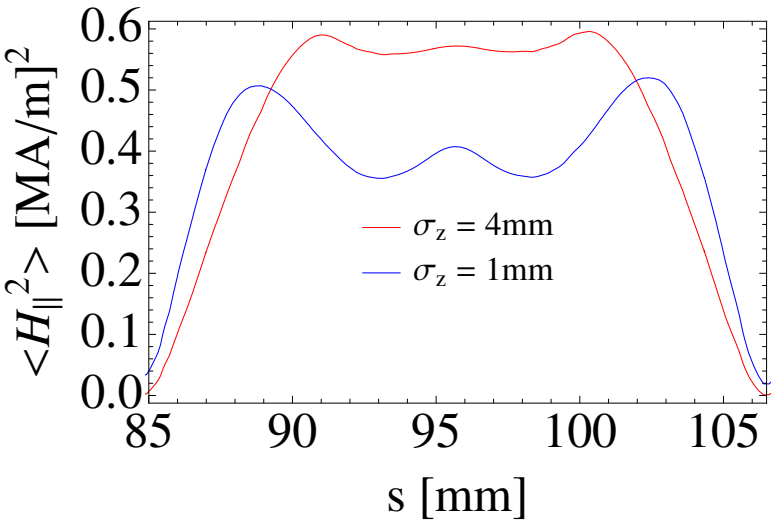

Figure 7.7: Time domain simulation results of the average square of the magnetic field reduction along the surface of the central cell in a detuned multi-harmonic cavity. Red is for fundamental mode only and blue is for a combination of fundamental and third harmonic.

Figure 7.7 shows the average $H_{\|}^2$ along the surface of the third harmonic collinear cavity. The plot shows the average field calculated in the time domain using the data from the middle cell from each of the two different simulations. The maximum anticipated surface field reduction for the eigenmode case was 19.3%. It was found in the time domain that there was a maximum reduction of 13.3%, corresponding to a difference between eigenmode and time domain of approximately 6%. This difference arises from several places. Firstly, a frequency filter can not be applied to the surface data (each data set extracted requires a large amount of memory, therefore only the surface data from steady state is extracted). This means that the surface field does not exclusively contain only the modes of interest, but may also contain a small contribution from other higher order modes. The total contribution from these higher harmonics could effect the average field in ways that have not yet been studied. Secondly, as was seen with the single mode case, the cavity frequencies are not the same as was simulated in eigenmode. The difference in the numerical method results in small shifts to the frequencies of each cell. Therefore, a field profile that had a flat field in eigenmode

simulations, does not have a flat field in time domain simulations. The third harmonic mode is much more sensitive to these shifts due to the higher frequency, therefore this can change the field strength in each cell.

The current required to achieve a gradient of 100MV/m can be calculated from the shunt impedances and the detuning angles i.e. by solving

$$\frac{I_1 R_{s,1}}{4}\sin\left(2\phi_1\right) + \chi\frac{I_1 R_{s,1}}{4}\sin\left(2\phi_2\right) = 100\ \text{MV/m} \tag{7.26}$$

For the parameters discussed here, $I_1 \approx 15$ A for $a/\lambda = 0.15$ and $\sigma_z = 1$ mm. However, there is a tradeoff between transformer ratio and current. High transformer ratios require much higher currents to the lower amplitude of the fields excited. The CLIC decelerating cavities require a drive beam current of approximately 35A, however the current is increased to reduce the overall length (and therefore machine impedance) of the accelerator. It is seen here that a factor of 2 is saved in the base level of drive beam current.

These results demonstrate there is a clear potential to reduce the pulsed temperature rise in multi-harmonic cavities, and with the detuning of each mode, could be used as the basis for a high gradient multi-harmonic two beam accelerating structure.

7.3 Mode Analysis

Throughout this study, it has been assumed that the test bunch is travelling a quarter of an rf period behind the drive bunch (this is in comparison with the typical CLIC bunch spacing of 6 rf buckets). This introduces a problem of strong longitudinal and transverse wakefields created by the drive bunches but acting on the test bunches that could potentially cause large emittance dilution or lead to a beam breakup instability. A doubling of the bunch spacing requires twice the current to maintain 100MV/m accelerating gradient. It was shown in Chapter 5 that the transformer ratio will remain the same when the bunch spacing is increased by integer multiples of the rf period. It is therefore critical to determine the closest bunch spacing allowable that will not give rise to emittance dilution. A full analysis of the longitudinal and transverse modes, through eigenmode and wakefield simulations, will be performed to determine this value.

In this section, the detuned multi-harmonic cavity that was introduced in Section 7.2 will be extended to include 6 additional mid-cells, making it now a 9-cell third harmonic cavity. This is so that it is similar to other 9-cell π-mode structures that are used (for example the TESLA or FLASH cavities). Eigenmode simulations will be undertaken to determine the mode composition for both longitudinal and transverse modes, and time domain simulations will show the wakefield in each case. This is in order to determine the strength of the wakefield, and to calculate how this will affect the required bunch spacing. The fundamental and third harmonic modes of the 9-cell cavity can be seen in figure 7.8.

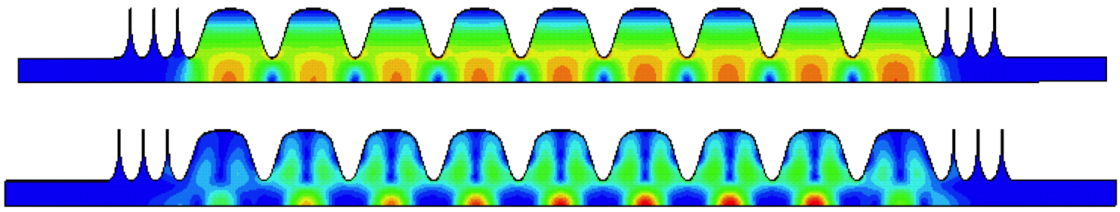

Figure 7.8: Field profiles for the fundamental accelerating mode and third harmonic mode for a 9-cell cavity.

The longitudinal and transverse dispersion curves can be found in figure 7.9. From the longitudinal dispersion curves, it can be seen that the fundamental accelerating π-mode is almost synchronous with a beam travelling at $\beta \approx 1$ (the mode is detuned so it is not expected to be perfectly intersecting with the light line). The third harmonic mode, which in this case is represented by the fifth band, is also almost synchronous with the beam with a phase advance of 3π per cell. The first 3 bands have been fitted using only the single chain circuit model, while the last 3 bands required a fit to be made to include next to nearest neighbour coupling. Figure 7.10 shows the normalised kick factor vs frequency for each of the different passbands. It can be seen in the longitudinal case (top plot) that the second and fourth bands have loss parameters of similar strength to the the fifth band (the third harmonic). These modes will be strongly excited and can have a large contribution to the longitudinal wakefield.

In the transverse plane, good agreement is seen between single mode, full cell and semi-emperical circuit model predictions. There are modes in the first two passbands which could be strongly excited due to their close proximity to the light line. The first two passbands

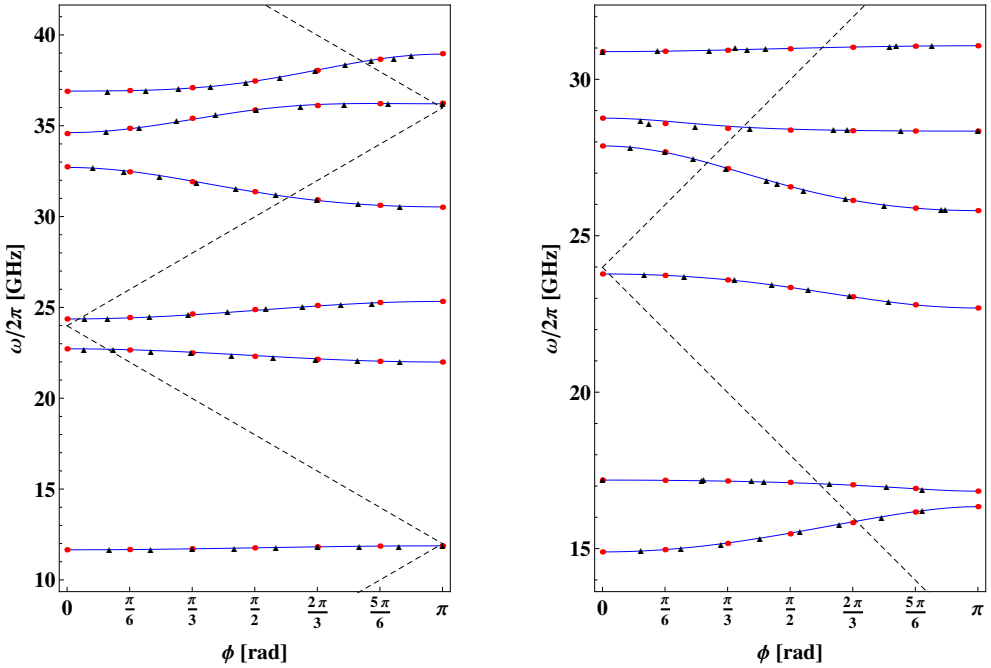

Figure 7.9: Dispersion curves for a 9-cell third harmonic detuned accelerating cavity. The left plot shows the longitudinal modes and the right shows the dipole modes. In both cases, the red points are from single cell simulations, black triangles are from multi-cell simulations (with end cells and beam pipes), the blue line is the circuit model prediction and the black dashed line is the light line.

couple strongly, as do the fourth and fifth. Weak coupling between the third and fourth and the fifth and sixth bands were required in order to get get good agreement between circuit model predictions and eigenmode. Figure 7.10 shows the transverse kick factor (bottom plot) as a function of frequency, and it can be observed that the modes with the strongest coupling to the beam are in the first and third bands, with another strong excitation in the second band.

The longitudinal and transverse wakefields can now be computed in T3P, in order to determine the field strength that will be experienced by a trailing test bunch. Initially, the longitudinal wakefield was computed using a drive bunch with Gaussian width $\sigma_z = 1$ mm with $Q_b = 1$ pC. The output from the simulation was normalised to structure length and is displayed for both short and long range cases in figure 7.11.

The Fourier transform of the longitudinal wakefield gives the longitudinal impedance. The real and imaginary parts of the impedance are found in figure 7.12. Due to the low

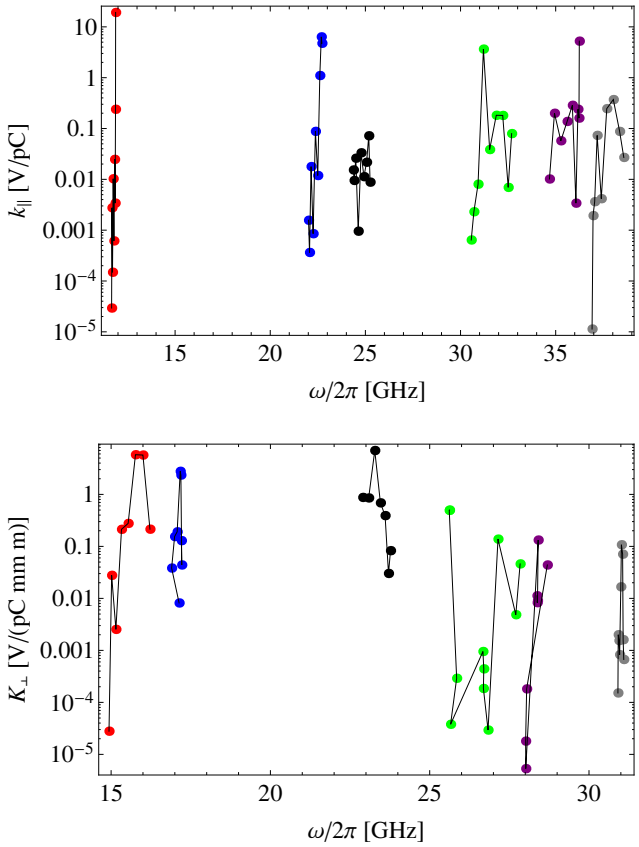

Figure 7.10: The top plot shows loss parameter vs frequency for each of the longitudinal modes in the cavity. The bottom plot shows normalised Kick factors vs frequency for each of the transverse modes. The different colours refer to the different passbands.

conductivity used on the surface (such that the fundamental modes $Q_c = 500$), it is not possible to resolve each mode within the passband. However, the passbands that contribute strongly can still be determined. It can be seen that the three major contributors to the wakefield are at 12GHz, 23GHz and 36GHz. This is in agreement with the distribution of the kick factors seen in figure 7.10.

The transverse wakefield can be found in figure 7.13 and the real and imaginary components of the transverse impedance can be found in 7.14. The impedance shows a strong coupling of the beam (relative to the other bands) to the passband at 24 GHz. Strong peaks are also observed at the first two passbands which is anticipated from figure 7.10.

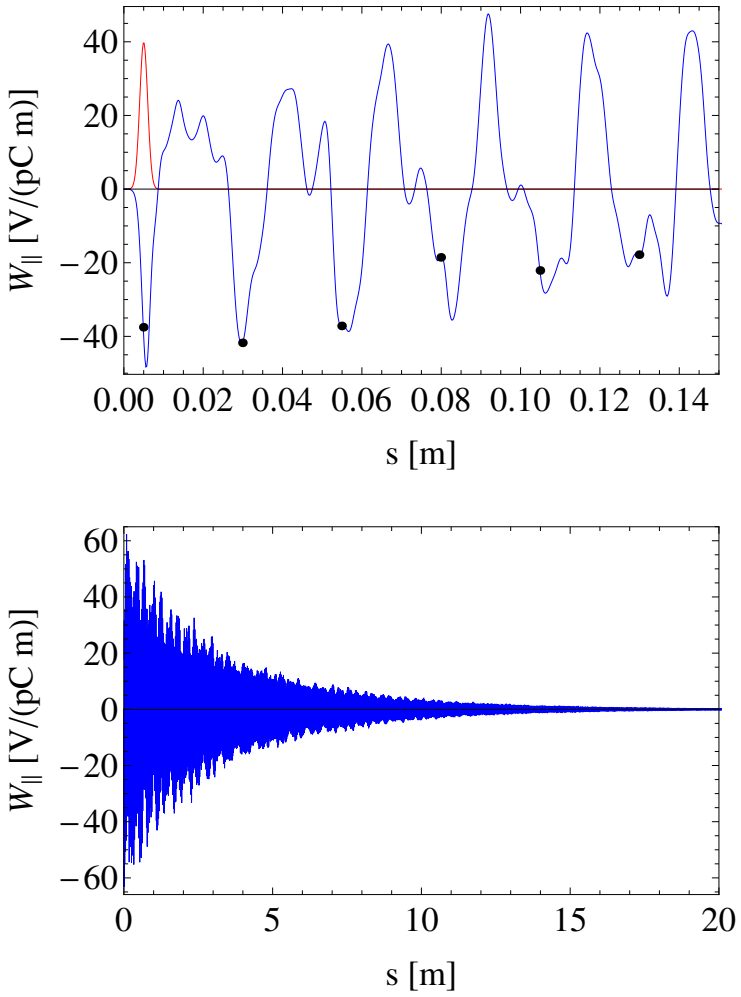

Figure 7.11: The longitudinal wakefield was simulated using the T3P code. The top figure shows the details of each oscillation over a short range. The red line gives the bunch distribution, the blue is the wakefield and the black points are arrival times of trailing drive bunches. The lower plot shows the full wakefield, with a damping time consistent with $Q_c = 500$.

The CLIC requirement on the transverse wakefield is that it must be lower than 6.6 V/(pC mm m) by the arrival time of the next bunch. Figure 7.13 shows the transverse wakefield, with black points referring to test bunches and red points referring to trailing drive bunches. It can be seen that a bunch that the first test bunch experiences an unacceptable high transverse wakefield, over 30 V/(pC mm m). It is not until approximately 8 rf buckets later that adequate damping has occurred such that a test bunch experiences a wakefield that satisfies the CLIC

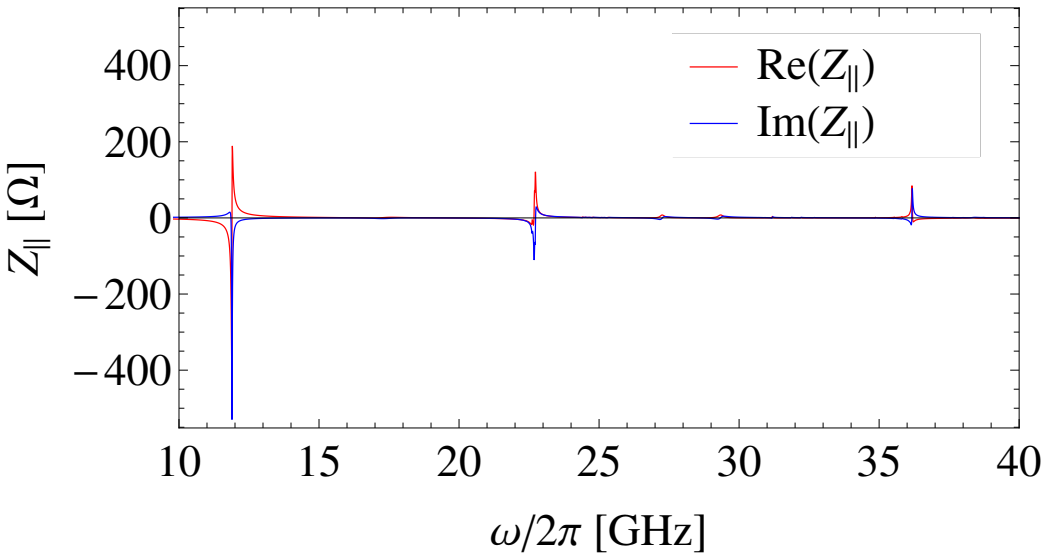

Figure 7.12: Real and imaginary components of the longitudinal impedance.

criteria. Earlier it was shown that the required current to achieve 100 MV/m for a multi-harmonic cavity was approximately 15A. With a spacing behind the drive bunch of 8 rf bucket, this needs to be increased by a factor of 8 in order to acquire 100MV/m, taking the required drive current to 120A. This is similar to the drive beam current of CLIC (100A).

It needs to be considered that the quality factor of all of the modes for this cavity are artificially low, due to the scaling of surface conductivity to give the fundamental mode $Q_c = 500$. Typical copper cavities would typically have $Q_c \approx 9000$ for monopole modes, which would require a more complex design (including HOM dampers) in order to reduce the required bunch spacing to 8 rf buckets. Were a cavity be designed that had couplers to extract and damp the HOM's this bunch spacing could be reduced further. However, challenges begin to arise in methods of damping transverse modes in between 12 GHz and 36 GHz. Any strongly excited modes will need to be removed using a method that does not negatively affect the third harmonic mode. Designing a cavity with these capabilities is the subject of future work.

This chapter has shown that a third harmonic cavity is most suitable for a beam driven

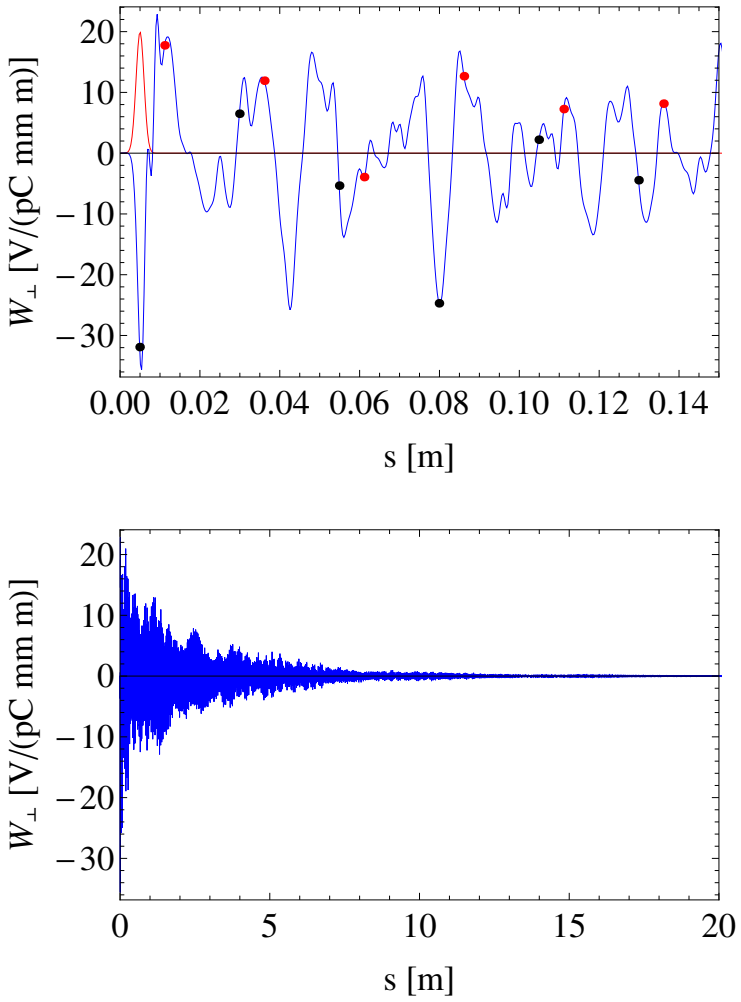

Figure 7.13: Short range (top) and long range (bottom) transverse wakefields simulated in T3P. The black points are the arrival time of the drive bunches, while the red points show the arrival time a quarter of a period (of the drive frequency) later.

collinear accelerating structure due to the high achievable transformer ratios. A structure was designed based on the elliptical cavities described in Chapter 6. Time domain simulations on the transformer ratio were shown to be in good agreement with those predicted from eigenmode simulations (within 0.5%) and the average surface magnetic field squared reduction was shown to 6% weaker in the time domain than with eigenmode simulations. This is due to the presence of other modes that were unable to be removed by the post processing.

The cavity was then extended to include additional mid cells, and a wakefield analysis

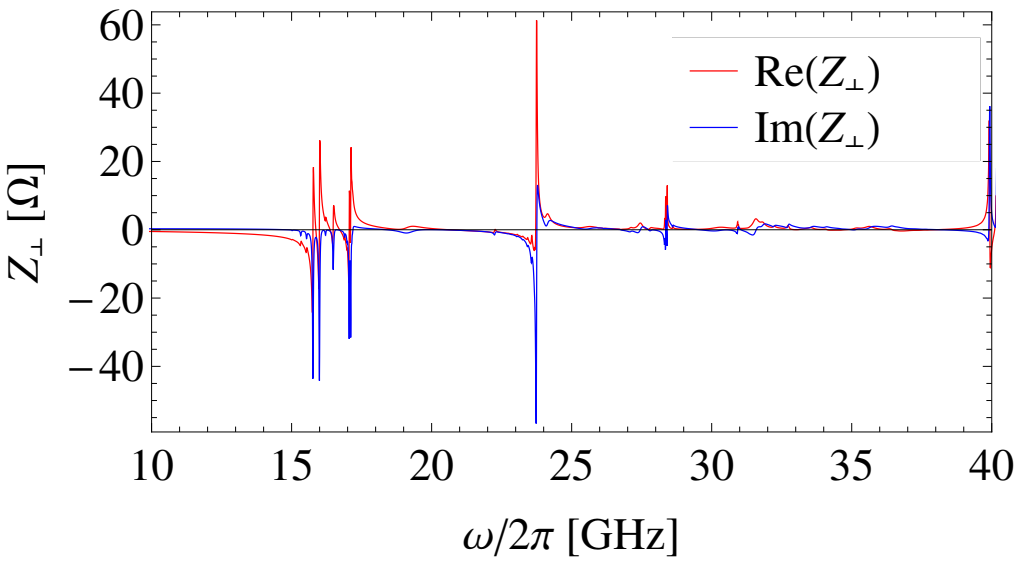

Figure 7.14: Real and imaginary components of the transverse wakefield.

was performed. This showed that in order for this cavity satisfy the CLIC requirements on the transverse wakefield, a bunch spacing of 8 rf periods is required. This would require 120A of drive beam current to achieve. However, this cavity has artificially low quality factors. As such, more complex geometries would need to be designed that can damp higher order modes if a cavity of this type was to be considered as an accelerating structure.

Chapter 8

Conclusions

This research on two beam accelerators was focused on displaying the fundamental mechanisms in collinear acceleration. Some potential to increase accelerating gradients while reducing the effects of pulsed surface heating in multi-harmonic cavities are introduced and a new analysis on the longitudinal stability of multi-harmonic cavities was performed.

Chapter 5 includes derivations of the transformer ratio in a fundamental mode detuned cavity that are based on the circuit model. A simple numerical model that approximated the beam-driven cavity field as a sum of sinusoids separated by the drive bunch repetition period was created. By calculating the ratio of the test bunch field to the drive bunch field, it was shown that the calculated transformer ratio was within 1% of the prediction from the analytical description for a wide range of detuning angles (up to $\approx 87.5°$). Larger detuning angles than this resulted in inaccurate calculations, due to the sensitivity arising from $\tan(\phi)$ dependence as the angle approaches $90°$.

Using ASTRA, an idealised bunch distribution was tracked through the E_z field extracted from simulations of a 9-cell TESLA cavity. The initial time offset of the bunch was varied in-line with the expected detuning angles of a cavity with $T = -22.5$. This tracking allowed the energy loss of a drive bunch and energy gain of a test bunch travelling $\pi/2$ behind the drive bunch to be calculated. The ratio of the energy gain of the test bunch and energy loss of the drive bunches gives the transformer ratio, which was shown to be within 0.01% of the anticipated value (from the input detuning angle). This tracking verified the methodology for calculating the transformer ratio when presented with a detuned oscillating field.

A three cell detuned cavity was then designed with $Q_c = 500$ and $\mathcal{T} = -10$ for time

domain simulations. Using the ACE3P simulation suite, the cavity was excited by a drive bunch with repetition frequency $f_d = 11.9942/2$ GHz. After filtering of higher order modes, and tracking artificial Gaussian bunches through the on-axis field, it was found that the transformer ratio was within 0.5% of the value obtained from eigenmode simulations. With the inclusion of artificial beam loading by manipulation of the cavity field, the equivalent reduction in transformer ratio was in good agreement with both theory. A second, similar cavity was designed with $\mathcal{T} = -22.5$ that showed agreement of the transformer ratio within 5% of the value calculated in eigenmode simulations. Errors arose from the achievable resolution of the bunch position caused by limited mesh density, which affects the resolution on the detuning angle. The inclusion of a low current test bunch in the simulations also showed excellent agreement with the beam loading relations derived using the circuit model. The time domain simulations that were performed are an original contribution to this area of study, and the results showed excellent agreement with theory and numerical models.

Chapter 6 moved the discussion onto multi-harmonic accelerating cavities, and attempted to quantify the benefits of temperature rise on the cavity surface, and the reduction in the onset of rf breakdown. Initially, second and third harmonic cavities π-mode standing wave cavities were designed. The accelerating gradient of each mode was normalised to 100 MV/m and the surface fields were extracted. By calculating the relative strengths of each mode, the surface fields were compared between the single mode alone and the contribution from both single and second harmonic, and single and third harmonic modes. In both cases, a reduction in the average pulsed surface heating squared was seen (the main contributor to the temperature rise on the cavity surface). This reduction was then reflected in the reduced temperature rise (which was calculated using the derivation described in Appendix C). Potentially large reductions were seen to be possible, approximately 20% for a second harmonic cavity and 12% for the third harmonic cavity. These reductions were also seen when simulating multiple coupled cells with beampipes.

A cavity that utilised the anode-cathode effect was then described. The basis of the anode-cathode effect is that a cavity can be designed such that the anode field is smaller than the cathode field on the surface. This was realised using an asymmetric second harmonic travelling wave cavity. By extracting the surface electric field for this cavity, it was shown that there was a large asymmetry in the total field over time. The peak cathode field is ap-

proximately a factor of 2 larger than the peak anode field. There are many different theories for rf breakdown, but a cavity that exhibits these properties could also be used in rf breakdown experiments. If this is indeed a mechanism for the onset of rf breakdown, then a cavity of this type could be a serious consideration for a high gradient multi-harmonic accelerating cavity.

The effect of the additional harmonic on the longitudinal beam dynamics was then explored. The Hamiltonian that describes the longitudinal motion of a particle relative to the synchronous particle for a general multi-harmonic cavity was derived and applied to second and third harmonic cavities. It was found that, depending on the phase relation desired between the fundamental and the harmonic mode, there is no damaging or limiting effect on the beam dynamics. The size and shape of the rf bucket does vary depending on the setup, but it behaves in a predictable manner. The framework required for the derivation of the Hamiltonian was based on literature, but had to extended to include additional harmonics in ways that had been seen previously. The work found in this section is currently in preparation for publication. Overall, the chapter showed there were clear benefits to the utilisation of multi-harmonic cavities, and that they could be used in a linear accelerator without compromising the longitudinal stability.

Finally, Chapter 7 combined the principles from the previous two chapters into one accelerating structure. A multi-harmonic detuned beam-driven accelerating structure was designed using eigenmode simulations. A third harmonic cavity is most suitable for beam driven applications, due to the fact that the transformer ratio for even harmonic modes is equal to -1. Therefore, a third harmonic cavity was designed such that $\mathcal{T}_1 \approx 9$ with $Q_{c,1} = 500$. The harmonic mode had its frequency tuned such that $\mathcal{T}_3 \approx -10.5$. The opposing signs allow the detuning angles of each mode to work with each other to increase (or maintain) the transformer ratio, rather than decreasing it, this is shown through calculations found in the beginning of the chapter. The cavity was modelled using a similar excitation model as to that found in Chapter 7, which also showed good levels of agreement. The cavity was simulated using the T3P code by exciting the fields with a drive bunch with repetition frequency $f_d = 11.9942/2$ GHz. Two simulations were performed, one with $\sigma_z = 4$ mm, which only allows strong excitation of the fundamental mode and another with $\sigma_z = 1$ mm, which allows strong excitation of modes with frequencies under approximately 40 GHz. It

was shown that in both the single mode and multi-mode case, the transformer ratios were in good agreement with the expected value. The surface fields were extracted from each of the simulations and the peak accelerating gradient was scaled to 100MV/m. In this case, and it could be determined that a 13% reduction in the average magnetic field squared on the surface is observed. A reduction of approximately 6% compared to what was expected from eigenmode simulations. This is the first set of time domain simulations for multi-harmonic collinear accelerating cavities, and show clearly the benefits that can be attained.

However, in order to quantify some issues relating to the transverse wakefield, a mode analysis was performed on the same cavity geometry (with an additional seven cells) that were used for the time domain simulations. However, it emerged that with a standard cavity with an artificially low Q, $Q_c = 500$, bunch spacings of up to 8 rf buckets are required to ensure the drive and test bunches do not see a field exceeding the current CLIC transverse wakefield requirement. This has the effect of increasing the required drive bunch current from approximately 15 A to 120 A. This is larger than the current CLIC drive beam current. If a structure can be designed that adequately damps the transverse wakefield, then this spacing can be reduced and the required current can be decreased and still achieve 100 MV/m.

In summary, each physics principle required for a multi-harmonic collinear accelerating structure has been shown to agree with theory. However, effects from the transverse wakefield require a more complex cavity geometry to be designed, one that is capable of damping the transverse wakefield without affecting the harmonic mode. In addition to this, experiments are currently planned at Yale University to develop a multi-harmonic rf source. This rf source is the precursor to a series of multi-harmonic breakdown studies that could lend some credence to the anode-cathode effect, and provide an experimental justification for the development and testing of cavities based upon this principle. Additionally, a single mode cavity has been designed that will allow a proof of principle experiment to be carried out on single mode detuning. The cavity has tuning rods that can detune the fundamental mode frequency. By using a beam positioning monitor, the drive bunches can excite both the BPM and the cavity (on resonance excitation). The cavity can then be detuned and the experiment repeated. The shift in the phase of the excited signals can be used to determine the detuning. This will allow a wide range of transformer ratios to be probed.

The cavities described here have shown that the physics of collinear acceleration and multi-harmonic cavities, both as individual or combined effects, are valid when considering idealised simulations. New areas of study will need to occur to show that cavities that exhibit these properties can be manufactured. These studies will provide the basis upon which a high-gradient two beam accelerator structure can be developed for use in high gradient linear colliders.

Bibliography

[1] LHC Collaboration. "LHC Design Report. Vol. I". CERN (2004).
http://ab-div.web.cern.ch/ab-div/Publications/LHC-DesignReport.html

[2] H. D. Young, R. A. Freedman, T. R. Sandin & A. L. Ford. "Sears and Zemansky's University Physics with Modern Physics". Pearson, thirteenth edition (1978).

[3] "Webpage of the Office of Naval Research".
http://www.onr.navy.mil/Media-Center/Fact-Sheets/Free-Electron-Laser.aspx

[4] I.F. Ginzburg. "Subcritical fission reactor based on linear collider".
http://inspirehep.net/record/688547

[5] S.Y. Lee. "Accelerator Physics". World Scientific (2007).

[6] K. S. Krane. "Introductory Nuclear Physics". John Wiley and Sons, first edition (1988).

[7] H. Braun, R. Corsini, J.P. Delahaye, A. de Roeck, S. Dbert, A. Ferrari, G. Geschonke, A. Grudiev, C. Hauviller, B. Jeanneret, E. Jensen, T. Lefvre, Y. Papaphilippou, G. Riddone, L. Rinolfi, W.D. Schlatter, H. Schmickler, D. Schulte, I. Syratchev, M. Taborelli, F. Tecker, R. Toms, S. Weisz & W. Wuensch. "CLIC 2008 Parameters".
http://cds.cern.ch/record/1132079?ln=en#

[8] S.Y. Kazakov, S.V. Kuzikov, Y. Jiang & J.L. Hirshfield. "High-Gradient Two-Beam Accelerator Structure", Phys. Rev. ST Accel. Beams, **13** (2010) 071303–071317.
http://link.aps.org/doi/10.1103/PhysRevSTAB.13.071303

[9] V.A. Dolgashev, S.G. Tantawi, C.D. Nantisa, Y. Higashi & T. Higo. "RF Breakdown in Normal Conducting Single-Cell Structures". In "Proceedings of the Particle Accelerator Conference 2005", pages 595–599 (2005).
http://inspirehep.net/record/703245/

[10] D. Pritzkau. "RF Pulsed Heating". Ph.D. thesis, Stanford University (2001).
http://www.slac.stanford.edu/grp/arb/tn/arbvol3/ARDB271.pdf

[11] R. Catherall, M. Augustin, C. Babcock, R. Barlow, A.P. Bernardes, S. Cimmino, M. Czapski, T. Fowler, T. Giles, M. Hermann, M. Huyse, Y. Kadi, S. Marzari, J. Montano, A. Perillo Marcone, A. Polato, T. Stora, A. Shornikov, G. Vandoni, P. Van Duppen, V. Venturi & F.J.C. Wenander. "An overview of the HIE-ISOLDE Design Study", Nucl.Instrum.Meth., **B317** (2013) 204–207.
http://inspirehep.net/record/1268555#

[12] R. Assmann et al. "Proton-driven plasma wakefield acceleration: a path to the future of high-energy particle physics".
http://inspirehep.net/record/1278193

[13] J. F. Annett. "Superconductivity, Superfluids and Condensates". OUP Oxford, first edition (2004).

[14] B.R. Martin & G. Shaw. "Particle Physics". Wiley (2008).

[15] K. Wille. "The Physics of Particle Accelerators". Oxford University Press (2005).

[16] A.C. Dexter, G. Burt, P.K. Ambattu, V. Dolgashev & R.M. Jones. "CLIC Crab Cavity Design Optimisation for Maximum Luminosity", Nucl.Instrum.Meth., **A657** (2011) 45–51.
http://inspirehep.net/record/1086285

[17] W. Herr & B. Muratori. "CAS: Intermediate Course on Accelerator Physics (Zeuthen 2003)". CERN (2003).
http://cds.cern.ch/record/941318/

[18] F. M. Renard. "Electron Positron Collisions". Edition Frontieres, first edition (1981).

[19] D. Griffiths. "Introduction to Elementary Particles". Wiley-VCH (2009).

[20] D.A. Edwards & M.J. Syphers. "An Introduction to the Physics of High Energy Accelerators". Wiley-VCH (2004).

[21] E. Todesco, L. Bottura, G. de Rijk & L. Rossi. "Dipoles for High-Energy LHC", IEEE Trans.Appl.Supercond., **24**, 3 (2014) 4004306.
http://inspirehep.net/record/1312460

[22] I.S. Grant & W.R. Phillips. "Electro-magnetism". Wiley (1990).

[23] H. Wiedemann. "Synchrotron Radiation".
http://www.slac.stanford.edu/cgi-wrap/getdoc/slac-r-637a.pdf

[24] "LEP Design Report. Vol. 2. The LEP Main Ring".
http://inspirehep.net/record/203828?ln=en

[25] S. Russenschuck. “Field Computation for Accelerator Magnets: Analytical and Numerical Methods for Electromagnetic Design and Optimization”. Wiley-VCH Verlag (2010).
http://onlinelibrary.wiley.com/doi/10.1002/9783527635467.ch1/summary

[26] ILC Collaboration. “International Linear Collider - Technical Design Report”. International Linear Collider Collaboration (2013).
http://www.linearcollider.org/ILC/Publications/Technical-Design-Report

[27] R. Wanzenberg. “Monopole, dipole and quadrupole passbands of the TESLA 9-cell cavity”.
http://inspirehep.net/record/565491?ln=en

[28] XFEL Collaboration. “The European X-Ray Free Electron Laser - Technical Design Report”. DESY XFEL Project Group (2007).
http://www.xfel.eu/documents/technical_documents

[29] H. Weise. “How To Produce 100 Superconducting Modules for the European XFEL in Collaboration and with Industry”, page WEIB03.
http://inspirehep.net/record/1313909

[30] H. Padamsee, J. Knobloch & T. Hays. “RF Superconductivity for Accelerators”. Wiley-VCH (2008).

[31] H. Hongtao, M. Zhenyu, M. Dongqing, F. Ziqiang, L. Chen, S. Jing, W. Yan, L. Zheng, X. Kai, Z. Yubin, Z. Xiang, Z. Shenjie, Z. Zhigang & L. Jianfei. “Studies of LL-type 500MHz 5-cell superconducting cavity at SINAP”, Chinese Physics C.
http://inspirehep.net/record/1305927#

[32] D. Reschke, R. Bandelmann, T. Buettner, K. Escherich, A. Goessel, B.v.d. Horst, J. Iversen, D. Klinke, G. Kreps, N. Krupka, L. Lilje, A. Matheisen, W.-D. Moeller, H. Zimmermann, C. Mueller, B. Petersen, D. Proch, M. Schmoekel, N. Steinhau-Kuehl, J.-H. Thie, H. Weise, H. Weitkaemper, R. Carcagno, T.N. Khabiboulline, S. Kotelnikov, A. Makulski, J. Nogiec, R. Nehring, M. Ross & W. Schappert. “Preparatory Procedure and Equipment for the European X-ray Free Electron Laser Cavity Implementation”, Phys. Rev. ST Accel. Beams, **13** (2010) 071001–071018.
http://link.aps.org/doi/10.1103/PhysRevSTAB.13.071001

[33] “International Linear Collider Reference Design Report”. http://www.linearcollider.org/about/Publications/Reference-Design-Report (2007).

[34] G. Caryotakis. “The Klystron: A Microwave source of surprising range and endurance”.
http://inspirehep.net/record/466664

[35] Y. Papaphilippou. "Status of the CLIC Damping Rings Design", ICFA Beam Dyn.Newslett., **62** (2013) 124–137.
http://inspirehep.net/record/1281308

[36] A. Grudiev, D. Schulte & Walter Wuensch. "Optimum frequency and gradient for the CLIC main linac accelerating structure", Conf.Proc., **C060626** (2006) 1867–1869.
http://inspirehep.net/record/737966

[37] W. Wuencsh, H. Braun, S. Döbert, I. Syratchev, I. Wilson, C. Achard & M. Taborelli. "A Demonstration of High-Gradient Acceleration". volume 1 of *Proceedings of the Particle Accelerator Conference 2003*, pages 495–497 (2003).
http://cds.cern.ch/record/619620

[38] S.T. Heikkinen, S. Calatroni & H. Neupert. "Thermal Fatigue Issues in High Gradient Particle Accelerators". In "6th International Congress on Thermal Stresses", (2005).
http://cds.cern.ch/record/921679/files/open-2006-004.pdf

[39] W. Wuensch. "Progress in Understanding the High-Gradient Limitations of Acceleration Structures". In "Proceedings of APAC 2007", Proceedings of APAC 2007 (2007).
https://accelconf.web.cern.ch/accelconf/a07/PAPERS/THYMA02.PDF

[40] A.Q. Chao. "Physics of Collective Beam Instabilities in High Energy Accelerators". Wiley Series in Beam Physics and Accelerator Technology. Wiley (1993).
http://www.slac.stanford.edu/~achao/wileybook.html

[41] V. Khan. "A Damped and Detuned Accelerating Structure for the Main Linacs of the Compact Linear Collider". Ph.D. thesis, University of Manchester (2011).
http://inspirehep.net/record/1186051/

[42] R.M. Jones. "Tranverse Wakefield Suppression Using Cell Detuning Assisted by Manifold Damping for High Gradient Linear Colliders", Nuclear Instruments and Methods in Physics Research A, **657**, 1 (2011) 59–70.
http://www.sciencedirect.com/science/article/pii/S0168900211009430

[43] A. Grudiev & W. Wuensch. "Design of the CLIC Main LINAC Accelerating Structure for CLIC Conceptual Design Report". Proceedings of LINAC 2010 (2010).
https://accelconf.web.cern.ch/accelconf/LINAC2010/papers/mop068.pdf

[44] R.M. Jones. "Wakefield Suppression in High Gradient Linacs for Lepton Linear Colliders", Phys. Rev. ST Accel. Beams, **12** (2009) 104801–104815.
http://journals.aps.org/prstab/abstract/10.1103/PhysRevSTAB.12.104801

[45] N. Shipman. "Experimental Study of DC Vacuum Breakdown and Application to High-Gradient Accelerating Structures for CLIC". Ph.D. thesis, University of Manchester

(2014).
https://cds.cern.ch/record/1999457/

[46] P.B. Wilson. "A Plasma model for RF breakdown in accelerator structures", eConf, **C00082** (2000) TUE05.
http://arxiv.org/ftp/physics/papers/0010/0010002.pdf

[47] V.A. Dolgashev & S.G. Tantawi. "RF Breakdown in X-Band Waveguides", pages 2139–2141.
http://inspirehep.net/record/609148?ln=en

[48] R.M. Jones, N.M. Kroll, T. Higo, Z. Li & R.H. Miller. "Dipole Wakefield Suppression in High Phase Advance Detuned Linear Accelerators for the JLC/NLC Designed to Minimise Electrical Breakdown and Cumulative BBU", Conf.Proc, **C0106181** (2001) 3810–3812.
http://inspirehep.net/record/560343/

[49] C. Adolphsen, W. Baumgartner, K. Jobe, R. Loewen, D. McCormick, M. Ross, T. Smith, J.W. Wang & T. Higo. "RF processing of X band accelerator structures at the NLCTA", eConf, **C000821** (2000) TUE01.
http://inspirehep.net/record/532237/

[50] W.D. Kilpatrick. "Criterion for Vacuum Sparking Designed to Include Both rf and dc", Review of Scientific Intstruments, **28**, 10 (1957) 824–826.
http://inspirehep.net/record/44645/

[51] T.J. Boyd. "Kilpatrick's Criterion". Los Alamos National Laboratory (1982).

[52] A. Degiovanni, U. Amaldi, R. Bonomi, M. Garlasché, A. Garonna, S. Verdú-AndréS & R. Wegnerers. "TERA high gradient test program of RF cavities for medical linear accelerators", Nucl.Instrum.Meth., **A657**, 1 (2011) 55–58.
http://www.sciencedirect.com/science/article/pii/S0168900211008886

[53] V.A. Dolgashev. "Progress on High-Gradient Structures", AIP Conference Proceedings, **1507**, 1 (2012) 76–84.
http://scitation.aip.org/content/aip/proceeding/aipcp/10.1063/1.4773679

[54] A Descoeudres, T Ramsvik, S Calatroni, M Taborelli & W Wuensch. "dc breakdown conditioning and breakdown rate of metals and metallic alloys under ultrahigh vacuum. DC Breakdown Conditioning and Breakdown rate of metals and metallic alloys under ultra-high vacuum".
http://cds.cern.ch/record/1248420?ln=en

[55] Antoine Descoeudres, Flyura Djurabekova & Kai Nordlund. "DC breakdown experiments with cobalt electrodes", , CERN-OPEN-2011-029. CLIC-Note-875.
https://cds.cern.ch/record/1355401?ln=en

[56] N.S. Ginzburg, I.I. Golubev, A.K. Kaminsky, A.P. Kozlov, S.V. Kuzikov, E.A. Perelstein, N.Y. Peskov, M.I. Petelin, S.N. Sedykh, A.P. Sergeev, A.S. Sergeev, A.A. Vikharev & N.I. Zaitsev. "Experiment on Pulse Heating and Surface Degradation of a Copper Cavity Powered by Powerful 30 GHz Free Electron Maser", Phys.Rev.ST Accel.Beams, **14** (2011) 041002.
http://inspirehep.net/record/896563?ln=en

[57] David Pritzkau. "Pulsed-Heating Calculations" (1996). ARDB-31.
http://www.slac.stanford.edu/grp/arb/tn/arbvol1/ARDB031.pdf

[58] D.P. Pritzkau & R.H. Siemann. "Results of an RF pulsed heating experiment at SLAC", eConf, **C000821** (2000) THA18.
http://inspirehep.net/record/531606

[59] Y. Jiang & J.L. Hirshfield. "Multi-Harmonic Accelerating Cavities for RF Breakdown Studies". In "Proceedings of IPAC 2013", Proceedings of IPAC 2013 (2013). WEPMA28.

[60] T. Wangler. "RF Linear Accelerators". Wiley-VCH (2008).

[61] J.D. Jackson. "Classical Electrodynamics". John Wiley & Sons (1962).

[62] T. Weiland & B. Zotter. "Wake Potentials of a Relativistic Current in a Cavity", Part.Accel, **11** (1981) 143–151.
http://inspirehep.net/record/155116/

[63] I. Shinton. "Longitudinal Wakefield analysis using Superfish". Tutorial Session - University of Manchester (2010).

[64] Roger M. Jones. "A study of higher-band dipole wakefields in X-band accelerating structures for the G/NLC". In "Linear accelerator. Proceedings, 22nd International Conference, Linac 2004, Luebeck, Germany, August 16-20, 2004", (2004).
http://www-public.slac.stanford.edu/sciDoc/docMeta.aspx?slacPubNumber=SLAC-PUB-10682

[65] K.L.F. Bane. "Wakefield Effects in a Linear Collider" (1986).
http://www.osti.gov/scitech/biblio/6365784

[66] K.L.F Bane & R.L. Gluckstern. "The Transverse Wakefield of a Detuned X-Band Accelerator Structure", Part.Accel., **42** (1993) 123–169.
http://inspirehep.net/record/333150/

[67] K.L.F. Bane. "Short-range dipole wakefields in accelerating structures for NLC" (2003).
http://inspirehep.net/record/614846/?ln=en

[68] P.B. Wilson. "Introduction to Wakefields and Wakepotentials", AIP.Conf.Proc., **184** (1989) 525–564.
http://inspirehep.net/record/276612/

[69] H. Wiedemann. “Particle Accelerator Physics”. Springer (2001).

[70] E.U. Condon. “Forced Oscillations in Cavity Resonators”, Journal of Applied Physics, **12** (1941) 129–132.

[71] W.K.H. Panofsky & W. Wenzel. “Some Considerations Concerning the Transverse Deflection of Charged Particles in Radiofrequency Fields”, Rev.Sci.Instrum., **27** (1956) 967.
http://inspirehep.net/record/14593

[72] B.W. Zotter & S.A. Kheifets. “Impedances and Wakes in High-Energy Particle Accelerators”. World Scientific (2000).

[73] A. K. Bandyopadhyay, A. Jostingmeier, A. S. Omar & R. Wanzenberg. “Wakes and impedance computations for the PETRA III longitudinal feedback cavity”.
http://inspirehep.net/record/769358

[74] H. Podlech. “Superconducting versus Normal Conducting Cavities”.
http://inspirehep.net/record/1225584

[75] C.S. Lee, S.W. Lee & S.L. Chuang. “Plot of Modal Field Distribution in Rectangular and Circular Waveguides”, IEEE Transactions on Microwave Theory and Techniques, **33**, 3 (1985) 271–274.
http://ieeexplore.ieee.org/xpl/articleDetails.jsp?arnumber=1132998

[76] R.M. Jones. “HOM Mitigation: Part II”. Lecture Series:CAS RF for Accelerators (2010).

[77] D. Alesini. “Power Coupling” (2011).
http://inspirehep.net/record/1081347

[78] D.E. Nagle, E.A. Knapp & B.C. Knapp. “Coupled Resonator Model for Standing Wave Accelerator Tanks”, Review of Scientific Instruments, **38**, 11 (1967) 1583–1587.
http://adsabs.harvard.edu/abs/1967RScI...38.1583N

[79] J.W. Jewett & R.A. Serway. “Physics for Scientists and Engineers”. Cengage Learning, Seventh Edition.

[80] Nawin Juntong. “Investigation of Optimised Electromagnetic Fields in SRF Cavities for the ILC”. Ph.D. thesis, University of Manchester (2011).
http://www.hep.manchester.ac.uk/u/nawin/thesis/afterVIVA/Nawin_PhDThesis_resubmit.pdf

[81] S. Döbert, A. Grudiev, G. Riddone, M. Taborelli, W. Wuencsh, R. Zennaro, S. Fukuda, Y. Higashi, T. Higo, S. Matsumoto, K. Ueno, K. Yokoyama, C. Adolphsen, V. Dolgashev, L. Laurent, J. Lewandowski, S. Tantawi, F. Wang & J.W. Wang. “High Power Test of a Low Group Velocity X-Band Accelerator Structure for CLIC”, , CERN-AB-2008-069.

CLIC-Note-767.
http://inspirehep.net/record/807233

[82] C. Adolphsen, W. Baumgartner, K. Jobe, F. Le Pimpec, R. Loewen et al. "Processing Studies of X-band Accelerator Structures at the NLCTA", Conf.Proc., **C0106181** (2001) 478–480.
http://inspirehep.net/record/561476

[83] B. Zotter & K.L.F Bane. "Transverse Modes in Periodic Cylindrical Cavities". CERN (1980).
http://cds.cern.ch/record/1307879/export/hx?ln=en

[84] G.A. Voss & T. Weiland. "The Wake Field Acceleration Mechanism", eConf, **C8209271** (1982) 287–309.
http://inspirehep.net/record/181817/files/C8209271-p287.PDF

[85] J.T. Seeman. "Collective Electron Driven Linac for High Energy Physics", IEEE Trans.Nucl.Sci., **30** (1983) 3180–3182.
http://inspirehep.net/record/204064?ln=en

[86] K.L.F. Bane, P. Chen & P.B. Wilson. "On Collinear Wake Field Acceleration", IEEE.Trans.Nucl.Sci., **32** (1985) 3524–3526.
http://slac.stanford.edu/pubs/slacpubs/3500/slac-pub-3662.pdf

[87] Y.Y. Lau, Y.S. Derbenev, R.M. Gilgenbach, J.W. Luginsland, J.M. Hochman & M.T. Walter. "A Novel Two-Beam Accelerator (Twobetron)". volume 331 of *AIP Conference Proceedings*, pages 451–462 (1995).
http://deepblue.lib.umich.edu/handle/2027.42/87548

[88] E. Esarey, P. Sprangle, J. Krall & A. Ting. "Overview of Plasma-Based Accelerator Concepts", IEEE Transactions on Plasma Science, **24**, 2 (1996) 252–288.
http://ieeexplore.ieee.org/xpl/articleDetails.jsp?arnumber=509991

[89] M. Tzoufras, W. Lu, F.S. Tsung, C. Huang, W.B. Mori, J. Vieira, R. A. Fonseca & L. O. Silva. "The Physical Picture of Beam Loading in the Blowout Regime". In "Proceedings of PAC 2007", Proceedings of PAC 2007, pages 3061–3063 (2007).
http://inspirehep.net/record/772322/citations?ln=en

[90] E. Adli, J.P. Delahaye, S.J. Gessner, M.J. Hogan, T. Raubenheimer, W. An, C. Joshi & W. Mori. "A Beam Driven Plasma-Wakefield Linear Collider: From Higgs Factory to Multi-TeV" (2013). SLAC PUB 15426.
http://arxiv.org/abs/1308.1145

[91] T. Katsouleas. "Physical Mechanisms in the Plasma Wakefield Accelerator", Physical Review A, **33**, 3.
http://journals.aps.org/pra/abstract/10.1103/PhysRevA.33.2056

[92] M. Tzoufras, W. Lu, F.S. Tsung, C. Huang, W.B. Mori, T. Katsouleas, J. Vieira, R.A. Fonseca & L.O. Silva. "Beam Loading in the Non-Linear Regime of Plasma Based Acceleration", Physical Review Letters, **101**, 14 (2008) 145002–145006.
http://journals.aps.org/prl/abstract/10.1103/PhysRevLett.101.145002

[93] I. Blumenfeld, C.E. Clayton, F.J Decker, M.J Hogan, C. Huang, R. Ischebeck, R. Iverson, C. Joshi, T. Katsouleas, N. Kirby, W. Lu, K.A. Marsh, W.B. Mori, P. Muggli, E. Oz, R.H. Siemann, D. Walz & M. Zhou. "Energy Doubling of 42 GeV Electrons in a Metre-Scale Plasma Wakefield Accelerator", **445**.
http://www.nature.com/nature/journal/v445/n7129/abs/nature05538.html

[94] W. Gai, P. Schoessow, B. Cole, R. Konecny, J. Norem, J. Rosenzweig & J. Simpson. "Experimental Demonstration of Wake-Field Effects in Dielectric Structures", Physical Review Letters, **61**, 24 (1988) 2756–2758.
http://journals.aps.org/prl/abstract/10.1103/PhysRevLett.61.2756

[95] B. M. Bolotovskii. "Theory of Cerenkov Radiation (III)", Soviet Physics Uspekhi, **4**, 5 (1962) 781.
http://iopscience.iop.org/0038-5670/4/5/A15

[96] W. Gai, M.E. Conde, R. Konecny, J. Power & P. Schoessow. "Experimental Demonstration of Dielectric Structure Based Two Beam Acceleration", eConf, **C010630** (2001) T801.
http://inspirehep.net/record/572546

[97] M.C. Thompson, H. Badakov, A.M. Cook, J.B. Rosenzweig, R. Tikhoplav, G. Travish, I. Blumenfeld, M.J. Hogan, R. Ischebeck, N. Kirby, R. Siemann, D. Walz, P. Muggli, A. Scott & R.B. Yoder. "Breakdown Limits on Gigavolt-per-Meter Electron-Beam-Driven Wakefields in Dielectric Structures", Physical Review Letters, **100**, 21 (2008) 214801–214805.
http://journals.aps.org/prl/abstract/10.1103/PhysRevLett.100.214801

[98] G. Andonian. "Electron-Beam Driven Dielectric Wakefield Accelerator Experiments in the Terahertz Regime". In "AIP Conference Proceedings 2012", volume 1507 of *AIP Conference Proceedings 2012* (2012).
http://scitation.aip.org/content/aip/proceeding/aipcp/10.1063/1.4773681

[99] A. Kanareykin & A. Altmark. "Beam-Breakup Analysis for an Annular Cherenkov High Gradient Wakefield Accelerator". In "Proceedings of IPAC 2012", Proceedings of IPAC 2012 (2012). WEPPP045.
https://accelconf.web.cern.ch/accelconf/IPAC2012/papers/weppp045.pdf

[100] S.V. Kuzikov & M.E. Plotkin. "Quasi-Optical Accelerating Structure Operated with a Superposition of Synchronised Modes". In "Infrared and Millimeter Waves, 2007 and the 2007 15th International Conference on Terahertz Electronics. IRMMW-THz. Joint 32nd International Conference on", pages 797–798 (2007).

[101] S. Kazakov, S.V. Kuzikov, M.E. Plotkin & J.L. Hirshfield. "Multimode Multi-Frequency Two-Beam Accelerating Structure, High Gradient Collaboration Workshop".

[102] S. Kazakov, S.V. Kuzikov, Y. Jiang & J.L. Hirshfield. "Two-Beam, Multi-mode Detuned Accelerating Structure", AIP Conf.Proc., **1086** (2009) 439–444.
http://inspirehep.net/record/816547/

[103] Y. Jiang. "Two-Beam Detuned-Cavity Electron Accelerator Structure". Advanced Accelerator Concepts Workshop.

[104] K. Ko, A. Candel, L. Ge, A. Kabel, R. Lee et al. "Advances in Parallel Electromagnetic Codes for Accelerator Science and Development".
http://inspirehep.net/record/889625

[105] R.N. Bracewell. "The Fourier Transform and its Applications". McGraw-Hill Kogakusha, Ltd., second edition (1978).

[106] D. Wisnivesky. "Multi-mode operation of the accelerator RF cavity". In "Particle accelerator. Proceedings, 18th Biennal Conference, PAC'99, New York, USA, March 29-April, 1999. Vol. 1-5", pages 792–794 (1999).
http://accelconf.web.cern.ch/AccelConf/p99/PAPERS/MOP57.PDF

[107] M. Yamamoto, M. Fujieda, Y. Mori, R. Muramatsu, C. Ohmori et al. "Multi-harmonic acceleration with high gradient MA cavity at HIMAC", pages 863–865.
http://inspirehep.net/record/510612

[108] V. Vogel, S.V. Kuzikov, A.A. Vikharev, J.L. Hirshfield & Y. Jiang. "A Multi-mode RF Photocathode Gun", Conf.Proc., **C110904** (2011) 1135–1137.
http://inspirehep.net/record/1183430

[109] Y. Jiang, S. Shchelkunov, V. P. Yakovlev, N. Solyak, S. V. Kuzikov & J. L. Hirshfield. "Multi-harmonic RF test stand for RF breakdown studies", AIP Conference Proceedings, **1507**, 1 (2012) 452–457.
http://scitation.aip.org/content/aip/proceeding/aipcp/10.1063/1.4773739

[110] V.A. Dolgashev, J. Neilson, S.G. Tantawi & A.D. Yeremian. "A Dual-mode Accelerating Cavity to Test RF Breakdown Dependence on RF Magnetic Fields", Conf.Proc., **C110904** (2011) 247–249.
http://inspirehep.net/record/1183680

[111] V.A. Dolgashev, S.G. Tantawi, A.D. Yeremian, S.P. Weathersby & J.R. Lewandowski. "Results of high power tests of dual mode accelerating structure". In "Vacuum Electronics Conference, IEEE International", pages 401–401 (2014).
http://ieeexplore.ieee.org/xpls/abs_all.jsp?arnumber=6857659

[112] Y. Jiang. “Unpublished”.

[113] L.R. Carver, R.M. Jones, Y. Jiang & J.L. Hirshfield. “Longitudinal Stability in Multi-Harmonic Accelerating Cavities for linacs”, Phys. Rev. ST Accel. Beams, **In Preparation** (2015) –.

[114] W.H. Press, S.A. Teukolsky, W.T. Vetterline & B.P. Flannery. “Numerical Recipes Third Edition”. Cambridge (2007).

[115] S.V. Kuzikov, S.Y. Kazakov, Y. Jiang & J.L. Hirshfield. “Asymmetric Bimodal Accelerator Cavity for Raising rf Breakdown Thresholds”, Physical Review Letters, **104** (2010) 214801. http://journals.aps.org/prl/abstract/10.1103/PhysRevLett.104.214801

[116] S.V. Kuzikov, S.Y. Kazakov, Y. Jiang & J.L. Hirshfield. “Multi-Harmonic Test Setup for RF Breakdown Studies”, Nucl.Instrum.Meth, **A657** (2011) 71–77. http://www.sciencedirect.com/science/article/pii/S0168900211011788

[117] P. Marchand. “Possible upgrading of the SLS RF system for improving the beam lifetime”. In “Particle Accelerator Conference, 1999. Proceedings of the 1999”, volume 2, pages 989–991 vol.2 (1999).

[118] K. Hanke. “Past and present operation of the CERN PS Booster”, International Journal of Modern Physics A, **28**, 13 (2013) 1330019.

[119] M. Pedrozzi, W. Gloor et al. “First operational results of the 3rd harmonic superconducting cavities in SLS and ELETTRA”. In “Particle Accelerator Conference, 2003. PAC 2003. Proceedings of the”, volume 2, pages 878–880 Vol.2 (2003).

[120] Jochen Grieser, Dieter Lens, Uta Hartel, Harald Klingbeil, Ulrich Laier et al. “A Digital Beam-Phase Control System for a Heavy-Ion Synchrotron with a Double-Harmonic Cavity System”, page WEPME004.

[121] E. Vogel, M. Bonezzi, A. Bosotti, M. Fusetti, P. Michelato et al. “Status of the XFEL 3.9 GHz Injector Section”, Conf.Proc., **C110904** (2011) 289–291.

[122] A. Chao & M. Tigner. “Handbook of Accelerator Physics and Engineering”. World Scientific (1999).

[123] F. Gerigk et al. “Conceptual Design of the Low-Power and High-Power SPL: A Superconducting H^- Linac at CERN”. CERN, Geneva (2014).

[124] R. Siemann. “Heat Diffusion” (1996). ARDB-25. http://www.slac.stanford.edu/grp/arb/tn/arbvol1/ARDB025.pdf

[125] M.L. Boas. “Mathematical Methods in the Physical Sciences”. John Wiley & Sons.

Appendix A

Frequency Scaling With Cavity Parameters

The choice of frequency for an rf cavity is very important, as a number of different effects become stronger for higher frequencies, while others may become weaker. Therefore, it is very useful to know how each of the different cavity parameters scales with frequency. This section will derive each of these relations by first deriving the surface resistance for NC and SC materials. It then becomes straightforward to see how these different effects factor in to the rest of the parameters.

This section is summarised from Refs. [5, 30, 60, 80]. Using Maxwells equations, it is possible to show that $\mathbf{E} = \mathbf{E}_0 \exp i\omega t$ with $\mathbf{j} = \sigma\mathbf{E}$ and that when considering a good conductor (valid for $\omega\epsilon \ll \sigma_c$), then

$$\nabla^2\mathbf{E} = \tau_n^2\mathbf{E}, \tag{A.1}$$

where $\tau_n = \sqrt{i\omega\sigma_c\mu_0}$, and σ_c is the conductivity of the material [30]. The approximation $\omega\epsilon \ll \sigma_c$ is valid for high frequencies, meaning the displacement current is negligible compared to the conduction current in metals.

Eqn. A.1 can be solved for a simple case, where $x > 0$ refers to a conductive region, and $x \leq 0$ is free space. Therefore a solution to the equation is

$$E_z = E_0 \exp(-\tau_n x). \tag{A.2}$$

Separating the real and imaginary components allows the equation to be re-written as

$$E_z = E_0 \exp(\frac{-x}{\delta}) \exp(\frac{-ix}{\delta}), \tag{A.3}$$

where δ is the skin depth of an AC field which is given by

$$\delta = \sqrt{\frac{2}{\omega\mu_0\sigma_c}} \propto \omega^{-1/2}. \tag{A.4}$$

Similarly for the magnetic field, the AC current density and magnetic fields are given by

$$j_z = j_0 \exp(-\tau_n x), \quad H_y = H_0 \exp(\tau_n x). \tag{A.5}$$

Analogous to the concept of ohms law for DC resistance, the surface impedance Z_s is defined as the ratio of the surface electric field E_0 to the current in the conductor I. In order to acquire the current, the current density is integrated over the entirety of the conductor

$$I = \int_0^\infty j_z(x)dx = \frac{j_0}{\tau_n}. \tag{A.6}$$

Using the fact that $j_0 = \sigma_c E_0$, the surface impedance can be re-defined as

$$Z_s = \frac{E_0}{j_0/\tau_n} = \frac{\tau_n}{\sigma_c} = \frac{\sqrt{i\omega\mu_0\sigma_c}}{\sigma_c} = R_s + iX_s. \tag{A.7}$$

The imaginary part corresponds to the surface field not being in phase with the current in the conductor due to the rate of change of magnetic flux in the conductor. R_s gives the AC resistance, whereas X_s gives the reactance. The surface resistance for a normal conducting material is thus

$$R_s = \sqrt{\frac{\omega\mu_0}{2\sigma_c}} \propto \omega^{1/2} \tag{A.8}$$

However, in the case of a superconductor, there is an additional current component on the surface of the material, the super current. In this case, the total current is the sum of the normal conducting and superconducting components. The normal component of the current is $j_n = \sigma_n E$ and

$$\sigma_n = \frac{n_n e^2 \tau}{m} \tag{A.9}$$

where n_n is the number of unpaired electrons and τ is the relaxation time. For rf currents,

$$j_s = j_{s0} \exp(i\omega t). \tag{A.10}$$

Using the first London equation, i.e.

$$\frac{\partial j_s}{\partial t} = \frac{1}{\mu_0 \lambda_L^2} E, \tag{A.11}$$

one can obtain

$$j_s = \frac{-i}{\omega\mu_0\lambda_L^2} E = -i\sigma_s E, \tag{A.12}$$

where

$$\lambda_L^2 = \frac{m}{n_s e^2 \mu_0}. \tag{A.13}$$

This gives the conductivity of the super current as

$$\sigma_s = \frac{n_s e^2}{m\omega} \tag{A.14}$$

The total current is now

$$j = j_n + j_s = (\sigma_n - i\sigma_s)E. \tag{A.15}$$

A similar treatment to the normal conducting case can now be applied. It can be shown that

$$\nabla^2 E = \tau_{tot}^2 E, \tag{A.16}$$

where

$$\tau_{tot} = \sqrt{\mu_0 \omega i(\sigma_n - i\sigma_s)}. \tag{A.17}$$

Similarly, the surface impedance is now given by

$$Z_s = \sqrt{\frac{i\omega\mu_0}{\sigma_n - i\sigma_s}}. \tag{A.18}$$

In order to derive the surface resistance for a superconducting material, the assumption that $\sigma_n \ll \sigma_s$ must be made. This is for two reasons, the first is that $\tau \ll 1/\omega$ because τ is of the order 10^{-14}s with $1/\omega$ of the order 10^{-9}s, the second is that at $T \ll T_c$, $n_n \ll n_s$ i.e. the number of unpaired electrons is much smaller than the number of paired electrons. This assumption allows the usual definition of impedance to be applied, which gives

$$R_s = \frac{1}{2}\sigma_n \omega^2 \mu_0^2 \lambda_L^2 \propto \omega^2, \tag{A.19}$$

with

$$X_s = \omega \mu_0 \lambda_L. \tag{A.20}$$

This means it is much more preferable to use SC cavities for low frequency operation, as the surface resistance are much lower than for NC.

The cavity radius is calculated from

$$b = \frac{j_0 c}{\omega} \propto \omega^{-1}, \tag{A.21}$$

where j_0 is the zeroth root of the Bessel function.

The power dissipation in a cavity is given by

$$P_d = \frac{1}{2} R_s \int_S |\mathbf{H}|^2 dS, \tag{A.22}$$

In order to make an accurate comparison, P_d is scaled to length giving P'_d. In the case of a NC cavity

$$P'_d \propto \omega^{1/2}\omega^{-1} \propto \omega^{-1/2}, \tag{A.23}$$

whereas for SC

$$P'_d \propto \omega^{2}\omega^{-1} \propto \omega^{1}. \tag{A.24}$$

The stored energy is given as

$$U = \frac{\epsilon_0}{2} \int_V |\mathbf{E}|^2 dV = \frac{\mu_0}{2} \int_V |\mathbf{H}|^2 dV. \tag{A.25}$$

Again, by scaling to length it is found that

$$U' \propto E^2 b^2 \propto \omega^{-2} \tag{A.26}$$

for both NC and SC. The quality factor of a cavity is determined by

$$Q_0 = \frac{\omega U}{P_d}. \tag{A.27}$$

For NC

$$Q_0 \propto \omega^{1}\omega^{-2}\omega^{1/2} \propto \omega^{-1/2}. \tag{A.28}$$

and for SC

$$Q_0 \propto \omega^{1}\omega^{-2}\omega^{-1} \propto \omega^{-2}. \tag{A.29}$$

R/Q_0 is determined by

$$\frac{R}{Q_0} = \frac{V^2}{\omega U}. \tag{A.30}$$

This parameter per unit length is independent of cavity material and is the same for both cases, given by

$$\frac{R'}{Q_0} \propto \omega^{-1}\omega^{2} \propto \omega. \tag{A.31}$$

Per unit length, this parameter scales as

$$\frac{R'}{Q_0} \propto \omega^{-1}\omega^{-2}. \tag{A.32}$$

This means that the shunt impedance can be calculated for NC as

$$R' \propto \omega^1 Q_0 \propto \omega^1\omega^{-1/2} \propto \omega^{1/2}, \tag{A.33}$$

while for SC

$$R' \propto \omega^1 Q_0 \propto \omega^1\omega^{-2} \propto \omega^{-1}. \tag{A.34}$$

The geometric factor is calculated from

$$G = \frac{\omega\mu_0 \int_V |\mathbf{H}|^2 dV}{\int_S |\mathbf{H}|^2 dS} \propto \frac{\omega^1\omega^{-3}}{\omega^{-2}} \propto \omega^0. \tag{A.35}$$

This parameter is independent of frequency and cavity material, which is to be expected as it is a parameter that depends only on the geometry of the cavity.

The longitudinal loss factor is calculated from

$$k'_{\parallel} = \frac{V^2}{4U} \propto \omega^2, \tag{A.36}$$

which is the same for NC and SC.

The transverse loss factor is given by

$$k'_{\perp} = \frac{k_L^{(n)}}{\omega_n r^2/c}, \tag{A.37}$$

where $k_L^{(n)} \propto \omega^2$ is the dipole loss factor for mode n, $\omega_1 \propto \omega$ is the corresponding frequency, with $r \propto \omega^{-2}$ as the axis offset the loss factor is calculated at. This factor scales as

$$k'_{\perp} \propto \frac{\omega^2}{\omega^1\omega^{-2}} \propto \omega^3. \tag{A.38}$$

The wakefields in the longitudinal and transverse plane scale with their respective loss

parameters, such that

$$W_{\perp} \propto \omega^2 \tag{A.39}$$

$$W_{\parallel} \propto \omega^3 \tag{A.40}$$

A table summarising the results can be found in below in table A.1.

Parameter	Super conducting	Normal conducting
Cavity radius (b)	ω^{-1}	ω^{1}
Surface Resistance (R_s)	ω^{2}	$\omega^{1/2}$
Power dissipation (P'_d)	ω^{1}	$\omega^{-1/2}$
Stored energy (U)	ω^{-2}	ω^{-2}
Quality factor (Q_0)	ω^{-2}	$\omega^{-1/2}$
Shunt impedance (R')	ω^{-1}	$\omega^{1/2}$
Geometric factor (G)	ω^{0}	ω^{0}
R over Q (R'/Q_0)	ω^{1}	ω^{1}
Longitudinal loss factor ($k'_{\parallel}$)	ω^{2}	ω^{2}
Transverse kick factor ($k'_{\perp}$)	ω^{3}	ω^{3}

Table A.1: Frequency scaling with cavity parameters for normal and super conducting cavities.

Appendix B

Circuit Model Applied to Beam Driven Detuned Accelerating Cavities

This section will derive, from the circuit model, the transformer ratio for two beams traversing the same cavity structure. This will be derived for only one fundamental accelerating mode, but this can be expanded in order to provide a framework for multi-harmonic multi-beam accelerator setups.

The theory found here is heavily reliant on work performed by Y. Jiang *et al*, found in Ref. [8].

The voltage in a parallel RLC circuit was derived in section 3.1, and is given by eq. 3.14, where $R = \frac{r_s}{2}$ with r_s as the shunt impedance [72]. For convenience, it can be found below

$$V = \frac{R}{1 + i2Q\delta} I. \tag{B.1}$$

For simplicity, the magnitude of detuning is the same for all cavities, however it may be advantageous to employ different signs of detuning in alternate cavities. These are henceforth referred to as "fixed" and "alternate" detuning.

The model employed has drive bunches and test bunches injected at the same frequency such that they are uniformly interleaved. For the following derivations, it is assumed that only one cavity mode is excited, however this can and will be extended to also include multi-mode excitation.

The test beam current $I_T(z,t)$ propagates along the $\hat{z}$ direction, with the drive beam current $I_D(z,t)$ propagating along either the $\hat{z}$ or the $-\hat{z}$ direction. Both beams are travelling on axis. Both of these currents can be considered as a superposition of harmonically related modal currents, with frequencies ω_s and wave numbers k_{T_s} and k_{D_s}.

$$I_T(z,t) = \sum_s I_{T_s} e^{i(\omega_s t - k_{T_s} z + \phi_{T_s})} \tag{B.2}$$

$$I_D(z,t) = \sum_s I_{D_s} e^{i(\omega_s t - k_{D_s}(z - z_0) + \phi_{D_s})} \tag{B.3}$$

where ϕ_{T_s} and ϕ_{D_s} are the initial temporal phases of the modes, the wave numbers $k_{T_s} = \frac{\omega_s}{\beta_T c}$ and $k_{D_s} = \frac{\omega_s}{\beta_D c}$ with β_T and β_D the normalised particle velocities, and z_0 is the separation between the drive and the test bunches.

The current has been decomposed into harmonically related modal currents, therefore the same can be said of the electric field. For purely axial currents, the excited spectrum is taken only to be composed of TM_{0m0} modes, which means it can be assumed that the E_z field on axis is constant within each cavity.

The steady state electric field in the nth cavity can be written as a Fourier series

$$E_z(z,t) = \sum_s E_s(z)e^{i\omega_s t}, \tag{B.4}$$

with $E = \frac{V}{g}$ where g is the cavity cap. The electric field for each mode is given as

$$E_s(z) = \frac{r_s}{2g^2}\frac{1}{1+i2Q\delta}\int_{n\Lambda-\frac{g}{2}}^{n\Lambda+\frac{g}{2}} I(z)dz \tag{B.5}$$

as follows from the parallel RLC circuit model, where n is the cavity number and Λ is the cavity period.

The integral calculates the total current that is in the cavity and normalises with respect to the cavity gap (the length of the integration). The current can be considered as

$$I(z)e^{i\omega_s t} = I_{D_s}(z,t) + I_{T_s}(z,t). \tag{B.6}$$

From this point onwards, only single modes are being considered. The sum has been removed, and the the subscript s has been suppressed, which gives

$$I_T(z,t) = I_T e^{i(\omega t - k_T z + \phi_T)} \tag{B.7}$$

$$I_D(z,t) = I_D e^{i(\omega t - k_D(z-z_0) + \phi_D)} \tag{B.8}$$

By substitution

$$\begin{aligned} I(z) &= I_T e^{i(\omega t - k_T z + \phi_T)}e^{-i\omega t} + I_D e^{i(\omega t - k_D(z-z_0)+\phi_D)}e^{-i\omega t} \\ &= I_T e^{i(\phi_T - k_T z)} + I_D e^{i(\phi_D - k_D(z-z_0))} \end{aligned} \tag{B.9}$$

Performing the integration without limits yields

$$\int I(z)dz = \frac{I_T e^{i(\phi_T - k_T z)}}{-k_T} + \frac{I_D e^{i(\phi_D - k_D(z-z_0))}}{-k_D} \tag{B.10}$$

The constant has been neglected as limits are being added

$$\begin{aligned}\int_{n\Lambda-\frac{g}{2}}^{n\Lambda+\frac{g}{2}} I(z)dz \quad &= [\frac{I_T e^{i(\phi_T-k_T z)}}{-k_T}+\frac{I_D e^{i(\phi_D-k_D(z-z_0))}}{-k_D}]_{n\Lambda-\frac{g}{2}}^{n\Lambda+\frac{g}{2}} \\ &= \frac{I_T e^{i(\phi_T-k_T(n\Lambda+\frac{g}{2}))}}{-k_T}+\frac{I_D e^{i(\phi_D-k_D(n\Lambda+\frac{g}{2}-z_0))}}{-k_D} \\ &+\frac{I_T e^{i(\phi_T-k_T(n\Lambda-\frac{g}{2}))}}{k_T}+\frac{I_D e^{i(\phi_D-k_D(n\Lambda-\frac{g}{2}-z_0))}}{k_D} \\ &= \frac{I_T}{k_T}(e^{i(\phi_T-k_T(n\Lambda-\frac{g}{2}))}-e^{i(\phi_T-k_T(n\Lambda+\frac{g}{2}))}) \\ &+\frac{I_D}{k_D}(e^{i(\phi_D-k_D(n\Lambda-\frac{g}{2}-z_0))}-e^{i(\phi_D-k_D(n\Lambda+\frac{g}{2}-z_0))})\end{aligned} \tag{B.11}$$

This can be re-arranged as

$$\frac{I_T}{k_T}e^{i(\phi_T-k_T n\Lambda)}(e^{\frac{ik_T g}{2}}-e^{-\frac{ik_T g}{2}})+\frac{I_D}{k_D}e^{i(\phi_D-k_D(n\Lambda-z_0))}(e^{\frac{ik_D g}{2}}-e^{-\frac{ik_D g}{2}}) \tag{B.12}$$

Using Eulers equation ($e^{i\theta}=\cos\theta+i\sin\theta$) it can be shown that

$$e^{ix}-e^{-ix}=\cos(x)+i\sin(x)-\cos(-x)-i\sin(-x)=2i\sin(x), \tag{B.13}$$

which means the integral can be simplified further to

$$\frac{I_T}{k_T}2i\sin(\frac{k_T g}{2}e^{i(\phi_T-k_T n\Lambda)}+\frac{I_D}{k_D}2i\sin(\frac{k_D g}{2}e^{i(\phi_D-k_D(n\Lambda-z_0))}. \tag{B.14}$$

By taking a factor of $1/g$ from the factor outside of the integral, and substituting the wave numbers the transit time factor can be defined as

$$\Theta_{T,D}=\frac{\sin(\frac{\omega g}{2\beta_{T,D}c})}{\omega g/2\beta_{T,D}c} \tag{B.15}$$

This now leaves

$$iI_T\Theta_T e^{i(\phi_T-k_T n\Lambda)}+iI_D\Theta_D e^{i(\phi_D-k_D(n\Lambda-z_0))}. \tag{B.16}$$

The modified current ratio can be defined as

$$\varsigma = \frac{I_T \Theta_T}{I_D \Theta_D} \tag{B.17}$$

and i can be treated as a phase shift of $\frac{\pi}{2}$ which yields

$$\frac{1}{g}\int_{n\Lambda-\frac{g}{2}}^{n\Lambda+\frac{g}{2}} I(z)dz = I_D\Theta_D(\xi e^{-i(\phi_T+k_T n\Lambda)} + e^{i(\phi_D+k_D(n\Lambda-z_0))}). \tag{B.18}$$

Combining this with the previous factor it is shown that

$$E_s(z) = \frac{r_s}{2g}\frac{1}{1+i2Q\delta} I_D\Theta_D(\xi e^{-i(\phi_T+k_T n\Lambda)} + e^{-i(\phi_D+k_D(n\Lambda-z_0))}). \tag{B.19}$$

The modulus of $1 + i2Q\delta$ can be calculated and combined with a phase shift, which gives $e^{i\theta}\sqrt{1+4Q^2\delta^2}$. By substitution, this yields

$$E_s(z) = \frac{r_s}{2g}\frac{e^{-i\theta_n}}{\sqrt{1+4Q^2\delta^2}} I_D\Theta_D(\xi e^{-i(\phi_T+k_T n\Lambda)} + e^{-i(\phi_D+k_D(n\Lambda-z_0))}), \tag{B.20}$$

where $\theta_n = \tan^{-1}(2Q\delta_n)$ is the phase angle between the electric field and current with $\delta_n = (-1)^{\xi n}\delta$ where $\xi = 0, 1$ for fixed or alternate detuning. Eqn. B.20 represents the detuned electric field inside a cavity. The propagator now needs to calculated. This is the factor that propagates the electric field from one cavity onto the next. This factor can be calculated according to

$$\Pi_E = \frac{E_z(z=\Lambda)}{E_z(z=0)}. \tag{B.21}$$

This can be calculated by substituting $n = 1$ and $n = 0$ into eqn. B.20 and taking the ratio. Therefore, the following expression can be obtained

$$\Pi_E = \frac{\xi e^{-ik_T\Lambda+i\phi_T} + e^{-k_D(\Lambda-z_0)+i\phi_D}}{\xi e^{i\phi_T} + e^{i(k_D z_0+\phi_D)}} e^{-i2\xi\theta}. \tag{B.22}$$

Similar, the propagation factor for the current is

$$\Pi_T = \frac{I_T(z=\Lambda)}{I_T(z=0)} = e^{-ik_T\Lambda} \tag{B.23}$$

In order to achieve phase synchronism, it is necessary for the ratio $\frac{\Pi_T}{\Pi_E}$ be equal to a real number i.e. with a zero imaginary component

$$R = \frac{\Pi_T}{\Pi_E} = \frac{\xi e^{i\phi_T} + e^{ik_D(z_0+\phi_D)}}{\xi e^{-ik_T\Lambda+i\phi_T} + e^{-i(k_D(\Lambda-z_0))+i\phi_D} e^{ik_T\Lambda}} e^{-i2\xi\theta} \tag{B.24}$$

$$= \frac{\xi e^{i\phi_T} + e^{ik_D(z_0+\phi_D)}}{\xi e^{i\phi_T} + e^{i(k_D z_0+\phi_D)} e^{i(k_t-k_D)\Lambda}} e^{-i2\xi\theta} \tag{B.25}$$

Four general cases can now be examined, fixed and alternate detuning and parallel and anti-parallel beams. The requirement for each of these cases is that the imaginary component must vanish. First, for fixed detuning $\xi = 0$, in order for R to be real $e^{i(k_T-k_D)\Lambda} = 1$, this occurs when

$$\Lambda(k_T - k_D) = 2m\pi. \tag{B.26}$$

Substituting the wave numbers gives

$$\frac{\Lambda\omega}{c}(\frac{1}{\beta_T} - \frac{1}{\beta_D}) = 2m\pi. \tag{B.27}$$

$$\frac{\beta_D}{\beta_T} = 1 + \frac{2m\pi c\beta_D}{\Lambda\omega} \tag{B.28}$$

$$\beta_T = \frac{\beta_D}{1 + \frac{2m\pi c\beta_D}{\Lambda\omega}} \tag{B.29}$$

For alternate detuning $\xi = 1$, it is necessary to evaluate the relation in the limit where the modified current ratio $\varsigma \to 0$, i.e. that the test beam current is much smaller than the drive beam current.

This leads to $e^{i(k_D-k_T)\Lambda} e^{-i2\theta} = 1$ which means

$$(k_D - k_T)\Lambda - 2\theta = 2m\pi \tag{B.30}$$

$$\frac{\Lambda\omega}{c\beta_D}(1 - \frac{\beta_D}{\beta_T}) = 2\pi(m + \frac{\theta}{\pi}) \tag{B.31}$$

$$\frac{\beta_D}{\beta_T} = 1 - (m + \frac{\theta}{\pi}\frac{2\pi c\beta_D}{\Lambda\omega} \tag{B.32}$$

$$\beta_T = \frac{\beta_D}{1 - (m + \frac{\theta}{\pi})\frac{2\pi c\beta_D}{\Lambda\omega}}. \tag{B.33}$$

The synchronism conditions can now be imposed on the expression for the electric field in the cavity.

In order to account for the time varying field, an extra factor needs to be included into B.20

$$E_s(z) = \frac{r_s}{2g}\frac{e^{-i\theta_n}}{\sqrt{1+4Q^2\delta^2}} I_D \Theta_D (\xi e^{-i(\phi_T + k_T n\Lambda)} + e^{-i(\phi_D + k_D(n\Lambda - z_0))}) e^{i\omega t} \tag{B.34}$$

The transformer ratio is defined as the ratio of the electric field seen by the test beam to the electric field seen by the drive beam i.e. $T = \frac{E_T}{E_D}$. In order to calculate the appropriate field, the real part of eq B.34 needs to be calculate and evaluated at the correct time.

Setting $A = \frac{r}{2g}\frac{\Theta_D I_D}{\sqrt{1+4Q^2\delta^2}}$, $M_T = nk_T\Lambda + \phi_T$ and $M_D = k_D(n\Lambda - z_0) + \phi_D$ gives

$$E(z,t) = Ae^{-i\theta_n}(\varsigma e^{-iM_T} + e^{-iM_D})e^{-i(-\omega t)} = Ae^{-i\theta_n}(\varsigma e^{-i(M_T - \omega t) + e^{-i(M_D - \omega t)}}) \tag{B.35}$$

Applying Eulers equation gives

$$E(z,t) = A(\cos\theta_n - i\sin\theta_n)(\varsigma[\cos(M_T - \omega t) - i\sin(M_T - \omega t)] \tag{B.36}$$

$$+ \cos(M_D - \omega t) - i\sin(M_D - \omega t)) \tag{B.37}$$

Multiplying out and taking the real part yields

$$E(z,t) = A[\cos\theta_n(\varsigma\cos(M_T - \omega t) + \cos(M_D - \omega t)) \tag{B.38}$$

$$- \sin\theta_n(\varsigma\sin(M_T - \omega t) + \sin(M_D - \omega t))] \tag{B.39}$$

Considering that $\theta_n = \tan^{-1} 2Q\delta$ then $\cos\theta_n = \frac{1}{\sqrt{1+4Q^2\delta^2}}$ and $\sin\theta_n = \frac{2Q\delta}{\sqrt{1+4Q^2\delta^2}}$.

Then

$$\frac{A}{\sqrt{1+4Q^2\delta^2}} = B = \frac{r}{2g}\frac{\Theta_D I_D}{1+4Q^2\delta^2} \tag{B.40}$$

Substituting

$$E(z,t) = B[\varsigma\cos(M_T - \omega t) + \cos(M_D - \omega t) - \tag{B.41}$$
$$2Q\delta\varsigma\sin(M_T - \omega t) - 2Q\delta\sin(M_D - \omega t) \tag{B.42}$$

The field that can do work on test particles at the centre of the nth cavity at $z = n\Lambda$ and at time $t = t_T = \frac{k_T n\Lambda}{\omega}$ is

$$E_T(n\Lambda, t_T) = \frac{r}{2g}\frac{\Theta_D I_D}{1+4Q^2\delta^2}(\varsigma\cos\phi_T + 2Q\delta\varsigma\sin\phi_T \tag{B.43}$$
$$+ \cos[k_D z_0 - (k_D - k_T)n\Lambda + \phi_D] \tag{B.44}$$
$$+ 2Q\delta\sin[k_D z_0 - (k_D - k_T)n\Lambda + \phi_D]) \tag{B.45}$$

Similarly, the excited field that acts on the drive beam particles at $t = t_D = \frac{k_D(n\Lambda - z_0)}{\omega}$ with $z = n\Lambda$ is given by

$$E_D(n\Lambda, t_D) = \frac{r}{2g}\frac{\Theta_D I_D}{1+4Q^2\delta^2}(\cos\phi_D + 2Q\delta\sin\phi_D \tag{B.46}$$
$$+ \varsigma\cos[k_D z_0 - (k_D - k_T)n\Lambda - \phi_T] - \tag{B.47}$$
$$2Q\delta\varsigma\sin[k_D z_0 - (k_D - k_T)n\Lambda - \phi_T]) \tag{B.48}$$

Eqns. B.43 and B.46 provide the basis from which a range of parameters for an accelerator setup can be explored. Here, only the electron model will be mentioned. The proton model is also included can be found in refs. [8].

For ultra relativistic electron acceleration, the drive beam and the test beam have $\beta_T \approx \beta_D \approx 1$, the beams propagate in the same direction so $k_T = k_D = k = \frac{\omega}{c}$. The transit time factors are equal $\Theta_D = \Theta_T = \Theta$ which means the modified current ratio is just the current ratio itself $\varsigma = \frac{I_T}{I_D}$. The initial phases are chosen to be $\phi_T = \phi_D = 0$. This gives the field seen by the electron test beam as

$$E_T(n\Lambda, t_T) = \frac{r}{2g}\frac{\Theta I_D}{1+4Q^2\delta^2}(\varsigma + \cos kz_0 + 2Q\delta\sin kz_0) \tag{B.49}$$

while for the co-propagating electron drive bunch. The electric field is given by

$$E_D(n\Lambda, t_D) = \frac{r}{2g}\frac{\Theta I_D}{1+4Q^2\delta^2}(1+\varsigma\cos kz_0 - 2Q\delta\varsigma\sin kz_0) \tag{B.50}$$

By choosing the appropriate phase delay between the test beam and the drive beam, then the equation for the transformer ratio can be determined.

Therefore

$$T = \frac{(\varsigma+\cos kz_0 + 2Q\delta\sin kz_0)}{(1+\varsigma\cos kz_0 - 2Q\delta\varsigma\sin kz_0)} \tag{B.51}$$

For $z_0 = (2j-\frac{1}{2})\frac{\pi}{k}$ for $j = 0$ or an integer. Then

$$T = \frac{\varsigma - 2Q\delta}{1+2Q\delta\varsigma} \tag{B.52}$$

Eq. B.52 is the beam loaded transformer ratio, and it takes into account the field excited by the test bunch as the well the drive bunch.

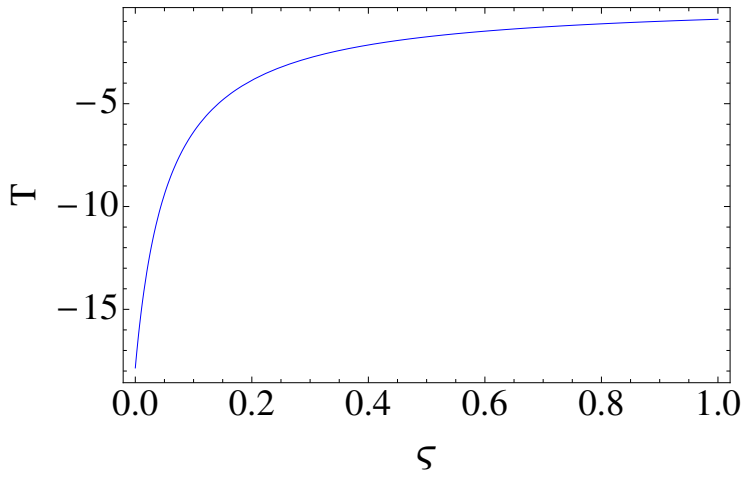

Figure B.1: Transformer ratio as a function of the modified current ratio.

Figure B.1 shows the transformer ratio versus the modified current ratio. For small values

of ς, the transformer ratio is very sensitive to the test beam current. The transformer ratio depreciates rapidly until the test bunch current is approximately 20 % the drive bunch current. By this time the transformer ratio has reduced to about 25 % the of the unloaded case.

$$\eta = -\varsigma T = \frac{2Q\delta\varsigma - \varsigma^2}{2Q\delta\varsigma + 1} \tag{B.53}$$

Appendix C

Theoretical Underpinning for Pulsed Surface Heating

This section will derive the expression used to calculate the temperature rise on the surface of a cavity due to the magnetic fields.

The following section is summarised from [10, 57, 124].

The diffusion equation is

$$\nabla^2 T + \frac{g}{k} = \frac{1}{\alpha_d^2}\frac{\partial T}{\partial t}, \tag{C.1}$$

where $\alpha_d = k/\rho c_\epsilon$, T is temperature, g is a driving source, c_ϵ is the specific heat, ρ is the density and k is the thermal conductivity of the material.

The Greens function [125] is an equation that gives the response of a system to a delta-function impulse. For the case of a one dimensional body, $\nabla \rightarrow \frac{\partial}{\partial x}$, however very similar results can be obtained for two or more dimensions [10].

In order to calculate what the response would be in this case, the driving source can be neglected, and the Greens function is given by the solution to

$$\frac{\partial^2 G(x,t)}{\partial x^2} = \frac{1}{\alpha_d^2}\frac{\partial G(x,t)}{\partial t}. \tag{C.2}$$

Taking the solution as an inverse Fourier transform of the Fourier transformed solution looks like

$$G(x,t) = \int_{-\infty}^{\infty} G(k,t)\exp(ikx)dk. \tag{C.3}$$

Substituting this solution into C.2 gives

$$-k^2 G(k,t) = \frac{1}{\alpha_d^2}\frac{\partial G(k,t)}{\partial t}, \tag{C.4}$$

which using the limits of t and t' can be integrated to give

$$G(k,t) = G(k,t')\exp(-\alpha_d^2 k^2 (t-t')). \tag{C.5}$$

By assuming a delta-function impulse at $x = x',\ t = t'$ such that $G(x,t') = \delta(x-x')$, then the Fourier transform around this point can be calculated in order to find $G(k,t')$, i.e.

$$G(k,t') = \frac{1}{2\pi}\int_{-\infty}^{\infty}\delta(x-x')\exp(-ikx)dx = \frac{\exp(-ikx')}{2\pi}. \tag{C.6}$$

Substituting these equations back into C.3 gives

$$G(x,t) = \frac{1}{2\pi}\int_{-\infty}^{\infty} \exp\left(ik(x-x')\right)\exp\left(-k^2\alpha_d^2(t-t')\right)dk. \tag{C.7}$$

By completing the square, the equation can be simply integrated by substitution to give the Greens function for the one-dimensional diffusion equation for heat as

$$G(x,t) = \begin{cases} 0 & t < t' \\ (4\pi\alpha_d(t-t'))^{-\frac{1}{2}}\exp(-\frac{(x-x')^2}{4\alpha_d(t-t')}) & t > t'. \end{cases} \tag{C.8}$$

This is a Gaussian function with width

$$\sigma = \sqrt{2\alpha_d(t-t')}. \tag{C.9}$$

As it is a one dimensional problem, a boundary can be taken at $x = 0$ where it is a vacuum when $x < 0$ and a metal when $x > 0$. The power per unit volume is given as

$$g(x,t) = \frac{dP(x,t)}{dAdx} = \frac{dP(t)}{dA}\frac{2}{\delta}\exp(-2x/\delta); \qquad x \geq 0, \tag{C.10}$$

where dP/dA is the power per unit area and δ is the skin depth. If the surface is adiabatic (no heat flow into the vacuum), heat that diffuses in the negative x-direction is reflected at the boundary. This can be accounted for with an image source or power that falls off exponentially from the surface

$$g(x,t) = \frac{dP(x,t)}{dAdx} = \frac{dP(t)}{dA}\frac{2}{\delta}\exp(2x/\delta); \qquad x \leq 0. \tag{C.11}$$

The initial and boundary conditions are:

$$T(x, t=0) = T_0 \tag{C.12}$$

$$\frac{\partial T}{\partial x}|_{x=0} = 0 \tag{C.13}$$

From the Greens function, the solution to an equation is given as a sum of all of the responses

of the equations to a series of impulses, given as

$$T(x,t) = T_0 + \frac{\alpha_d}{k}\int_0^t \int_{-\infty}^{\infty} g(x',t')G(x,t,x',t')dx'dt'. \tag{C.14}$$

The Greens function, the power per unit volume given in eqns. C.10 and C.11, can all be combined to give the temperature rise with time at any point along the material [10], shown to be

$$T(x,t) = T_0 + \frac{\alpha_d}{k}\int_0^t dt' \int_{-\infty}^{\infty} dx' \frac{dP(x',t')}{dAdx'} G(x-x', t-t'). \tag{C.15}$$

Substituting the expression for the power, the integral can be split over the two different regions giving

$$T(x,t) = T_0 + \frac{1}{\delta\rho c_\epsilon\sqrt{\pi\alpha_d}}\int_0^t \frac{1}{\sqrt{t-t'}}dt'\frac{dP(t')}{dA}[\int_{-\infty}^{0} dx' \exp(\frac{2x'}{\delta} - \frac{(x-x')^2}{4\alpha_d(t-t')}) + \int_0^{\infty} dx' \exp(-\frac{2x'}{\delta} - \frac{(x-x')^2}{4\alpha_d(t-t')})]. \tag{C.16}$$

Using

$$\beta = \frac{k}{\rho c_\epsilon}(t-t'), \tag{C.17}$$

Performing the integral with respect to x' yields

$$T(x,t) = T_0 + \frac{1}{\rho c_\epsilon \delta}\int_0^t dt' \exp(4\beta/\delta^2)\frac{dP(t')}{dA}[\exp(-2x/\delta)\text{cerf}(\frac{2\sqrt{\beta}}{\delta} - \frac{x}{2\sqrt{\beta}}) + \exp(2x/\delta)\text{cerf}(\frac{2\sqrt{\beta}}{\delta} + \frac{x}{2\sqrt{\beta}}))], \tag{C.18}$$

where cerf(x) is the complimentary error function.

When the skin depth can be neglected, the limit $\delta \to 0$ can be applied, an approximation can also be made that states

$$\text{cerf}(x) \approx \frac{1}{\sqrt{\pi}x\exp(x^2)} \tag{C.19}$$

This gives

$$T(x,t) = T_0 + \frac{1}{\sqrt{\pi}\rho c_\epsilon}\int_{-\infty}^{t} \frac{dt'}{\sqrt{\beta}} \exp(-x^2/4\beta)\frac{dP(t')}{dA}. \tag{C.20}$$

Assuming a square pulse

$$\frac{dP(t')}{dA} = \frac{R_s}{2}\hat{H}^2; \qquad 0 < t' < T_p, \tag{C.21}$$

where T_p as the pulse length and $\hat{H}$ as the peak tangential magnetic field at $x = 0$ (the surface), the limits can be changed to account for the temperature rise only when a power source is present. This can be substituted into C.20, to give temperature rise due to heating of the cavity walls for zero skin-depth is given by [10]

$$\Delta T(t) = \frac{1}{\rho c_\epsilon \sqrt{\pi \alpha_d}} \int_0^{T_p} \frac{dt'}{\sqrt{t - t'}} [\frac{1}{2} R_s |H_{\|}(t')|^2]. \tag{C.22}$$